Software-in-the-Loop combined Artificial Intelligence for Optimised Design and Dynamic Performance Prediction of Floating Offshore Wind Turbines

Peng Chen

School of Engineering

Newcastle University

for the degree of

Doctor of Philosophy

Date of Submission: 17/02/2022

Abstract

Floating Offshore Wind Turbines (FOWTs) have shown a promising future due to the goal of Net Zero emissions by 2050. However, the highly coupled nonlinear performances of FOWTs bring many challenges to the implementation of numerical and basin experimental methods in design and optimisation. This PhD project proposes an innovative method, named SADA (**S**oftware-in-the-Loop combined **A**rtificial Intelligence Method for **D**ynamic **A**nalysis of Floating Wind Turbines), to optimise the design and predict dynamic performances of FOWTs. SADA is built based on a coupled aero-hydro-servo-elastic programme *DARwind* and Machine Learning Algorithms. Firstly, the concept of Key Disciplinary Parameters (KDPs) is inspired by FOWT-related disciplinary theories. Secondly, *DARwind* will take continuous action through the Software-in-the-Loop (SIL) model to obtain more accurate prediction results. Thirdly, SADA can build data sets and analyse deep-seated physical laws of FOWTs.

Then, case studies were conducted to prove the feasibility of the SADA method on the basin experiment data. The results show that the mean values of some physical quantities can be predicted by SADA with higher accuracy than the original *DARwind* simulation results. In addition, full-scale case studies were conducted by extending SADA to engineering applications, though some design parameters are not accessible. Furthermore, other physical quantities that cannot be obtained directly in full-scale measurement easily but are of great concern to industry can also be obtained from a more credible perspective.

The proposed SADA method could benefit the wind industry by taking advantage of the numerical analysis method and AI technology. This brings a new and promising solution for overcoming the handicap impeding direct use of traditional basin experimental technology or full-scale measurement. Therefore, designers in the wind industry can optimise FOWTs designs to a higher level, thereby achieving a better method of and maintaining safe operation of FOWTs in a complex sea state.

Acknowledgements

I would like to thank Newcastle University for supporting my research and my supervisor, Prof Zhiqiang Hu, for his excellent guidance. His rigorous research attitude and thoughts on conducting research guided my entire master and doctoral studies. I am also grateful to ORE Catapult for sharing operational data of *Hywind* Scotland to support my PhD project research and providing me with valuable opportunities so that I can personally experience cutting-edge technology in the wind industry.

Thanks also to my great family. They are unadorned and wholeheartedly contributed to my education and growth. They supported me financially for the five years of living and studying in the UK and tremendous encouragement. Special thanks to my uncle Liu and Guo and my excellent and gorgeous sister Jin Liu for giving me spiritual support as a benchmark in my life and path. I hope that submitting this PhD thesis is the beginning of my return to them.

Thanks to those friends who have lived with me in the UK and the Marine, Offshore and Subsea Technology Group members for helpful discussions and generally creating a friendly workplace. Special thanks to Yichi Zhang, Yihong Li, Yerong Zhang, Jihuai Yang, and other research team members. It allows me to concentrate on academic work in such a harmonious academic atmosphere.

Finally, thanks to the scholars who have worked with me during the exchanges at Shanghai Jiao Tong University, especially Dr Jiahao Chen, who inspired and helped me a lot in the first year of my PhD research.

Table of Contents

Lists of Figures

Lists of Tables

List of abbreviations

ANN	**A**rtificial **N**eural **N**etworks
AI	**A**rtificial **I**ntelligence
BC	**B**oundary **C**ondition
BEMT	**B**lade **E**lement **M**omentum **T**heory
BF	**B**rute-**F**orce method
BP	**B**ack **P**ropagation algorithm
CFD	**C**omputational **F**luid **D**ynamics
COB	**C**entre **O**f **B**uoyancy
COG	**C**entre **O**f **G**ravity
CT	**C**ombining **T**raining in SADA
DARwind	**D**ynamic **A**nalysis for **R**esponse of **wind** turbines
DDPG	**D**eep **D**eterministic **P**olicy **G**radient algorithm
DL	**D**eep **L**earning
DOF	**D**egree **O**f **F**reedom
DPG	**D**eterministic **P**olicy **G**radient
DQN	**D**eep **Q**-learning **N**etwork
DRL	**D**eep **R**einforcement **L**earning
EPQs	**E**xperimental **P**hysical **Q**uantities
EPSRC	**E**ngineering and **P**hysical **S**ciences **R**esearch **C**ouncil
FOWTs	**F**loating **O**ffshore **W**ind **T**urbine**s**
FPSO	**F**loating **P**roduction, **S**torage and **O**ffloading
HIL	**H**ardware-**I**n-the-**L**oop
KDPs	**K**ey **D**isciplinary **P**arameter**s**
MAPE	**M**ean **A**bsolute **P**ercentage **E**rror

MARIN	**M**aritime **R**esearch **I**nstitute **N**etherlands
MBS	**M**ulti-**B**ody **S**ystem
MC Learning	**M**onte **C**arlo Learning
ML	**M**achine **L**earning
MPQs	**M**easured **P**hysical **Q**uantities
MRU	**M**otion **R**eference **U**nit
MT	**M**odel **T**est
MW	**M**ega **W**att
NON-EPQs	**NON-E**xperimental **P**hysical **Q**uantities
NON-MPQs	**NON- M**easured **P**hysical **Q**uantities
NREL	**N**ational **R**enewable **E**nergy **L**aboratory
NTNU	Norwegian University of Science and Technology
OC3	**O**ffshore **C**ode **C**omparison **C**ollaboration
OC4	**O**ffshore **C**ode **C**omparison **C**ollaboration, **C**ontinuation
OC5	**O**ffshore **C**ode **C**omparison **C**ollaboration, **C**ontinuation, with **C**orrelation
OC6	**O**ffshore **C**ode **C**omparison **C**ollaboration, **C**ontinued, with **C**orrelation, and un**C**ertainty
ORCA	**O**ffshore **R**obotics for **C**ertification of **A**ssets
O&G	**O**il and **G**as
PDF	**P**robability **D**ensity **F**unction
RAO	**R**esponse **A**mplitude **O**perator
RL	**R**einforcement **L**earning
RTHA	**R**eal-**T**ime **H**ybrid **A**pproaches
R&D	**R**esearch **& D**evelopment

SADA	**S**oftware-in-the-Loop combined **A**rtificial Intelligence Method for **D**ynamic **A**nalysis of Floating Wind Turbines
SJTU	**S**hanghai **J**iao **T**ong **U**niversity
SIL	**S**oftware-**I**n-the-**L**oop
ST	**S**ingle **T**raining in SADA
STC	**S**par **T**orus **C**ombination
TCNNA	**T**extural **C**lassifier **N**eural **N**etwork **A**lgorithm
TD Learning	**T**emporal **D**ifference Learning
TLB	**T**ension-**L**eg-**B**uoy
TLP	**T**ension-**L**eg **P**latform
TSR	**T**ip **S**peed **R**atio
WWC	**W**ind and **W**ave and **C**urrent

Nomenclature

A	Action in reinforcement learning
$\mathcal{A}$	Action space in reinforcement learning
a	the induction factor
a_c	*Glauert* correction in aerodynamic
a_{int}	An intermediate value in dynamic inflow model
a_{qs}	Quasi-static value in dynamic inflow model
a_{skew}	Modified aerodynamic induction factor in aerodynamic
C_{ld}^{H}	Added linear viscous damping matrix in hydrodynamic
C_{r}^{H}	Added linear restoring matrix in hydrodynamic
$C_{d_{Tower}}^{A}$	Tower drag in aerodynamic
$C_{d_{Platform}}^{H}$	Platform drag in hydrodynamic
C_{D}^{T}	Drag coefficient for cylindrical structures
C_D	Drag coefficients in aerodynamic
C_L	Lift coefficients in aerodynamic
C_T	Thrust coefficient in aerodynamic
e_g	Global inertial frame
e_p	Body-fixed frame of the platform
$\boldsymbol{F_H}$	Hydrodynamic loads
$\boldsymbol{F^R}$	Linear wave radiation force
$\boldsymbol{F^S}$	Restoring force of the static water in hydrodynamic
$\boldsymbol{F^V}$	Hydrodynamic damping
$\boldsymbol{F^w}$	Excitation load
$\boldsymbol{F_s^w}$	Second-order wave forces
F_P	Prandtl's tip loss factor in aerodynamic
F_r	Froude number
F_{static}	Added static force in hydrodynamic
$\boldsymbol{g}$	The gradient of the objective function
$\tilde{\boldsymbol{g}}$	The stochastic gradient
H_A	Horizontal tension in mooring dynamic

H_F	The horizontal force of the fairlead
H_s	Significant wave height
$H_{1/3}$	The mean of the one third highest waves
I_t	Turbulence intensity
K	The von Karman constant
l_b	The length of the bottom section in contact with the seabed
l_s	The length of the mooring line from the bottom point
M_{AS}	Axial stiffness in mooring dynamic
M_{C_d}	Mooring drag in mooring dynamic
M_{W_d}	Wet density in mooring dynamic
$O_{target\ data}$	Target data in percentage difference evaluation
$O_{initial\ KDPs}$	Numerical results by initial KDPs
$O_{weighted\ KDPs}$	Numerical results by weighted KDPs
$P_{initial}$	Percentage Differences of initial results
$P_{present}$	Percentage Differences of present results
$P_{difference}$	Percentage difference in SADA
$\hat{q}$	Prediction in Temporal-Difference Learning
R	Reward in reinforcement learning
R_e	Reynolds numbers
S	State in reinforcement learning
$\mathcal{S}$	State space in reinforcement learning
S'	New state in reinforcement learning
T_F	The tension of the fairlead
T_{Gen}	Generator torque in control dynamic
T_p	Spectral peak wave period
T_1	Mean wave period
u^*	The friction velocity
$\boldsymbol{U}_0$	Three-dimensional beam deformation
$U_{(z)}$	Horizontal component of the wind velocity with height
$U_{c(z)}$	Current velocity with vertical depth below the water surface
U_t	Return in reinforcement learning

V_A	Vertical tension in mooring dynamic
V_c	Current speed
V_w	Wind speed
$\boldsymbol{V_0^{wind}}$	Velocity component of upstream wind speed
$\boldsymbol{V_{TE}}$	Velocity component of the cross-section of the tower
x_k	The normalization function factor, mapminmax, in MATLAB
x_{min}	The smallest number in the data sequence
x_{max}	The largest number in the sequence
x_{norm}	The normalized value
X	Value of KDPs
X_{SF}	Significant figures of the KDPs value
Y	Number of digits to the left of the decimal point
z	The height concerning the ground level
z_0	The roughness length
z_{ref}	Related to properties at a reference height
ρ_{air}	Air density
ρ_c	The correlation coefficient
γ	Spectral peak parameter
$\boldsymbol{\phi}$	Spatial shape function matrix
φ_x^1	Polynomial Flap 1st vibration modes
φ_x^2	Polynomial Flap 2nd vibration modes
φ_y^1	Polynomial Edge 1st vibration modes
$\pi(a\|s)$	Policy function
$Q_\pi(s_t, a_t)$	Action-value function
$Q_*(s_t, a_t)$	Optimal action-value function
$V_\pi(s_t)$	State-value function
$\boldsymbol{\theta}_{new}$	the current policy network parameter
$\boldsymbol{\theta}_{now}$	The new policy network parameter

List of publications and Projects

Journal publications:

Chen, P., Chen, J. and Hu, Z. (2020) 'Review of Experimental-Numerical Methodologies and Challenges for Floating Offshore Wind Turbines', *Journal of Marine Science and Application*, 19(3), pp. 339-361 https://doi.org/10.1007/s11804-020-00165-z.

Chen, P., Chen, J. and Hu, Z. (2021) 'Software-in-the-Loop Combined Reinforcement Learning Method for Dynamic Response Analysis of FOWTs', *Frontiers in Marine Science*, 7(1242) https://doi.org/10.3389/fmars.2020.628225.

Chen, P., Song, L., Chen, J.-h. and Hu, Z. (2021) 'Simulation annealing diagnosis algorithm method for optimized forecast of the dynamic response of floating offshore wind turbines', *Journal of Hydrodynamics*, 33(2), pp. 216-225 https://doi.org/10.1007/s42241-021-0033-9.

Chen, P., Jia, C., Ng, C. and Hu, Z. (2021) 'Application of SADA method on full-scale measurement data for dynamic responses prediction of Hywind floating wind turbines', *Ocean Engineering*, 239, p. 109814 https://doi.org/10.1016/j.oceaneng.2021.109814.

Chen, J., Pei, A., Chen, P. and Hu, Z. (2021) 'Study on Gyroscopic Effect of Floating Offshore Wind Turbines', *China Ocean Engineering*, 35(2), pp. 201-214 https://doi.org/10.1007/s13344-021-0018-z.

Conference publications:

Chen, P., Hu, Z. and Hu, C. (2019) 'Software-In-the-Loop Method to Predict the Global Dynamic Responses of Full-scale Floating Wind Turbines by Artificial Neural Network', *11th International Workshop on Ship and Marine Hydrodynamics (IWSH2019)*. Hamburg, Germany. Available at: http://hdl.handle.net/11420/9015.

Chen, P., Hu, C. and Hu, Z. (2021) 'Software-in-the-Loop Combined Machine Learning for Dynamic Responses Analysis of Floating Offshore Wind Turbines', *Proceedings of the ASME 2021 40th International Conference on Ocean, Offshore and Arctic Engineering*. Virtual, Online, June 21-30. Available at: https://doi.org/10.1115/OMAE2021-65524.

Chen, P., & Hu, Z. Q. (2021, December). Blade deformation prediction of floating wind turbine based on an AI-based SADA method. In *Developments in the Analysis and Design of Marine Structures: Proceedings of the 8th International Conference on Marine Structures (MARSTRUCT 2021, 7-9 June 2021, Trondheim, Norway)* pp. 461. CRC Press.

Chen, P and Hu, Z. (2021) 'Software-in-the-loop Combined Machine Learning Method for Dynamic Response Analysis of FOWTs', *The 9th Conference on Computational Methods in Marine Engineering*. Online, 2nd and the 4th of June. Journal Hosting Service of the University of Edinburgh.

Chen, P., Hu, Z. and Hu, C. (2022) 'Dynamic Performance Prediction of Hywind Floating Wind Turbine based on SADA Method and Full-Scale Measurement Data', *6th International Conference on Maritime Technology and Engineering*. Lisbon. (Accepted)

Chen, P. and Hu, Z. (2022) 'Platform Motion Forecast of Hywind Floating Offshore Wind Turbine Based on SADA Method and Full-Scale Measurement Data', *41st International Conference on Ocean, Offshore and Arctic Engineering*. Hamburg, Germany. ASME. (Accepted)

Projects and activities:

Exchange studying in SJTU University in 2018

Offshore Code Comparison Collaboration, Continued, with Correlation, and uncertainty **(OC**6) during 2019-2022

Chapter 1. Introduction

This chapter mainly introduces the background knowledge of Floating offshore wind turbines (FOWTs). The application of artificial intelligence (AI) technology in marine technology and onshore wind turbine technology will also be introduced to show the novelty and contribution of this PhD research project to the wind industry.

1.1. Background of the offshore wind industry

Faced with the rapidly increasing energy demands and increasingly harsh environmental conditions, traditional energy supplies will be difficult to meet the demand for sustainable development. Therefore, offshore wind has enormous potential for renewable energy markets (James and Ros, 2015). Compared with the traditional fixed-bottom offshore wind power generation, the FOWTs can make use of the abundant wind resources in the deep sea and have the capacity to be towed to the wind power generation site and assembled at the port (Stewart and Muskulus, 2016b). In addition, the visual and noise impacts will be reduced due to their distance far from the coast (Musial *et al.*, 2004). General design details of offshore structures can be found in the literature (Halkyard, 2005).

Being dependent on the way of supporting the platform to obtain stability and restoring force (Froese, 2019), four main basic concepts (**Figure 1.1**) were proposed which are (Butterfield *et al.*, 2007):

- Spar-buoy type;
- Tension-leg platform (TLP) type;
- Semi-submersible type (Column stabilised);
- Pontoon-type (Barge-type).

Figure 1.1 Types of floating wind foundations (Froese, 2019).

The following content will introduce their features.

Spar type

For the spar-type, the designed centre of gravity (COG) is lower than the centre of buoyancy (COB), and the water plane is small. Therefore, the floating body has the characteristics of self-stabilisation, and the wave load received is also small. However, due to the high height of the top wind rotor at the rated wind speed, the wind can lead to a larger platform pitch. Through reasonable design, the natural frequency of the platform can avoid the range of the first-order wave force and it is also insensitive to the second-order wave force. However, the large draft design of the platform leads to a special requirement for the working water depth, which is usually more than 100 m (Muliawan *et al.*, 2013).

Semi-submersible (Semi) type

The Semi-type can generate a restoring moment to resist the tilting motion of the platform through the distributed buoy structure. The applicable water depth is usually greater than 40 m (Cao *et al.*, 2021). The motion of the platform is moderate in all directions. However,

it is sensitive to the second-order force of low-frequency waves. It is suitable for a wide range of water depths and can be transported by wet dragging with flexible deployment and relatively mature technology.

TLP type

The TLP-type balances the excess buoyancy of the floating body upward by vertical mooring tension. Therefore, it has good vertical motion performance. However, the installation process is complicated, the cost of the tension tendon structure is high and relevant experience in manufacturing and construction installation is required. The applicable water depth is usually greater than 40 m (Kausche *et al.*, 2018), and is sensitive to the second-order force of high-frequency waves.

Barge type

The Barge-type is similar to a ship, using the buoyancy of the platform to offset gravity. Its adaptability to water depth is usually greater than 30 m (Kopperstad *et al.*, 2020). It is simple in structure, easy to manufacture and has good instability. However, the natural frequency of vertical motion of the barge type is within the first-order wave frequency range. Therefore, it is more sensitive to the wave frequency response, and it is necessary to optimise the platform motion frequency in design.

In summary, **Table 1.1** summarizes the advantages and disadvantages of the four types of FOWTs foundations. Although there are many similarities between the FOWT platform and the offshore oil platform, it also has some coupling effects with the wind turbine. Therefore, it is necessary to study its stability by checking calculations and criteria under different working conditions according to its basic structure and function characteristics.

Table 1.1 Four types of FOWT foundations (Chen *et al.*, 2020a).

Types	Operation	Advantages	Disadvantages
Semi	• Wide area • Water depth>40m	• Suitable for shallow to deep water • Easy to installation • Easy to repairs	• Complex structure • Higher cost (active ballast systems)
Spar	• Water depth>100m	• Simple structure • High stability, no need for dynamic stabilization system	• Water depth limit • Requires lifting capacity to install boat • Not easily towed back to port for repairs
TLP	• Water depth>40m	• Lightweight structure •High stability, no need for dynamic stabilization system	• Complicate installation • The anchor chain is heavily loaded and prone to metal fatigue
Barge	• Water depth>30m • Sensitive to environment.	• Simple structure • Flexible transportation	• The wave frequency response is more sensitive, and needs to be optimized during design

In an earlier development of FOWTs, a significant R&D effort has been made with the appearance of coupled numerical tools (Jonkman and Sclavounos, 2006; Wayman, 2006; Jonkman, 2009). Several projects have extensively promoted the development of FOWTs. For example, *Hywind* and DeepCwind in the OC projects (Jonkman and Musial, 2010; Robertson *et al.*, 2014; Robertson *et al.*, 2017; Robertson *et al.*, 2020) and OO-Star Wind Floater (Pegalajar-Jurado *et al.*, 2018), Nautilus steel semi-submersible (Galván *et al.*, 2018), IDEOL concrete floater (Beyer *et al.*, 2015) in the LIFES50+ project, etc. **Table 1.2** shows the main contents of the two series of projects.

FOWT is a highly complex system, accounting for the coupling between aero-hydro-servo-elastic dynamics. Due to the high cost of the floating substructure and foundations, there is a sizeable overall cost difference (Wu *et al.*, 2019). More precisely, the preliminary design or analysis may cause an increase in the operation and maintenance cost of the wind farm, such as gearbox failures; accelerated blade surface erosion; accidental ship collisions. The deterioration of the mooring line over time will lead to an

increase in the failure of single or multiple lines (Lugsdin, 2012). Regardless of the aspect, only based on reasonable and reliable R&D can minimise exposure to technical risks and reduce the cost of FOWTs.

Table 1.2 OC6 and LIFE50+ projects (IEA, 2022; LIFES50+, 2022).

Types	**Task 30**	**LIFES50+**
Aim	• Validating FOWTs design tools by engineering-level modelling tools and higher-fidelity tools to measurement data.	• FOWTs in water depths from 50m to 200m • Reducing cost in short term of 10MW Offshore wind farm
Objectives and achievements	• Assessing the accuracy and reliability of simulations results. • Identifying and validating the capabilities and limitations of implemented theories • Investigating and refining applied analysis methodologies • Identifying further research and development needs.	• Two innovative substructure designs for 10MW turbines • Develop a streamlined and KPI (key performance indicator) based methodology for the evaluation and qualification process of floating substructures

1.2. Doctoral programmes overview

1.2.1. The research background and significance

Although FOWT has broad development prospects, it is still a cutting-edge emerging technology. Related research is still in the initial stage, many theoretical models are not mature, and some technical engineering problems have not been resolved. Many theories involved in FOWTs' dynamic models include massive functions and formulas conventionally determined based on assumptions and empirical parameter values. However, many assumptions and empirical parameters were not initially proposed for FOWTs but inherited from land-based wind turbines, traditional floating offshore units, or other engineering applications. For example, the lift or drag coefficient of wind turbine blades in aerodynamics can bring potential problems to the numerical simulation of the entire system. Many other critical environmental parameters, such as viscous damping in

hydrodynamics, mooring line damping values etc., are also challenging to be issued unique values during the analysis (Chen *et al.*, 2021b).

1.2.2. Motivation

The existing FOWTs' technology has gaps between academia and industry, especially integrated design, and dynamic performance prediction. Based on the above discussion, an innovative AI-based method, SADA, has been proposed in this thesis. Designers in the wind industry can optimise the FOWT designs to a higher level through SADA to achieve a better method of maintaining the safe operation of FOWTs in a complex sea state.

1.2.3. Aim and objectives

The work presented in this thesis aims to propose an innovative method for the optimised design and dynamic performance prediction of FOWTs based on AI technology. In addition, **Figure 1.2** shows the workflow during the entire PhD project. To achieve this aim, the following key objectives are identified:

- To propose an AI-based method, SADA, which uses artificial neural network technology to fit the experimental results and the numerical results of *DARwind* to optimise the dynamic performance prediction of the FOWTs.
- To expand the SADA method based on deep reinforcement learning and the concept of KDPs (the data transmission interfaces) to optimise the design and dynamic performance prediction of the FOWTs.
- To conduct case studies to verify the feasibility of the SADA method by using basin experimental data of a spar-type FOWT.
- To extend the SADA application to optimise the dynamic performance of a *Hywind* FOWT by using full-scale measurement data.

- To carry out in-depth qualitative research on KDPs in terms of boundary conditions, categories, impact, etc., to help other scholars better understand SADA and the characteristics of KDPs.

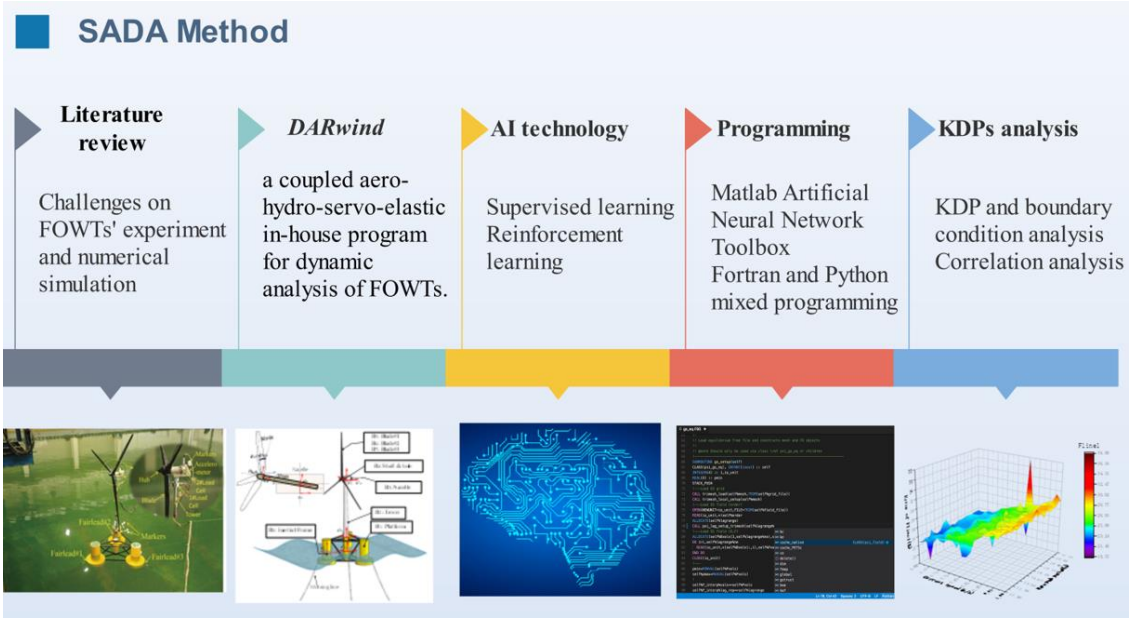

Figure 1.2 Workflow during the entire PhD program.

1.2.4. Outline of the thesis

The research content and ideas of this thesis are shown in **Figure 1.3**. More specifically, the general scope of each chapter is arranged as follows:

Chapter 2: A literature review of FOWTs' experimental and numerical techniques is conducted in this chapter. The advantages and disadvantages of the current FOWTs design and verification method are summarised. The challenges of the basin experiment of FOWTs are discussed in detail. The development of numerical simulation and hybrid approaches are summarised as well.

Chapter 3: This chapter introduces the overall of the novel SADA method, including the whole structure and methodology. The process of the entire SADA method is presented in detail in terms of experimental and full-scale measured data collection and AI technology implantation.

Chapter 4: A novel concept of KDPs in the SADA method is proposed in this chapter. The determination of the KDPs is one of the most critical steps in the SADA method. The concept of the KDPs involved in FOWTs and their impacts are introduced in this chapter in terms of Environmental KDPs, Disciplinary KDPs and Specific KDPs. Some examples are given to illustrate the details of these KDPs.

Chapter 5: An essential basis of the SADA method, in-house programme *DARwind*, is introduced in this chapter. The compilation process and theoretical basis of the time-domain coupling program *DARwind* for FOWTs are presented, including the calculation process of each functional module, the coupling method between each module, and the program's composition.

Chapter 6: The algorithms and applications of ML are introduced in this chapter. The BP algorithm and DRL methodology are the core of this chapter. Their strengths and weaknesses combined with *DARwind* will be summarised. Three training models are introduced: discrete model, continuous model and segmented model.

Chapter 7: This chapter conducts case studies for the SADA method using basin experimental data. The technical details of a Spar-type FOWT basin experiment are briefly introduced.

Chapter 8: This chapter conducts cases-of-studies for the SADA method by using full-scale measurement data collected from the *Hywind* Scotland wind farm. The details of the wind farm will be introduced, and some technical challenges of full-scale measurement will be summarised as well. Finally, two groups of KDPs were adopted to conduct the case studies.

Chapter 9: This chapter conducts a further analysis of KDPs in the SADA method. Four main issues regarding the concept of KDPs in the SADA method are investigated in this chapter: (1) What physical quantities are included in KDPs in the field of FOWTs? (2)

What is the influence of different numbers of KDPs affecting the dynamic response of FOWTs? (3) What is the influence of boundary conditions of KDPs affecting the dynamic response of FOWTs? (4) How to adjust the boundary conditions of KDPs in response to specific situations?

Chapter 10: This chapter concludes the present work. It gives remarks about the novel aspects which help this work to evolve as a contribution to FOWTs research. Finally, directions and possibilities for future research are discussed.

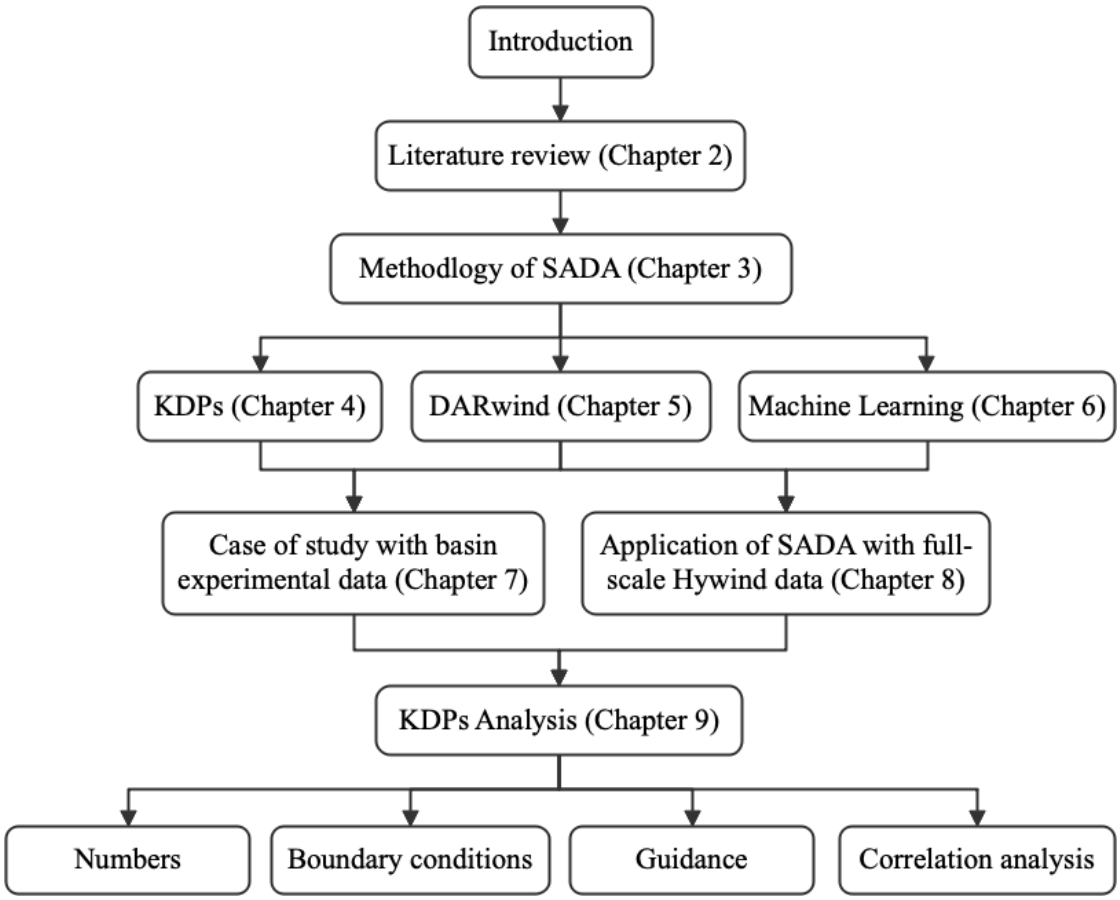

Figure 1.3 The content of this thesis.

1.2.5. Overview of novelties

Based on the above research content, the novelties of this research project can be summarized as follows:

1) Optimize existing programs *DARwind* and combine AI technology to create a novel methodology SADA using big data and numerical simulation.

2) Comprehensive use of aero-hydro-servo-elastic theories of FOWTs to build an integrated coupled dynamic model. In addition, put forward the concept of interdisciplinary KDPs involved in the prediction of a full-scale *Hywind* FOWT.

Chapter 2. Literature review

This chapter aims to critically compare and conclude the state-of-the-art approaches in the horizontal axis FOWTs design and validation method to help researchers make a footstone for proposing a more efficient and functional hybrid basin experimental method. Firstly, a brief introduction is given to the technical issues of FOWTs. Secondly, scaling problem and rotor simulation in basin model test of FOWTs. Thirdly, some numerical codes of FOWTs and the application of the hybrid basin experiment are summarised. Finally, the AI application for offshore engineering and wind industry was introduced.

2.1. Introduction of Technical issues

There are still some challenges impeding the success of more accurate prediction of FOWTs and validation of new full-scale concepts under high coupling effects. These challenges have received significant attention and led to many efforts by both academia and industry. In general, scaled model experiments, numerical simulation and full-scale measurement are three reasonable methods to demonstrate the technical feasibility of FOWTs. Chen *et al.* (2020b) summarised several inherent challenges and validation techniques in these three reasonable methods. A brief comparison of these three methods is provided in **Table 2.1**.

Table 2.1 Comparison of three different methods

Methods	**Advantages**	**Disadvantages**
Full-scale measurement	More accuracy. The actual sea state.	Limit published data. Difficult to measure. Expansive cost and high risk. Time-consuming high resources required.
Numerical simulation	Faster, Cheaper, Convenient.	High fidelity of the model. Hard to simulate nonlinear phenomena.
Model scale experiment	Nonlinear phenomena. Better controls and repeatable environmental conditions.	Scaling issues, High specific facilities are required.

2.1.1. Full-scale measurements of FOWTs

For full-scale measurements, some existing prototype projects of FOWTs are also summarised in **Table 2.2** (Chen *et al.*, 2021c). These evolving prototype projects have promoted the long-term development of the floating wind industry. For example, one commercialised wind farm in the UK since 2017 (Equinor, 2019), shown in **Figure 2.1**.

Figure 2.1 Location of *Hywind* Scotland Pilot Park (Equinor, 2019).

Table 2.2 Some prototype projects of FOWTs

	Project	Company	Capacity and Site
Semi-submersible	WindFloat	Principle Power	2MWin Aguçadoura, Portugal (2011) and Kincardine, Scotland (2018)
Barge	Damping Pool	Ideol	2MW in Le Croisic, France (2018) and 3MW in Kitakyushu, Japan (2018)
Spar	*Hywind*	Equinor	2.3MW in Karmøy, Norway (2009)
TLP	Blue H	Blue H	2.4 MW in Brindisi, Italy (2009)

Other countries and companies have also been intensively emerging in this field. Many notable projects have analysed the dynamic response of FOWTs through basin

experiments and numerical simulations. There are some commercial software and open-source programmes available now, but they are not globally acknowledged due to the difficulty of credible verifications by basin experimental data. Therefore, full-scale measurement data is one of the possible solutions. However, how to compare the results from numerical simulations and basin experiments with full-scale measurement data and make the software and codes acknowledged by the FOWTs industry is still a significant challenge. This challenge is mainly reflected in the fact that previous theoretical foundations based on onshore wind turbines or traditional offshore platforms are not necessarily fully applicable to highly coupled FOWTs.

Nonetheless, there are not many public works of literature on full-scale data in this area due to business confidentiality. Although full-scale measurement projects are seldom in FOWTs, they have been widely used in traditional offshore oil & gas engineering fields. For example, Van den Boom *et al.* (2005) discussed the importance of marine environmental conditions and platform dynamic response monitoring and related technologies. Matos *et al.* (2010) explored the slow motions of the semi-submersible platform by monitoring the frequency spectrum, thus proving the importance of considering the resonant roll and pitch motion in the design of the large-capacity semi-submersible platform. Garcia-Pineda *et al.* (2013) utilised the Textural Classifier Neural Network Algorithm (TCNNA) to process Synthetic Aperture Radar data to map oil spills in the Gulf of Mexico. In their TCNNA structure, similar environmental parameters such as wind speed are also considered. The shear index of the vertical wind profile at the height of the hub was proposed by Hasager *et al.* (2013) observing the airflow at the hub height on the North Sea offshore platform. Ma *et al.* (2013) defined the phenomenon of “swing” in the large-scale measured project of floating production, storage, and offloading (FPSO). They also show that changes in environmental factors in actual measurement need to be determined and optimised compared with traditional theories. Zhou *et al.* (2014) analysed the dynamic response of turret-moored FPSO to mooring

forces under typhoon weather. Sun *et al.* (2020a) reviewed the actual full-scale measurement of the wake effect of the wind turbine. Gao *et al.* (2018) introduced the physical testing, transportation, installation, operation, and maintenance of offshore wind turbines.

Early research on the comparison of measured data and simulated responses of the *Hywind* demonstration project can be found in Hanson *et al.* (2011). They used HAWC2 (Larsen and Hansen, 2007), SIMO (Ocean, 2017) and RIFLEX (Fylling and Soedahl, 1995) to compare the tower's bending moments, pitch and roll motions under three short-term load cases with statistical parameters. The comparison of natural frequencies and dynamic responses shows good agreement. However, the simulated high-frequency elastic response is under-predicted. Since the wave data was obtained between January and April 2010, it did not include extreme wave conditions. More verification of the *Hywind* prototype can be found in the works of literature (Skaare *et al.*, 2015; Driscoll *et al.*, 2016). In Japan, Utsunomiya *et al.* (2013) attempted to explore more. In their verification under the Typhon Sanba (1216), the highest wind speed and significant wave height reached 35.6m/s and 9.5m, respectively. Similar research can be explained in more detail in the literature (Utsunomiya *et al.*, 2014; Tanaka *et al.*, 2020).

In general, whether it is the acquisition of measured data or the application of simulation software in the previous verification of measured data, limitations are caused by many challenges. For actual measurement, obtaining the data with high accuracy is a relatively straightforward consideration. The natural sea environmental loads of floating wind farms are much more complicated than land-based wind farms. The wave-induced forces can be computed in the time domain through the wave elevation of the undisturbed wavefield at the site. However, the actual wave height acting on the floating platform is challenging to obtain, especially for the floating wind farm. It is only possible to obtain the turbulent wind field through different measurements and statistical parameters combinations. Most notably, the wind forces acting on the tower, the nacelle and the platform have other

effects. Therefore, the determination of different drag coefficients in each component is also a challenging task for the relative wind speed. The wake effect of FOWTs is another consideration for wind speed measurement. To estimate the wake losses, the wind resource distribution of the construction area will be measured via years of sampled onsite wind speed first (Hou *et al.*, 2019). As the service age increases, many factors for dynamic analysis of FOWTs will change quite a lot due to the deformation and erosion of rotor blades and marine growth on the components under wave surface. In addition, marine growth on the mooring lines and cables can damage the structures and change the hydrodynamic characteristics of the components below the water surface. In summary, these factors will affect the design and dynamic response prediction of FOWT.

2.1.2. Experimental research of FOWTs

The experiment of the scale model within a controlled environment can also be seen as an essential validation step of the qualification process of system behaviour, nonlinear phenomena, extreme and detailed loads and validating codes (Bachynski *et al.*, 2016). For example, extreme wave and viscous loads or wave-current interaction effects on floating moored structures are impossible to simulate or model in numerical simulations in the current state (Sauder *et al.*, 2016). Therefore, experimental assessments in terms of preliminary platform, turbine controller and mooring lines have been regarded as valuable and reliable methods to predict the global dynamic response of floating structures in the overall design and validation process apart from novel challenges. In addition, time efficiency and risk assessment have been required while demonstrating better controls, repeatable environmental conditions and accurate data than numerical simulation and full-scale measurement (Chen *et al.*, 2018).

Nonetheless, there are critical challenges when conducting basin experiments of FOWTs. The impossibility of applying traditional basin testing data-processing technology directly for FOWTs testing is for the listed reasons:

- **Scaling issues:** Froude number (F_r) and Reynolds number (R_e) cannot be satisfied simultaneously in the basin model test of FOWTs. However, the aerodynamic performance and hydrodynamic performance of FOWTs are both essential, and neither can be neglected. Coupling effects between aero-hydro and structural dynamics responses are also significant. Thus, full-scale performance cannot be obtained by transferring model-scale data using the traditional method, which usually neglects R_e And uses F_r as the unique dominating factor.
- **Blade pitch control strategies:** Simulation of pitch control for FOWTs is challenging to conduct under basin testing scenarios due to the mass sensitivity and signal delay.
- **Experimental facilities and calibration methods:** There are also some other challenges, including mass property simulation, installation of measurement devices and wind-wave generator techniques.

To accurately measure the coupling response of FOWT under aerodynamic load and hydrodynamic load, it is necessary to design and manufacture a controllable wind system and wave generators and wave absorbing devices. However, modelling wind, wave, and current at the same time in experiments is very challenging. This challenge lies in the very high requirements for the space and facilities of the experimental site.

Most wind generation systems are movable, which is convenient for generating wind speeds in different directions. However, the stable area for wind generators must cover the moving range of wind turbines. Taking the research of Duan *et al.* (2016a) as an example, the wind-generating system consists of 9 independent fans arranged in a 3x3 square array. Its height reached nearly 4 meters. In addition, the simulation of unsteady wind is complicated, and requires automatic computer control. A high sensitivity hot-wire anemometer is needed to measure wind speed, so that the measured instantaneous wind speed can enter the computer acquisition and analysis system.

The simulation of waves requires the laboratory to be equipped with special wave generators and wave-absorbing devices. However, current has a significant impact on the waveform. For example, the current in the same direction will lengthen the waveform, while the current in the opposite direction will shorten the waveform. Therefore, in the basin, before simulating irregular waves, the specified current speed and direction should be generated first. Similarly, in the case of wind load simulation, the simulation of irregular waves needs to be modified accordingly.

Scholars have made many efforts and summarised the current experimental and numerical progress (Stewart and Muskulus, 2016b). **Table A.1** (in Appendices) shows the different methods for conducting the experiment of FOWTs. For numerical methods, the balance between accuracy and speed (calculation time) is also an essential consideration for evaluating the dynamic response of FOWTs. The linear (or quasi-linear) method is used in the preliminary research phase. In addition, nonlinear methods are suitable for non-moderate design situations (e.g., wave-structure interaction under extreme events). Cruz and Atcheson (2016) gave a detailed explanation of the principles and applications of numerical methods and related experimental verification. They also summarised the specific issues that the designers are concerned about (for example, design load (Nichols *et al.*, 2016) and guidelines (Ronold *et al.*, 2010). However, the numerical fidelity of different software is still under testing in terms of innovative optimisation methodologies, computational efficiency, and accuracy.

2.2. Scaling issues

The first significant challenge is the scaling issues that extend to blade design problems and control strategies caused by dissimilar low Reynolds. This involves the consideration of the dynamic similarity criterion. Generally, the exact simulation of hydrodynamic and aerodynamic forces depends on the similarity of F_r and R_e, respectively. Scaling incompatibility is induced by these two factors. The appropriate scale rule and eliminating

the scale effect as much as possible can be regarded as a significant point to obtain a reasonable overall dynamic response of the whole system. Early scholars have summarised the current experiments in response to these existing challenges. Stewart and Muskulus (2016b) reviewed nine experiments of FOWTs in detail as a preliminary preparation for the Integrated Research Program on Wind Energy. In the seven experiments they discussed, the difference in scaling using Froude is mainly due to the size of the basin facility. And one of the main differences is how aerodynamic loads are applied. Three of the experiments used wind fields generated by fans. The rest of the experiments used simple constant forces to simulate steady thrust or discs instead of rotors. Although these simulated aerodynamic actuators provide dynamic feedback and correct scaling, they are limited by aerodynamic simulators. Müller *et al.* (2014) listed some representative basin experiments and projects in the past and put forward a methodology for the existing problems by redesigning model scale rotors. However, aerodynamic torque and gyroscopic momentum are not scaled correctly with their Software-in-the-Loop (SIL) procedure. Alternatively, rotating scaled mass was used to represent the rotor inertia to match the gyroscopic effects. The concept of SIL can be seen in **Figure 2.2**.

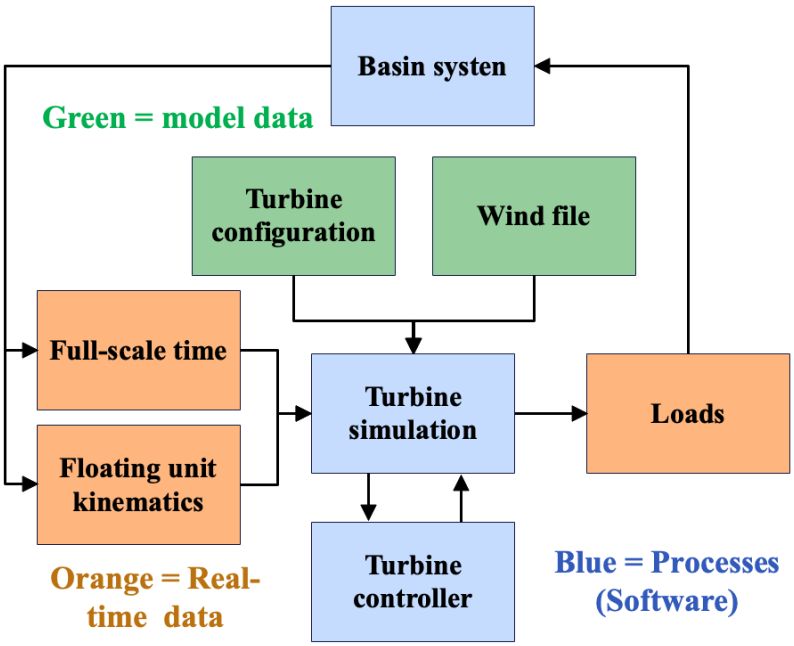

Figure 2.2 SIL operating principle (Antonutti *et al.*, 2020).

In the SIL model, the simulation of the virtual software will be regarded as a very important part, especially when it is combined with the model experiment. Using virtual software to simulate hydrodynamic or aerodynamic loads can solve scaling issues. However, this method based on the SIL model also sacrifices the coupling response of the original complete FOWT system under different loads.

2.2.1. Hydrodynamic simulation

For the basin model experiment of the traditional floating structure, Froude-scale is usually the priority because gravitational forces are the main factor that impacts the hydrodynamics of the floater rather than viscous forces. The gravitational and inertial forces in the wave force components can be accurately simulated, which are the dominant external loads for ships or floating offshore structures. A steady thrust force has been replicated using a constant horizontal force corresponding to a steady wind from Utsunomiya *et al.* (2009). Myhr *et al.* (2011) performed a 1/100th scale TLP platform in 2011. As further work in 2014, they exploited another 1/40th scale TLP. They tested to validate the hydro-elastic properties of three different Tension-Leg-Buoy (TLB) floaters, compared with an aero-servo-hydro-elastic simulation tool (3DFloat). In 2012, a simplified 1/80th scaled TLP model testing was performed by Wehmeyer *et al.* (2013) under the ultimate limit state, therefore no aerodynamic loading and gyroscopic effects were modelled. Sethuraman and Venugopal (2013) conducted a 1/100th scaled stepped-spar basin experiment at the University of Edinburgh. Their study better captures the non-linearities of the mooring lines and the four-point mooring configuration is found to offer significant reduction in surge motions. Based on the data of previous basin model tests, Gueydon (2016) carried out the validation (without control). Two numerical models were established to examine the design concept and the small-scale constructed physical model, matched at operating speed, wave, and steady wind at a fixed rate. However, these experiments focused only on hydrodynamic parts and did not consider the coupling effect of the rotor, blade. Therefore, the coupling effects between aero and hydro cannot be presented well by controller-induced platform motion.

2.2.2. Aerodynamic simulation

The R_e is usually adopted in wind tunnel tests to validate the size and parameters of the blade and rotor (Jamieson, 2018), to ensure that the viscous forces and inertial forces in the correct airflow field can be obtained. However, the R_e will become much smaller on the basin experiment of FOWTs under the Froude-scale, for example, the R_e will reduce to 1/350 under 1/50th Froude-scale (Hall *et al.*, 2014). Therefore, the R_e cannot be considered simultaneously with the F_r in FOWTs' experiment, which means difficulty replicating the coupling between aero-hydro dynamic forces (Bayati *et al.*, 2017).

If the similarity of the R_e cannot be simulated by inappropriately, a significant impact on the aerodynamic performance such as blade performance (lift and drag forces), aerodynamic damping, resulting in dissimilar thrust force, thus affecting the dynamic response performance of the entire system. Currently, the F_r is still adopted in the experiment of FOWTs to simulate the correct wave force and inertial force effect, which are also the premise rather than the R_e. For this composite model test, the density and dynamic viscosity of the airflow field are unlikely to simulate. Despite some related aerodynamic properties affected by the R_e, it mainly reflects the relative relationship between the viscous force and the inertia force (Martin, 2011). As a result, the viscous effect is usually neglected in the model test to equal the Froude similarity between model and full-scale to satisfy the gravitational and inertial similarity.

The most critical and significant aerodynamic loads are gyroscopic momentum, thrust force, and torque. These three loads are transmitted from the blade to the floater, which mainly represents aerodynamic performance (Martin *et al.*, 2014). Gyroscopic momentum can be obtained by satisfying the blade's weight, centre of gravity (COG), and rotating speed under the Froude scale. Many scholars have studied the gyroscopic effect (Gyro-effect) (Murai and Nishimura, 2010; Fujiwara *et al.*, 2011; Bahramiasl *et al.*, 2018; Chen *et al.*, 2021a). The gyro-effect of rotating blades-induced yaw motion has

been proved to not reduce generator power sharply. An experiment and numerical simulation of Gyro-effect on coupled dynamic responses has been done by Fujiwara *et al.* (2011), and the derivation of formulas for gyroscopic damping and motions. In addition, the 6 Degree of Freedoms' (DOFs') equation in the frequency domain has been provided in terms of aerodynamic loads (Semi), model test and numerical simulation (TLP) in the research of Blusseau and Patel (2012) and Bahramiasl *et al.* (2018). Karimirad (2011) demonstrated the instability of FOWTs, due to high amplitude in yaw and pitch motion coupled by Gyro-effect.

If the thrust and torque are not corrected, it cannot meet the requirements for correctly simulating the corresponding relationship of the full-scale. In addition, it is necessary to determine the priority relationship between thrust force and torque if they cannot be satisfied simultaneously. The thrust force is directly transmitted to the tower and platform, significantly impacting the whole system. Therefore, providing a correctly scaled thrust force is more accessible and feasible since torque is less critical for global dynamic responses (Martin *et al.*, 2014). In the case where the motor instead of the wind drives the rotation axis of the blade. The platform undergoes 6DOF motions under the action of wind and waves. The aerodynamic load of the wind turbine aggravates the responses of the platform. At the same time, the motion of the platform is induced by the speed of the rotor to change the flow field. Unsteady distribution, the aerodynamic load of the rotor adjusts accordingly. As the rotor rotates continuously, its aerodynamic loads generally change with the rotational position, and the platform motion affects this periodically varying load. Therefore, platform motion and rotor load are mutually coupled processes.

This coupling problem poses a challenge for the design and analysis of FOWTs and it has received much attention in recent years. Based on the free wake vortex method, Sebastian and Lackner (2012) analysed the interaction between the rotor and the downwind vortex under the pitch motion of the platform. It is considered that the change in the aerodynamic loads caused by the platform pitching motion is not negligible. Sebastian and Lackner

(2013) also assumed that the platform motions caused an unsteady flow field, compared the aerodynamic loads of fixed, and studied the freedom of motion of the platform with different influences on aerodynamics under various platform forms. Jeon *et al.* (2014) also analysed the effects of pitch motion using the vortex lattice method. Farrugia *et al.* (2014) carried out experimental research on the aerodynamic performance of the floating platform, measured the load and wake state of the rotor, and proposed that the FOWTs should reduce the longitudinal motion to avoid running at a relatively high tip speed. Rockel *et al.* (2014) studied the influence of the platform's pitch motion on the wake through wind tunnel tests. The other DOF motion of the floating body may also complicate the wake. Wu *et al.* (2015) used the Computational Fluid Dynamics (CFD) method to study the effects of platforms' sway, pitch, and yaw motions on the aerodynamic loads of the whole rotor and single blade, combined with the velocity distribution of the disk surface and wake. Power and load changes caused by platform motion. The analysis was carried out, and these changes will be considered important challenges in the study of control systems, structural fatigue, and strength. However, these studies are only for the degree of freedom of the platform motions, lack of comprehensive analysis and comparison of the 6DOF.

2.3. Rotor simulation & Blade-pitch control

The dissimilarity of direct geometric scaling of the blades cannot match the aerodynamic performance as expected. Several researchers have proposed a more sophisticated "non-geometrical" scaling approach to avoid the discussed dissimilar problem. New Froude-scale rotors and blades have been redesigned to make up for performance reductions of the aerodynamic load modelling in the experiment, including drag disk by Wan *et al.* (2015) and Cermelli *et al.* (2010) or modified low-Reynold airfoils with enlarged chord lengths (Duan *et al.*, 2016a) to only match the full-scale thrust force (de Ridder *et al.*, 2013; Fowler *et al.*, 2013; de Ridder *et al.*, 2014; Make, 2014).

2.3.1. Drag disk

Principle Power conducted a 1/67th scale model test in the first phase of WindFloat (Cermelli *et al.*, 2009; Cermelli *et al.*, 2010). Considering the excessive complexity of simulation control execution, a compromise approach was adopted, even disk instead of blades to get enough thrust. In 2010, the R_e has been well overcome by using enlarged blades in unique airfoils and roughened leading edge (Martin, 2011). The National Renewable Energy Laboratory (NREL) 5MW blade was the prototype of that Froude-scale rotor. They increased the wind speed to match the thrust force to balance the aero-hydro dynamic force between the model and full scale. Following this in 2013, second-round testing was conducted based on a semi-type of the platform, and the hybrid combination of potential flow theory and Morison's equation was considered in this specific experiment. The detailed parameters, the definition of external wave conditions, and the specification of installation (sensors) have been provided in their papers. However, limited experimental results have been published. MARIN (Maritime Research Institute Netherlands) tested FOWTs equipped with such blades in basin model tests and they were only applied to a semi-submersible platform until this project ended.

Based on Phase IV of OC3, Shin (2011) used model blades to replicate the thrust disks to conduct a 1/128th scale model test under stochastic wind and wave. Motions of the platform and rotating rotor effect include linear hydrostatics, excitation force (incident waves), radiation (outgoing), and nonlinear effects (added mass effects and viscous forces), have been discussed in their research. In addition, the spar torus combination (STC) proposed at the Norwegian University of Science and Technology (NTNU) (Wan *et al.*, 2015; Wan *et al.*, 2016; Wan *et al.*, 2017) and semi-wind energy and flap-type wave energy converter (SFC) (Luan *et al.*, 2014; Michailides *et al.*, 2014; Gao *et al.*, 2016; Michailides *et al.*, 2016) have been studied by model tests and numerical validation, based on EU FP7 MARINA Platform project. They adopted a drag disk on the top of the tower

to replicate the mean thrust on the rotor because it mainly validates the structural integrity of STC under severe sea states.

2.3.2. Re-deign rotor and blade

In 2014, three-scale relationships, including prototype-to-model (Chakrabarti, 1998), Froude-scaled wind and TSR (Jonkman, 2010), were discussed by Martin *et al.* (2014). Hansen *et al.* (2014) studied a 1/200th scale TLP with an optimised rotor and low R_e through an alternative pitch angle distribution. Duan *et al.* (2016a) conducted a 1/50th scale spar-type model test by comparing the testing results of the TMBS and GMBS under different environmental conditions. Du *et al.* (2016) examined similar geometrical blades' aerofoils, showing only 24.3% of the target. They optimised the thrust force of the model, and the lift and drag coefficient was obtained by the RANS method. The improved blade referenced by Fowler *et al.* (2013) has better aerodynamic performance than the original geometrically similar blade. This is more in line with the target value, which largely compensates for the inability of the geometrically similar blade to simulate the rotor's performance accurately. A quasi-static and unsteady methodology has been proposed by Salehyar and Zhu (2015) to analyse the aerodynamic dissipation effect. Although MARIN and SJTU have taken relevant remedial measures at low R_e, its structure for non-rotor parts (such as towers) and details of the float above the water surface will also produce unwanted extra thrust. To ensure the correct simulation of the axial thrust, the accurate collection of other aerodynamic loads, such as torque, was abandoned.

Ahn and Shin (2017) conducted a 1/128 scaled 3-leg catenary spread mooring system with a delta connection. The water depth of the entire system is matched numerically and experimentally in various combinations, including wind and rotor rotation, to predict platform performance. The validity of the numerical simulation they proposed can be assured by comparing the significant motion and response amplitude operators (RAOs) with conventional and irregular waves. Due to the small size, the blade had to be re-

corrected for the thrust force and surge excursion because the flap-wise surface of the 3D blade model was the only match in their project. For this reason, 3D printing can be used as another optimal solution for the construction of a small-scale experimental physical model.

In general, the geometric downsizing of the rotor effectively alters the aerodynamics of the scaling issues (Jain *et al.*, 2012). In this method, gyroscopic forces can be provided by a correct mean thrust force and aerodynamic damping is spinning. However, whether it is a drag disk or a modified blade, the thrust force is the only condition that has been considered in the preview experiment. More detailed investigations' fidelity will be lose if the torque, rotor blades' load, scalability for aerodynamic damping at different wind speeds and advanced blade pitch control cannot be considered.

2.3.3. Blade-pitch control strategies

How to simulate the rotation of the rotor is related to control technology. Adjusting the blade-pitch angle and generator torque is one of the essential requirements in most wind turbines (Pao and Johnson, 2011), which are discussed above briefly. In general, under different wind speed, the control strategies vary.

- **Wind speed < rated:** The maximum power is the priority, and the generator torque will adjust (pitch angle keeps 0).
- **Wind speed > rated:** The generator's torque constant by adjusting pitch angle to maintain stable power output.

It is appropriate for both land-based and floating types. However, due to the particularity of FOWTs, the standard land-based control strategies cannot apply to the floating turbine blade directly (Jonkman, 2008). It is a challenge to use the controller on a floating platform, which will make the floater unstable, especially when the damping and the controller mode are within the same bandwidth (Savenije and Peeringa, 2014, p. 2). This

is precisely mentioned above, the poly-trope of thrust force on the rotor. In this case, good control strategies for active turbine blades and generator control ensure stable operation of FOWTs, including maintaining appropriate rotating speed and power regulation (Pardalos *et al.*, 2013), as well as reducing the motions and a substantial load of floaters (Savenije and Peeringa, 2014). In general, not only do the motions of the floater impact the superstructure, but the controllers will influence the floaters, which are also coupled effects.

Many scholars have conducted numerous studies on these specific blade-pitch control strategies. Namik and Stol (2013) provide a detailed review of FOWTs' controllers. Savenije and Peeringa (2014) provided a brief review of control development for FOWTs and compared four different controllers, including FPfloat (fixed pitch), OC3 float, ECNland (without modifications) and ECNfloat. Some researchers have investigated the active blade-pitch control and generator control based on global dynamic responses of FOWTs (Bredmose *et al.*, 2017; Goupee *et al.*, 2017; Yu *et al.*, 2017). Although some blade-pitch control systems have been investigated in this area and achieved specific results, few references are available to how the control strategies are combined with a real-time hybrid experiment, especially the influence of active turbine controls.

José *et al.* (2014) proposed another approach that performed a 1/40th scale test of semi-type FOWTs. They applied a ducted fan to provide the required thrust force. Although it was controlled via a real-time numerical simulation with active controls, it still had a limited ramping rate and results integrated with simulation results very well. Goupee *et al.* (2014) compared campaigns using a geometrically similar and improved performance-matched DeepCwind model (OC4 Phase II) conducted in 2011 and 2013, respectively. As a corrective measure, the wind speed was increased to obtain the correct mean thrust force in the 2011 campaign. The coupled aero-hydro-elastic response in region three and active blade pitch control were tested in 2013, not executed in 2011.

Yu *et al.* (2017) conducted a 1/60th scale Triple Spar floater, a hybrid between a spar-buoy and semi-submersible tri-floater, tested with an active blade-pitch control DHI Denmark for the first time. The aerodynamic damping, interaction effects induced by wind and wave and blade-pitch control are discussed in their work. They applied a real-time active controller to the model. In this campaign, different control methodologies related to negative aerodynamic damping and simulation have been investigated to show the possibility of a low Reynolds rotor to control the rotor speed by adjusting the blade pitch angle. The calibration of the simulation model has also been proposed due to the lift and drag coefficients, aerodynamic losses, and drivetrain mechanical friction.

2.3.4. Summary in rotor simulation

The model size of the blade is large. The scaled mass is very light. At the same time, it needs to bear various wind loads in the test to meet sufficient strength and rigidity, which involves blade manufacturing technology. The upper structure of the FOWTs is very lightweight and, at the same time, the most complicated part of the arrangement and installation. It needs to install the motor, connect the hub, the six-component force sensor, the accelerometer sensor, the various components, etc., to meet the objective scale quality involving control strategies and mass control techniques.

In summary, the mass adjustment of the blade-pitch physical model (gear and motor) and a wind speed estimation is the primary consideration. Also, the coupling effect of the controller induced dynamic behaviour in terms of platform pitch motion damping (Goupee *et al.*, 2017) and extra aerodynamic damping (e.g., negative damping phenomenon (Larsen and Hanson, 2007; Thiagarajan and Dagher, 2014) which do still not have the conclusion, because of the limited research.

2.4. Experimental facilities and calibration methods

To accurately measure the coupling response of FOWTs under the action of both aerodynamic and hydrodynamic loads, a set of controlled wind field rectification systems needs to be specially designed for the experiment to achieve spatial and temporal uniformity. Wind-generation techniques may not be feasible on an open basin (Martin *et al.*, 2014), especially for less advanced facilities. Improved wind generation systems have been proposed by Courbois *et al.* (2011), Newton *et al.* (2015) and Philippe *et al.* (2013).

Before the experiment, other vital factors are calibrated, directly influencing the whole experiment, involving tuning the platform, tower, and aerodynamic parameters. Wind turbine geometry, mass properties, aerodynamic losses and drivetrain mechanical friction in simulated rotor and blade models should be examined. Decay tests are required to determine the approximate constants of the initial conditions. Through the decay test, the stiffness, mass and added mass, the moment of inertia and damping accuracy of the model system can be verified. Stewart *et al.* (2012) and Browning *et al.* (2014) proposed a method called further decay tests and also gave some details for calibration and validation (physical and numerical). The hammer test can test the natural frequency of the tower. Rotor and nacelle parts are not included in the hammer test. However, the influence of the sensor and cable is not negligible.

For this reason, the mass of the wind turbine has a distinct difference from the design value in the basin model test. Yu *et al.* (2017) and Bredmose *et al.* (2017) discussed calibration partly in the Triple spar campaign. Based on the previous work of Duan *et al.* (2016b), Li *et al.* (2018) proposed an improved deficient thrust force correction approach that used the wind to drive the rotor rather than the motor.

2.5. Real-Time Hybrid Approach

Under the premise mentioned above, many scholars selectively avoided simulating aerodynamic issues when studying the dynamic responses of FOWTs, mainly focusing on the effects of hydrodynamic forces, or using the original disk to replicate the required thrust force in a much easier way. With the limitations of methods and facilities, these practices were popular in early research. However, very few details have been thoroughly open to the public. By improving theoretical & numerical models' fidelity and increased computational power, the RTHA (Real-Time Hybrid Approaches) has been proposed recently. It consists of physical and virtual subsystems defined as basin experiments and Hardware-In-the-Loop (HIL). A numerical model in HIL simulation accounted for the transient and degraded responses, interfacing with the scale model through sensors and actuators (Plummer, 2006). This presented method applied all aerodynamic load components (thrust force and torque) on a wind turbine model in a new way, while, unlike previous similar champions, only satisfying thrust force.

In RTHA, the wind turbine or floating platform will replace some actuation systems. And a full range of transient aero-hydro-servo-elastic dynamics force, which is calculated in a numerical model simulation in real-time, will be applied to the model by these actuators. A thorough introduction of the working mechanism of RTHA in the context of floating structures and proposes its use in basin experiments of FOWTs have been provided by Chabaud *et al.* (2013). Different usual numerical simulation, delays, and dynamics are undesired compensations in this alternative approach, which means one feedback-controlled facility was settled to emulate aerodynamic forces (Hall *et al.*, 2014; Hall *et al.*, 2018; Hall and Goupee, 2018) or wave forces (Bayati *et al.*, 2014; Bottasso *et al.*, 2014; Filippo *et al.*, 2014). The aero-elastic response of the tower and blades is usually neglected in basin experiments. However, these can be simulated with a scale model in software using BEMT (Blade Element Momentum Theory) and beam bending models in

RTHA. Additionally, this method created an easy way to solve wind generator techniques at model scale effectively and relatively simply by utilising non-generic designs.

2.5.1. Code Development

The rapid development of software technology promoted the birth of RTHA. Moreover, hardware and software played significant roles in the experiment. Therefore, it is necessary to overview numerical simulation before briefly discussing RTHA. Currently, researchers have been exploiting numerous numerical simulation tools for analysing full-scale FOWTs, which can be classified into two categories (Liu *et al.*, 2016): frequency-domain and time-domain analysis. In recent years, many new numerical simulation tools have been created, and most related experiments are undergoing code-to-code or code-to-experiment validation, especially in hybrid basin experiments. This section will briefly introduce and summarise the numerical simulation tools.

2.5.1.1. Frequency-domain analysis

Glauert proposed the BEMT to apply the aerodynamic forces of the wind turbine based on the one-dimensional momentum theory (Hansen, 2015). According to Cordle and Jonkman (2011), BEMT is an aerodynamic model currently used to calculate aerodynamic loads. However, the presence of significant low-frequency motion in FOWTs makes the flow field around the blade more complex than a fixed wind turbine. Therefore, researchers have proposed many correction methods for this theory (Hansen *et al.*, 2006; Hansen, 2015): *Prantl's* tip loss correction factor and *Glauert's* correction.

The calculation of the hydrodynamic load of FOWTs usually depends on the structure of the floater. For a spar-type floater, the analysis of hydrodynamic loads is a complex coupling problem that requires consideration of incident wave excitation force, potential flow radiation damping, and added mass. The Morison empirical formula can solve the hydrodynamic load calculation of the floating structure. Subsequently, the formula is

widely used to analyse cylinders' hydrodynamic loads (Faltinsen, 1993; Wei *et al.*, 2014). This formula is also the earliest model for hydrodynamic calculation of FOWTs. But it is mainly applied to analysing hydrodynamic loads of offshore fixed wind turbines. The Morison formula is primarily suitable for applications on small-scale structures since it ignores the memory effect of the free surface and uses a long-wave approximation to simplify the diffraction problem. All these make the Morison formula not applicable to large-scale structures. Later, the researchers numerically analysed the FOWTs in the frequency domain under the linear assumption.

For linear systems, when a periodic load of a single frequency is applied to the system, such as a floating body under the action of a regular wave, the excitation response should be a single frequency. The RAO is defined in the traditional ship, and ocean engineering is based on this linear input-output hypothesis to reflect the responses of the floating body by the wave excitation load. Therefore, for the traditional floating platform, the frequency function can be solved by direct frequency-domain calculation to predict the responses of the floating body under the wave excitation load (Ma *et al.*, 2014). However, for FOWTs, its normal operating state is subject to wind and wave loads. In the case of turbine blades rotating at a specific speed, the wave load of a single frequency can no longer be seen as a single input. At the same time, a single frequency wave load excitation can also result in multiple frequency responses. This nonlinear characteristic is mainly caused by the rotation effect of the blade and the system instability induced by the blade-pitch controller (Jonkman *et al.*, 2010). Therefore, for FOWTs, the system's response to wave excitation cannot directly solve the frequency function or the RAO from the traditional frequency-domain equation. Secondly, when evaluating the system's responses induced by wave excitation, the regular operation of the wind turbine, that is, the rotation effect of the blade and the wind load effect, cannot be ignored. This is determined by the system characteristics of the FOWTs themselves. Otherwise, only the response characteristics of the wave load are considered. The forecast is of little significance in practice.

Inspired by the technologies of offshore O&G industries in the field, some researchers have studied the dynamic characteristics of FOWTs using frequency-domain analysis tools. For example, Lee (2005) and Wayman *et al.* (2006) performed a series of investigations on TLP and analysed shallow-drafted barge and the MIT/NREL TLP, respectively. Wang *et al.* (2017) proposed a frequency-domain approach to analyse the coupling effects of FOWTs. However, FOWTs are typical nonlinear system, which are not capable of modelling, involves the influence of coupling between aerodynamic loads, structural elastic deformation, and motion modes.

2.5.1.2. Time-domain analysis

In traditional ocean engineering, the floating structure is considered a single rigid body, which can be used to establish the dynamic equation of the structure. And this rigid body must have no relative motion between the various mass points inside the structure. However, when the FOWTs are operating, the rotor rotates continuously. There is relative motion between the rotor, blade, nacelle structure and platform, which does not meet the conditions for the single rigid body dynamic theory. Therefore, the FOWTs could be regarded as a fully coupled aero-hydro-servo-elastic model by solving the dynamical equations of numerous DOFs in the time domain. The DOF of FOWTs' systems (except mooring system) mainly are:

- 6DOF motions of the supporting platform.
- Modal coordinates of the elastic deformation of the tower in all directions.
- The rotation of the nacelle relative to the top of the tower.
- The rotation of the rotor relative to the nacelle.
- The rotation of each blade is relative to the hub of the end of the transmission rotor.
- Modal coordinates of the elastic deformation of each blade.

To study a simple system consisting of a small number of rigid bodies, it is convenient and feasible to use any mechanical method. However, a more general mechanical model needs to be established for a plurality of rigid bodies, even systems containing flexible bodies. Some objects are assumed to be rigid bodies in multi-body systems, and some things must consider elastic deformation. The mechanical model is called the rigid-flexible multi-body system.

The traditional hybrid coordinates model ignores the quadratic coupling term when considering the coupling between the large-scale rigid body motion and the high-frequency elastic deformation motion of the flexible body at low frequencies. It directly uses the analysis results suitable for small deformation displacement in structural dynamics. It is not only unable to deal with the dynamic stiffening phenomenon brought by the rigid body motion to the flexible body but also causes the negative stiffness phenomenon when the large-scale rigid body motion is very large or the flexible beam is long, which affects the solution of the flexible beam motion displacement. The longer the length of the flexible beam, the more pronounced the phenomenon of dynamic stiffening, and the elastic deformation is reduced. The coupling effect of high-order elastic deformation and large-scale rigid body motion should be considered for the large and slender flexible structures. Therefore, the time-domain analysis method has come into the mainstream gradually.

Karimirad and Moan (2011) conducted extreme structural responses and fatigue loads of spar-type FOWTs. Bachynski *et al.* (2013) researched transient events in time-domain analysis. In addition to unique research & development (R & D), some researchers have made improvements from O & G industries or other existing codes. For example, Jonkman and Buhl Jr (2005) added hydrodynamic mooring loads to the FAST code, developed for onshore bottom-mounted wind turbines, originally by Wilson *et al.* (1999). Several time-domain numerical tools have been generated from commercially available general-purpose multibody-system (MBS) codes. ADAMS and SIMPACK have been

used by combining additional aerodynamic, mooring and hydrodynamic subroutines for Withee (2004) and Matha *et al.* (2011), respectively. Ormberg and Bachynski (2012) described the RIFLEX extension of aerodynamic load on elastic structural components. Also, aNySIM has been developed and validated by MARIN to provide clients with a more integrated simulation package including multi-body side-by-side, the mooring system and, dynamic positioning capability studies (Naciri *et al.*, 2007; De Wilde *et al.*, 2009; Serraris, 2009). Another integrated code, *DARwind,* has been proposed by Chen *et al.* (2019a). Some theoretical backgrounds can be found in their papers, which are also verified by code-to-experiments (Chen *et al.*, 2017).

With the development of computer technology, CFD has become one of the robust tools to analyse the global dynamic responses of FOWTs. Zhao and Wan (2014) and Liu *et al.* (2015) conducted a series of investigations using their own CFD tool, NAOE-FOAM-SJTU. Comparisons of the wave load effects of TLP by combining potential flow theory approaches and CFD were conducted by Nematbakhsh *et al.* (2015). Tran *et al.* (2014) applied the CFD method to study the influence of periodic pitching motion on the aerodynamics of FOWTs and compared other calculation models. In the simulation of large-scale pitch motion, the CFD method has a smaller load than the traditional aerodynamic model. It can be a more accurate calculation of the effects of unsteady loads and random motion of the platform.

In summary, previous works have concluded the different numerical simulation tools in each module (Liu *et al.*, 2016). Nonetheless, limited studies have elaborated on the rigid-flexible coupling multi-body methodologies implemented in FOWTs. Detailed testing data is hardly openly available to the public. The development of CFD technology has played a specific role in promoting FOWTs research. However, due to the high hardware or software requirements, prolonged time consumption, and lack of accurate verification, compared with the traditional numerical simulation method, it still needs to be improved. Although some of these tools have been used in a wide range and even been benchmarked

through code-to-code check work. For instance, FAST and HAWC2, but few of these numerical tools have been accepted consistently for their reliabilities. These tools are used solely to predict global responses of FOWTs. In addition, in numerical tools, the coupling effect is a challenge to be considered in an integrated way. Due to some assumptions or simplifications introduced in theoretical calculations, such as hydrodynamic calculations without considering second-order wave forces, potential flow calculations neglecting viscous effects, etc., it will bring inaccuracies in some aspects of the simulation results of numerical simulation tools. For example, the hydrodynamic calculation linearisation cannot account for the second-order frequency wave force, which causes the oscillation of the surge, pitch, and heave under wave excitation to be correctly simulated at the natural frequency; the second-order harmonic wave force cannot be considered. It is possible that the vibration of the tower at its natural frequency cannot be sufficiently exciting. But this coupling effect can be reflected and obtained in a basin model test.

2.5.2. Hybrid basin experiment

A real-time hybrid method was first applied to the earthquakes of civil engineers in the 1970s in Japan by Carrion and Spencer Jr (2007). They tried to validate the assumption of large-scale structural behaviour, which can be realised and interface experiments with simultaneous simulation. A review of this RTHA has been applied to simulate aerodynamic forces within the automotive car industry, where Plummer (2006) made the individual parts (Klerk *et al.*, 2008; De Klerk, 2009; Li, 2014). The development of this method has been promoted in the United States by Shao and Griffith (2013) and Europe by Pinto *et al.* (2004). As the development of RTHA, challenges arose because of its interaction between multi-disciplinary simulation, including software, hardware, fabricating measurement, experimental methods, signal processing, control engineering and data acquisition, which all require instantaneity and precision for real-time coupling.

Some examples of each discipline's actual progress or advanced methods have been provided by Sauder *et al.* (2016) including control strategies (Carrion and Spencer Jr, 2007) and stability analyses (Kyrychko *et al.*, 2006). The application of RTHA in renewable energy and marine technology can be found in (Li *et al.*, 2006; Munteanu *et al.*, 2010; Signorelli *et al.*, 2011; Cao and Tahchiev, 2013; Chabaud *et al.*, 2013). The objective aerodynamic thrust and generator torque should be considered or actuated, and have the most significant effects on floaters when using a modified numerical simulation.

Gyroscopic moments, non-thrust loads (pitch and yaw moment, sway, and heave force), dynamic torque, and thrust directionality have been neglected in RTHA (Bachynski *et al.*, 2015). Bachynski *et al.* (2016) and Sauder *et al.* (2016) also offered a brief review of the RTHA testing adopted for FOWTs' experiments by limiting a part of the environment to avoid the discussed scaling problem. Their experiment proposed one method to apply wind-wave induced forces and the blade-pitch control algorithm by using a series of tensioned wires to connect the turbine and actuators to provide the transient simulated force rather than a ducted one. The specific process of this hybrid method on a 1/30th scaled 5MW semi-type wind turbine has been proposed in terms of qualification, quantification, possible error sources and performance of FOWTs. In the last stage, Berthelsen *et al.* (2016) introduced a methodology of using experimental data to calibrate the numerical model and quantify and mitigate equipment. Karimirad *et al.* (2017) used SIMA to extend previous work by Berthelsen *et al.* (2016) regarding the BEM model for rotor forces and second-order loads compared with experimental data. In addition, coupled aerodynamic simulations were conducted to avoid potentially incorrect modelling of the aerodynamic damping (Stewart and Muskulus, 2016a). Results of experimental data and full-scale numerical simulation from hybrid testing of 1/50th scale FOWTs have been provided by Hall *et al.* (2014) and five considerations of RTHA have been proposed: Actuator displacement; Velocity and acceleration envelopes; Actuator force envelopes; Motion tracking accuracy; Force actuation accuracy and system latency.

Bayati *et al.* (2013) performed a 2-DOF (Pitch and Surge motion) experimental rig-HexaFloat in a wind tunnel to simulate the motion of a 1/25th scale DTU 10 MW wind turbine model which combined hydrodynamic and aerodynamic loads within LIFES50+ project (Bayati *et al.*, 2016). Following year, HexaFloat (**Figure 2.3**) expanded to 6DOF (Bayati *et al.*, 2014). In 2017, they proposed an aerodynamic design methodology and a scale model technology for a 1/75th scale DTU 10 MW wind turbine rotors (Bayati *et al.*, 2017).

Figure 2.3 Hexafloat robot (Bayati *et al.*, 2014).

In general, the technical issues and methodologies of this hybrid/HIL test can be found in (Delbene *et al.*, 2015). In the former case, Bayati *et al.* illustrated the method of blade design. However, they did not put the turbine system in actual water and simplified the 6DOF motions of the supporting platform to a large extent. They ignored the coupling effect between the blade-pitch controller-induced instable of the floater and the aerodynamic load due to blade rotation and wave excitation. Therefore, it can be pointed out that the model test in a wind tunnel is a promising way to predict global responses of floating wind turbines but still in the face of many challenges.

Another real-time hybrid approach was validated by Hall *et al.* (2018) and Hall and Goupee (2018), as shown in **Figure 2.4**. In their experiment, an actuation system combined numerical wind turbine model was set to simulate the thrust force of winch and cables, pulling fore and aft on the nacelle. Three controls are integrated, which was executed by changing cable length.

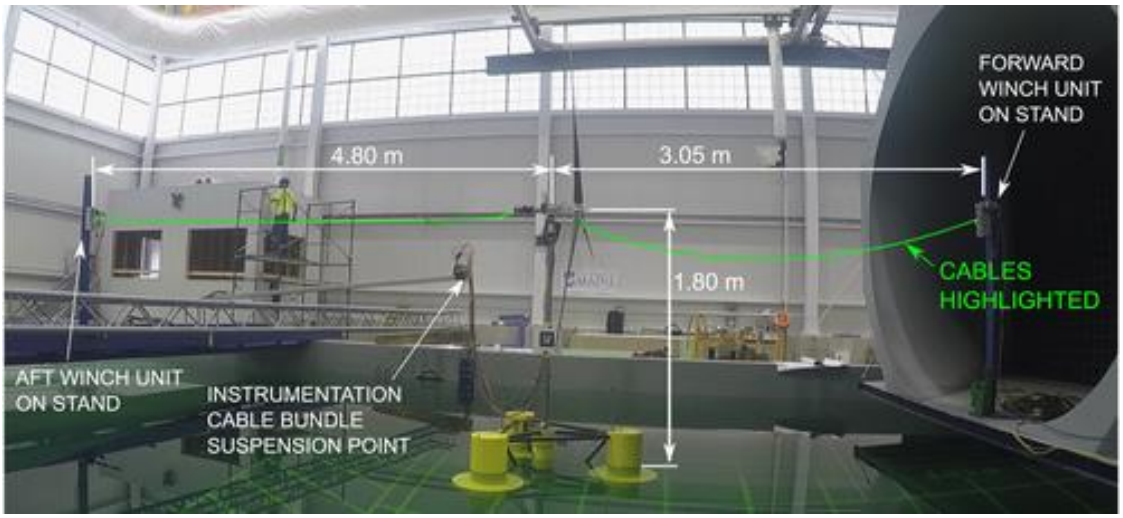

Figure 2.4 Arrangement of cable system (Hall *et al.*, 2018).

Hall also demonstrated the benefits and possible disadvantages of some hybrid approaches and compared them with physical wind-wave tests, which showed satisfactory agreement. However, some other aerodynamic forces and moments have been neglected. In addition, the mean value of the platform surge motion has a significant difference of up to 17% (no wind) and 14% (steady wind), respectively. This may be due to unidirectional dynamic forces on the nacelle by the actuation system. Hall *et al.* (2018).

Vittori *et al.* (2018) proposed one hybrid experimental method using the SIL method, which validates that generated code has the same behaviour as was tested in the model simulation and does not need a hardware interface. This SIL method was applied to OC4 to integrate the aerodynamic performance. Results of all the cases in the experiment compared with numerical software. However, since the data type accuracy is set in the SIL, all the calculations inevitably cause calculation errors.

In summary, the scalability and fidelity of the basin experiment could be improved by RTHA. The dissimilar scaling issue can be avoided, and any scale can be modelled. Requirements of experimental facilities can be reduced, and blade-pitch control can be modelled without the limitations of small-scale actuation. This makes the model test of FOWTs more accessible and flexible for researchers. However, there are still possible disadvantages. The significant difficulty in numerical modelling of FOWTs is the accurate estimation of the influence of sensor cables (Coulling *et al.*, 2013). Since the model of FOWTs is very light, the impact of the sensor cable can be said to be non-negligible and even very important. In addition, sensor cables of various test institutions globally are not the same, and the arrangement of cables in basin tests cannot be unified. The influence of cables may even be nonlinear, so it is difficult to estimate the impact of cable accurately. Errors may also arise due to the various inaccuracies and delays. In addition, the quality of virtual subsystems will improve the results. In addition, almost all the theories have been adopted in numerical simulation, which relies on assumptions (Sebastian and Lackner, 2013; Jeon *et al.*, 2014; Farrugia *et al.*, 2016). Most importantly, more problems (design, manufacture, and optimisation) may come due to finding an alternative actuation system.

2.6. AI application of offshore engineering and wind industry

Artificial Intelligence is a large category of technology, which includes various algorithms and applications. **Figure 2.5** illustrates their relationships in a Venn diagram.

In AI technology development, data-driven technology has been gradually being recognised by academia and industry. Machine Learning is one of the most important extensions of the AI field, and it can be divided into the following methods (Alpaydin, 2020):

- Supervised Learning.
- Unsupervised Learning.
- Reinforcement Learning.

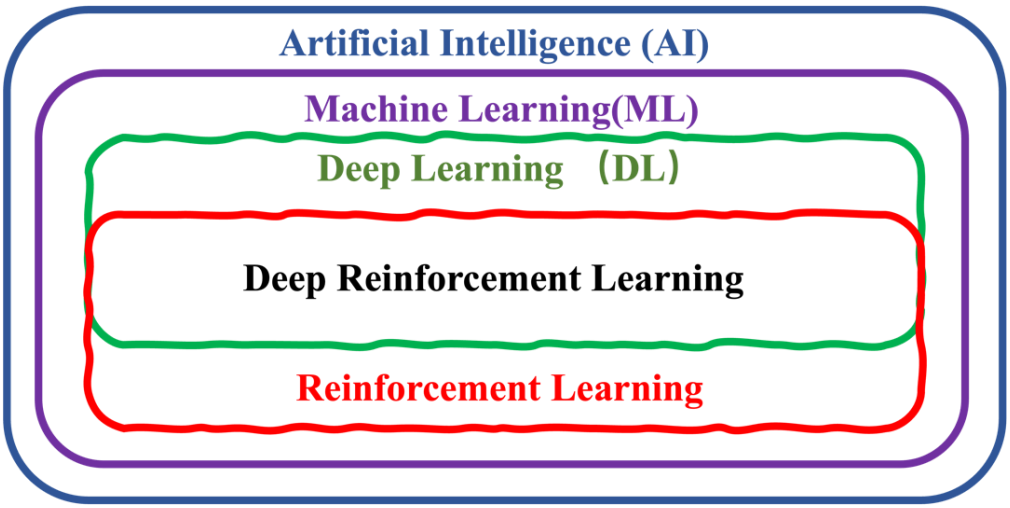

Figure 2.5 Relationship of AI (Dong *et al.*, 2020).

Major research institutions and government organisations also value applying artificial intelligence technology in the future. For example, the UK's EPSRC (Engineering and Physical Sciences Research Council) launched four robotics and AI centres in 2017 to meet this challenge (EPRSC, 2018). The ORCA Hub, led by Heriot-Watt University and the University of Edinburgh, is pioneering the development of fully autonomous remote services to monitor, maintain and repair offshore assets such as offshore wind turbines (ORCA, 2021). There have been some promising applications for introducing ML techniques in the offshore renewable energy field. For example, Li *et al.* (2019) and Li *et al.* (2020) studied the wave energy control algorithm with Artificial Neural Networks (ANN) to implement real-time wave force prediction.

However, most existing applications are based on land-based wind turbines for wind energy harvesting devices. Li and Shi (2010) used ANN to forecast wind speed, critical for wind energy conversion systems. Further research has been done by Pelletier *et al.*

(2016) who used ANN to obtain the power curves of the wind turbine at six parameters. Li (2003) discussed the temporal characteristics of wind power generation. The recurrent multilayer perceptron neural network is trained based on the time algorithm of the extended Kalman filter to predict the wind turbine's power. Kusiak *et al.* (2009) used weather forecast data generated on different time scales and ranges to establish short-term and long-term wind power prediction models. They also verified that the model developed by the neural network is superior to other models in both short-term and long-term predictions.

The wake effect is also a significant and complex issue in the wind power industry. Sun *et al.* (2020b) proposed a power prediction model based on an ANN and optimised the yaw angle to minimise the impact on the overall wake of the wind turbine. The model can estimate the total power generation of a wind turbine for a given wind speed, wind direction and yaw angle. In particular, the supervised learning algorithm can also optimise the FOWTs platform's motion (Chen *et al.*, 2019b). Stetco *et al.* (2019) conducted a systematic review of conditions for monitoring in 2019. For example, blade failure detection or generator temperature monitoring. In addition, they classified the ML model, including data source, feature selection and extraction, model selection (classification, regression), verification and decision-making. Neural networks, support vector machines, and decision trees are mainly used among them. In general, the application of ML in traditional wind energy is relatively mature and widely recognised by the scientific community. Nowadays, most applications are based on the supervised learning method, relying on a large amount of data for training and analysis. Through supervised learning, knowledge can be obtained from the data without needing to master the comprehensive nonlinear inter-relationship of FOWTs. However, supervised learning means that the labelled data must satisfy independent and identical distributions (i.i.d.); there is no correlation between them. If there is a connection, this network is not easy to learn.

Although AI technology has extensively promoted the development of the traditional wind industry, its applications in the FOWT industry are few, especially for the innovative design methodology and validation approach. Understanding the phenomenon more deeply and promoting the further development of the theories by AI technology is the focus of the academic community at this moment, rather than simply explaining and predicting the phenomenon. Therefore, the combination of fundamental theories based on numerical tools and AI technology could work better for developing FOWTs in the future, especially when the experiment is not so easy to carry out.

2.7. Summary

With the commercialisation of FOWTs and their engineering applications, more academic issues will emerge. For example, the current OC6 project aims to understand the under-prediction of loads/motion in floating semi-submersibles in pitch/surge natural frequencies. In addition, it is also aimed to develop and employ more rigorous validation practices through the OC6 project (Robertson *et al.*, 2020), in terms of identifying a specific validation objective, using metrics to assess validation success, and calculating associated experimental uncertainty of metrics. Furthermore, with the maturity of experimental technology and the improvement of hardware and software equipment, the method of RTHA will be applied, promoted, and innovated to a greater degree. The dissimilarity of the scaling issue can be solved. Requirements of experimental facilities can be lower, and blade-pitch control can be simulated effectively. This makes the model test of FOWTs more affordable to researchers. However, there are still some challenges in basin experiment technology. For instance, testing errors may arise due to various inaccuracies, delays, and theories are adopted in the numerical simulation. Most importantly, more problems (design, manufacture, and optimisation) may come due to finding an alternative actuation system. All the above may be problems to be solved in the future application of the RTHA method. In addition, the application of artificial intelligence technology has also brought new ideas to the FOWT industry.

Chapter 3. Methodology of SADA

This Chapter provides a fundamental description of the methodology of the SADA method. The details, including the KDPs concepts, *DARwind* programme and AI algorithm are given in Chapter 4-6.

3.1. Introduction

SADA is a novel concept to integrate AI technology (Artificial Neural Networks and Deep Reinforcement Learning) and *DARwind* (a coupled aero-hydro-servo-elastic programme) for optimized design and dynamic performance prediction of FOWTs. **Figure 3.1** shows the general flowchart of the entire SADA algorithm.

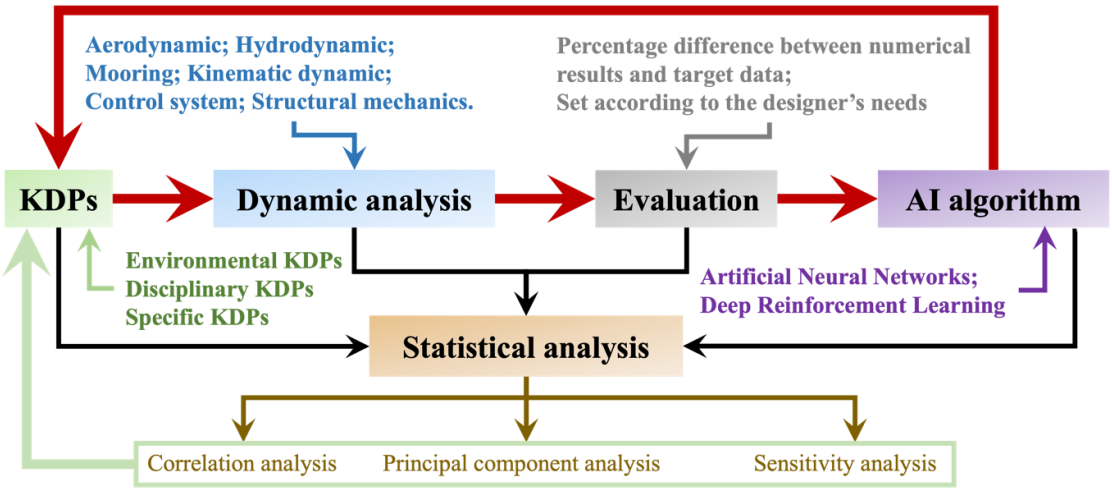

Figure 3.1 General flowchart of SADA method.

Firstly, the concept of Key Disciplinary Parameters (KDPs) is proposed, and it is the most crucial concept in SADA, working as a data transmission interface between AI technology and disciplines in numerical simulation of FOWTs. Specifically, the KDPs can be divided into three categories (Environmental KDPs, Disciplinary KDPs, Specific KDPs), with their unique boundary conditions in SADA.

Secondly, *DARwind* can be trained to be more intelligent and give more accurate predictions for FOWTs by ANN or DRL algorithms on target data (experimental or full-

scale measured data). All information generated in the iterative loop will be recorded, including the change of KDPs and the corresponding percentage difference of FOWTs simulation.

Finally, this information will be integrated to carry out relevant statistical analysis to feedback on the optimal selection of KDPs. The following sections will introduce these aspects separately.

3.2. KDPs

This section briefly introduces the KDPs selection and analysis, and the full details can be found in **Chapter 4**.

3.2.1. KDPs selection

It is challenging to obtain an accurate forecast and develop an integrated design by measurement, experiments (basin or wind tunnels) and numerical simulation. The disciplinary knowledge involved in FOWTs is very complex and has strong nonlinearity. Therefore, KDPs are proposed in SADA as a concept covering multiple disciplines and aspects, including various uncertain or experience-based parameters.

In SADA, KDPs interface traditional numerical computation and neural network parameter optimization, which can be adjusted based on the percentage difference evaluation with the specific target data and the weighting of the deep neural network. However, the corresponding boundary conditions limit each KDP.

The flowchart of KDPs selection is shown in **Figure 3.2**. Among them, the fix range represents that in the program loop, the value of KDPs remains unchanged. The small and large ranges represent that KDPs allow small and large changes in the adjustment process, respectively. No limit means that KDPs are not constrained in the program loop. The specific decision process is as follows:

- Step 1: Choose the corresponding KDPs in three categories.
- Step 2: Use the concept of significant figures to set the boundary conditions according to the specific values of each KDP.
- Step 3: Determine the percentage difference between the numerical results and the target data.
- Step 4: Adjust the boundary conditions appropriately.

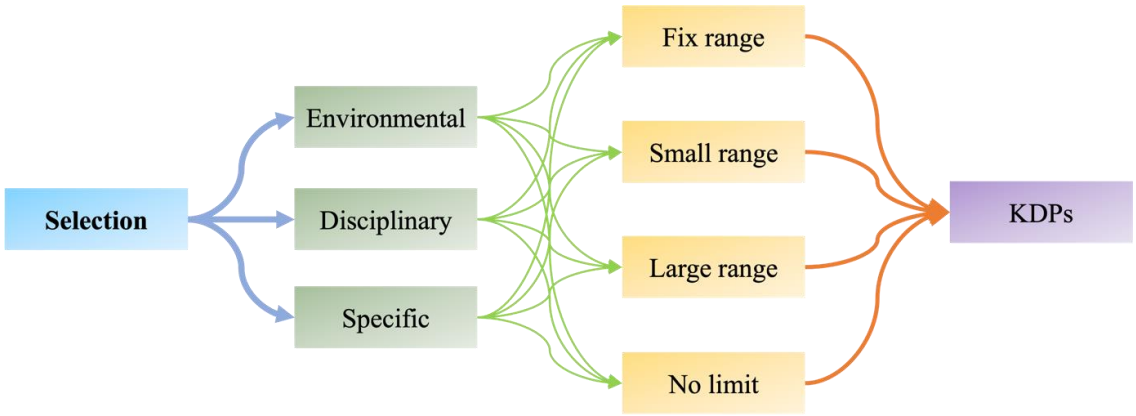

Figure 3.2 KDPs selection flowchart.

3.2.2. KDPs analysis

The database established by SADA can statistically analyse the changes of KDPs and the dynamic response of related FOWTs. Correlation analysis is used to explore the influence of KDPs on the entire FOWTs system in the coupled state, which is fed back to the selection and theoretical revision of KDPs in the first stage. Taking the Spearman correlation coefficient as an example, for a sample with a sample size of n, n raw data is converted into rank data, and the correlation coefficient ρ is

$$\rho_c = \frac{\sum_i (x_i - \bar{x})\,(y_i - \bar{y})}{\sqrt{\sum_i (x_i - \bar{x})^2 \sum_i (y_i - \bar{y})^2}} \qquad \textbf{Eq. 3.1}$$

For a more detailed analysis, please refer to **Section 9.3**

3.3. *DARwind*

This section briefly introduces the *DARwind* programme, and the full details can be found in **Chapter 5**.

FOWTs bear complex sea environmental loads, including wave, current, wind, etc. In addition to mooring systems and control systems, these are usually decoupled from the main structure and calculated as external forces in the numerical calculation. Therefore, a fully coupled aero-hydro-servo-elastic method was developed and then programmed as an integrated code *DARwind* (Dynamic Analysis for Response of wind turbines) to simulate the dynamic response of FOWTs (Chen *et al.*, 2019a). The current version of *DARwind* is written in the high-level programming language FORTRAN, verified by a series of code-to-experiment comparisons to show its feasibility. The functional modules of the *DARwind* program can be roughly divided into Input module, Solver module and Output module, as shown in **Figure 3.3**.

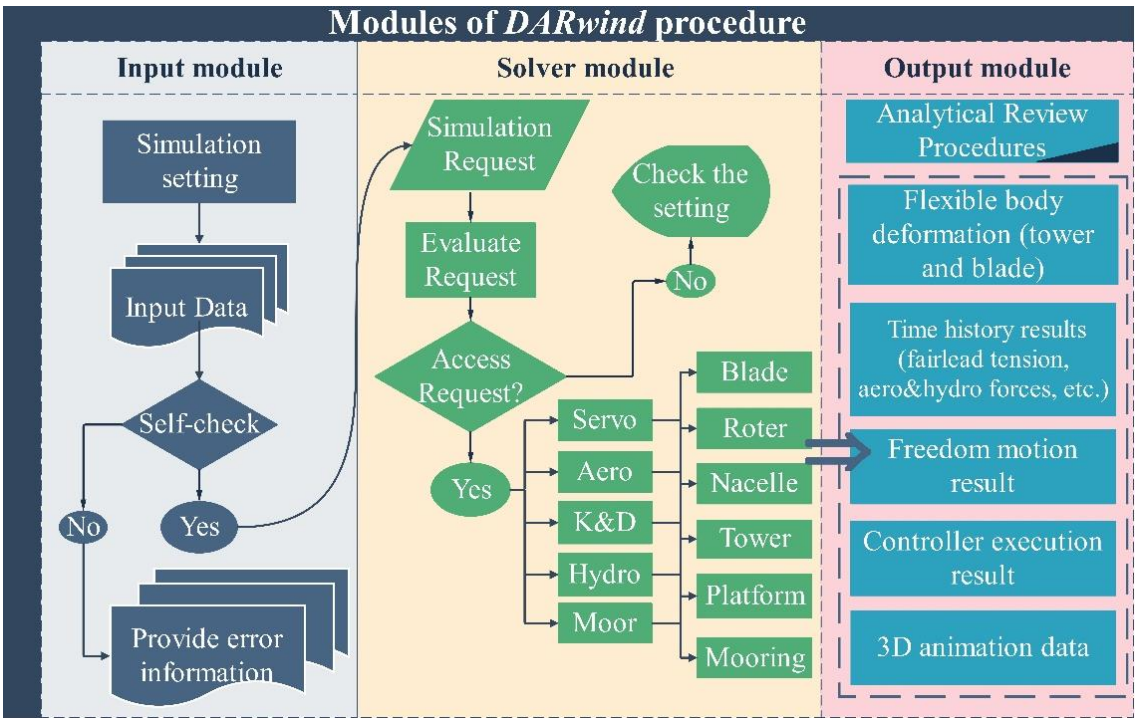

Figure 3.3 Modules of *DARwind* procedure.

3.4. AI technology application

This section introduces the AI technology used in the SADA method, including Artificial Neural Networks and Deep Reinforcement Learning. For more details on these methods, please refer to **Chapter 6**.

3.4.1. Artificial Neural Networks application

The application of ANN is pervasive, mainly for nonlinear fitting according to the input information in terms of image recognition, information processing, neural differential equation solving, etc. The traditional ANN concept does not require relevant dynamic knowledge, but trains massive data based on the "black box". Nevertheless, in SADA, it is optimized based on *DARwind*.

In SADA, ANN can directly optimize the prediction of the FOWT platform motions' physical quantity. The application of BP neural networks has such feasibility. **Figure 3.4** shows the application of BP-optimised prediction in SADA. In this flowchart, the initial numerical result of *DARwind* is used as the input parameter of ANN, such as the amplitude of the platform's 6DOF motions.

Before the training, the data were normalized. All data is converted into [0, 1]. SADA uses the Min-max normalization, as shown in **Eq. *3.2*** below. The normalization function uses the original function, map minmax, in MATLAB:

$$x_{norm} = \frac{(x_k - x_{min})}{(x_{max} - x_{min})} \qquad \textbf{Eq. 3.2}$$

Where x_{min} is the smallest number in the data sequence; x_{max} is the largest number in the sequence. The purpose is to remove the different order of magnitude of the data, avoiding the significant difference in the orders of magnitude of the input and output data. In addition, disrupting the data allows the input data to satisfy the conditions of independent distribution approximately.

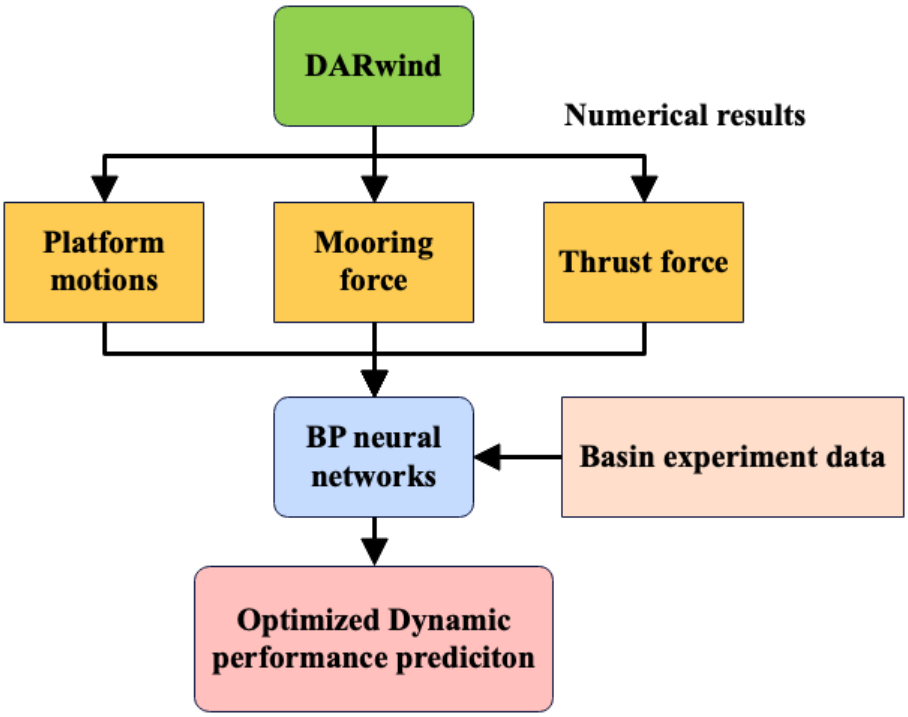

Figure 3.4 BP optimized prediction in SADA.

3.4.2. Reinforcement learning application

In this section, the application of RL in SADA is introduced, mainly feature engineering and reward engineering in DRL. Furthermore, the RL module's two algorithms in SADA are the Brute-force algorithm and the deep reinforcement learning algorithm.

3.4.2.1. Notations

The development of RL is rapid, but its mathematical principles are very complex, far more than deep learning. The most successful applications are basically in Atari, Go and other games (Holcomb *et al.*, 2018). In summary, the application of RL in SADA is the most innovative highlight. The specific notations and nouns combining FOWTs and RL in SADA can be seen in **Figure 3.5**.

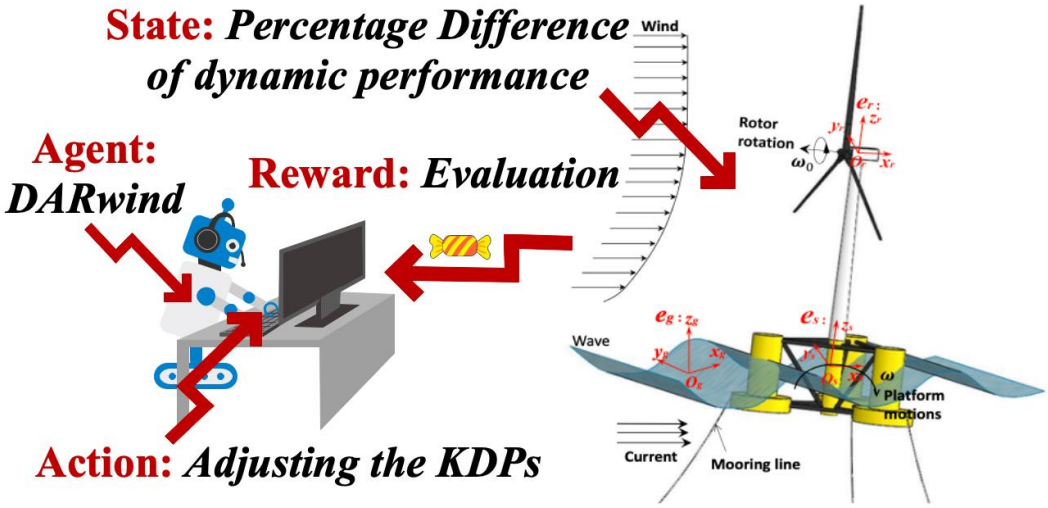

Figure 3.5 RL notations in SADA.

3.4.2.2. Feature engineering

As an agent, *DARwind* will take continuous action through the SIL algorithm, i.e., adjusting KDPs appropriately to obtain more accurate prediction results and minimize the percentage difference of dynamic performance of FOWTs. The action here affects the immediate reward and the next state, thus the subsequent reward. The purpose of *DARwind* is to find what action can be taken to maximize the numerical reward signal. The roles of the deep neural networks are amplified to record [state, action, reward, next state] in different situations through the SIL algorithm. The reward here is the feedback of the evaluation of percentage difference, which are:

$$\begin{cases} P_{initial} = \left| \dfrac{O_{target\ data} - O_{initial\ KDPs}}{O_{target\ data}} \right| \times 100\% \\ P_{present} = \left| \dfrac{O_{target\ data} - O_{weighted\ KDPs}}{O_{target\ data}} \right| \times 100\% \\ P_{difference} = P_{initial} - P_{present} \end{cases} \quad \textbf{Eq. 3.3}$$

$O_{target\ data}$ is the target data which can be the experimental results or measured data. $O_{initial\ KDPs}$ is the numerical results by initial KDPs. $O_{weighted\ KDPs}$ is the numerical results by weighted KDPs. $P_{difference}$ is used to measure whether the results of SADA is better than the initial KDPs. If $P_{difference}$ is positive, it means that the difference

between the target data and numerical results has decreased by SADA, otherwise the difference has increased. In short, evaluation of $P_{difference}$ is to establish a reward mechanism to tell *DARwind* how much benefit has been obtained in this iteration.

In addition to the $P_{difference}$ evaluation in feature engineering and reward engineering, target data is not the only criterion. One of the challenges of setting reward engineering in SADA is that the *DARwind* needs to learn, approach in actions, and finally, achieve the goal that the designer hopes. If the designer's goal is easy to distinguish, this task may be solved well, such as finding the most minor $P_{difference}$ of a physical quantity or balancing the $P_{difference}$ among multiple physical quantities. Nevertheless, in some problems, the designer's goal is challenging to quantify, and it is not easy to be translated into a loss function, especially when these problems require the agent to make very skilful actions to complete complex tasks or a series of tasks.

However, due to different FOWT models and structures, some target data obtained from experiments and actual measurements may be very small. Therefore, in SADA, corresponding weighting parameters are designed for different target physical quantities. Take the platform motions as an example, the difference of some motions needs to be weighted due to the small amplitude. The specific weighting method of mean absolute percentage difference (MAPE) can be shown in equation:

$$\boldsymbol{MAPE} = \frac{1}{m}\sum_{i=1}^{m} w_i \left|\frac{y_i - \hat{y}_i}{\hat{y}_i}\right| \times 100\% \qquad \textbf{Eq. 3.4}$$

Where: m is the number of platform motions, and w_i is the weight difference of each physical quantity. y_i means the numerical results and $\hat{y}_i$ means the experimental results.

3.4.2.3. Reward engineering

In practice, a reasonable result signal can make the agent learn successfully and efficiently and can effectively feedback and guide the agent to learn during the process of interacting

with the environment. For SADA, reward engineering is not unique. For example, when the surge and pitch are used as the target physical quantities, the reward project is based on $P_{difference}$ of these two physical quantities. The change in $P_{difference}$ reflects the feedback on the quality of the action. In addition to the profit target of $P_{difference}$, $P_{difference}$ continuity of each iteration will also be randomly selected in the reward engineering.

In summary, as shown in **Figure 3.6**, SADA starts by selecting the initial critical KDPs by FOWTs designers. Then, some physical quantities such as 6DOF platform motions are chosen as the states in the RL algorithm.

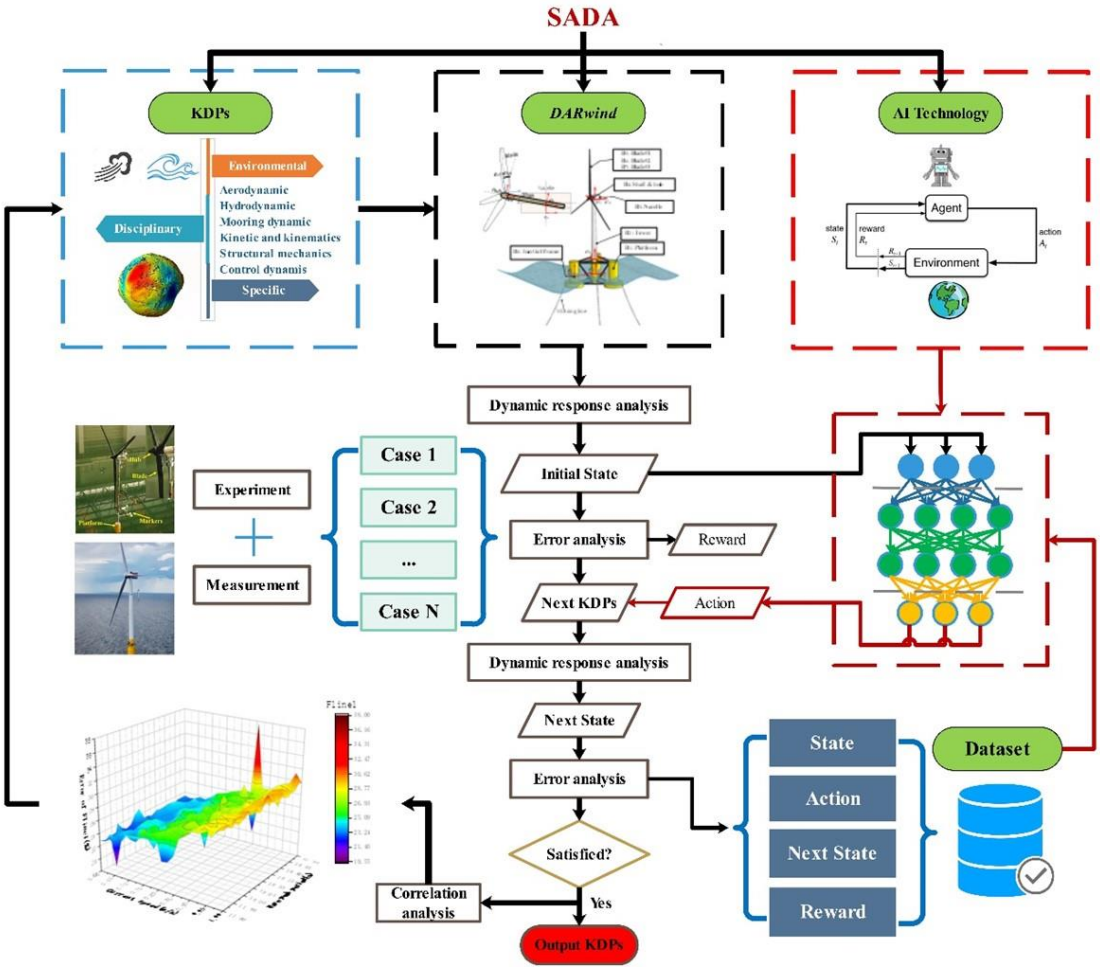

Figure 3.6 The layout of SADA.

According to the states, the agent will give the corresponding action to adjust the KDPs values properly to run the next loop if the evaluation is not satisfied. When $P_{difference}$ is reduced to an acceptable range, this means that the program is good enough to conduct the final numerical analysis. In addition, some other physical quantities that cannot be measured directly in the experiment or measurement can be predicted as well. Such as the deformation of blade and tower. Besides, SADA can also exclusively complete the FOWTs dynamic response analysis in the sea states different from those used in basin experiments or measurement through the training process.

3.4.2.4. RL (Brute-force algorithm) application

Brute-force (BF) algorithm is inspired by the concept of RL framework. In BF, all decisions of the agent are random and obtained through interaction with the environment. The agent needs to explore the environment by constantly interacting with the environment, which requires a lot of trial and training. More specifically, *DARwind* continuously weights the selected KDPs through an exhaustive method. **Figure 3.7** shows the framework of the proposed Brute-force algorithm in SADA. Each action is weighted by random gaussian distribution. Each KDP has its own unique boundary conditions to prevent value overflow.

In the specific process, the designers should first select the initial KDPs in different disciplines and find the corresponding positions of these KDPs in *DARwind* programme. For the weighted KDPs, the second dynamic response analysis and difference analysis are performed again.

The specific process of SADA (Brute-force) in **Figure 3.7** is as follows:

- Step 1. Manual selection of KDPs from different disciplines.
- Step 2. Use initial KDPs to run dynamic response analysis in *DARwind* to obtain state.
- Step 3. Use target data for percentage difference evaluation.
- Step 4. Select actions according to the Gaussian distribution of random noise.
- Step 5. KDPs in *DARwind* are weighted by actions.
- Step 6. Use weighted KDPs to run dynamic response analysis to obtain next state.
- Step 7. Determine whether the percentage difference meets the requirements. If yes, output KDPs, if not, return to Step 3.
- Step 8. Use final KDPs to run dynamic response analysis in *DARwind*.

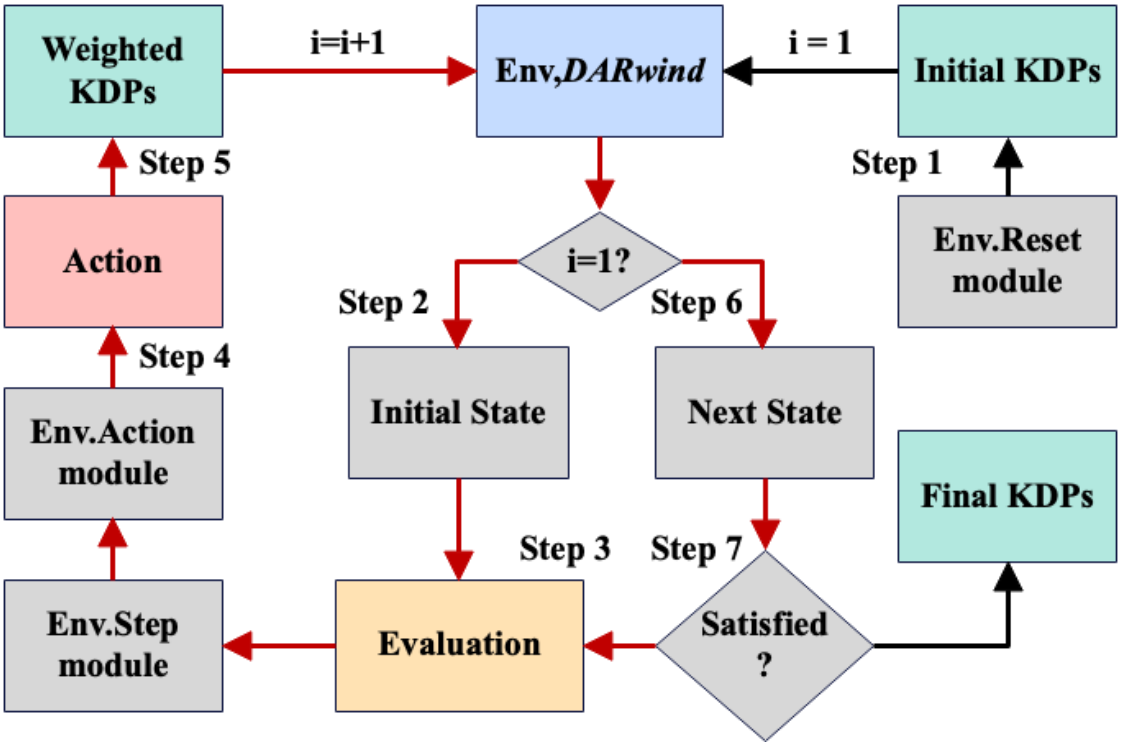

Figure 3.7 The framework of Brute-force algorithm, in SADA

3.4.2.5. *Deep Reinforcement Learning*

This section will introduce the DRL algorithm in SADA in detail. The flowchart of DRL frame is presented in **Figure 3.8**.

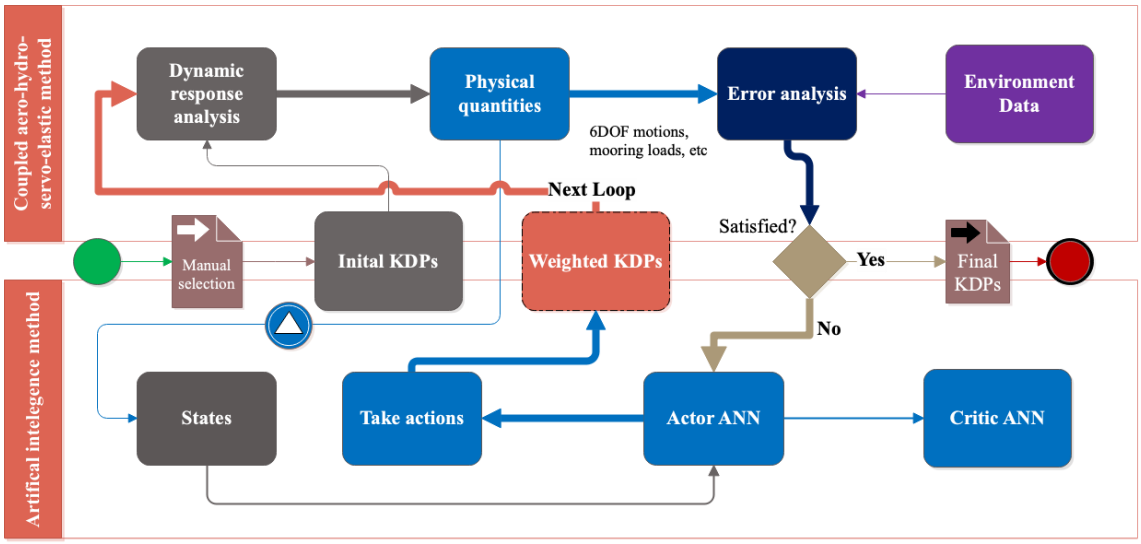

Figure 3.8 The flowchart of the SADA algorithm.

Firstly, the Deep Deterministic Policy Gradient (DDPG) algorithm is adopted in SADA to estimate the optimal policy to adjust the KDPs. The DDPG algorithm (Lillicrap *et al.*, 2015) can be regarded as a combination of the deterministic policy gradient (DPG) algorithm and deep neural networks. The whole pseudocode is list in **Table A.2.**

It aims to tackle the problem with continuous action spaces that deep Q-learning network (DQN) cannot be straightforwardly applied to. The detail algorithm of SADA method (with DDPG) is listed in **Figure 3.9**, and the main loop is the thick black solid line. The difference from the BF algorithm is that the decision is made by a deep neural network instead of a random Gaussian distribution function. Based on the DDPG algorithm and Brute-force algorithm, the AI-based *DARwind* can be applied in different demands.

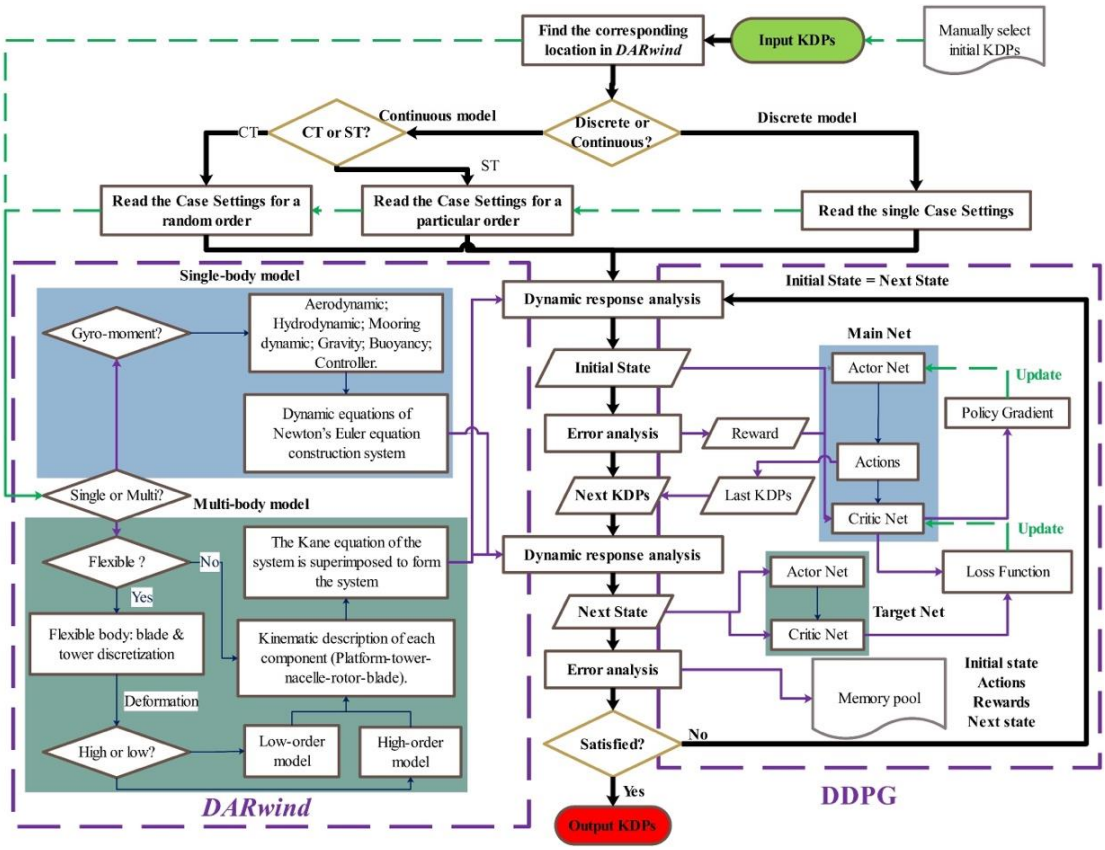

Figure 3.9 The algorithm of SADA.

3.4.2.6. DRL training model

The DRL module in SADA has three training models: Segmented model, Discrete model, and Continuous model. In the Segmented model, the duration of the data for one specific case will be divided into multiple segments for training. As for the remaining two models, they are summarized as follows:

- Discrete model: Suitable for analysing a single known sea state and working condition. For example, SADA can optimize KDPs to reduce differences in a single case further.
- Continuous model: Suitable for analysis of known (implemented in the experiment) and unknown (not implemented in the experiment) sea states and working conditions. For example, the optimizable working conditions are not limited to experiment.

In the Continuous model, two continuous methods are proposed for comparing their efficiency. The single training (ST) method uses independent cases for training in a specific permutation. In combining training (CT) method, the cases will be selected in a random order for training the model (**Figure 3.10**).

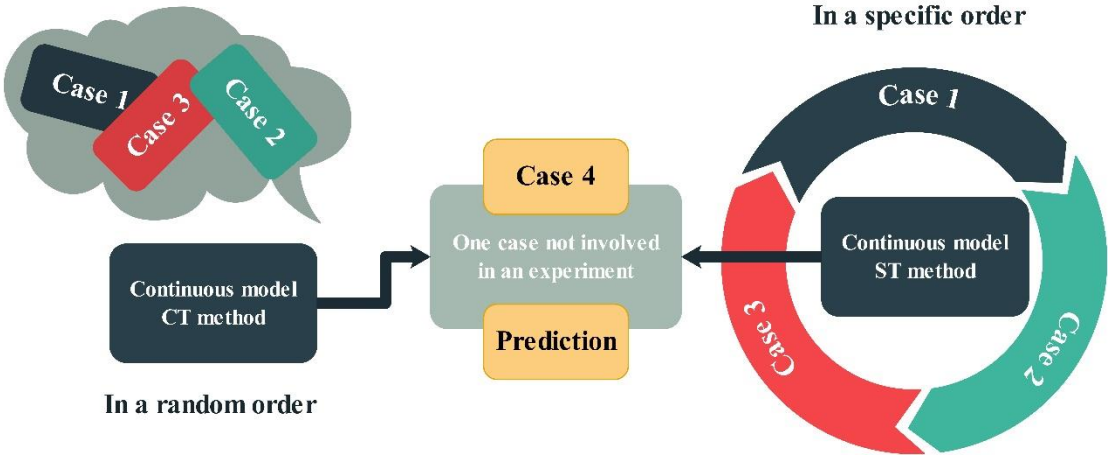

Figure 3.10 Two training methods in the Continuous model.

For example, case 1 gets a new state through action, and the number of this action is manually set (if 10). However, after ten actions, the training does not end, but the model automatically and intelligently updates the new numerical calculation settings according to the given case list, starts the calculation of the following case and loops in turn. This means that the three cases do not necessarily represent only three loops. Instead, it can repeatedly train in three cases in several loops. There is no fixed exit condition in actual operation. Generally, only one maximum number of loops is set. Unlike classification and identification problems, due to the limitations of numerical software, it is currently difficult to define the exit conditions, which are determined according to the designer's needs. It can be the percentage difference of the platform's motions between numerical and experimental results or other conditions.

3.5. Summary

This chapter introduces the overall structure of the SADA method including the selection of KDPs, *DARwind* programme and the AI module. More details will be introduced in the following chapters.

Chapter 4. Key Disciplinary Parameters

This chapter aims to demonstrate the concept of KDPs, which come from the highly coupled nature of FOWTs. Many theories involved in FOWT dynamic models include massive functions and formulas conventionally determined based on assumptions and empirical parameter values. However, many assumptions and empirical parameters were not initially proposed for FOWTs but inherited from land-based wind turbines, traditional floating offshore units, or other engineering applications. For example, the lift or drag coefficient of wind turbine blade in aerodynamics can bring potential problems to the later numerical simulation of the entire FOWTs system. Many other key environmental parameters, such as viscous damping in hydrodynamics, mooring line damping values etc., are also challenging to be issued unique values during the analysis. These parameters belong to the category of KDPs, which can be shown in **Figure 4.1**.

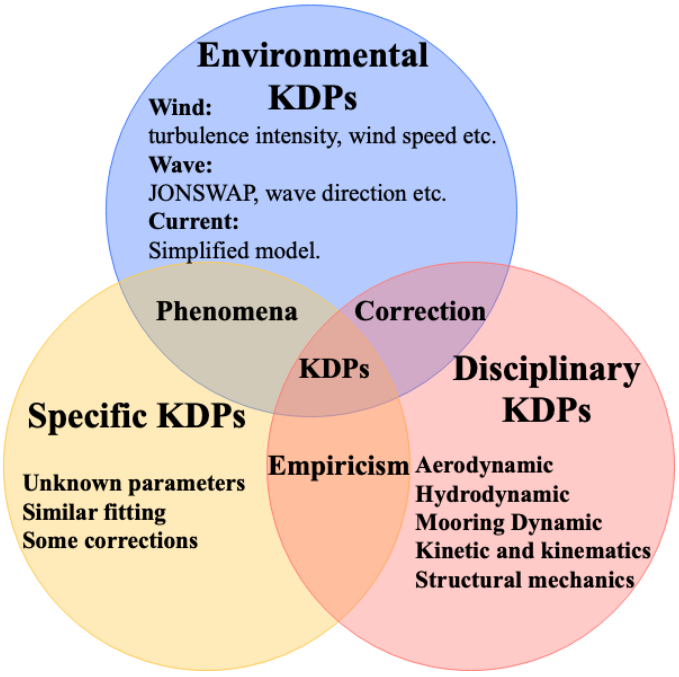

Figure 4.1 The Venn diagramme of KDPs.

These KDPs are very representative of uncertain parameters in the field of FOWTs and reflect the complexity of their coupling. The proposal of KDPs is of great importance for

a practical application of FOWTs and the SADA method. They are the data transfer interface between AI technology and FOWTs design and application. Although they have changed under the coupling effect of FOWTs, their boundary conditions can help the designer to define their variability to some extent.

4.1. Environmental KDPs

In the most current numerical simulation for dynamic analysis of FOWTs, a wide range of parameters rely on empirical data and require manual input. These parameters vary with different models and locations, such as gravitational acceleration, water density, air viscosity, operational water depth, etc.

Firstly, air density can be taken as an example. With the difference in altitude, temperature and air pressure in various regions, the air density is also different. Under different air pressure, temperature, and water vapour pressure, the calculation formula of air density can be defined as:

$$\rho_{air} = \frac{1.276}{1 + 0.00366t} \times \frac{p - 0.38e}{1000} \qquad \textbf{Eq. 4.1}$$

Where the p is the pressure, the t is the temperature, and e is the water vapour pressure. The height of offshore floating wind turbines is significant. For example, 5MW FOWT *Hywind* has a tower height of 77.6 and a blade length of 63. This means that the blades or tower height and wake effect will vary air density and viscosity. It will impact the wind load applied on the rotating blades, though these effects have been mostly neglected in the current numerical program. The empirical formula for calculating air density changes with altitude is (Lu and Zhou, 2018):

$$\rho_{air} = 1.225e^{-0.0001h} \qquad \textbf{Eq. 4.2}$$

Where ρ is the air density corresponding to height h. Therefore, in this example, the empirical value of -0.0001 before h can be considered a KDP. The value of this

parameter can be changed within a range in the SADA method to consider the variation of the air density.

Secondly, the wind profile and wind turbulence intensity are other examples. It is well known that wind speed can be calculated based on vertical wind profile such as the logarithmic profiles or power law (Pelletier *et al.*, 2016):

$$\begin{cases} U(z) = \dfrac{u^*}{K} ln\left(\dfrac{z}{z_0}\right) \\ U(z) = U(z_{ref})\left(\dfrac{z}{z_{ref}}\right)^{\alpha} \end{cases} \quad \textbf{Eq. 4.3}$$

Where U is the horizontal component of the wind velocity, z is the height concerning the ground level, u^* is the friction velocity, K is the von Karman constant, z_0 is the roughness length, α is the exponent for the power law, and the subscript ref is related to properties at a reference height. In this case, the friction velocity u^*, von Karman constant K and roughness lengths z_0, etc., can all be considered within the scope of environmental KDPs.

Besides, the turbulence intensity, also often referred to as turbulence level, is defined as (Nishi *et al.*, 1993):

$$I \equiv \frac{u'}{U} \quad \textbf{Eq. 4.4}$$

Where u' is the root-mean-square of the turbulent velocity fluctuations, and U is the mean velocity (Reynolds averaged). If the turbulent energy, k, is known, u' can be computed as:

$$u' \equiv \sqrt{\frac{1}{3}\left({u'_x}^2 + {u'_y}^2 + {u'_z}^2\right)} = \sqrt{\frac{2}{3}k} \quad \textbf{Eq. 4.5}$$

U can be computed from the three mean velocity components U_x, U_y and U_z as:

$$U \equiv \sqrt{{U_x}^2 + {U_y}^2 + {U_z}^2} \qquad \textbf{Eq. 4.6}$$

In this example, the turbulent energy parameter k in the above formula can be selected as a KDP, which have a vital influence on the power generation of wind turbines. Different changes mean that the wind turbine may need to adjust the pitch angle of the blades to maintain a constant power generation. This also means that there will be a chain reaction to the dynamic response of the entire FOWTs system, including platform motions, tower and blade deformation and fatigue, etc. Therefore, the turbulent energy parameter k is selected as a KDP in the SADA method.

Considering the viscous effect of sea level on wind speed, change of the average wind speed gradient along the height conforms to the logarithmic rate:

$$\bar{u}(z) = \bar{u}(h)\left(\frac{z}{h}\right)^{1/n} \qquad \textbf{Eq. 4.7}$$

Where, h is the reference height above sea level is usually 10 m; $\bar{u}(h)$ is the average wind speed at the reference height; z is above sea level; $\bar{u}(z)$ is the average wind speed at z; n is the wind profile index, which characterizes the sea level roughness. For the open coastal area, the value of n is usually 3; for the uncovered sea area, the value is usually 7 ~ 8. However, its real value varies and depends on quite a lot of experience in simulation, so parameter n is chosen as one KDP.

Thirdly, for wave load calculation, the JONSWAP (Joint North Sea Wave Project) type spectrum is popularly used to simulate the irregular waves in FOWT analysis. The 17th ITTC recommended the following JONSWAP type spectrum for limited fetch (Faltinsen, 1993):

$$S(\omega) = 155\frac{{H_{1/3}}^2}{{T_1}^4\omega^5}exp\left(\frac{-944}{{T_1}^4\omega^4}\right)3.3^{exp\left[-\left(\frac{0.191\omega T_1-1}{\sqrt{2}\sigma}\right)^2\right]} \qquad \textbf{Eq. 4.8}$$

Where:

$$\sigma = \begin{cases} 0.07 & for\ \omega \leq {}^{5.24}/_{T_p} \\ 0.09 & for\ \omega > {}^{5.24}/_{T_p} \end{cases}$$

$H_{1/3}$ is the significant wave height defined as the mean of the one third highest waves and T_1 is a mean wave period. In the JONSWAP spectrum. Their value can be adjusted in the SADA method during the AI optimization process. Similarly, the peak period, and the wave direction can all be selected as KDPs in the SADA method.

Fourthly, the parameters of current also can be selected as KDPs. The current model in numerical analysis can be expressed as below:

$$U_C(z) = U_0\left(\frac{z+h}{h}\right)^c \qquad \textbf{Eq. 4.9}$$

Where, z is the vertical depth below the water surface; h is the depth of the water to the bottom; U_0 is the velocity of the water. Parameter c commonly uses empirical value 1/7, but it varies for different sea states. Thus, c can be chosen as one of the environmental KDPs.

In general, the above-mentioned environmental KDPs, especially wind and waves, have a significant impact on the dynamic response of the FOWTs system. A slight difference may significantly change the entire system's dynamic response because the FOWT is a high nonlinear coupling system, and all the disciplines involved are highly coupled to others. This characteristic makes the application of AI technology in the analysis essential.

4.2. Disciplinary KDPs

Disciplinary KDPs constitute the largest category of KDPs. Those empirical formulas and parameter values in the fundamental theories for calculating loads, motions, and all the dynamic responses of FOWTs can be put in the disciplinary KDPs category. Many of the

empirical formulas and parameters involved in physical modelling are determined based on assumptions or practical fitting works. Some assumptions and empirical parameters are not explicitly designed for FOWTs but are inherited from land-based wind turbines and offshore oil & gas engineering practices. Therefore, many KDPs can be defined in this category. The following will use KDPs in aerodynamics, hydrodynamics, servo dynamic and kinematics as examples to introduce the disciplinary KDPs.

4.2.1. Aerodynamic parameters KDPs

Aerodynamic load is one of the dominating loads applied on FOWTs. Conventional aerodynamics theories include one-dimensional momentum theory (ideal disk) and 2-D BEMT for the simulation and experimental design. There are many assumptions and empirical parameters popularly used in these theories. For the BEMT model, there are some critical assumptions, such as no radial dependency. Many correction models also use empirical parameter values, such as *Prandtl's* tip loss factor and *Glauert* correction parameters.

4.2.1.1. Glauert correction

For aerodynamic calculation, when the axial induction factor becomes more significant than approximately 0.4, the simple momentum theory breaks down. Different empirical relations between the thrust coefficient C_T and axial induction factor a can be made to fit with measurements, for example:

$$C_T = \begin{cases} 4a(1-a)F & a \le a_c \\ 4a\left(1-\frac{1}{4}(5-3a)a\right)F & a > a_c \end{cases} \qquad \textbf{Eq. 4.10}$$

F is Prandtl's tip loss factor and corrects the assumption of an infinite number of blades. The last expression is found in (Hansen, 2015) and a_c is approximately 0.2. Because a_c is an empirical value, it is chosen as one KDP.

4.2.1.2. Prandtl's tip loss factor

Take Prandtl's tip loss factor as an example. For a rotor with a finite number of blades, the vortex system in the wake is different from a rotor with an infinite number of blades. The relevant formula is as follows (Hansen, 2015):

$$\begin{cases} F_P = \frac{2}{\pi} arcsin(e^{-f}) \\ f = \frac{N(R-r)}{2rsin\varphi} \end{cases} \quad \textbf{Eq. 4.11}$$

Where, N is the number of blades. R is the total radius of the rotor, r is the local radius of the blade element, φ is the flow angle. In some cases, when f is less than 7, it can be calculated according to the F_P parameter. When f is greater than 7, the change is small so that the tip loss can be neglected. Therefore, the threshold value seven plays an essential role in the aerodynamic load calculation. However, this threshold value was initially proposed and determined based on onshore wind turbines theories. For FOWTs, this threshold value could be different, and therefore it can be defined as a disciplinary KDP.

4.2.1.3. Lift and drag coefficients

In the BEMT method, reliable lift and drag coefficients are required and are usually obtained from model experiments. However, the model experiment can only be conducted for a small angle of attack until stall mode. Beyond stall mode, the Viterna method is commonly used. The technique predicts the lift and drag coefficients from stall angle to 90 deg. Beyond that range, the original flat plate theory assumption can also be adopted (Mahmuddina, 2016). The Viterna method is formulated to extrapolate the lift and drag coefficients using the following equation:

$$\begin{cases} C_L = A_1 sin2\alpha + A_2 \dfrac{\cos^1 \alpha}{sin\alpha} \\ C_D = B_1 sin^2\alpha + B_2 cos\alpha \end{cases} \quad \textbf{Eq. 4.12}$$

Where,

$$\begin{cases} A_1 = \dfrac{c}{2} \\ C_{D_{max}} = 1.11 + 0.018AR \\ B_1 = C_{D_{max}} \\ A_2 = \left(C_{L_{stall}} - C_{D_{max}} sin\alpha_{stall} cos\alpha_{stall}\right) \dfrac{sin\alpha_{stall}}{cos^2\alpha_{stall}} \\ B_2 = \dfrac{C_{D_{stall}} - C_{D_{max}} sin^2\alpha_{stall}}{cos\alpha_{stall}} \end{cases}$$

The symbol AR stands for aspect ratio, obtained from the BEMT application where finite blade length affects the flat plate assumption. The recommended value for AR is 10 for most computations. However, using different values of AR will impact the results (Mahmuddin *et al.*, 2017). Therefore, AR can be considered as the category of disciplinary KDPs.

4.2.1.4. Tower drag coefficient

Due to the large-scale motion of the platform, its tower structure has more significant deformation and vibration than the fixed wind turbine. Therefore, it is necessary to perform an aerodynamic load calculation on the tower, especially under severe wind conditions. The tower needs to be divided into many differential units in the analysis. The aerodynamic load of each discrete tower unit is calculated according to the following empirical formula. It is equivalent to the centre of each unit.

$$d\boldsymbol{F^T} = \frac{1}{2}\rho C_D^T D\left(\boldsymbol{V_0^{wind}} - \boldsymbol{V_{TE}}\right)\left|\boldsymbol{V_0^{wind}} - \boldsymbol{V_{TE}}\right|\delta L \quad \textbf{Eq. 4.13}$$

C_D^T is the drag coefficient for cylindrical structures, usually 0.5; D is the local tower diameter; $\boldsymbol{V_0^{wind}}$ is the velocity component of the upstream wind speed perpendicular to the tower axis; $\boldsymbol{V_{TE}}$ is to consider the velocity component of the cross-section of the

tower caused by platform motion and tower vibration perpendicular to the tower axis; δL is the length of the differential element. The uncertainty of the drag coefficient is an essential component of KDPs.

4.2.1.5. Yaw correction

There is a local yaw state when there is a non-orthogonal relationship between the incoming wind and the wind turbine disk surface.

$$\begin{cases} a_{skew} = a_0 \left[1 + \frac{r}{R} tan\frac{\chi}{2} cos(\theta_b - \theta_0)\right] \\ \chi = (0.6a_0 + 1)\gamma \end{cases} \quad \textbf{Eq. 4.14}$$

a_{skew} is a modified aerodynamic induction factor; a_0 is an uncorrected aerodynamic induction factor; γ is the angle between the incoming wind direction and the normal of the disk surface, the yaw angle; χ is the angle between the inclination direction of the wake and the normal direction of the disc surface; θ_b is the current azimuth of the blade; θ_0 is the azimuth angle when the blade points to the deepest part of the wake. The azimuth angle can be determined by the direction of the projected component of the incoming wind on the wind turbine disk surface. The accurate yaw angle is one of the key parameters that affect the dynamic response of FOWTs, and it can also be considered a part of KDPs here.

4.2.1.6. Dynamic inflow model

A dynamic inflow model must be applied to consider the time delay with the aerodynamic loads. In two EU-sponsored projects (Schepers and Snel, 1995; Snel and Schepers, 1995), different engineering models were tested against measurements. One of these models, proposed by S. Øye, is a filter for the induced velocities consisting of two first-order differential equations (Liu *et al.*, 2019):

$$\begin{cases} a_{int} + \tau_1 \cdot \dfrac{da_{int}}{dt} = a_{qs} + \kappa \cdot \tau_1 \cdot \dfrac{da_{qs}}{dt} \\ a + \tau_2 \cdot \dfrac{da}{dt} = a_{int} \end{cases} \quad \textbf{Eq. 4.15}$$

a_{qs} is the quasi-static value. a_{int} is an intermediate value and a the final filtered value used as the induced velocity. The two constants are calibrated using a simple vortex method as:

$$\begin{cases} \tau_1 = \dfrac{1.1}{(1 - 1.3a)} \cdot \dfrac{R}{v_0} \\ \tau_2 = \left[0.39 - 0.26 \times \left(\dfrac{r}{R}\right)^2\right] \cdot \tau_1 \end{cases} \quad \textbf{Eq. 4.16}$$

R is the rotor radius, $\kappa = 0.6,$ and a is the axial induction factor defined for zero yaw as a is not allowed to exceed 0.5. Parameter κ and induction factor a can also be considered part of KDPs.

4.2.2. Hydrodynamic parameters KDPs

Potential flow theory and Morison's equation are commonly used methods for hydrodynamic load calculation in FOWT analysis. Nevertheless, the potential flow damping cannot consider the viscous effect of fluids accurately.

4.2.2.1. Viscous damping correction

As for FOWTs, when the supporting platform is a Spar type floater, the calculation of viscous damping force can use Morrison's equation:

$$d\boldsymbol{F}_{\boldsymbol{m}}^{\boldsymbol{V}} = -\frac{\rho}{2} C_D^M D dz \cdot (\boldsymbol{v}_{\boldsymbol{w}} - \boldsymbol{v}_{\boldsymbol{s}}) \cdot |\boldsymbol{v}_{\boldsymbol{w}} - \boldsymbol{v}_{\boldsymbol{s}}| \quad \textbf{Eq. 4.17}$$

Where, D is the diameter of the cylinder; $\boldsymbol{v}_{\boldsymbol{w}}$ and $\boldsymbol{v}_{\boldsymbol{s}}$ are the velocity component of the fluid velocity when the water mass is not disturbed and the cross-sectional slice velocity of the underwater component perpendicular to the cross-section axis; C_D^M is drag coefficient; Among these parameters, drag coefficient and added mass coefficient

both have empirical values and are quite crucial for the hydrodynamic load calculation. The drag coefficient and added mass coefficient can also be selected as disciplinary KDPs.

4.2.2.2. Added restoring force matrix

In the static water flow field, the FOWTs will also change the wet surface due to the motions of the floating body, which will cause the static water pressure to change and be affected by the restoring force of the static water.

$$F^S = [0 \quad 0 \quad \rho g V_\nabla \quad 0 \quad 0 \quad 0]^T - \boldsymbol{C} \cdot \boldsymbol{X} \qquad \textbf{Eq. 4.18}$$

$$\boldsymbol{C} = \begin{bmatrix} 0 & 0 & 0 & 0 & 0 & 0 \\ 0 & 0 & 0 & 0 & 0 & 0 \\ 0 & 0 & \rho g A_w & 0 & 0 & 0 \\ 0 & 0 & 0 & \rho g (I_x + z_B V_\nabla) & 0 & 0 \\ 0 & 0 & 0 & 0 & \rho g (I_y + z_B V_\nabla) & 0 \\ 0 & 0 & 0 & 0 & 0 & 0 \end{bmatrix} \qquad \textbf{Eq. 4.19}$$

The restoring force also needs to be compared with the experimental results in the numerical calculation. The parameters in the added restoring force matrix are very significant KDPs.

4.2.3. Servo dynamics

4.2.3.1. Low-pass filter

The generator torque controller uses the generator speed as the signal source. To filter the high-frequency components in the signal to avoid causing the frequency response of the controller, the following low-pass filter can be used for signal slip:

$$\begin{cases} y[n] = (1-\alpha)u[n] + \alpha y[n-1] \\ \alpha = e^{-2\pi T_s f_c} \end{cases} \qquad \textbf{Eq. 4.20}$$

y is the generator speed signal after passing through the filter; u is the original generator speed measurement signal without filtering wave; n is the current value of the number of discrete-time intervals; α is the low-pass filter coefficient; T_s is a discrete-time

interval; f_c is the corresponding angular frequency. Among them, the low-pass filter coefficient α can be considered as KDPs.

4.2.3.2. Generator torque constant

Control operation will induce some unexpected dynamic responses of FOWTs, so some control parameters are selected as KDPs. The wind speed is greater than the cut-in wind speed but less than the rated wind speed. Different speeds can be further divided into three stages, namely, zone 1½ (wind turbine start to work), zone 2 (partial power operation) and zone 2½ (rated power operation). The generator torque constant in the wind speed operation region is chosen as one of the KDP in the SADA method. When in area 1½, the wind turbine starts to use wind energy, and the generator torque is proportional to the rotor speed to maintain a better power factor. At this moment, there is a linear relationship:

$$T_{Gen} = k_1(\omega - \omega_1)N \cdot m \qquad \textbf{Eq. 4.21}$$

When the wind speeds further increase, the rotation speed also increases accordingly. At this moment, region two is entered, and the generator torque is adjusted to a quadratic relationship proportional to the rotation speed.

$$T_{Gen} = k_2\omega^2 N \cdot m \qquad \textbf{Eq. 4.22}$$

When the wind speed is close to the rated wind speed, the generator speed is also close to the rated speed, then enter the area 2½, the generator torque and speed are readjusted to a linear relationship, as a transition area between rated and non-rated conditions.

$$T_{Gen} = k_3(\omega - \omega_{sy})N \cdot m \qquad \textbf{Eq. 4.23}$$

The value of the k_1, k_2, k_3 usually are determined as an empirical value of FOWTs. But it varies for a different type. Therefore, k_1, k_2, k_3 can be chosen as KDPs as well.

4.2.4. Kinematics and Dynamics

The mode method (Andreaus *et al.*, 2016) is used in *DARwind* to approximate the finite DOF of the three-dimensional beam deformation $\boldsymbol{U_0}$, as follows:

$$\boldsymbol{U_0} = \boldsymbol{\phi} \cdot \boldsymbol{Q} \qquad \textbf{Eq. 4.24}$$

Among them, the axial and lateral deformation are as follows:

$$\begin{cases} l_1 = \sum_{i=1}^{n} \phi_{xi} q_{xi} = \boldsymbol{\phi_x}^{\boldsymbol{T}} \boldsymbol{q_x} = \boldsymbol{q_x}^{\boldsymbol{T}} \boldsymbol{\phi_x} \\ l_2 = \sum_{i=1}^{n} \phi_{yi} q_{yi} = \boldsymbol{\phi_y}^{\boldsymbol{T}} \boldsymbol{q_y} = \boldsymbol{q_y}^{\boldsymbol{T}} \boldsymbol{\phi_y} \\ l_3 = \sum_{i=1}^{n} \phi_{zi} q_{zi} = \boldsymbol{\phi_z}^{\boldsymbol{T}} \boldsymbol{q_z} = \boldsymbol{q_z}^{\boldsymbol{T}} \boldsymbol{\phi_z} \end{cases} \qquad \textbf{Eq. 4.25}$$

Where the spatial shape function matrix is:

$$\boldsymbol{\phi} = \begin{bmatrix} \boldsymbol{\phi_x}^{\boldsymbol{T}} & \mathbf{0} & \mathbf{0} \\ \mathbf{0} & \boldsymbol{\phi_y}^{\boldsymbol{T}} & \mathbf{0} \\ \mathbf{0} & \mathbf{0} & \boldsymbol{\phi_z}^{\boldsymbol{T}} \end{bmatrix} \begin{matrix} \boldsymbol{\phi_x} = [\phi_{x1} & \phi_{x2} & \cdots & \phi_{xn}]^T \\ \boldsymbol{\phi_y} = [\phi_{y1} & \phi_{y2} & \cdots & \phi_{yn}]^T \\ \boldsymbol{\phi_z} = [\phi_{z1} & \phi_{z2} & \cdots & \phi_{zn}]^T \end{matrix} \qquad \textbf{Eq. 4.26}$$

The coefficients of polynomial mode ϕ_{x1} value is 0.0622 as an empirical value of *Hywind*. But it varies for a different type of structure and material. Therefore, ϕ_{x1} will be adopted as one KDP in the kinematics & structural module, the x-axis component of spatial shape function.

4.3. Specific KDPs

For specific KDPs, some experimental models or design parameters of the full-scale FOWTs are different from the actual physical models. In addition, due to commercial confidentiality, it is impossible to obtain all the design parameters. In this case, users can only take similar physical models to replace them or design according to the original

model. For FOWTs, there are many new physical phenomena worth exploring, and if these phenomena involve an additional force, moment, and damping, they can also be considered in specific KDPs.

Besides, some experiments used static lines or cables to replace a static thrust from a given turbine' thrust curve or drag discs to reproduce the static wind loading (Roddier *et al.*, 2010; Guanche *et al.*, 2011; Wan *et al.*, 2016c). There is also the simplification of the mooring lines model: use the quasi-static catenary equation to replace the delta link of multi-lines by increasing the yaw stiffness. As for potential flow theory, there are also some empirical parameters based on previous experiments. Their values might not be accurate for FOWTs calculation, and these empirical parameters involved can be classified as specific KDPs.

4.4. Boundary conditions of KDPs

To adjust KDPs efficiently in the SADA method, the boundary conditions of the KDPs must be adequately defined. This section will discuss the boundary conditions of KDPs. **Figure 4.2** shows the flowchart of KDP and boundary conditions in SADA.

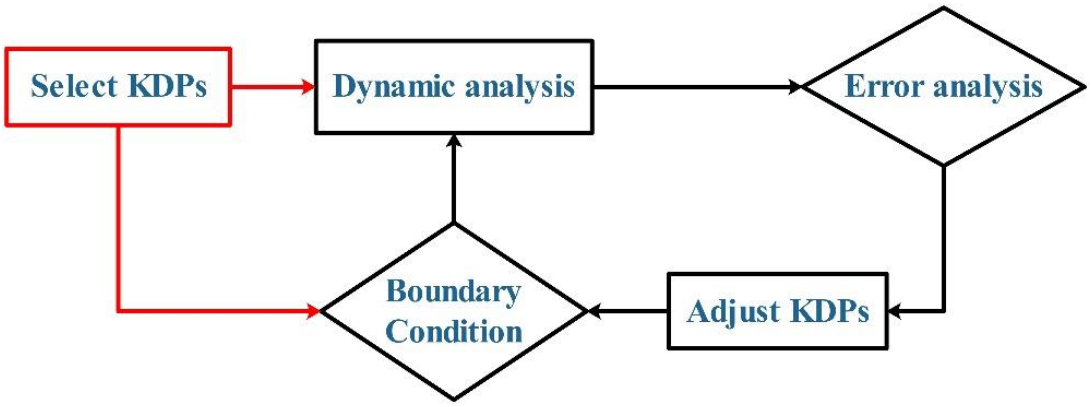

Figure 4.2 The flowchart of KDP and boundary conditions.

A good boundary condition can speed up the convergence of SADA and reflect the rationality of the dynamic response of FOWTs accurately. Each KDP has a specific value, and the magnitude of their values may vary significantly, so the boundary conditions are

also set on this basis. Although the amplitude of each KDP is different, the significant figures of these KDPs values can also provide a reliable classification and setting method.

Therefore, based on significant figures of each KDP, the general formula for defining their boundary conditions can be defined as:

$$\begin{cases} X \in \left[X - a \cdot 10^{(-X_{SF})}, X + a \cdot 10^{(-X_{SF})}\right], & 0 \le |X| \le 1 \\ X \in \left[X - a \cdot 10^{(Y-X_{SF})}, X + a \cdot 10^{(Y-X_{SF})}\right], & 1 < |X| \le 10 \\ X \in \left[X - a \cdot 10^{(Y-2)}, X + a \cdot 10^{(Y-2)}\right], & |X| > 10 \end{cases} \quad \textbf{Eq. 4.27}$$

Where, X is the value of KDPs; Y is the number of digits to the left of the decimal point; X_{SF} is the significant figures of the KDPs value; a is the boundary condition coefficient, which determines the range of the boundary conditions of KDPs. The four specific ranges in equation 4.28 are shown in the following formulas:

$$BC = \begin{cases} Fix\ range & a = 0 \\ Small\ range & a \in [-1,1] \\ Large\ range & a \in [-5,5] \\ No\ range\ limit & |a| > 5 \end{cases} \quad \textbf{Eq. 4.28}$$

To better understand the definitions of **Eq.4.27** and **Eq.4.28**, take wind speed V_{wind}^{A} in aerodynamics and viscous damping coefficient $C_{VD(1,1)}^{H}$ and current speed $V_{current}^{H}$ in hydrodynamics as examples to demonstrate how to use **Eq.4.27** and **Eq.4.28** to choose the corresponding boundary conditions.

As for the steady wind speed in aerodynamics, if V_{wind}^{A}=9.5 m/s, then Y=1, $X_{SF} = 2$, So the three boundary conditions are:

$$V_{wind}^{A}(BC) = \begin{cases} Small\ range \in [9.49,9.51] & a = 0.1 \\ Large\ range \in [9,10] & a = 5 \\ No\ range\ limit \in [0,19.5] & a = 100 \end{cases} \quad \textbf{Eq. 4.29}$$

In the boundary condition without range limitation, the value of a is 15. The original boundary condition should be $[-0.5, 19.5]$. The steady wind speed cannot be negative, so the default here is $[0, 19.5]$.

As for the added viscous damping coefficient in hydrodynamics, if $C^H_{VD(1,1)}$=10000.0, then Y=5, So the three boundary conditions are:

$$C^H_{VD(1,1)}(BC) = \begin{cases} Small\ range \in [9000,11000] & a = 1 \\ Large\ range \in [5000,15000] & a = 5 \\ No\ range\ limit \in [-1000,21000] & a = 11 \end{cases} \quad \textbf{Eq. 4.30}$$

Similar to current speed, if $V^H_{current}$=0.05 m/s, then X_{SF}=3, So the three boundary conditions are:

$$V^H_{current}(BC) = \begin{cases} Small\ range \in [0.049, 0.051] & a = 1 \\ Large\ range \in [0.045, 0.055] & a = 5 \\ No\ range\ limit \in [0, 0.1] & a = 50 \end{cases} \quad \textbf{Eq. 4.31}$$

The above discussion and classification of KDPs boundary conditions are only for general situations. For some specific KDPs, the actual boundary conditions must be combined to make judgments based on their value of them.

4.5. Summary

This chapter introduces the concept of KDPs. As the data transmission interface between AI technology and *DARwind*, KDPs play a pivotal role in SADA. The choice of KDPs is very challenging. It requires designers to understand the knowledge of the entire FOWTs system in various disciplines and requires a lot of verification work to verify its quantitative impact on the dynamic performance of FOWTs. In summary, one example list of the most KDPs has been provided in **Table *4.1***. More specific details about the study of KDPs will be found in **Chapter 9**.

Table 4.1 Example list of KDPs

KDPs	
Aero	Wind speed
	Glauert correction
	Tower drag
Hydro	Current speed
	Added linear viscous damping matrix
	Added linear restoring matrix
	Added linear mass matrix
Mooring	Wet density
	Axial stiffness
Kinematics And Structural	Polynomial Flap 1st vibration modes
	Polynomial Flap 2nd vibration modes
	Polynomial Edge 1st vibration modes
Servo	Generator torque constant

Chapter 5. *DARwind*

This chapter introduces the methodology of *DARwind* briefly, and for more specific information about *DARwind*, please refer to the published literature (Chen *et al.*, 2019a). The following sections will discuss the methodology of each subdivision module in the solver.

5.1. Aerodynamic module

A brief introduction to the aerodynamic load calculation methods is described in this section.

5.1.1. BEMT method

The Blade Element/Momentum theory (BEMT) with aerodynamic corrections is currently applied in the code (Hansen, 2015). The blade is discretized into many differential units (blade elements), and it is assumed that the blade elements at different radial distances are independent of each other. The aerodynamic force does not affect each other between the blade elements. The wind turbine blade is divided into several micro-segments along its radial direction, and the forces (lift, drag and aerodynamic torque) of each blade element are calculated independently. The resultant force of the entire blade is obtained by integration. The blade element model and the aerodynamic relationship of the blade are shown in **Figure 5.1**.

Among them, v_0 is the inflow wind speed of the blade element. a is the axial induction coefficient, a' is the tangential induction coefficient, ωr is the relative tangential velocity caused by the blade rotation, r is the radial distance from the hub centre to the section centre, and v_{rel} is the final relative wind speed, θ is the local pitch angle of the blade, φ is the structural twist angle of the blade, ϕ is the angle between the final relative wind speed and the rotation plane, that is, the inflow angle, and α is the local inflow angle of attack of the blade element.

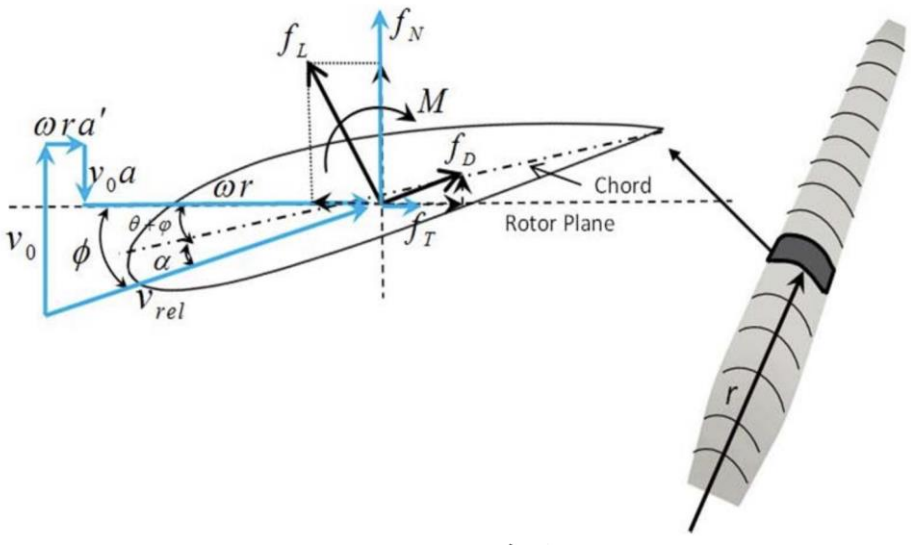

Figure 5.1 Blade element model (Chen *et al.*, 2019a).

In BEMT, each element's axial and tangential induction factors are iteratively calculated in turn, and then each aerodynamic physical quantity can be obtained. The specific steps are as follows:

- Step (1) Initialize axial a and tangential a' inducer, typically $a = a' = 0$.
- Step (2) Compute the flow angle ϕ.
- Step (3) Compute the local angle of attack α.
- Step (4) Read off lift coefficient $C_l(\alpha)$, drag coefficient $C_d(\alpha)$, and pitching moment coefficient $C_m(\alpha)$ from table based on the local angle of attack α.
- Step (5) Compute thrust coefficient C_n and tangential force coefficient C_t.
- Step (6) Calculate axial inducer a and tangential inducer a'.
- Step (7) If a and a' has changed more than a certain tolerance, go to step (2) or finish.
- Step (8) Compute the local loads on the segment of the blades.

After completing the calculation of each blade element according to the above process, the overall thrust and power of the wind turbine can be obtained as follows:

$$\begin{cases} T = \int_0^R dT(r) = 4\pi\rho v_0^2 \int_0^R a(1-a) r dr \\ P = \int_0^R dM(r) \cdot \omega = 4\pi\rho v_0^2 \omega^2 \int_0^R a'(1-a) r^3 dr \end{cases} \quad \textbf{Eq. 5.1}$$

In summary, the process of aerodynamic force calculation is shown in **Figure 5.2** (Chen *et al.*, 2019a).

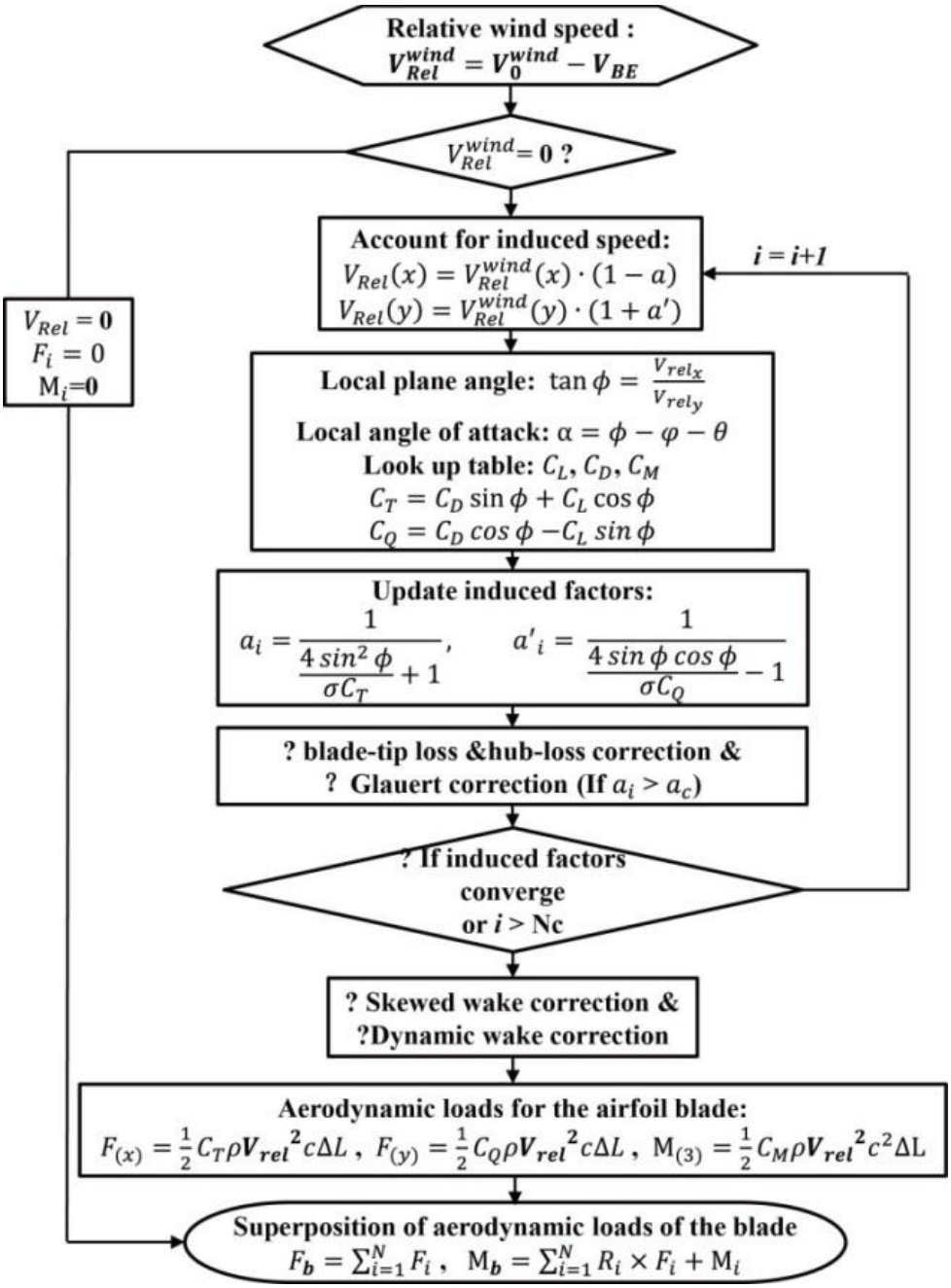

Figure 5.2 Flow chart of the aerodynamic (Chen *et al.*, 2019a).

5.1.2. Aerodynamic correction

The models in BEMT are based on some idealized assumptions, which are different from the aerodynamic loads experienced by FOWTs. For example: when the aerodynamic induction coefficient exceeds a specific value, the calculation accuracy of BEMT may be reduced; the influence of the existence of the hub is not considered; the time delay of actual aerodynamic response needs to be considered. These need to be modified to improve the accuracy of the BEMT method in the application of FOWTs.

Therefore, aerodynamic corrections have been taken to improve the accuracy of the BEMT method in the *DARwind*, which are shown in **Table 5.1**.

Table 5.1 Comparison of three different methods

Corrections	**Object**	**References**
Prandtl's tip-loss and hub-loss corrections	Consider the vortices shed at these locations	(Hansen, 2015)
Glauert's correction	Take the large induction velocities into account	(Hansen, 2015)
Skewed wake correction	Consider the effects of incoming flow that is not perpendicular to the rotor plane.	(Spera, 2009)
Dynamic wake correction	Consider the aerodynamic time delay effect	(Hansen, 2015)

5.2. Hydrodynamic module

This section will introduce the hydrodynamic calculation in *DARwind.*

5.2.1. Definition of Coordinate System

The hydrodynamic calculation uses two cartesian coordinate systems, shown in **Figure 5.3**: the global inertial frame e_g: $O_0 - x_0y_0z_0$ and the body-fixed frame of the platform e_p: $O_1 - x_1y_1z_1$. The 6 degrees of freedom (DOFs) of the FOWTs' platform can be defined as three translational DOFs (surge (x_0), sway (y_0), and heave (z_0)) and three rotational DOFs (roll (x_1), pitch (y_1) and yaw (z_1)).

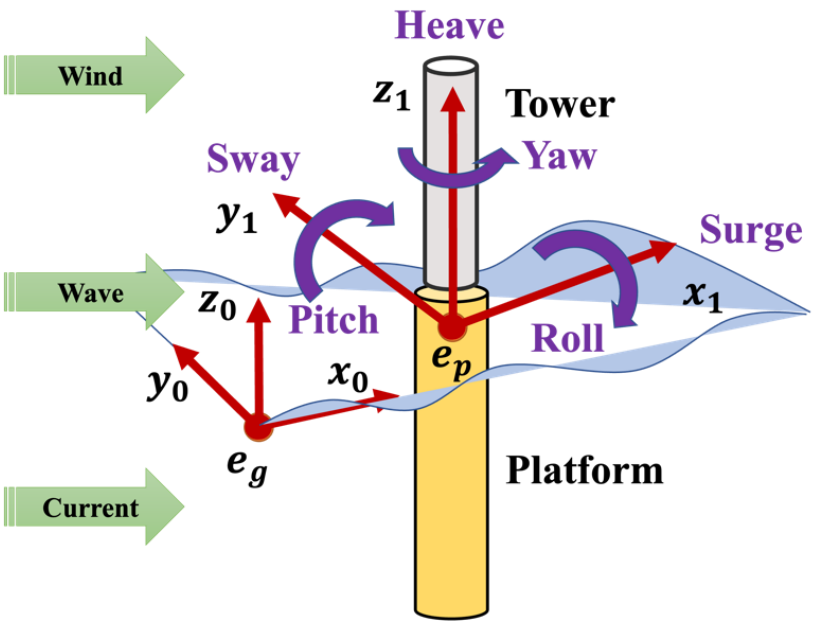

Figure 5.3 Coordinate systems defined in the hydrodynamic module.

5.2.2. Hydrodynamic loads calculation

The calculation involving hydrodynamic loads ($\boldsymbol{F_H}$) in *DARwind* includes the following five parts:

$$\boldsymbol{F_H = F^w + F_s^w + F^R + F^V + F^s} \qquad \textbf{Eq. 5.2}$$

Where, $\boldsymbol{F^w}$ is the excitation load; $\boldsymbol{F_s^w}$ is the second-order wave forces; $\boldsymbol{F^R}$ is the linear wave radiation force; $\boldsymbol{F^V}$ is the hydrodynamic damping; $\boldsymbol{F^s}$ is the buoyancy and hydrostatic restoring forces. The current models involved in *DARwind* include sub-surface, near-surface, and depth-independent (Jonkman *et al.*, 2014). In summary, the hydrodynamic calculation of *DARwind* is shown in **Figure 5.4**.

First, through the three-dimensional frequency domain potential flow software WAMIT, the hydrodynamic force of the FOWTs' platform is pre-calculated. In addition, significant hydrodynamic parameter files are generated, such as the platform's static water restoring force coefficient, the first-order wave excitation force transfer function, first-order wave excitation force transfer function, wave radiation force parameters etc. In the early stage

of operation, the program establishes an environment based on the read-in hydrodynamic data files and related environmental information parameters. Subsequently, the program sets a time-domain wave field based on the Airy linear wave model and related wave parameters and establishes a current time history model. Finally, the program calculates the first-order wave force, second-order wave force, wave radiation force, hydrostatic restoring force, and the viscous damping force modified by the Morrison method (or steady viscosity coefficient matrix).

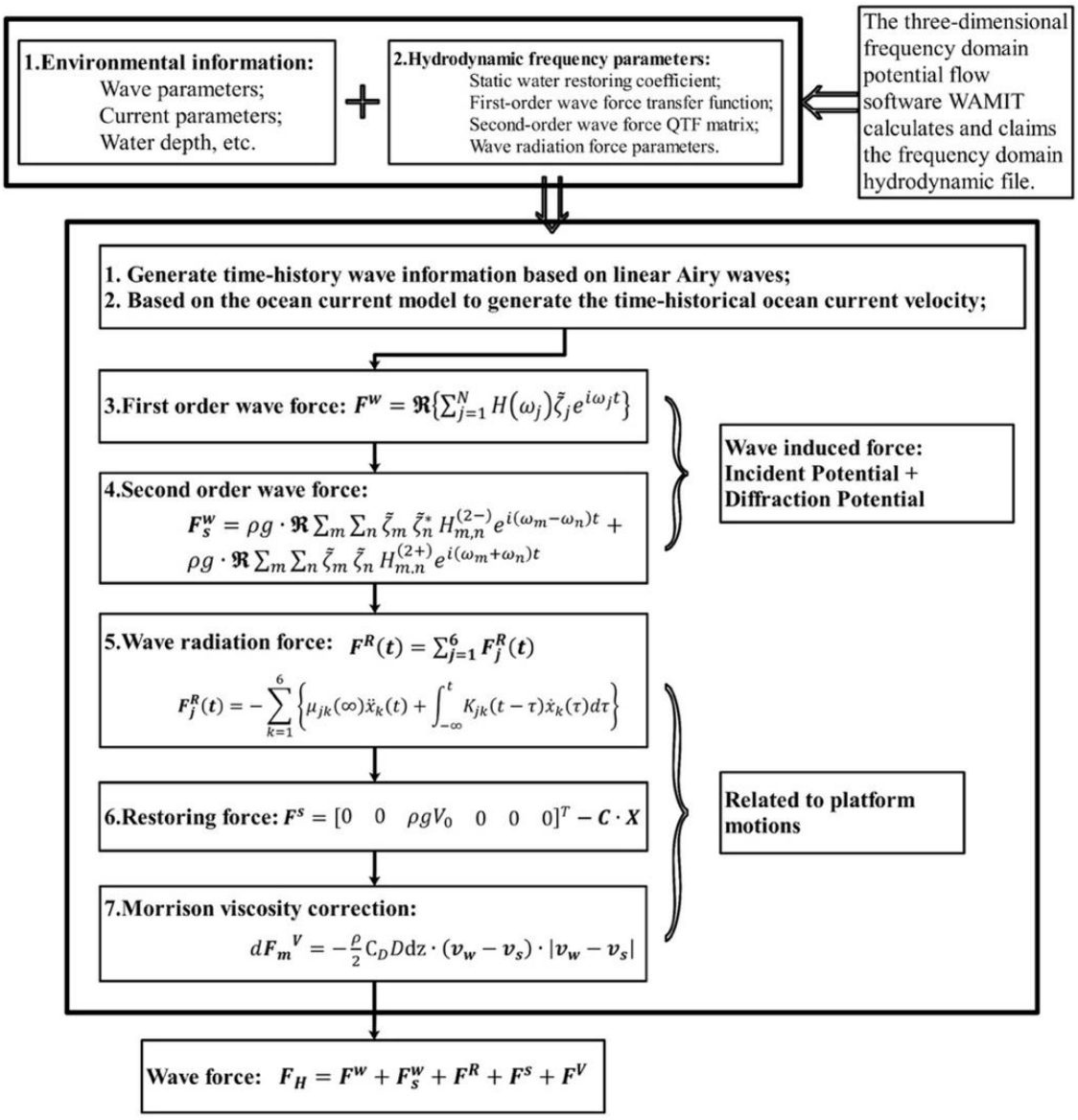

Figure 5.4 Procedure of hydrodynamic module.

5.3. Mooring dynamic module

This section will introduce the mooring system in *DARwind.* More details can be found in the literature (Chen *et al.*, 2019a).

5.3.1. Quasi-static model

The gravity catenary mooring system is more commonly used in FOWTs. Since the mooring line is much denser than water and moves slowly, a quasi-static catenary mooring model can be used in numerical calculations (Masciola *et al.*, 2013) to calculate the restraint loads platform from the mooring system. A local coordinate system is established for a single catenary mooring model in *DARwind* with anchor point, mooring line, fairlead, as shown in **Figure 5.5**.

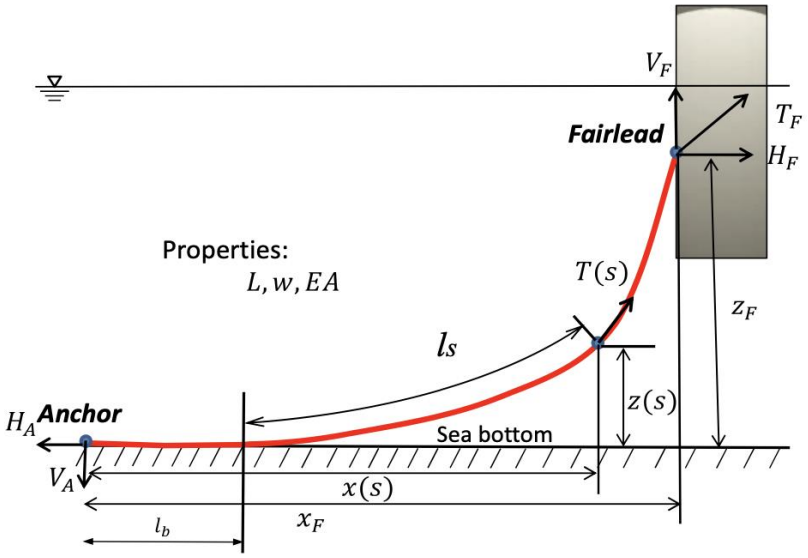

Figure 5.5 Catenary mooring line (Chen *et al.*, 2019a).

Among them, the anchor points are subjected to horizontal tension H_A and vertical tension V_A. The length of the bottom section (the part of the anchor chain in contact with the seabed) is l_b. The tension at any point of the mooring line is $T(s)$. The horizontal tension is H and the vertical tension is V. The horizontal distance from the anchor point is $x(s)$. The length of the mooring line from the bottom point for l_s. The tension of the

fairlead is T_F and the horizontal force is H_F. The vertical distance from the fairlead to the seabed is z_F, and the overall horizontal projection length of the anchor chain is x_F. The total length of the mooring line is L, the wet density is w, the cross-sectional area of the mooring line is A, and the axial stiffness is EA.

When there is a mooring line in contact with the seabed (lying on the bottom), i.e., $l_b \neq 0$ in **Figure 5.5**, the mooring line is not tensioned at the anchor point. The vertical tension at the anchor point is zero. According to the horizontal (x_F) and vertical (z_F) distances between the fairlead and the anchoring point, the horizontal and vertical tension of the anchor chain at the fairlead of the platform is related as follows:

$$\begin{cases} f_1 = L - \dfrac{V_F}{w} + \dfrac{H}{w} \cdot \ln \dfrac{V_F + \sqrt{{V_F}^2 + H^2}}{H} + \dfrac{H \cdot L}{EA} - x_F = 0 \\ f_2 = \dfrac{1}{w}\left(\sqrt{{V_F}^2 + H^2} - H\right) + \dfrac{w l_s^2}{EA} - z_F = 0 \end{cases} \quad \textbf{Eq. 5.3}$$

When the mooring line is not in contact with the seabed (not lying on the bottom), i.e., $l_b = 0$ in **Figure 5.5**, the anchor chain at the anchor point is in a tensioned state. So, the relationship is as follows:

$$V_A = V_F - wl \quad \textbf{Eq. 5.4}$$

Therefore, the horizontal tension and vertical tension at the fairlead have the following relationship:

$$\begin{cases} f_1 = \dfrac{H}{w} \cdot \ln \dfrac{V_F + \sqrt{{V_F}^2 + H^2}}{V_F - wL + \sqrt{(V_F - wl)^2 + H^2}} + \dfrac{HL}{EA} - x_F = 0 \\ f_2 = \dfrac{1}{w}\left(\sqrt{{V_F}^2 + H^2} - \sqrt{(V_F - wl)^2 + H^2}\right) + \dfrac{1}{EA}\left(V_F - \dfrac{wL}{2}\right) \cdot L - z_F = 0 \end{cases} \quad \textbf{Eq. 5.5}$$

5.3.2. Mooring force calculation in DARwind

The calculation process of the mooring system module of the program is shown in **Figure 5.6**. The program first reads in the attribute parameters of the mooring lines and calculates the spatial position information of each fairlead according to the motions of the platform. Then, according to the quasi-static calculation method, the dynamic equation of each anchor chain is constructed to calculate the tension of mooring lines. The nonlinear equations are solved by Newton's iteration method. The solved tension of each fairlead must be uniformly transformed into the platform coordinate system for load superposition to obtain the total force and moment of the mooring system.

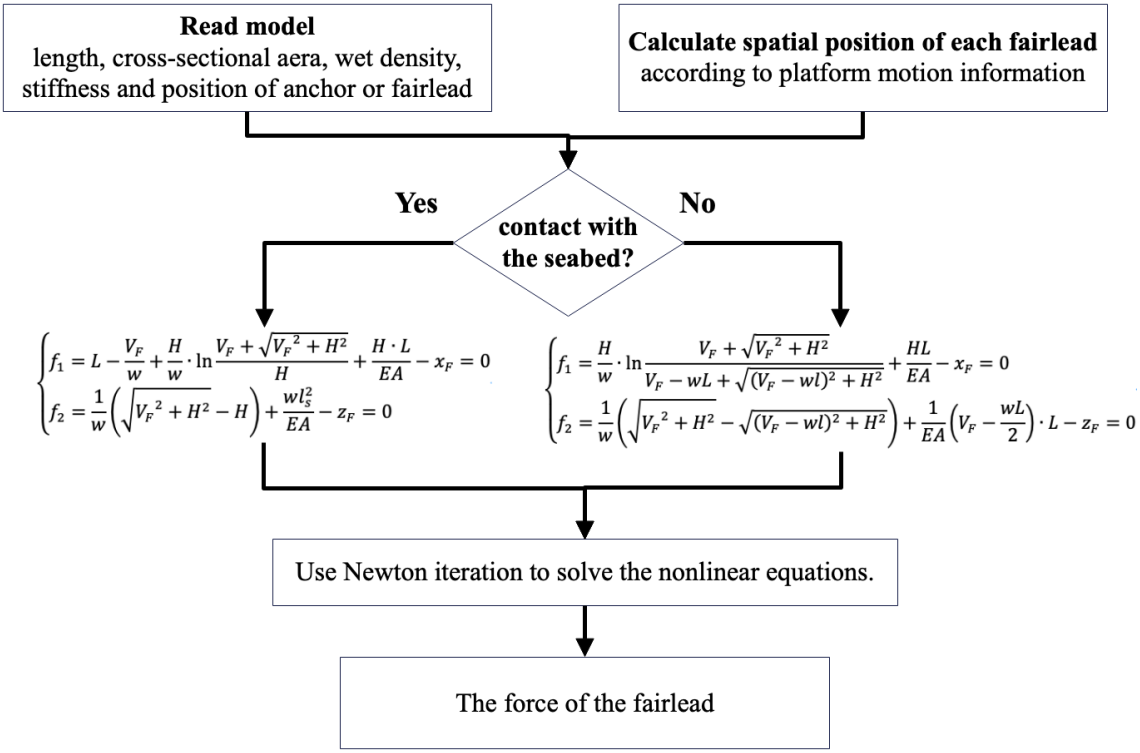

Figure 5.6 Procedure of the mooring dynamic.

5.4. Kinematics and dynamic calculation and control system

This section will introduce the fundamentals of Kinematics and dynamic calculation (Chen *et al.*, 2019a) and control system (Chen *et al.*, 2019a) in *DARwind.*

FOWTs are complex multi-body system models, which will be simplified in *DARwind*. Some components with little or no deformation that do not affect the overall kinematics can often be reduced to rigid bodies. The structural deformation of parts such as the hub, nacelle, and platform of FOWTs is relatively small to be simplified as a rigid body. Other slender structures such as wind turbine blades, towers, and mooring lines can be simulated as flexible bodies to maintain accuracy. In summary, the procedure of the kinetics module introduced in **Figure 5.7**.

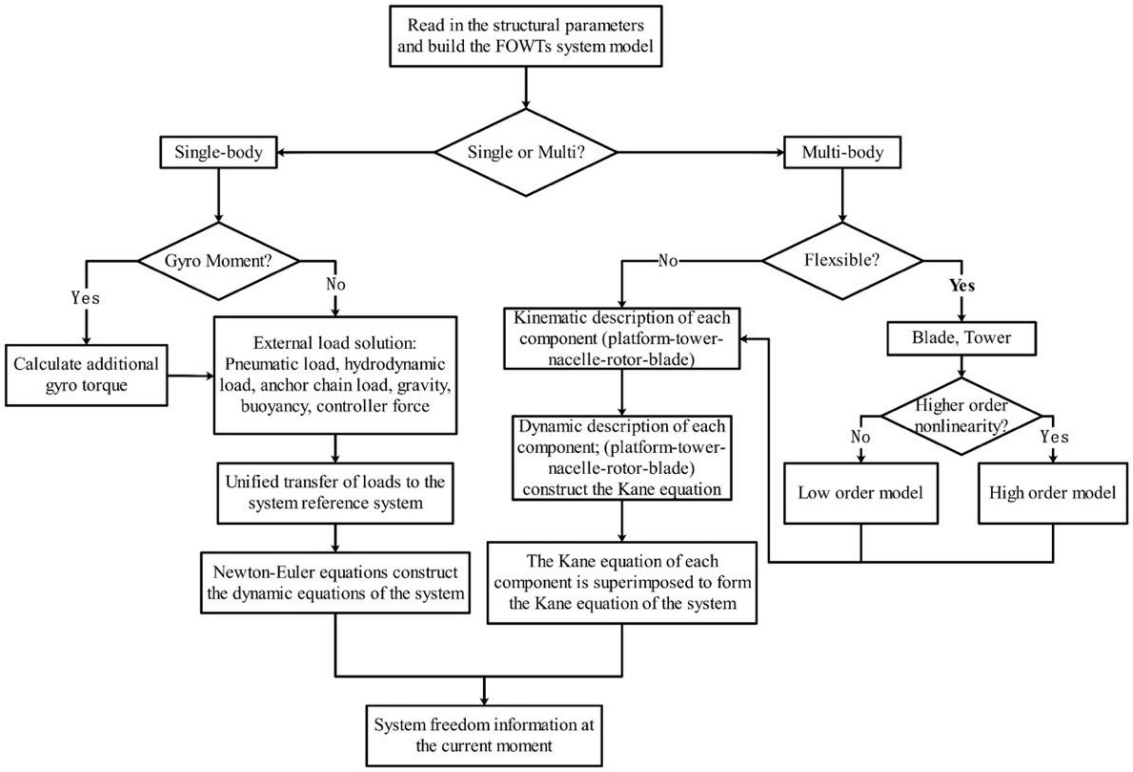

Figure 5.7 Procedure of the kinetics module.

The control system involved in *DARwind* consists of a generator torque controller and a unified pitch controller. When the wind turbine is in normal operation and is below the rated operating condition, the generator torque controller is mainly used to maintain the optimal tip speed ratio of the wind turbine and maximize the wind energy capture efficiency. Above the rated operating condition, the pitch angle controller is mainly used, and the goal is to constrain and stabilize the generator speed and power to avoid overload

and excess. The calculation process of the entire servo controller module is shown in **Figure 5.8**.

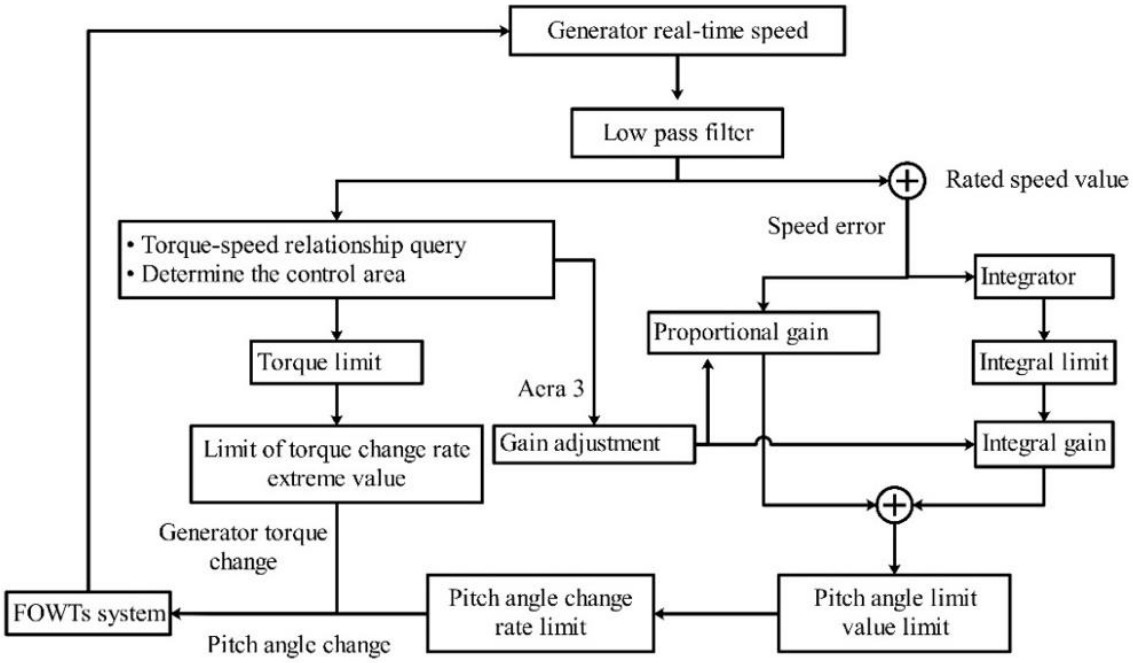

Figure 5.8 Procedure of the servo module.

5.5. Summary

The combination of the AI technology in the SADA method is based on a reliable numerical calculation software. Therefore, the purpose of this chapter is mainly to introduce the basic principles of the *DARwind* program. More details about the AI-based *DARwind* algorithm will be found in **Chapter 6.**

Chapter 6. AI technology in SADA

This chapter introduces the AI technology used in SADA, Artificial Neural Networks (ANN) and Reinforcement Learning (RL).

AI technology has benefited so much from the rapid development of computing power and data volume that it can already outperform humans on many tasks (Dong *et al.*, 2020). As one of the most important key technologies of AI, Machine Learning (ML) has also been called a topic in recent years, mainly divided into supervised learning, unsupervised learning, and reinforcement learning. For the development and application of artificial neural networks (ANN), please refer to the work of Walczak (2019). Furthermore, Deep reinforcement learning (DRL) combines the content of Deep Learning (DL) based on the original RL algorithm. In SADA, the prediction based on ANN was tried as the first step, followed by the application of DRL. Therefore, in the following sections, the content of ANN and DRL will be introduced.

6.1. ANN

This section mainly introduces ANN from the Perceptron model and the Backpropagation (BP) algorithm. The perceptron model is the most basic ANN concept, and the BP model is its specific application combined with error backpropagation.

ANN is a modern information processing model intended to simulate the structure and function of brain neurons and neural networks. The essence of ANN is to connect many processing units according to a particular mathematical algorithm or model. The historical development of ANN is roughly divided into five stages (Wen and Ru, 2019):

- **Stage 1**: embryonic period (the 1940s-1960s)

  It mainly discusses how to build a model that can simulate neurons and nervous systems.

- **Stage 2**: trough period (the 1960s-1970s)

  ANNs were questioned by the rise of integrated circuits and computers because ANN could not train complex networks.

- **Stage 3**: development period (the 1970s-1980s)

  With the emergence of high-performance computers, the bottleneck of ANN research has been gradually broken.

- **Stage 4**: agglomeration period (the 1980s-2000s)

  Research on ANN is rapidly advancing, and the theory is constantly being promoted.

- **Stage 5**: the explosion period (the 2000s-)

  The concept of deep learning is proposed by learning the deep nonlinear network structure, characterizing the input data, and realizing complex function approximation.

The characteristics of ANN mainly include nonlinearity, parallel processing, fault tolerance and associative ability, self-learning, self-organizing and adaptive ability. ANN can handle nonlinear problems well. There will be a complex nonlinear relationship between input and output in practical problem processing. By designing ANN, these complex nonlinear functions can be fitted and approximated to solve problems where the environmental information is very different, and the knowledge background and reasoning rules are unclear. The structure of ANN uses many processing units to be combined in parallel, and the order of processing is also parallel. Therefore, its information storage method is distributed to all connection weights. Each neuron stores not only one external information but parts of multiple types of information. If some neurons are damaged, it will not impact the whole system. The distributed storage algorithm integrates operation and storage. When the data is incomplete, it can be restored

through associative memory. Therefore, ANN also has extreme fault tolerance and self-learning ability. That is, appropriate weights and structures can be obtained in continuous training. Adaptive allows ANN to use different application environments by changing its structure and conditions.

6.1.1. Perceptron model

This subsection briefly introduces a single-layer and multi-layer neural network named the Perceptron model, the first ANN that can be fully described algorithmically. As **Figure 6.1** shows, the neuron model consists of a linear accumulator (Σ) and transfer function unit (f). The input signal is weighted by the synapse, summed together with the bias by an accumulator, and then passed through the transfer function unit to obtain the output. Where x is the input signal, w is the weight, Σ is the accumulated symbol, b is the bias, n is the response value, f is the transfer function, and y is the output.

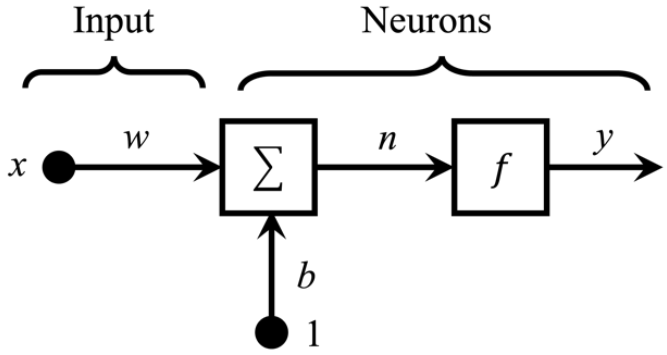

Figure 6.1 Structure diagram of Perceptron.

The accumulator can sum the signal and bias to get the response value. The output of the Perceptron with transfer function can be expressed as:

$$\begin{cases} n = wx + b \\ y = f(n) = f(wx + b) \end{cases} \quad \textbf{Eq. 6.1}$$

Where wx represents the inner product, when the output is different from the target feature, the weights and biases can be adjusted.

6.1.1.1. Single-layer Perceptron

Figure 6.2 is a specific single-layer Perceptron structure, and its simplified symbol, including the directly connected input and output layers.

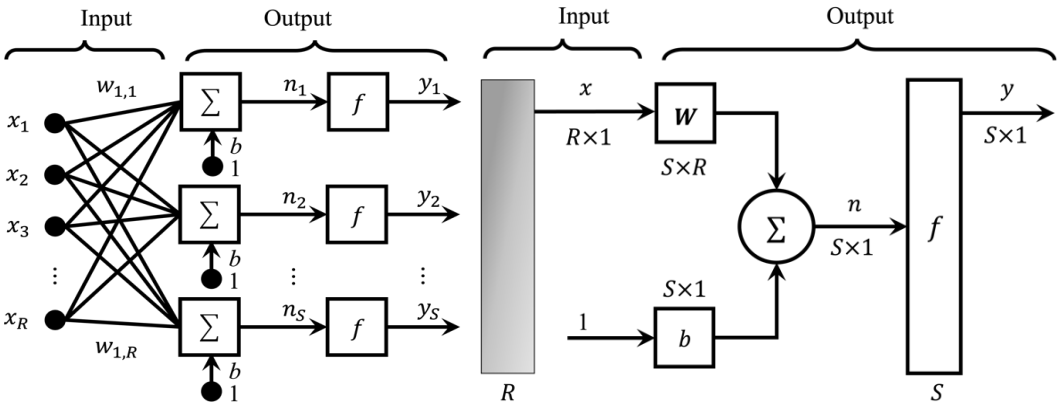

Figure 6.2 Structure and symbol diagram of single-layer Perceptron.

The input layer accepts external signals, and each input node receives an input signal. The output layer processes information. Among them, S represents the number of neurons of the Perceptron model, R represents the input element, $w_{i,j}$ is the corresponding weight. According to **Figure 6.2**, the output of the i-th accumulator and output layer are:

$$\begin{cases} n_i = \sum_{j=1}^{R} w_{i,j}x_j + b \ \ (i = 1,2,\cdots,S; j = 1,2,\cdots,R) \\ y_i = f(n_i) = f\left(\sum_{j=1}^{R} w_{i,j}x_j + b\right) \end{cases} \quad \textbf{Eq. 6.2}$$

The weight matrix $\boldsymbol{W}$ is:

$$\boldsymbol{W} = \begin{bmatrix} w_{1,1} & w_{1,2} & \cdots & w_{1,R} \\ w_{2,1} & w_{2,2} & \cdots & w_{2,R} \\ \vdots & \vdots & \ddots & \vdots \\ w_{S,1} & w_{S,2} & \cdots & w_{S,R} \end{bmatrix} \quad \textbf{Eq. 6.3}$$

The i-th row vector in the weight matrix $\boldsymbol{W}$ is defined as:

$$\boldsymbol{w_1} = [w_{1,1} \quad w_{1,2} \quad \cdots \quad w_{i,R}]^T \qquad \textbf{Eq. 6.4}$$

Then the weight matrix $\boldsymbol{W}$ can be expressed as:

$$\boldsymbol{W} = [\boldsymbol{w_1^T} \quad \boldsymbol{w_2^T} \quad \cdots \quad \boldsymbol{w_S^T}]^T \qquad \textbf{Eq. 6.5}$$

Since $\boldsymbol{w_i}$ represents the i-th row vector, $\boldsymbol{w^T}$ contains $w_{1,1}$, the output of the i-th output neuron according to a specific transfer function in the Perceptron is:

$$y_i = f(n_i) = f\left(\boldsymbol{w_i^T x} + b\right) \qquad \textbf{Eq. 6.6}$$

6.1.1.2. Multi-layer Perceptron

The multi-layer Perceptron model adds a hidden layer to the single-layer structure, which is a full connection of the two networks. Each neuron in the multi-layer Perceptron contains a differentiable nonlinear transfer function. Furthermore, there are more hidden neurons between the network's input and an output layer. These hidden neurons continuously extract proper feature values from the input and allow the network to complete more complex tasks. By changing the weights and the number of nodes, the network can have more robust continuity. **Figure 6.3** shows the structure of a multi-layer Perceptron.

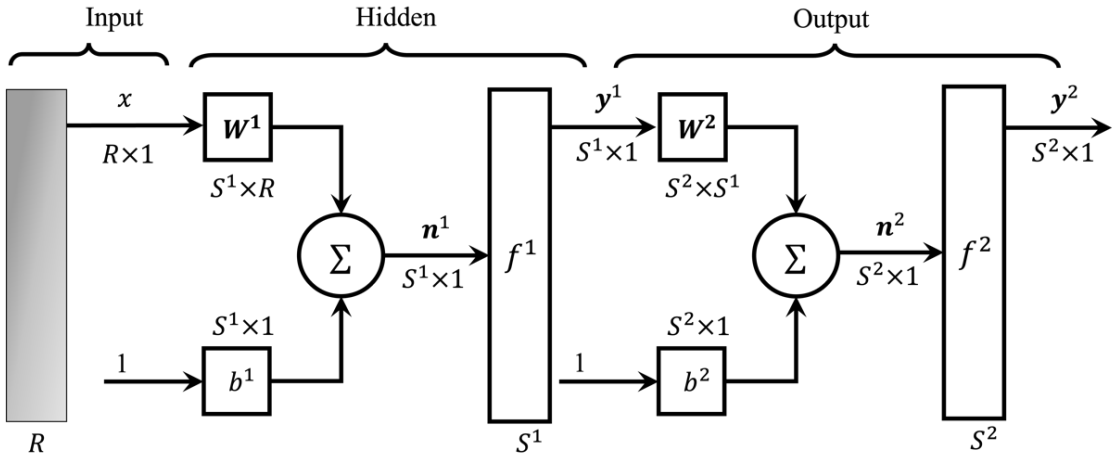

Figure 6.3 Structure diagram of multi-layer Perceptron.

6.1.2. Back propagation Neural Network

This subsection aims to introduce the Back propagation Neural Network model (BP model) A single perceptron cannot handle the XOR loop, and the BP model is proposed to solve this problem effectively. McClelland et al. (1987) described an algorithm based on directional propagation and gave a complete mathematical extension with strong computing power.

The BP model consists of forwarding information propagation and backpropagation of errors. The input layer receives data and passes it to the hidden layer responsible for data processing. In practice, the hidden layer can be one or more layers. The last hidden layer transmits information to the output layer, which is the forward propagation process of the BP model. When the error between the actual output and the target output exceeds expectations, it is necessary to conduct the process of backpropagation of the error. First, the weights of each layer are modified according to the gradient descent method from the output layer and then propagated to the hidden layer and the input layer. Through continuous forward propagation of information and backpropagation of errors, the weights of each layer will be continuously adjusted. The training ends when the output error is reduced to the excepted level or the iterations finish.

6.1.2.1. Structure of BP model

A typical structure diagram of the BP model is shown in **Figure 6.4**, which consists of an input layer, hidden layers, and an output layer:

- **Input:** External information is passed to the next layer.
- **Hidden:** Information process and transform.
- **Output:** output information feature determined by a transfer function.

The M layer in **Figure 6.4** is set to be greater than or equal to 2. Except for the input layer, each layer has a weight matrix $\boldsymbol{W}$, a bias vector $\boldsymbol{b}$, a net input vector $\boldsymbol{n}$ and an output vector $\boldsymbol{y}$. In addition, the first layer in the M layer network has R input and S^1 neuron nodes and the second layer has S^1 inputs and S^2 neuron nodes. The M-th layer has S^{M-1} inputs and S^M neuron nodes. Each input connection to the next layer of neuron nodes has different weights.

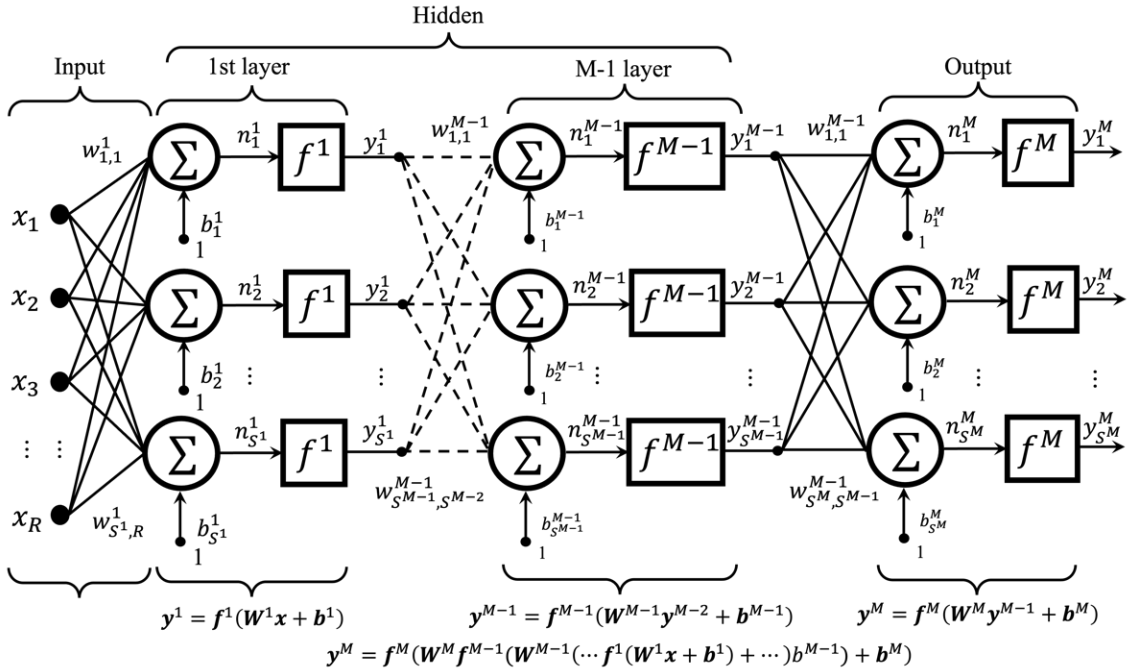

Figure 6.4 Structure diagram of BP model.

6.1.2.2. The BP algorithm

Figure 6.5 shows simplified symbol diagram of BP model.

From forward propagation, the sum of input nets is:

$$n_i^m = \sum_{j=1}^{S^{m-1}} w_{i,j}^m \, y_j^{m-1} + b_i^m, m = 1,2,\cdots,M \ (M > 2) \qquad \textbf{Eq. 6.7}$$

Where, n_i^m represents the input sum of the weights and biases, and M represents the number of layers. So, the output of the m-th layer is:

$$\boldsymbol{y}^m = \boldsymbol{f}^m(\boldsymbol{n}^m) \qquad \textbf{Eq. 6.8}$$

Where, $\boldsymbol{f}^m$ represents the transfer function of this layer.

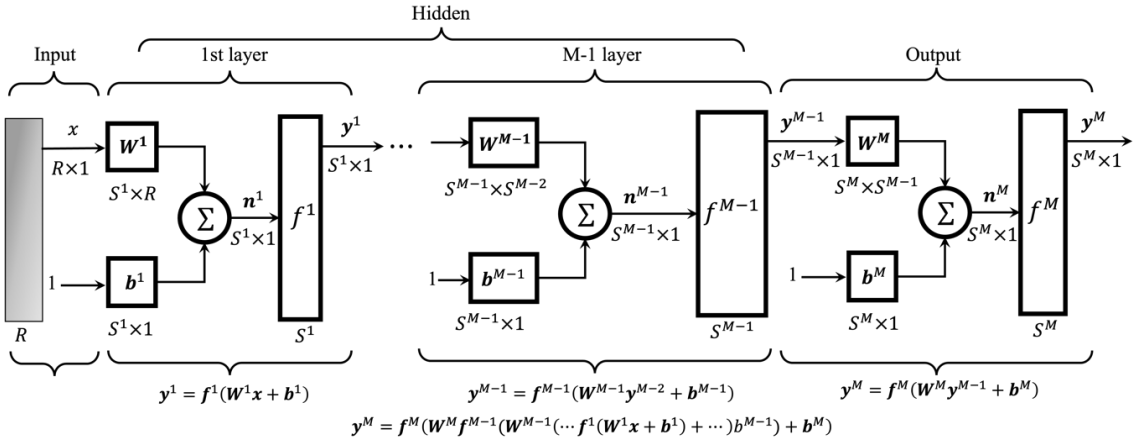

Figure 6.5 Simplified symbol diagram of BP model.

When $m = 1$, $\boldsymbol{y}^1$ represents the output information of the first layer neuron node, so $\boldsymbol{y}^1$ can be expressed as:

$$\boldsymbol{y}^1 = \boldsymbol{f}^1(\boldsymbol{W}^1\boldsymbol{x} + b^1) \qquad \textbf{Eq. 6.9}$$

At this point, the output of the BP network is the output of the last layer:

$$\boldsymbol{y} = \boldsymbol{y}^M \qquad \textbf{Eq. 6.10}$$

Backpropagation needs to consider loss function, weight correction, update method, and sensitivity. The loss function used by the BP algorithm is the mean square error function. The samples are taken as the input (x_R) and the target output: (t_R): $\{x_1, t_1\}, \{x_2, t_2\}, \cdots, \{x_R, t_R\}$. For each input sample, the output of the network is compared to the target output to minimize the mean squared error:

$$F(\boldsymbol{z}) = E[e^2] = E[(t - y)^2] \qquad \textbf{Eq. 6.11}$$

Where, $E[\ \ ]$ represents the expected value, and $\boldsymbol{z}$ is the vector of weights and biases, expressed as $\boldsymbol{z} = [w \quad b]^T$. If BP has multiple outputs, **Eq. 6.11** can be expressed as:

$$L(\boldsymbol{z}) = E[\boldsymbol{e}^T\boldsymbol{e}] = E[(\boldsymbol{t}-\boldsymbol{y})^T(\boldsymbol{t}-\boldsymbol{y})] \quad \textbf{Eq. 6.12}$$

If $\hat{L}(\boldsymbol{z})$ is used to approximate the mean squared error, **Eq. 6.12** can be expressed as

$$\hat{L}(z) = \big(\boldsymbol{t}(k)-\boldsymbol{y}(k)\big)^T\big(\boldsymbol{t}(k)-\boldsymbol{y}(k)\big) = \boldsymbol{e}^T(k)\boldsymbol{e}(k) \quad \textbf{Eq. 6.13}$$

Where, k means k-th iteration. The gradient descent method with **Eq. 6.13** can be used to correct the weights:

$$\begin{cases} w_{i,j}^m(k+1) = w_{i,j}^m(k) - \eta\dfrac{\partial\hat{L}}{\partial w_{i,j}^m} \\ b_i^m(k+1) = b_i^m(k) - \eta\dfrac{\partial\hat{L}}{\partial b_i^m} \end{cases} \quad \textbf{Eq. 6.14}$$

where η represents the learning rate. The partial derivatives are solved using the chain rule:

$$\begin{cases} \dfrac{\partial\hat{L}}{\partial w_{i,j}^m} = \dfrac{\partial\hat{L}}{\partial n_i^m}\times\dfrac{\partial n_i^m}{\partial w_{i,j}^m} \\ \dfrac{\partial\hat{L}}{\partial b_i^m} = \dfrac{\partial\hat{L}}{\partial n_i^m}\times\dfrac{\partial n_i^m}{\partial b_i^m} \end{cases} \quad \textbf{Eq. 6.15}$$

From **Eq. 6.7**:

$$\frac{\partial n_i^m}{\partial w_{i,j}^m} = y^{m-1}, \qquad \frac{\partial n_i^m}{\partial b_i^m} = 1 \quad \textbf{Eq. 6.16}$$

If $s_i^m = \frac{\partial\hat{L}}{\partial n_i^m}$ is used to denote sensitivity:

$$\begin{cases} \dfrac{\partial\hat{L}}{\partial w_{i,j}^m} = s_i^m y^{m-1} \\ \dfrac{\partial\hat{L}}{\partial b_i^m} = s_i^m \end{cases} \quad \textbf{Eq. 6.17}$$

The recurrence relation for sensitivity requires the use of the Jacobian:

$$\frac{\partial \boldsymbol{n}^m}{\partial \boldsymbol{n}^{m-1}} = \begin{bmatrix} \frac{\partial n_1^m}{\partial n_1^{m-1}} & \frac{\partial n_1^m}{\partial n_2^{m-1}} & \cdots & \frac{\partial n_1^m}{\partial n_{s^{m-1}}^{m-1}} \\ \frac{\partial n_2^m}{\partial n_1^{m-1}} & \frac{\partial n_2^m}{\partial n_2^{m-1}} & \cdots & \frac{\partial n_2^m}{\partial n_{s^{m-1}}^{m-1}} \\ \vdots & \vdots & \ddots & \vdots \\ \frac{\partial n_{s^m}^m}{\partial n_1^{m-1}} & \frac{\partial n_{s^m}^m}{\partial n_2^{m-1}} & \cdots & \frac{\partial n_{s^m}^m}{\partial n_{s^{m-1}}^{m-1}} \end{bmatrix} \quad \textbf{Eq. 6.18}$$

Computing the expression in **Eq. 6.18** must considers the i, j elements:

$$\begin{cases} \frac{\partial n_j^m}{\partial n_j^{m-1}} = \frac{\partial \left(\sum_{i=1}^{s^{m-1}} w_{i,j}^m y_i^{m-1} + b_i^m \right)}{\partial n_j^{m-1}} = w_{i,j}^m (f^{m-1})' f\left(n_j^{m-1}\right) \\ (f^{m-1})' f\left(n_j^{m-1}\right) = \frac{\partial f^{m-1}\left(n_j^{m-1}\right)}{\partial n_j^{m-1}} \end{cases} \quad \textbf{Eq. 6.19}$$

So, the Jacobian matrix is abbreviated as:

$$\frac{\partial \boldsymbol{n}^m}{\partial \boldsymbol{n}^{m-1}} = \boldsymbol{W}^m (\boldsymbol{L}^{m-1})' \boldsymbol{n}^{m-1} \quad \textbf{Eq. 6.20}$$

$$(\boldsymbol{L}^{m-1})' \boldsymbol{n}^{m-1} = \begin{bmatrix} (f^{m-1})'(n_1^{m-1}) & 0 & \cdots & 0 \\ 0 & (f^{m-1})'(n_2^{m-1}) & \cdots & 0 \\ \vdots & \vdots & \ddots & \vdots \\ 0 & 0 & \cdots & (f^{m-1})'\left(n_{s^{m-1}}^{m-1}\right) \end{bmatrix} \quad \textbf{Eq. 6.21}$$

Therefore, the recurrence relation of the sensitivity matrix can be obtained as:

$$\boldsymbol{s}^{m-1} = \frac{\partial \hat{L}}{\partial \boldsymbol{n}^{m-1}} = \left(\frac{\partial \boldsymbol{n}^m}{\partial \boldsymbol{n}^{m-1}} \right)^T \frac{\partial \hat{L}}{\partial \boldsymbol{n}^m} = (\boldsymbol{L}^{m-1})' (\boldsymbol{n}^{m-1}) (\boldsymbol{W}^m)^T s^m \quad \textbf{Eq. 6.22}$$

$$\boldsymbol{s}^m = \frac{\partial \hat{L}}{\partial \boldsymbol{n}^m} = \begin{bmatrix} \frac{\partial \hat{L}}{\partial n_1^m} & \frac{\partial \hat{L}}{\partial n_2^m} & \cdots & \frac{\partial \hat{L}}{\partial n_s^m} \end{bmatrix}^T \quad \textbf{Eq. 6.23}$$

Then, the sensitivity can be backpropagated from the last layer through the network to the first layer: $\boldsymbol{s}^m \rightarrow \boldsymbol{s}^{m-1} \rightarrow \cdots \rightarrow \boldsymbol{s}^2 \rightarrow \boldsymbol{s}^1$. In addition, **Eq. 6.22** shows that for the BP algorithm to perform backpropagation, it must first calculate the value of the S^M:

$$s_i^M = \frac{\partial \hat{L}}{\partial n_i^M} = \frac{\partial (\boldsymbol{t}-\boldsymbol{y})^T(\boldsymbol{t}-\boldsymbol{y})}{\partial n_i^m} = -2(t_i - y_i)\frac{\partial y_i}{\partial n_i^M} \qquad \textbf{Eq. 6.24}$$

Because:

$$\frac{\partial y_i}{\partial n_i^M} = \frac{\partial y_i^M}{\partial n_i^M} = \frac{\partial f^M(n_i^M)}{\partial n_i^M} = (f^M)'(n_i^M) \qquad \textbf{Eq. 6.25}$$

The **Eq.** ***6.24*** can be rewritten and the matrix form are:

$$\begin{cases} s_i^M = -2(t_i - y_i)(f^M)'(n_i^M) \\ \boldsymbol{s}^M = -2(\boldsymbol{L}^M)'(\boldsymbol{n}^M)(\boldsymbol{t}-\boldsymbol{y}) \end{cases} \qquad \textbf{Eq. 6.26}$$

The weights and biases are updated as:

$$\begin{cases} w_{i,j}^m(k+1) = w_{i,j}^m(k) - \eta s_i^m y_j^{m-1} \\ b_i^m(k+1) = b_i^m(k) - \eta s_i^m \end{cases} \qquad \textbf{Eq. 6.27}$$

If expressed in matrix form, it is:

$$\begin{cases} \boldsymbol{W}^m(k+1) = \boldsymbol{W}^m(k) - \eta \boldsymbol{s}^m(\boldsymbol{y}^{m-1})^T \\ \boldsymbol{b}^m(k+1) = \boldsymbol{b}^m(k) - \eta \boldsymbol{s}^m \end{cases} \qquad \textbf{Eq. 6.28}$$

6.2. Reinforcement Learning

This section will introduce the RL. For a thorough introduction referred to standard textbooks (Sutton and Barto, 2018).

RL originates from the two directions of "trial-and-error" (animal psychology) and optimal control. Trial and error learning (TE learning) focuses on selecting actions that lead to better outcomes in subsequent decision-making processes. The first scholar who proposed this idea, Thorndike, named it "Law of Effect" in 1927 (Hovanky, 2017). It

contains two essential concepts: choice and association. More precisely, the former refers to choosing one of the many optional actions in each state. The latter refers to remembering the most effective action in a specific situation.

The second main direction of RL mainly explores designing a control system to measure the action of a dynamic system. Richard Bellman proposed the "state" and "value function" to construct the Bellman equation and used the dynamic programming algorithm to solve the optimal control problem of the dynamic system (Wei *et al.*, 2018). Markov decision process (MDP) is the discrete random version proposed by Bellman (Guo and Hernández-Lerma, 2009). Howard (2002) proposed a policy iteration method to solve the MDP problem. In addition, Temporal Difference Learning (TD learning) is also a unique and novel method in later RL development. These concepts are all essential in today's RL algorithms. In conclusion, unlike supervised learning, RL does not require labelled datasets, which emphasizes information collection through the system's interaction with the environment.

6.2.1. Basic concepts of RL

This section will introduce some basic concepts of RL and their integration with FOWTs in SADA. In general, RL's mathematical basis and modelling tool is the Markov decision process, which includes state space, action space, state transition function, reward function, etc. It will therefore be discussed in detail in these sections.

6.2.1.1. Environment and Agent

The main body of RL is called an agent, which often makes decisions or actions. For example, vehicles are agents in the application of automatic driving. Correspondingly in SADA, *DARwind* will adjust the KDPs and conduct dynamic response analysis of FOWTs, so *DARwind* is an agent. The environment is what the agent interacts with, which can be abstractly understood as the rules or mechanisms in the interaction process. In automatic

driving applications, the actual physical world is the environment. In the same way, it is the actual environment of FOWTs.

6.2.1.2. State space and transition

The state is not unique, and it can be the feedback of the environment or the feedback of the agent. In the example of autonomous driving, the analysis of road conditions and the state of the car (vehicle speed, fuel consumption, etc.) can be considered states. In the SADA method, the dynamic responses of FOWTs can be considered as states. The observation of the environment can be real-time or partial. For example, vehicle speed and changes in road conditions need to be observed in real-time. States in strategy games like Red Alert and StarCraft are partially observed because the current refresh frame rate is not enough for the player to decide. In SADA, the observation of states depends on the designer's needs, which are:

- **Real-time observation**: consider the dynamic response of FOWTs in real-time.
- **Partial observations**: consider the dynamic response of FOWTs over the mean time.

The state-space refers to the set $\mathcal{S}$ of all existing states, which can be discrete or continuous, a finite set or an infinitely countable set. In the automatic driving example, the state-space is infinite. In SADA, the states of FOWTs also belong to an infinite set.

The agent is transitioning from the state s at the current time t to the next state s'. From one iteration to the next iteration is considered a state transition in SADA. In RL, state transitions are described by state transition probability functions, often assumed to be random, depending on the environment. In the current state s, the probability of the next state s' obtained by action a. Referred to as:

$$p(s'|s,a) = \mathbb{P}(S' = s'|S = s, A = a)$$

6.2.1.3. Action space

Actions are decisions made by the agent based on the current state. The selection of actions can be deterministic or random. Random refers to the selection of actions with a certain probability. Action space is the set of all possible actions, denoted $\mathcal{A}$. It can be discrete, continuous, finite, or infinite sets. There are many actions to control the car in autonomous driving, including braking, accelerator, steering wheel, indicator lights, etc. These actions include discrete actions (playing the indicator light) and continuous actions (playing the steering wheel). In SADA, the actions are adjustments to KDPs. Since the values of KDPs belong to a continuous distribution, the action space in SADA belongs to a continuous infinite set.

6.2.1.4. Reward

After the agent acts, the environment gives the agent feedback (reward: r). The designer can define this feedback, and the definition of reward will dramatically affect the result of RL. The reward function is denoted as:

$$r(s, a, s')$$

Where s is the current state, a is the current action, and s' is the next state.

Assume that the reward function is bounded that is, for all a and s', there is $r\ (s, a, s') < \infty$. For example, the percentage difference of surge is considered a criterion for judging good or bad action in SADA. Depending on the value of the percentage difference, corresponding rewards are given.

6.2.1.5. Policy

The essence of the policy is to decide the action based on the state. The stochastic policy function π can be expressed as:

$$\pi(a|s) = \mathbb{P}(A = a|S = s)$$

The input of the policy function is the state s and the action a. The output is a probability value of 0-1. However, the determining policy has no randomness. The deterministic policy can be thought of as a particular case of a stochastic policy.

6.2.1.6. Return and discounted return

The return is the sum of all rewards in one episode. An episode is one complete play of the agent interacting with the environment in the general RL setting. The return is also called cumulative future reward. The agent's goal is to find a policy to take action that maximizes the expected return (the optimal policy). The goal of maximizing here refers not to the current reward but the cumulative reward. Let the return at time t be the random variable U_t. If the program ends, take the reward u_t as all rewards that have been observed:

$$U_t = R_t + R_{t+1} + R_{t+2} + R_{t+3} + \cdots + R_n$$

Discount factor γ is usually given on a discounted return:

$$\begin{aligned} U_t &= R_t + \gamma \cdot R_{t+1} + \gamma^2 \cdot R_{t+2} + \gamma^3 \cdot R_{t+3} + \cdots + \gamma^n \cdot R_{t+n} \\ &= R_t + \sum_{i=1}^{n} \gamma^i \cdot R_{t+i} \end{aligned} \qquad \textbf{Eq. 6.29}$$

Where, $\gamma \in [0,1]$.

6.2.1.7. Agent environment interaction

The agent observes the state s and takes action a, the action changes the state of the environment, and the environment feeds back to the agent a reward r and a new state s'. **Figure 6.6** shows a schematic diagram of the agent-environment interaction.

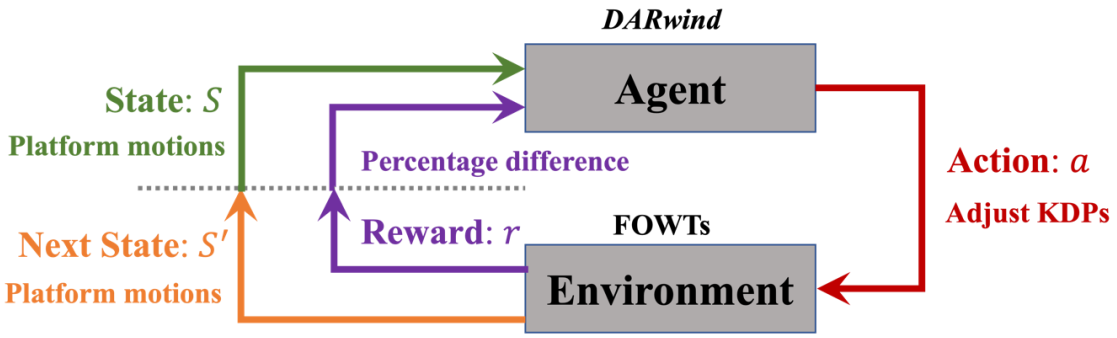

Figure 6.6 Agent-environment interaction.

The environment has a set of rules that describe itself, called the dynamics of the environment, which determine the agent's information. When all the information is open to the agent, the environment is **fully observable**. When the environment only exposes part of the information to the agent, the environment is **partially observable**. Some agents can model the dynamics of the environment through observation and reward information and then decide the agent's actions according to the model. The model established by the agent can be very close to the dynamic of the environment, or it can be quite different from the dynamic of the environment. A complete model usually predicts the agent's next state after acting and the reward from the environment. The actual physical world in which FOWTs work is the environment in SADA, and *DARwind* is an agent. The numerical simulation accuracy of *DARwind* may never be accurate (simplified model, the nonlinearity). However, the knowledge of various disciplines is constantly improving, so the established FOWTs numerical simulation program is also constantly improving.

In RL, describing policies in mathematical language is a mapping from agent state to action. The two policies (random and deterministic policy) have application scenarios. When solving RL problems, agents usually build one or more of the three components: policy, model, and value function. The agent accumulates experience and forms memory through interaction with the environment, so as to continuously learn TE to optimize its

strategy, model or value function, and gradually approach the optimal solution of the problem. According to these characteristics, agents in RL can be classified as follows:

- **The value function only**: such an agent has an estimation function for the value of the state, but there is no direct policy function, which is obtained indirectly by the value function.
- **The policy only**: The action is directly generated by the policy function, and the agent does not have a value function of each state.
- **Actor-Critic**: Agent has both value and policy functions, and the two are combined to solve problems.

In addition, agents can be divided into two categories according to whether they build a model for the dynamics of the environment:

- **Model-free**: The Agent do not attempt to understand how the environment works but focus only on value and policy functions, or either.
- **Model-based**: The Agent attempts to build a model that describes the operational process of the environment to guide the update of the value or policy function.

In summary, the *DARwind* is a model-based agent.

6.2.2. Value function

The specific values function can evaluate the states and actions. For RL problems with small scale and few states, the Table Lookup algorithm can store the value of each state and action with independent data (like a giant table). A similar data structure is used in programming implementations through which the value of state and actions are obtained. However, many problems are very complex in practice. Some problems have a vast number of states and actions or are continuous. If the Table Lookup algorithm is used for these problems, the efficiency will be very low or even impossible to solve. Hence, the

concept of value function is proposed to approximate the value of a state or action by constructing a specific function. The advantage of this design is that there is no need to store the data of each state or action value and only a limited number of parameters and function designs. After introducing the value function, designing, and solving the function's parameters become the main work of RL. Function approximation is mainly divided into linear function approximation and nonlinear approximation. The mainstream design of nonlinear approximation is to use deep ANN technology. The ANN can be solved according to the standard training process: establishing an appropriate objective function, selecting an appropriate optimization algorithm, preparing a training data set, training a network, etc.

6.2.2.1. Action-value function

Suppose that state s_t has been observed and action a_t is selected. Then the randomness in U_t will come from all states and actions from time $t+1$:

$$S_{t+1}, A_{t+1}, S_{t+2}, A_{t+2}, \cdots, S_n, A_n$$

Evaluating the conditional expectation of U_t with respect to this variable can get:

$$Q_\pi(s_t, a_t) = \mathbb{E}_{S_{t+1}, A_{t+1}, \cdots, S_n, A_n}[U_t | S_t = s_t, A_t = a_t] \qquad \textbf{Eq. 6.30}$$

Where $S_t = s_t, A_t = a_t$ is the condition, the value of the state and action has been observed. The action-value function $Q_\pi(s_t, a_t)$ at time t depends on the following three factors:

- **Current state s**: The better the current state, the greater the value of $Q_\pi(s_t, a_t)$, and the greater the expected return. For example, the better the percentage difference of the dynamic response of FOWTs, the better the state, and the greater the value of $Q_\pi(s_t, a_t)$.

- **Current Action $\boldsymbol{a}$**: The better the agent performs, the greater the value of $Q_\pi(s_t, a_t)$. For example, *DARwind* adjusts well for KDPs, so the value of $Q_\pi(s_t, a_t)$ is also good.

- **Policy function $\boldsymbol{\pi}$**: The policy determines the quality of future actions: the better the policy, the greater the value of $Q_\pi(s_t, a_t)$.

The optimal action value function can remove the influence of the policy and only evaluate the quality of the current state and action:

$$Q_*(s_t, a_t) = \max_\pi Q_\pi(s_t, a_t), \forall s_t \in \mathcal{S}, a_t \in \mathcal{A} \qquad \textbf{Eq. 6.31}$$

The optimal action-value function depends only on s_t and a_t, regardless of the policy. It can guide the agent to make the correct decision. For example, in simulating the dynamic response of FOWTs, given the current state s_t (percentage difference of 6DOF platform motions), it is assumed that the agent's action space is:

$$\mathcal{A} = \begin{bmatrix} \text{reduce wind speed} \\ \text{unchange wind speed} \\ \text{increase wind speed} \end{bmatrix}$$

If the Q_* function is known, then these three actions can be scored, for example:

$$\begin{cases} Q_*(s_t, reduce\ V_w) & = 100 \\ Q_*(s_t, V_w\ no\ change) & = -50 \\ Q_*(s_t, increase\ V_w) & = 200 \end{cases}$$

The Q_* value is the expected return, which represents the maximum cumulative expectation researched after the end of iteration. If *DARwind* chooses to reduce the wind speed in the next iteration, then no matter what policy π *DARwind* adopts afterwards, the expectation of return U_t will not exceed 100. Similarly, if *DARwind* choose to increase the wind speed, the expectation of return will not exceed 200. Undoubtedly,

increasing the wind speed in next loop in the numerical simulation can close to the actual response.

6.2.2.2. State-value function

Suppose *DARwind* uses the policy function π to adjust KDPs in iteratively steps. The state-value function can be used to judge the current state s_t whether achieves the terminal state:

$$V_\pi(s_t) = \mathbb{E}_{A_t \sim \pi(\cdot|s_t)}[Q_\pi(s_t, A_t)]$$
$$= \sum_{a \in \mathcal{A}} \pi(a|s_t) \cdot Q_\pi(s_t, a_t)$$

Where, A_t is a random variable, and $V_\pi(s_t)$ only depends on the policy π and current state s_t, not on actions. $V_\pi(s_t)$ is also the expected return U_t:

$$V_\pi(s_t) = \mathbb{E}_{S_{t+1}, A_{t+1}, \cdots, S_n, A_n}[U_t | S_t = s_t] \quad \textbf{Eq. 6.32}$$

A larger value of $V_\pi(s_t)$ means a larger expected return U_t. The state-value function can be used to measure the quality of policy π and state s_t.

6.2.3. Monte-Carlo and Temporal-Difference Learning

This part mainly introduces the methods of Monte Carlo and Temporal-Difference Learning. These two methods are one of the essential tools in dealing with RL problems.

6.2.3.1. Monte-Carlo Reinforcement Leaming

Monte-Carlo learning (MC learning) is a general term for randomized algorithms and an essential element of many RL algorithms. The essence of MC learning is to estimate the actual value through random samples. It has many applications, such as approximating values, estimating areas, and approximating definite integrals. This part focuses on the application of MC learning to approximate expectations and stochastic gradient.

Let X be a d-dimensional random variable whose value range is $\Omega \subset \mathbb{R}^d$. The function $p(x)$ is the probability density function of X. Let $f: \Omega \to \mathbb{R}$ be an arbitrary multivariate function. Then its expectation about the variable X can be expressed as:

$$\mathbb{E}_{X\sim p(\cdot)}[f(X)] = \int_{\Omega} p(x) \cdot f(x) dx \qquad \textbf{Eq. 6.33}$$

Since the expectation is a definite integral, uniform sampling is performed in the set Ω, and the obtained sample is used to approximate the definite integral. On the other hand, the probability density function $p(x)$ can be used to conduct non-uniform sampling:

1. Perform non-uniform random sampling on the set Ω according to the probability density function $p(x)$, and obtain samples n and record them as vectors $x_1, x_2, \cdots x_n \sim p(\cdot)$.
2. Average the $f(x_1), \cdots, f(x_n)$:

$$q_n = \frac{1}{n}\sum_{i=1}^{n} f(x_i)$$

3. Return q_n as the estimated value of **Eq. *6.33***.

Stochastic gradient algorithms can also be conducted through MC learning. Let w be the parameters of the neural network. Then the loss function can be $L(X; \boldsymbol{w})$. The smaller the value of loss function L, the more accurate the prediction made by the model. Therefore, the training of ANN can be defined as an optimization problem to adjust the w to minimize the expectation of loss function:

$$\min_{w} \mathbb{E}_{X\sim p(\cdot)}[L(X; \boldsymbol{w})] \qquad \textbf{Eq. 6.34}$$

The gradient of the objective function $\mathbb{E}_X[L(X; \boldsymbol{w})]$ with respect to $\boldsymbol{w}$ is:

$$\boldsymbol{g} \triangleq \nabla_{\boldsymbol{w}} \mathbb{E}_{X\sim p(\cdot)}[L(X;\boldsymbol{w})] = \mathbb{E}_{X\sim p(\cdot)}[\nabla_{\boldsymbol{w}} L(X;\boldsymbol{w})] \qquad \textbf{Eq. 6.35}$$

Gradient descent can be done to update $\boldsymbol{w}$ to reduce the objective function $\mathbb{E}_X[L(X;\boldsymbol{w})]$:

$$\boldsymbol{w} \leftarrow \boldsymbol{w} - \alpha \cdot \boldsymbol{g} \qquad \textbf{Eq. 6.36}$$

Here, α is the learning rate. To compute gradients quickly, the Monte Carlo approximation ($\boldsymbol{g} = \mathbb{E}_{X\sim p(\cdot)}[\nabla_{\boldsymbol{w}} L(X;\boldsymbol{w})]$) to the expectation is required (stochastic gradient $\tilde{\boldsymbol{g}}$) to update $\boldsymbol{w}$:

1. According to the probability density function $p(x)$, random sampling is performed to obtain n samples, which are denoted as: $\tilde{x}_1, \cdots, \tilde{x}_n$.
2. Calculate the gradient $\nabla_{\boldsymbol{w}} L(\tilde{x}_i;\boldsymbol{w}), \forall i = 1, \cdots, B$ and average it:

$$\tilde{\boldsymbol{g}} = \frac{1}{n}\sum_{i=1}^{n} \nabla_{\boldsymbol{w}} L(\tilde{x}_i;\boldsymbol{w})$$

   $\tilde{\boldsymbol{g}}$ is the stochastic gradient, which is an unbiased estimate of $\boldsymbol{g}$.

3. Do stochastic gradient descent to update $\boldsymbol{w}$:

$$\boldsymbol{w} \leftarrow \boldsymbol{w} - \alpha \cdot \boldsymbol{g}$$

The number of samples n is called the batch size, which is usually called mini-batch. In the probability density function $p(x)$ of the sample is generally unknown. When training an ANN, a training dataset will be used to solve the empirical risk minimization:

$$\min_{w} \frac{1}{n}\sum_{i=1}^{n} L(x_i;\boldsymbol{w}) \qquad \textbf{Eq. 6.37}$$

6.2.3.2. Temporal-Difference Learning

This part will introduce the Temporal-Difference Learning (TD learning) in detail which can learn from incomplete state episode.

Suppose there is a model $Q(s, d;\ \boldsymbol{w})$ in SADA, where s is the initial state (percentage difference of surge) by initial KDPs, and d is the optimal state by weighted KDPs. $\boldsymbol{w}$ is the parameter of ANN. Model Q can predict the number of iterations required from s to d. This model may be randomly inaccurate in the beginning. But as continue to train and collect data, the model will become more accurate. *DARwind* will have a prediction $\hat{q} = Q(s, d;\ \boldsymbol{w})$ before iterating. When *DARwind* finishes the iteration of this episode, the actual number of iterations y is fed back to the model. The $\hat{q} - y$ reflects the evaluation effect of the model and corrects the model.

Suppose the prediction of the model before *DARwind* starts iterating is:

$$\hat{q} \triangleq Q(S_{inital}, S_{final};\ \boldsymbol{w}) = 10 \qquad \textbf{Eq. 6.38}$$

Where S_{inital} means the initial difference of surge between numerical results and target data. S_{final} means the final difference of surge, which can be defined by designer. For example, under 10%. When *DARwind* obtained a more accurate prediction of FOWTs response by adjusting KDPs, the actual number of iterations $y = 20$, and it was fed back to the model. So gradient descent can be used to update the model:

$$L(\boldsymbol{w}) = \frac{1}{2}\left[Q(S_{inital}, S_{final};\ \boldsymbol{w}) - y\right]^2 \qquad \textbf{Eq. 6.39}$$

Using the chain rule to calculate the gradient of the loss function:

$$\nabla_w L(\boldsymbol{w}) = (\hat{q} - y) \cdot \nabla_w Q(S_{inital}, S_{final};\ \boldsymbol{w}) \qquad \textbf{Eq. 6.40}$$

Then update the model parameters $\boldsymbol{w}$:

$$\boldsymbol{w} \leftarrow \boldsymbol{w} - \alpha \cdot \nabla_w L(\boldsymbol{w}) \qquad \textbf{Eq. 6.41}$$

Where, α is learning rate.

Suppose the initial surge difference is 20%. According to **Eq. *6.38***, $\hat{q} = 10$. When the surge difference drops to 15%, the actual number of iterations is $r = 8$ currently. Then, the model predicts the surge difference will reach the required value 10% that is the $\hat{q}' = 7$. According to the model, the total iteration number now is:

$$\hat{y} \triangleq r + \hat{q}' = 8 + 7 = 15$$

The original forecast $\hat{q}$ estimate was without any factual component. $\hat{y}$ is also an estimate but has the actual observations r. Based on the above discussion, it can be seen that, $\hat{y} = 15$ is the TD target which is much reliable than $\hat{q} = 10$. Therefore, the $\hat{y}$ can be used to modify the model in **Eq. *6.39***.

$$L(\boldsymbol{w}) = \frac{1}{2}\left[Q(S_{inital}, S_{final};\ \boldsymbol{w}) - \hat{y}\right]^2 \qquad \textbf{Eq. 6.42}$$

According to **Eq. *6.29***:

$$U_t = R_t + \gamma \cdot \underbrace{\sum_{k=t+1}^{n} \gamma^{k-t-1} \cdot R_k}_{= U_{t+1}} \qquad \textbf{Eq. 6.43}$$

Combined with **Eq. *6.31***, the optimal Bellman equation can be expressed as:

$$Q_*(s_t, a_t) = \mathbb{E}_{S_{t+1}\sim\pi(\cdot|s_t,a_t)}\left[R_t + \gamma \cdot \max_{A\in\mathcal{A}} Q_*(S_{t+1}, A) | S_t = s_t, A_t = a_t\right] \qquad \textbf{Eq. 6.44}$$

It can be obtained by Monte Carlo approximation:

$$Q_*(s_t, a_t) \approx r_t + \gamma \cdot \max_{a\in\mathcal{A}} Q_*(s_{t+1}, a) \qquad \textbf{Eq. 6.45}$$

Replacing the optimal action-value function $Q_*(s, a)$ in **Eq. *6.45*** with a neural network $Q(s, a;\ \boldsymbol{w})$:

$$Q(s_t, a_t;\ \boldsymbol{w}) \approx r_t + \gamma \cdot \max_{a \in \mathcal{A}} Q_*(s_{t+1}, a) \qquad \textbf{Eq. 6.46}$$

$\widehat{q_t} \triangleq Q(s_t, a_t;\ \boldsymbol{w})$ is the prediction made by the neural network at time t without any factual component. The TD target $\widehat{y_t} = r_t + \gamma \cdot \max_{a \in \mathcal{A}} Q_*(s_{t+1}, a)$ is the prediction made by the neural network at time $t+1$, which is a partially based on true observations r_t. $\widehat{q_t}$ and $\widehat{y_t}$ are all estimates of the optimal action-value function. The loss function can be:

$$L(\boldsymbol{w}) = \frac{1}{2}[Q(s_t, a_t;\ \boldsymbol{w}) - \widehat{y_t}]^2 \qquad \textbf{Eq. 6.47}$$

Compute the gradient of L with respect to $\boldsymbol{w}$:

$$\nabla_w L(\boldsymbol{w}) = \underbrace{(\widehat{q_t} - \widehat{y_t})}_{TD\ error\ \delta_t} \cdot \nabla_w Q(s_t, a_t;\ \boldsymbol{w}) \qquad \textbf{Eq. 6.48}$$

Then update the model parameters $\boldsymbol{w}$:

$$\boldsymbol{w} \leftarrow \boldsymbol{w} - \alpha \cdot \delta_t \cdot \nabla_{\boldsymbol{w}} Q(s_t, a_t;\ \boldsymbol{w}) \qquad \textbf{Eq. 6.49}$$

Given (s_t, a_t, r_t, s_{t+1}),

$$\widehat{q_t} = Q(s_t, a_t;\ \boldsymbol{w})$$

and TD target and TD error:

$$\begin{cases} \widehat{y_t} = r_t + \gamma \cdot \max_{a \in \mathcal{A}} Q(s_{t+1}, a) \\ \delta_t = \widehat{q_t} - \widehat{y_t} \end{cases}$$

The TD algorithm uses **Eq. *6.49*** to update the parameters.

6.2.4. Policy objective function

The agent aims to obtain as many cumulative rewards as possible in the process of interacting with the environment, and a good policy can accurately reach this goal. This

objective function excludes the factor of state S and only depends on the parameters $\boldsymbol{\theta}$ of the policy network π. The better the policy, the larger the value of $J(\boldsymbol{\theta})$. Policy learning can be described as an optimization problem:

$$\max_{\boldsymbol{\theta}}\{J(\boldsymbol{\theta}) \triangleq \mathbb{E}_{\boldsymbol{S}}(V_{\pi}(S))\} \qquad \textbf{Eq. 6.50}$$

The objective function is larger by updating the parameters $\boldsymbol{\theta}$ of the policy network. Therefore, gradient ascent needs to be used to update $\boldsymbol{\theta}$. Suppose the current policy network parameter is $\boldsymbol{\theta}_{now}$. The new parameter $\boldsymbol{\theta}_{new}$ is obtained by gradient ascent:

$$\boldsymbol{\theta}_{new} \leftarrow \boldsymbol{\theta}_{now} + \beta \cdot \nabla_{\boldsymbol{\theta}} J(\boldsymbol{\theta}_{now}) \qquad \textbf{Eq. 6.51}$$

The subscripts now and new represent the weights in the neural network before and after the update, respectively. Where $\nabla_{\boldsymbol{\theta}} J(\boldsymbol{\theta})$ is the policy gradient, and its theorem is proved as:

$$\nabla_{\boldsymbol{\theta}} J(\boldsymbol{\theta}) = \mathbb{E}_{S}\left[\mathbb{E}_{A\sim\pi(\cdot|S;\boldsymbol{\theta})}[Q_{\pi}(S,A)\cdot\nabla_{\boldsymbol{\theta}} ln\pi(A|S;\boldsymbol{\theta})]\right] \qquad \textbf{Eq. 6.52}$$

6.2.5. Actor-Critic method

The Actor-Critic algorithm contains a policy function and an action value function. The policy function $\pi(a|s;\boldsymbol{\theta})$ acts as an Actor, generating and interacting with the environment; the action value function $q(s,a;\boldsymbol{w})$ acts as a Critic, which is responsible for evaluating the Actor's performance and guiding the Actor's subsequent action. Critic's action value function is an approximation given to the policy:

$$\boldsymbol{Q}_{*}(\boldsymbol{s},\boldsymbol{a}) \approx \boldsymbol{Q}_{\boldsymbol{\pi}}(\boldsymbol{s},\boldsymbol{a})$$

The Actor-Critic method in this section will approximate Q_{π} with a neural network. **Figure 6.7** shows the relationship of this method.

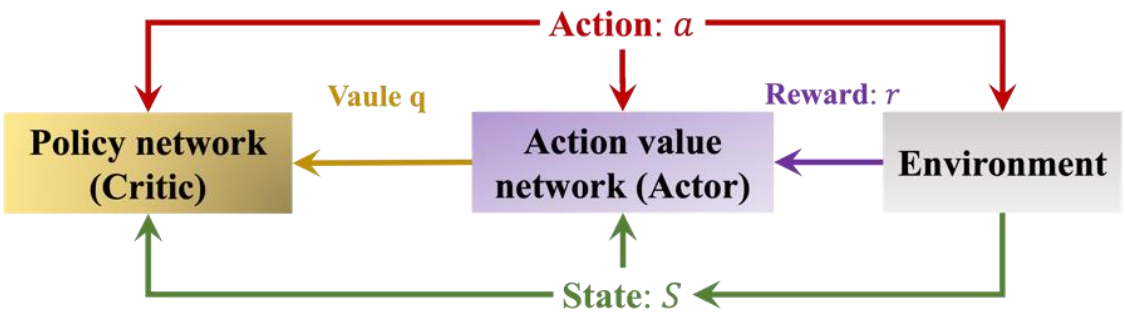

Figure 6.7 Actor-Critic relationship diagram.

6.2.5.1. Policy network

The policy network needs the value network to improve actions. When the policy network outputs an action, the value network feeds back the corresponding output score $\hat{q} \triangleq q(s, a; \boldsymbol{w})$ to the policy network. The policy network uses the state s, action a, and $\hat{q}$ of the value network to calculate the approximate policy gradient to update the parameters $\boldsymbol{\theta}$. In this way the $\hat{q}$ value is maximized.

Training a policy network requires updating the parameters $\boldsymbol{\theta}$ using an approximation of the policy gradient $\boldsymbol{\nabla_{\theta} J(\theta)}$:

$$\boldsymbol{g}(s, a; \boldsymbol{\theta}) \triangleq Q_{\pi}(s, a) \cdot \nabla_{\boldsymbol{\theta}} ln\pi(a|s;\boldsymbol{\theta}) \qquad \textbf{Eq. 6.53}$$

The value network $\boldsymbol{q(s, a; w)}$ approximates the action value function $\boldsymbol{Q_{\pi}(s, a)}$, so $\boldsymbol{Q_{\pi}}$ in the above formula is replaced by the value network:

$$\tilde{\boldsymbol{g}}(s, a; \boldsymbol{\theta}) \triangleq q(s, a; \boldsymbol{w}) \cdot \nabla_{\boldsymbol{\theta}} ln\pi(a|s;\boldsymbol{\theta}) \qquad \textbf{Eq. 6.54}$$

Finally do gradient ascent:

$$\boldsymbol{\theta} \leftarrow \boldsymbol{\theta} + \beta \cdot \tilde{\boldsymbol{g}}(s, a; \boldsymbol{\theta}) \qquad \textbf{Eq. 6.55}$$

6.2.5.2. Value network

The method of training the policy network is based on the value network. Therefore, the policy network can only improve when the $\widehat{\boldsymbol{q}}$ of the value network can truly reflect the action value $\boldsymbol{Q_\pi}$. In the initial stage, the parameters $\boldsymbol{w}$ of the value network are random. As the parameters are updated, the output of the value network also gets closer to $\boldsymbol{Q_\pi}$. The reward $\boldsymbol{r}$ of each feedback from the environment is used as the criterion for optimizing the value network.

At time $\boldsymbol{t}$, the output of the value network is $\widehat{\boldsymbol{q}} = \boldsymbol{q}(\boldsymbol{s}, \boldsymbol{a}; \boldsymbol{w})$. It is an estimate of the action-value function $\boldsymbol{Q_\pi}(\boldsymbol{s_t}, \boldsymbol{a_t})$. At time $\boldsymbol{t+1}$, $\boldsymbol{r_t}$, $\boldsymbol{s_t}$, $\boldsymbol{a_t}$ are observed. So, the TD target is calculated: $\widehat{\boldsymbol{y_t}} \triangleq \boldsymbol{r_t} + \boldsymbol{\gamma} \cdot \boldsymbol{q}(\boldsymbol{s_{t+1}}, \boldsymbol{a_{t+1}}; \boldsymbol{w})$. It is also an estimate of the action-value function $\boldsymbol{Q_\pi}$. However, the $\boldsymbol{r_t}$ part of the formula is to give facts. Therefore, the value network parameter $\boldsymbol{w}$ is updated with the help of the TD error. Define the loss function as:

$$L(\boldsymbol{w}) \triangleq \frac{1}{2}[q(s_t, a_t;\ \boldsymbol{w}) - \widehat{y_t}]^2 \qquad \textbf{Eq. 6.56}$$

Suppose $\widehat{\boldsymbol{q}} \triangleq \boldsymbol{q}(\boldsymbol{s}, \boldsymbol{a}; \boldsymbol{w})$. Then the gradient of the loss function is:

$$\nabla_w L(\boldsymbol{w}) = \underbrace{(\widehat{q_t} - \widehat{y_t})}_{TD\ error\ \delta_t} \cdot \nabla_w q(s_t, a_t;\ \boldsymbol{w}) \qquad \textbf{Eq. 6.57}$$

Update $\boldsymbol{w}$ according to gradient descent in **Eq.** *6.41***.**

1. Observe state s_t, and then randomly sample action $a_t \sim \pi(\cdot\,|s_t; \boldsymbol{\theta}_{now})$.
2. Agent performs action a_t and observe reward r_t and new state s_{t+1}.
3. Randomly sample action $a_{t+1} \sim \pi(\cdot\,|s_{t+1}; \boldsymbol{\theta}_{now})$. (Agent does not perform action a_{t+1}.)
4. Let the value network score the (s_t, a_t):

$$\hat{q}_t = q(s_t, a_t; \boldsymbol{w}_t)$$

5. Let the target network score the $(s_{t+1}, \hat{a}_{t+1})$:

$$\hat{q}_{t+1} = q(s_{t+1}, \hat{a}_{t+1}; \boldsymbol{w}_t)$$

6. Compute the TD target and error:

$$\begin{cases} \hat{y}_t = r_t - \gamma \cdot \hat{q}_{t+1} \\ \delta_t = \hat{q}_t - \hat{y}_t \end{cases}.$$

7. Update the value and policy network:

$$\begin{cases} w_{t+1} \leftarrow w_t - \alpha \cdot \delta_t \cdot \nabla_{\boldsymbol{w}} q(s_t, a_t;\ \boldsymbol{w_t}) \\ \theta_{t+1} \leftarrow \theta_t + \beta \cdot \hat{q}_t \cdot \nabla_{\boldsymbol{\theta}} ln\pi(a_t|s_t;\boldsymbol{\theta_t}) \end{cases}$$

6.3. Summary

The purpose of this chapter is to give a brief introduction to the AI technology involved in SADA. More importantly, it introduces how to combine AI technology with the concepts of *DARwind*, KDPs and FOWTs.

Chapter 7. Case study for the SADA method with basin experimental data

This chapter aims to conduct a case study of the SADA method using basin experimental data. The basin experiment was carried out in the Deepwater Offshore Basin at Shanghai Jiao Tong University. The experiment was conducted by Duan *et al.* (2016a) who from the previous research team. The details of the basin experiment for a Spar-type FOWT are demonstrated in **section 7.1**. Then, the application of the SADA method with basin experimental data is demonstrated in two:

- Using ANN to predict the dynamic performance of FOWT directly.
- Using the DRL in the SADA method to optimize the dynamic performance of FOWT.

In the DRL framework, KDPs are used as the data transmission interface between AI technology and *DARwind*, and experimental data are used as target parameters. The average value of the platform will be used as an evaluation criterion to train the decision-making network to optimize the prediction of *DARwind*. Among them, three models will be discussed separately: ANN, brute force and DDPG (**section 7.4**). Random Gaussian distribution will provide a decision-making mechanism to adjust KDPs in each *DARwind* calculation in the brute force method. In DDPG, the decision-making mechanism comprises two types of typical deep neural networks, namely action and actor networks. More specifically, three training modes are discussed separately: the discrete method, continuous method, and segmented method. More details discussed in the following sections.

7.1. Basin experiment description

A brief description of this experiment is given in this section. The experiment was conducted at the Deepwater Offshore Basin at Shanghai Jiao Tong University for a Spar-

type FOWT. The ratio scale of the basin experiment was 1:50, and the Spar-type FOWT is shown in **Figure 7.1**. The main scantlings of the spar-type floater are shown in **Figure 7.2**. More details about the experimental executions, such as the testing model fabrication, wind field generation, decay test, and wind-wave test, can be found in reference (Duan *et al.*, 2016b).

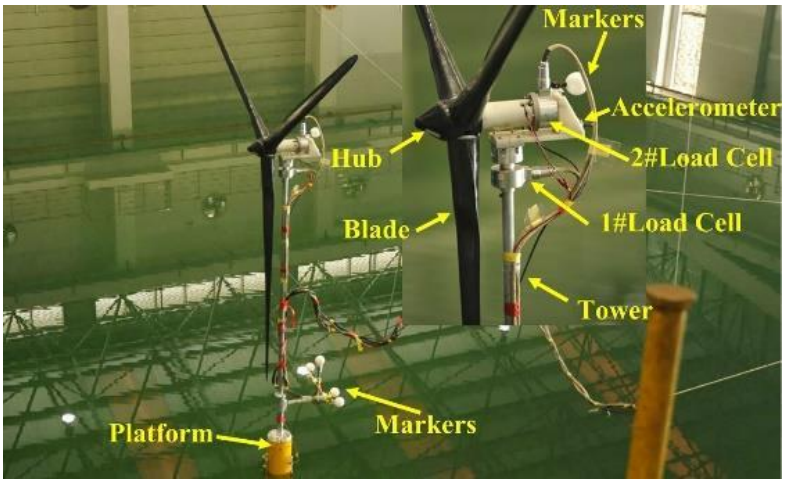

Figure 7.1 Spar-type FOWT model.

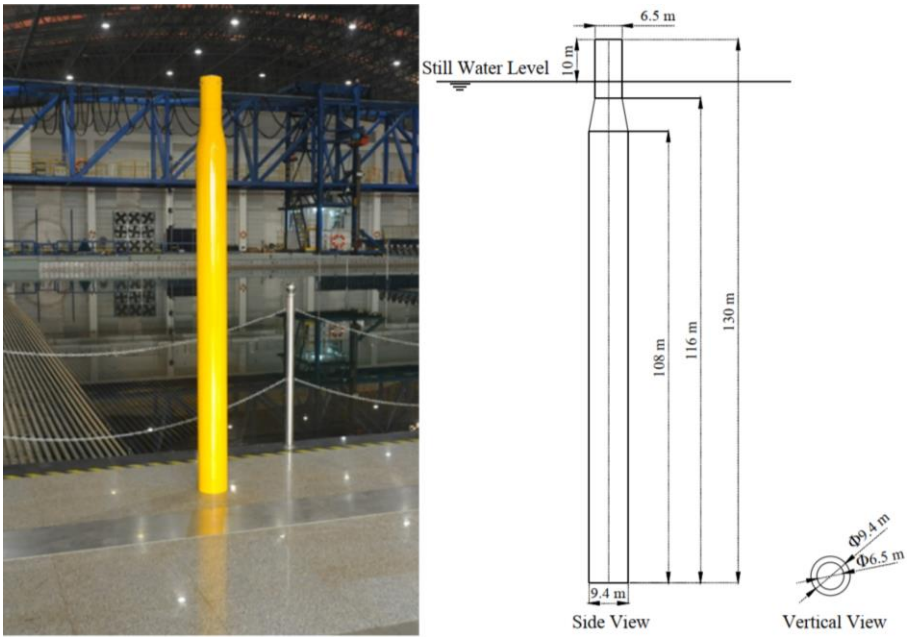

Figure 7.2 Dimensions of spar-type floater (Duan *et al.*, 2016b).

The wind turbine model was designed and fabricated to emulate the prototype parameters in NREL's 5-MW wind turbine for the OC3 project (Jonkman *et al.*, 2009). The blade

model properties reported by Martin (2011) were utilized to fabricate the blade models. The design and fabrication of the tower were also based on the tower properties in the model testing program of the University of Maine, as reported (Martin, 2011). The prototype water depth modelled in the experiment was 200 m and was consistent with MARIN's tests (Koo *et al.*, 2014). For the model basin experiments conducted at MARIN, Koo *et al.* (2014) reported that their taut mooring system utilized a delta connection to simulate the Statoil Hywind configuration, and the delta mooring design was adopted in this basin experiment. The layout of the mooring system configuration can be found in Duan *et al.* (2015). Also noted are the three tension sensors used to measure the tension of the mooring system. The full-scale properties of the mooring system are based on those reported by Koo *et al.* (2014). The main properties of the experimental FOWT at full-scale is shown in **Table 7.1**.

Table 7.1 Main properties of model at full-scale.

Item	Measurements
Blade (kg)	52,659
Hub(kg)	57,272
Nacelle(kg)	232,291
Tower (kg)	287,128
Platform Mass, including Ballast (kg)	7,316,578
Platform Roll and pitch Inertia around the CM (kg m^2)	4,656,382,813
Mass of the entire floating system (kg)	8,066,110
CM locations of the entire floating system (m).	−78.947
Radius & depth of an anchor (m)	445; 200
Radius & depth of a fairlead (m)	5.2; 70
Diameter of A, B and C lines (m)	0.167; 0.125
Unstretched length of A, B and C lines (m)	424.35; 30
Extensional stiffness (N)	121E6; 68E6
Unit weight of lines in fluid (kg/m)	22.5; 12.6

7.2. ANN prediction

This section introduces the application of the SADA method to predict the dynamic responses of the FOWTs by using artificial neural networks (ANN). In ANN optimized prediction, the results of *DARwind* simulation of 3DOF motions will be the input data,

and the basin experimental results will be the target data. The BP algorithm will be adopted, and the differences between the output data and targe data is used for ANN training. The load cases for the following works are time-domain data from the experiment introduced earlier, as shown in **Table 7.2**.

Table 7.2 Test matrix of BP prediction.

Case No.	V_w (m/s)	Wave parameter			V_c (m/s)
		H_s (m)	T_p (s)	γ	
LC1	11.4	—	—	—	—
LC2	11.4	7.1	12.1	2.2	—
LC3	11.4	7.1	12.1	2.2	0.5

The irregular wave cases are based on the JONSWAP wave spectrum. The ANN adopts a double hidden layer structure, and the comparison mainly focuses on the motions of the platform in terms of 3DOF (Surge, Heave and Pitch) with total sets of 10221 & 10121 data respectively. The results from *DARwind* and the experiment will be the primary data. The specific classification can be found in **Table 7.3**, which shows the main components of input and output data of ANN.

Table 7.3 ANN data collection.

Item	**LC2**		**LC3**	
Total Sets	10221	3618s	10121	3583s
Training input data (DAR)	1-9721	3441s	1-9621	3406s
Training Output data (EXP)	1-9721	3441s	1-9621	3406s
Test input data (DAR)	9721-10221	177s	9621-10`21	177s
Test output data (EXP)	9721-10221	177s	9621-10`21	177s
Input data	Surge, Sway, Heave, Roll, Pitch, Yaw			
Output data	Surge, Heave, Pitch			

In these two cases, the training data was selected randomly ordered. The remaining 500 sets of data (177s) for each condition are used as network test data. In **Figure 7.3** and **Figure 7.4**, the results after optimization by the ANN keep the same trend as the results of the basin model test (MT).

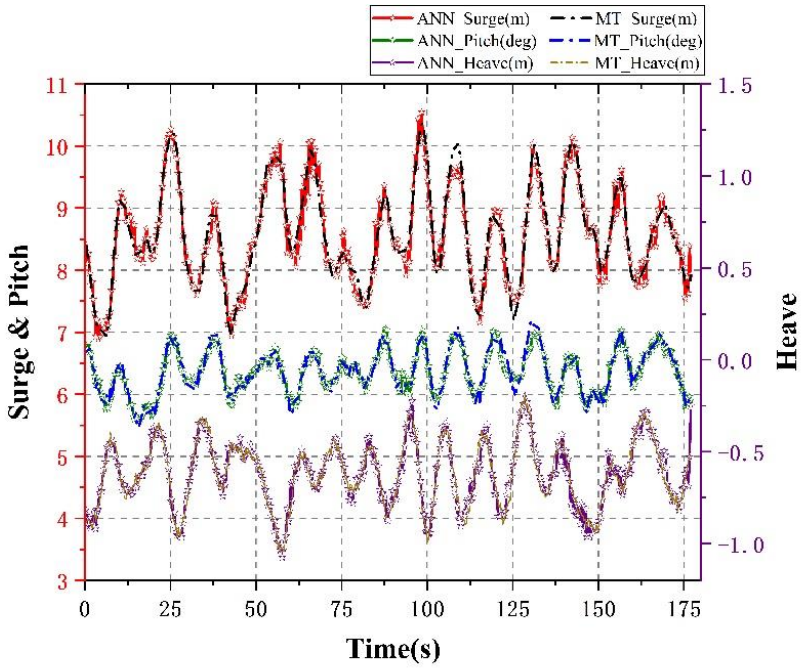

Figure 7.3 The prediction of ANN under LC2.

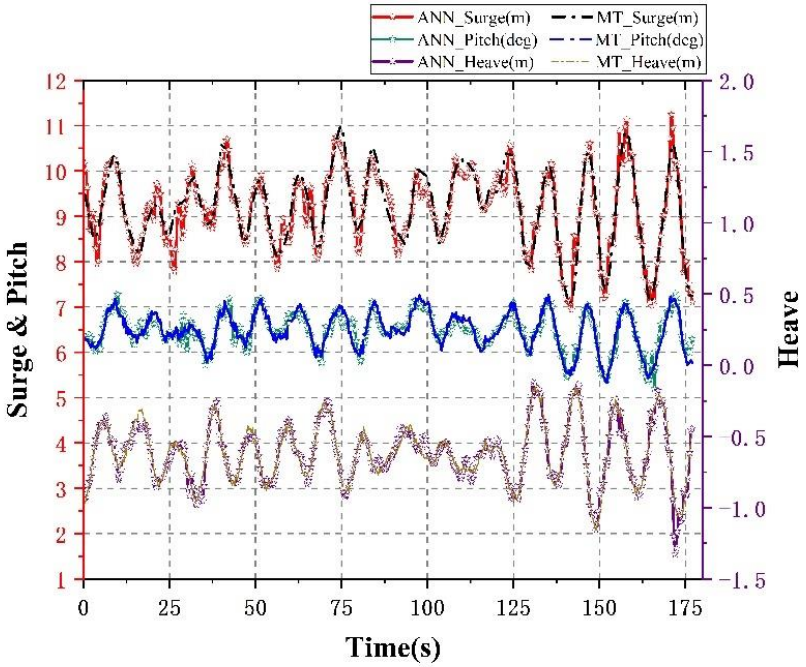

Figure 7.4 The prediction of ANN under LC3.

The maximum difference occurs in LC3 in **Table 7.4**. The difference between ANN and MT of minimum value of the surge motion is 1.626m, and the maximum value of the Pitch motion is 0.22deg. Furthermore, the percentages differences are 29.862% and

328.358%, respectively. However, the magnitude of pitch motion under LC3 is minimal, and it is found through a complete data time-domain comparison that only a few minority prediction differences are significant. In addition, from the standard deviation results, the maximum difference between ANN and MT are 0.873m and 0.201deg, respectively, which is the same as the experimental results of 0.862m and 0.201deg, and the results are similar to the average data volatility is not substantial so that it can be accepted. An illustration of the average comparison can be seen in **Figure 7.5**.

Table 7.4 Statistical comparison of BP prediction.

Response		Surge (m)		Heave (m)		Pitch (deg)	
		ANN	MT	ANN	MT	ANN	MT
LC2	AVG	8.559	8.581	-0.620	-0.619	6.364	6.369
	Max	10.547	10.368	-0.194	-0.184	7.060	7.204
	Min	6.892	6.928	-1.075	-1.043	5.569	5.458
	Stdev	0.770	0.789	0.175	0.175	0.344	0.363
LC3	AVG	9.172	9.209	6.486	6.485	-0.619	-0.614
	Max	11.243	10.980	7.302	7.266	0.067	-0.153
	Min	5.445	7.071	5.195	5.325	-1.327	-1.154
	Stdev	0.873	0.862	0.399	0.410	0.210	0.201

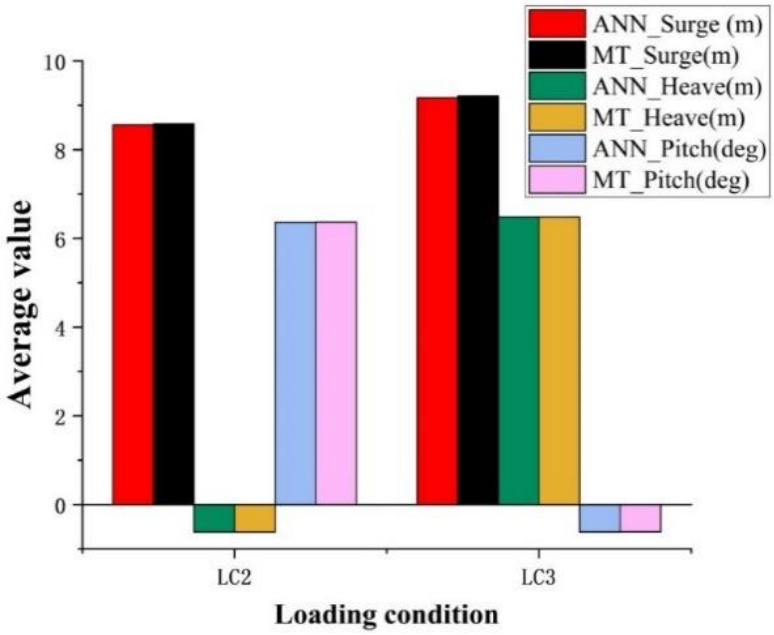

Figure 7.5 Comparison results with ANN and experiment.

Table 7.5 and **Figure 7.6** give a comparison of the percentage difference of the average value, which allows a more intuitive comparison of the differences between the SADA and *DARwind* results. It is not difficult to see that the difference percentage of numerical simulation results after optimization by ANN is significantly reduced in every motion, especially in Heave and Pitch.

Table 7.5 Average percentage difference (%) of BP prediction.

Response		Surge (m)		Heave (m)		Pitch (Silver *et al.*)	
		ANN	DAR	ANN	DAR	ANN	DAR
LC2	AVG	1.701	6.910	6.159	63.912	1.305	11.710
LC3	AVG	2.570	6.932	2.054	10.243	11.574	51.724

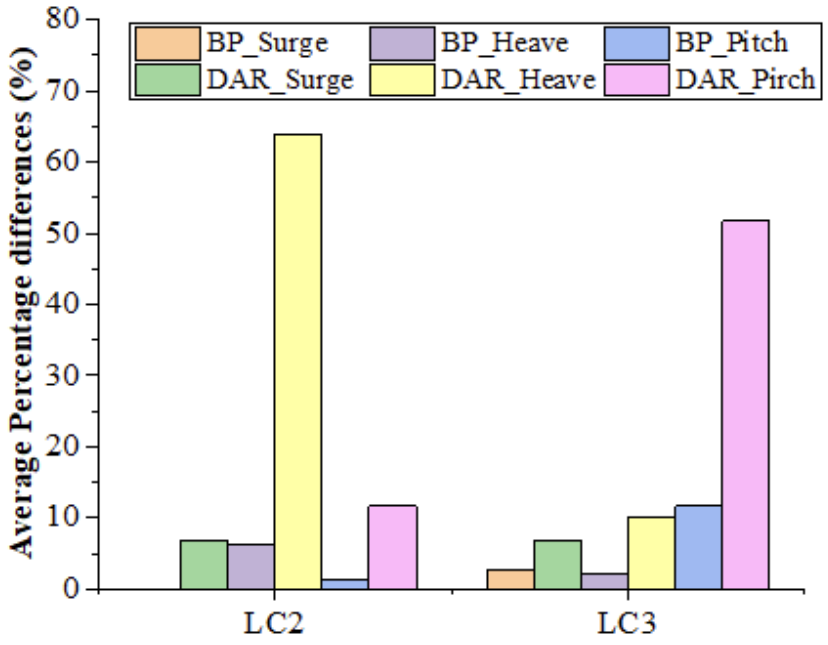

Figure 7.6 Average percentage difference (%) between BP and *DARwind*.

It should also be mentioned that although the average percentage difference of the platform Heave & Pitch motion in the *DARwind* calculation results is as high as 63.9% and 51.7% under LC2 and LC3, respectively, the result is still acceptable because the actual amplitude of these two motions is small.

7.3. Brute-Force prediction

This section will use the selected KDPs and experimental data to optimize the forecast results of *DARwind*, to improve the accuracy. The cases for the following works are time-domain results from the experiment, as shown in **Table 7.6**.

Based on the framework of RL, SADA will use the BF method to modify and weight KDPs. **Table 7.7** summarizes 11 KDPs used in this section. More KDPs have not been considered, which will be added in KDPs analysis in next **section 7.4**.

Table 7.6 Test matrix of Brute-force.

Case No.	Classified	V_w	Wave			V_c
		m/s	H_s (m)	T_p (s)	γ	m/s
1	current only	-	-	-	-	1.2
2	wave only	-	2	7.1	12.1	-
3	wind only	10.9	-	-	-	-
4	wind and current	10.9	-	-	-	1.2
5	wind & irregular wave	10.9	7.1	12.1	2.2	-
6	WWC	10.9	7.1	12.1	2.2	1.2
7		11.4	2	8	3.3	0.6

Table 7.7 Selected KDPs in BF.

Discipline	KDPs
Aero	Wind speed
	Glauert correction
Hydro	Current speed
	Added linear restoring matrix
	Added linear viscous damping matrix
	Added quadratic viscous damping matrix
	Added static force
Mooring	Wet density
	Axial stiffness
Structural	Polynomial Flap 1st vibration modes
Servo	Generator torque constant

Table 7.8 shows the maximum percentage difference change of the 6DOF motions in each case. The positive value in the table represents how much the difference of the result

calculated by the weighted KDPs is lower than the initial difference of the unweighted KDPs in 500 loops. A negative number means the difference has increased.

Table 7.8 Statistics of maximum percentage difference in BF.

Case No.	Surge	Sway	Heave	Roll	Pitch	Yaw
1	2.48	0.02	77.58	0.14	2.22	0.05
2	15.30	3.19	33.81	3.80	0.40	1.29
3	5.94	10.37	165.17	31.86	4.48	4.03
4	9.46	8.03	34.40	76.63	5.14	4.85
5	4.69	16.39	0.91	1.97	3.79	2.67
6	8.15	7.77	25.32	178.16	4.42	4.56
7	8.05	15.66	28.19	8.88	4.56	6.69

The concept of total difference is to measure the agent's performance after an action. Since only surge and pitch have the largest amplitude, the total difference is the sum of these two differences. **Table 7.9** selects the statistics result of the most significant decline of total percentage difference among 500 actions of each case. The percentage difference of the 6DOF motions calculated by weighted KDPs corresponds to the most significant decline of the total percentage difference.

Table 7.9 Statistics of maximum total percentage difference in BF.

Case No.	Total difference	Surge	Sway	Heave	Roll	Pitch	Yaw
1	4.66	2.35	-0.02	71.48	-0.11	1.75	-0.01
2	14.62	13.98	-2.33	27.28	0.87	-0.39	-0.24
3	9.97	5.76	0.08	97.39	-2.70	4.36	0.37
4	16.41	8.36	1.52	21.54	-9.87	4.04	2.30
5	5.88	4.55	-8.18	-4.47	1.40	3.65	1.85
6	11.60	6.01	1.44	12.84	-52.50	3.68	2.60
7	14.28	7.49	-9.25	12.76	4.71	4.06	3.16

From **Table 7.9**, the difference of some motions has increased. For example, in case 1, the sway, roll, and yaw differences increased by 0.02%, 0.11% and 0.01%, respectively. Surge and pitch reduced by 2.35% and 1.75%, and their experimental average amplitudes were 2.469 m and 0.763 deg. The average amplitude of roll, pitch and yaw are only 0.161m, -0.025 deg and 0.113 deg. Therefore, the increase in their difference is within an

acceptable range. From the comprehensive point of view of 7 cases, the difference change of surge (**Figure 7.7**) remains between [-5%, 5%] during 500 actions, except for case 2 (Wave only), which is only affected by a single environmental factor (wave).

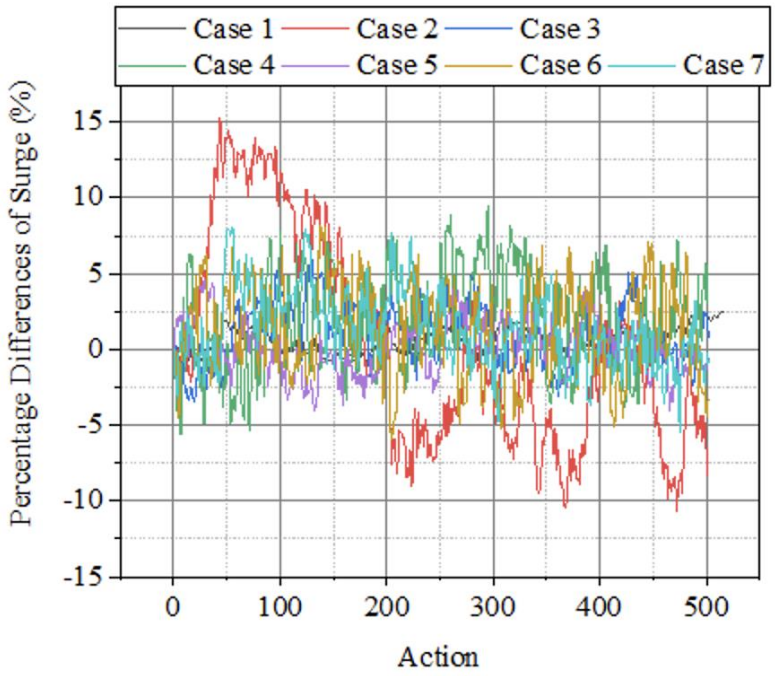

Figure 7.7 Percentage difference of surge in 500 actions in BF.

The difference of surge is reduced in all 7 cases in **Figure 7.8**. For example, the LC1 is only affected by current, which eliminates wind and waves. The influence can be preliminarily judged whether there is a deviation in the numerical calculation or the measurement of the current speed in the experiment under this case.

The difference of heave (**Figure 7.9**) has fluctuation. In the case of non-couple cases, heave's performance is more ideal than other cases. The limitations of the KDPs may cause it. Adding static force will have a significant impact on heave in coupling cases if added static force is included.

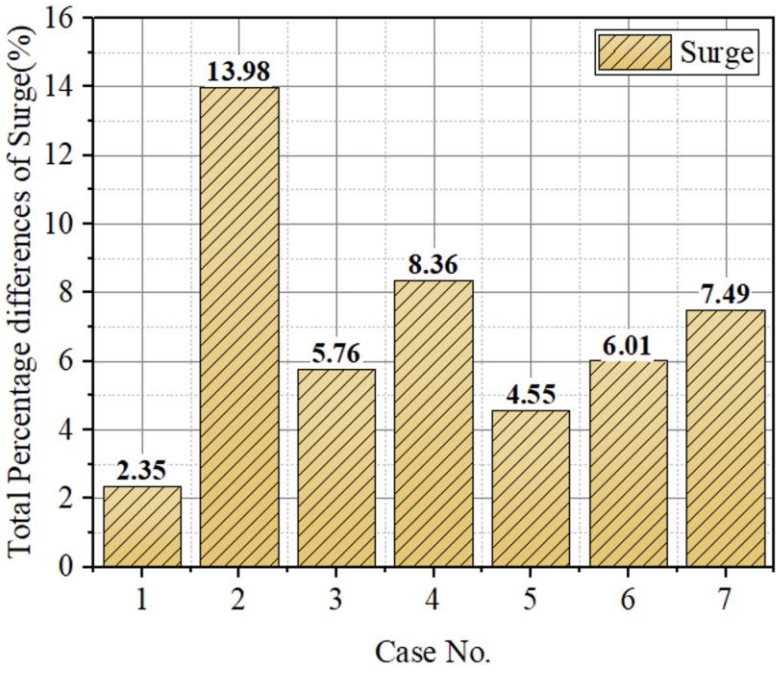

Figure 7.8 Total Percentage difference of surge in BF.

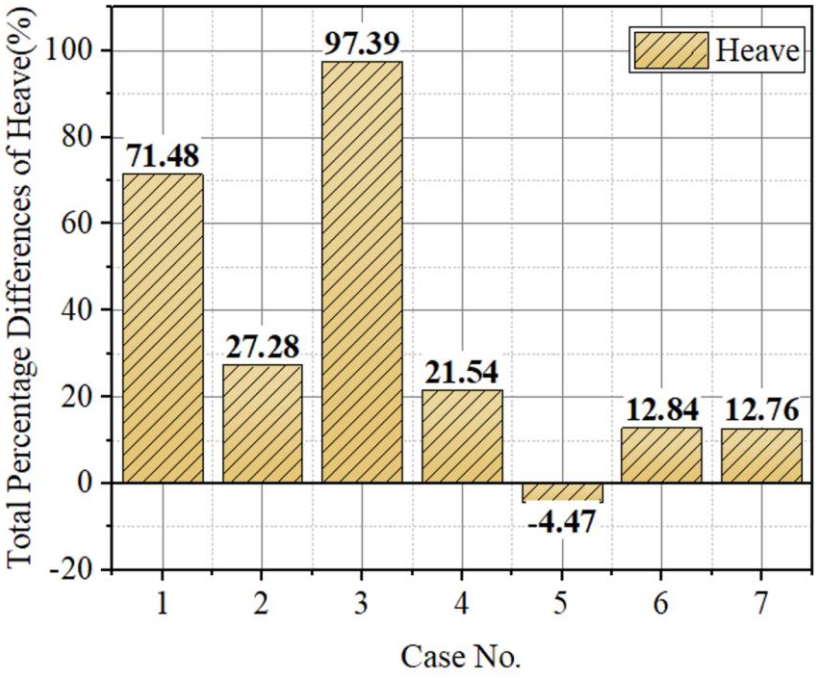

Figure 7.9 Total Percentage difference of Heave in BF.

The difference of pitch (**Figure 7.10**) shows a declining state, except case2. Comparing cases 6 and 7, the experimental values of pitch are 4.367 deg and 4.164 deg, respectively. Represented by this order of magnitude, the amplitude change corresponding to 4% of different in case 7 is about 0. 17deg.

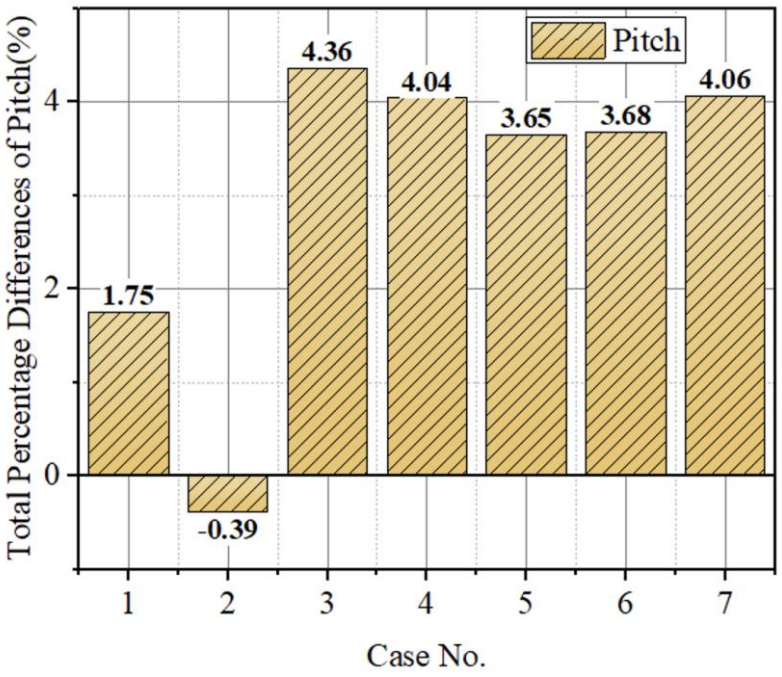

Figure 7.10 Total Percentage difference of Pitch in BF.

For yaw (**Figure 7.11**), in a non-coupled environment, it cannot effectively reduce the difference based on the initial calculation results. In a coupled environment, the reduced difference is also limited. Moreover, the initial numerical simulation results of yaw have significant differences.

The BF method uses random Gaussian distribution to weight KDPs, with a certain degree of randomness. However, these KDPs can achieve continuous distribution changes during the training process due to boundary conditions. Nevertheless, this cannot be based on the powerful intelligence of the program.

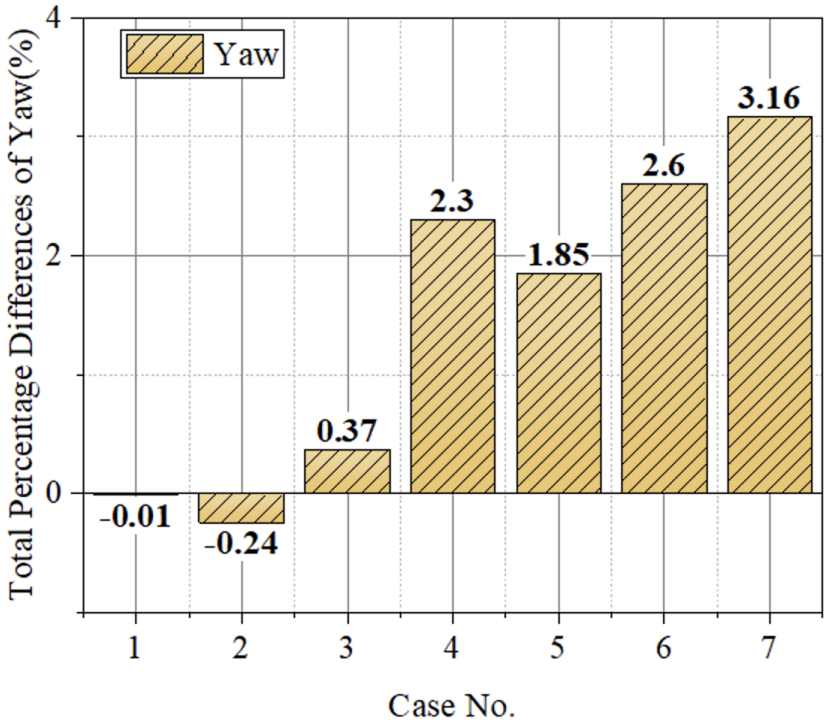

Figure 7.11 Total Percentage difference of Yaw in BF.

7.4. DDPG prediction

The DDPG and BF methods are based on a reinforcement learning framework. The difference is that its decision-making network uses a deep neural network instead of Gaussian distribution. The case studies of Discrete model, Continuous model, and Segmented model in SADA are discussed in this section.

7.4.1. Discrete model

The Discrete model is suitable for analysing a single known sea state and working condition. For example, optimise KDPs to reduce differences in a single case further. In this subsection, nine testing cases will be selected for AI training, shown in **Table 7.10**.

In **Table 7.11**, the positive value shows that SADA reduced the difference between numerical calculation and experiment by percentage and vice versa. The number of actions taken in each case is different, determined according to the specific case.

Table 7.10 Test matrix of discrete model in DDPG.

Case No.	Classified	V_w	Wave			V_c
		m/s	H_s(m)	T_p(s)	γ	m/s
1	current only	-	-	-	-	0.3
2		-	-	-	-	0.5
3	wind only	9.4	-	-	-	-
4	wind only	12.8	-	-	-	-
5	wind and current	11.1	-	-	-	0.85
6	wind & irregular wave	10.9	7.1	12.1	2.2	-
7		12.8	7.1	12.1	2.2	-
8	WWC	11.4	2	8	3.3	0.6
9		10.9	7.1	12.1	2.2	1.2

Table 7.11 Percentage difference in discrete model.

Case No.	Surge	Heave	Pitch	Yaw
1	21.065	-0.84	0.629	0.021
2	9.937	0.787	1.239	0.001
3	4.324	10.615	0	-0.964
4	0.939	-2.227	0.792	1.631
5	12.666	-14.725	0.244	-0.115
6	0.947	-1.01	0.73	1.151
7	2.053	-1.322	1.527	0.64
8	4.05	-4.261	1.706	1.587
9	1.62	-8.184	1.875	1.213

In case 1 (**Figure 7.12**), SADA weighs the KDPs 7 times. In the first four actions, the difference of surge has changed significantly by each action. However, the fifth action is unchanged compared to the fourth one. The weighted KDPs has been chosen as the most suitable one. Therefore, the difference of each step is unchanged from the previous step. In some cases, only part of the sea state has been considered, for example, in the wind only (case 3 &4), which will not be changed with some KDPs (current speed, wave loads, etc.).

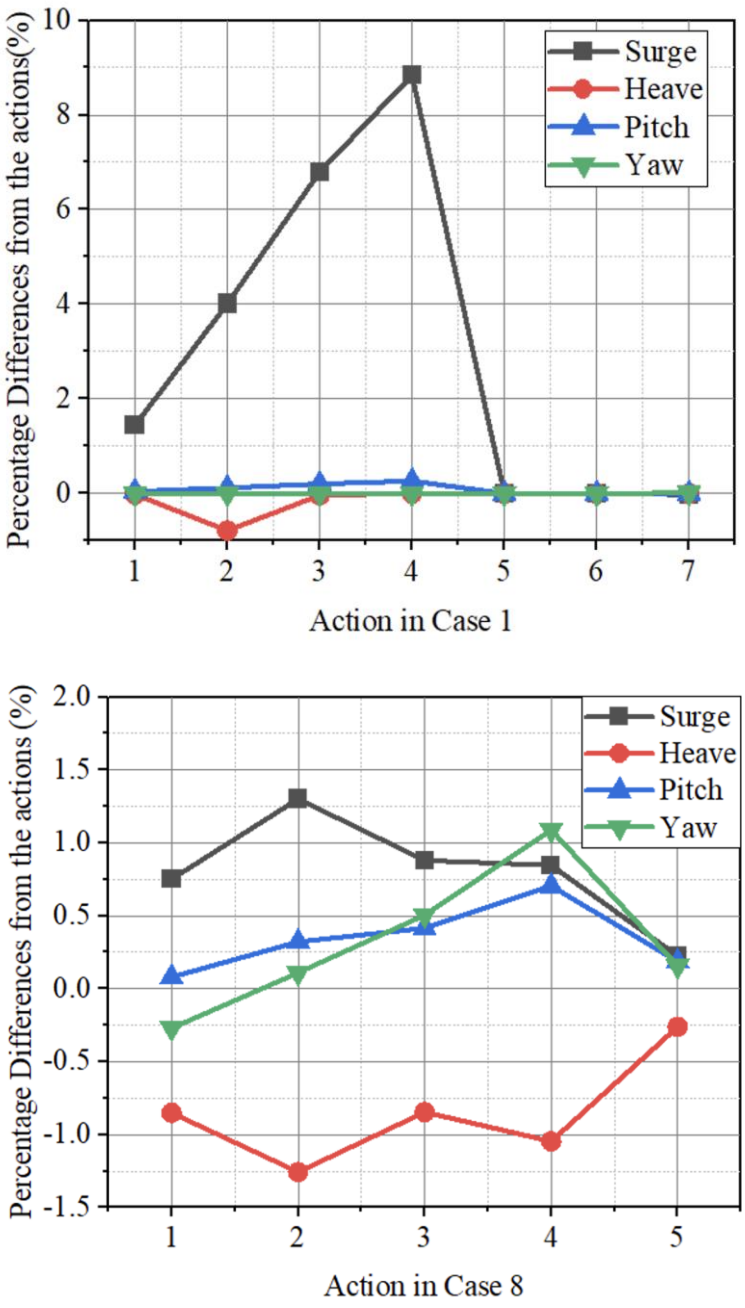

Figure 7.12 Comparison under case 1 & 8 discrete model.

Figure 7.13 shows the trend of the average amplitude of surge with each action. As shown, the solid red line is the average experimental value of 7.07 m, and the red dashed line is the 5% tolerance in the range of 6.7165 m.

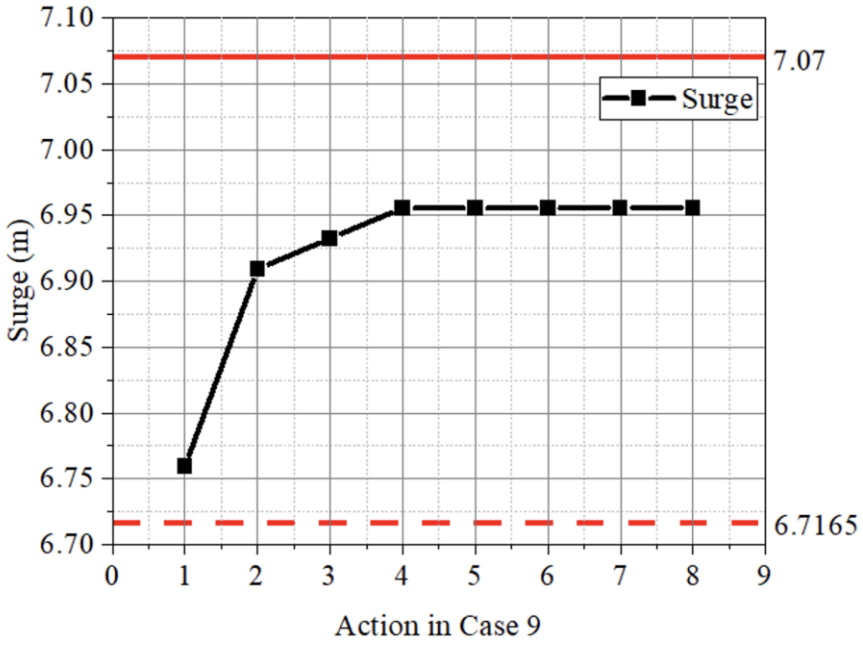

Figure 7.13 Average surge amplitude change in discrete model.

Similar to the situation encountered in case 1, surge amplitude remains unchanged after the fourth weighting action in a fully coupled environment (WWC). It can be seen from **Table 7.11** that the difference of Heave in case 9 is increased, while the experimental result of Heave in case 9 is only 0.307m, so the slight change is within the tolerable difference range. The results of other cases are not listed, all provided in **Table 7.11**. From **Figure 7.14**-**Figure 7.17**, the entire FOWTs system is in a shutdown state, without the influence of wind and waves in case 1 (current only).

Compared with wind only and case 5, it shows that in the coupled environment of wind and current, weighted KDPs can effectively reduce the difference of surge. In the last four couple cases, the surge amplitude is very close to the experimental value in these coupled cases. Therefore, the difference remains stable. Although the Heave decreases in most cases, its experimental value is only 0.065m. In general, the amplitude of Heave in all 9 cases is two decimal places. In addition, there are not many KDPs that directly affect the Heave. Therefore, the added static force and added linear restoring matrix could also be considered for further optimisation.

Comparing case 6 and case 7, it is found that the higher the wind speed, the better the optimisation of the pitch in the wind and wave environment. The average amplitude of pitch is 6.42 deg and 4.512 deg in case 6 and case 7, respectively. The 11 KDPs can achieve the most significant optimisation in the last two cases. If KDPs are expanded from 11 to 31 and more factors included, then it is conceivable that there will be a massive change in pitch in the WWC environment. The percentage difference of yaw is more dramatic. In the current only case, the percentage difference did not change, showing that the current speed does not significantly impact the yaw motion. The wind only has a more significant impact due to the difference in wind speed.

Nevertheless, comparing experimental results (-0.281deg and -0.866 deg), the more considerable wind speed causes yaw amplitude to increase. In addition, the differences are all reduced under the combined wind and wave conditions. The wind will inhibit the motion of the platform under wave conditions, and the hydrodynamic parameters in KDPs have been corrected more accurately.

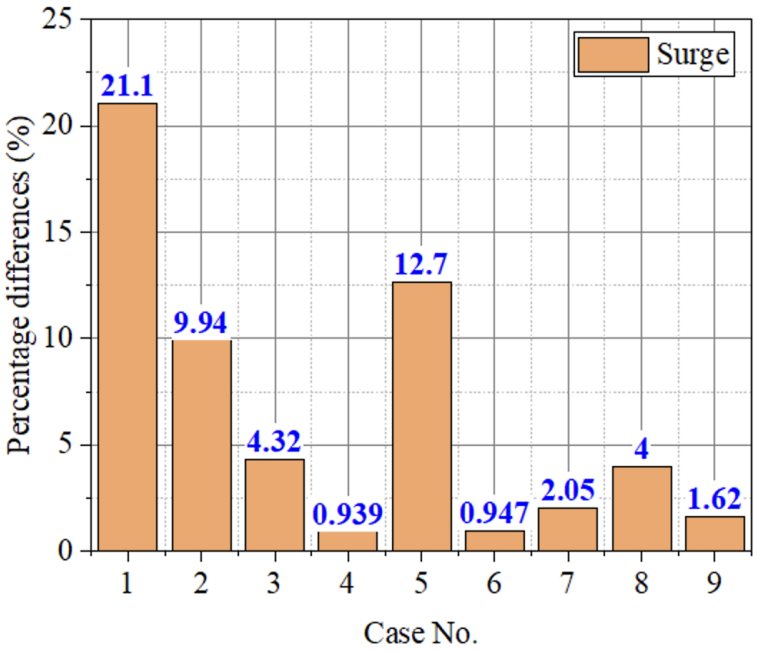

Figure 7.14 Percentage difference of Surge in discrete model.

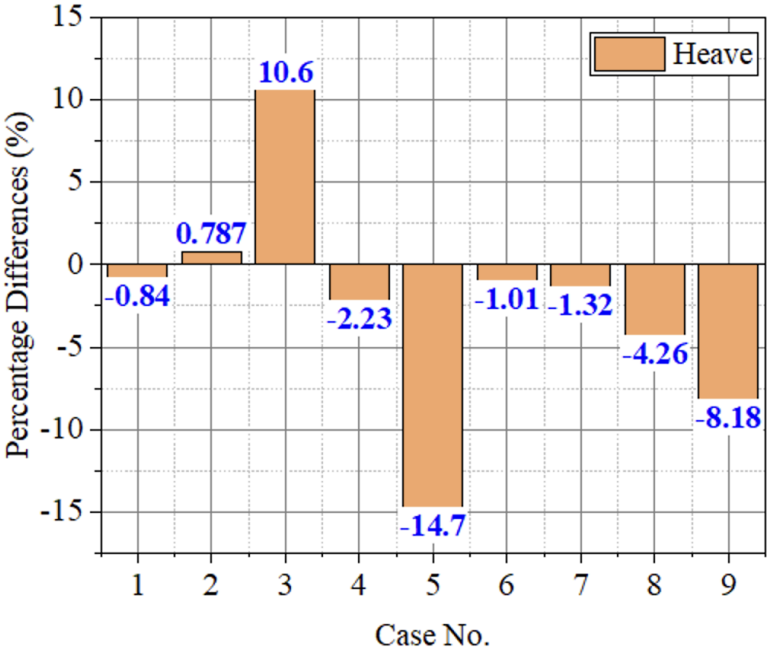

Figure 7.15 Percentage difference of Heave in discrete model.

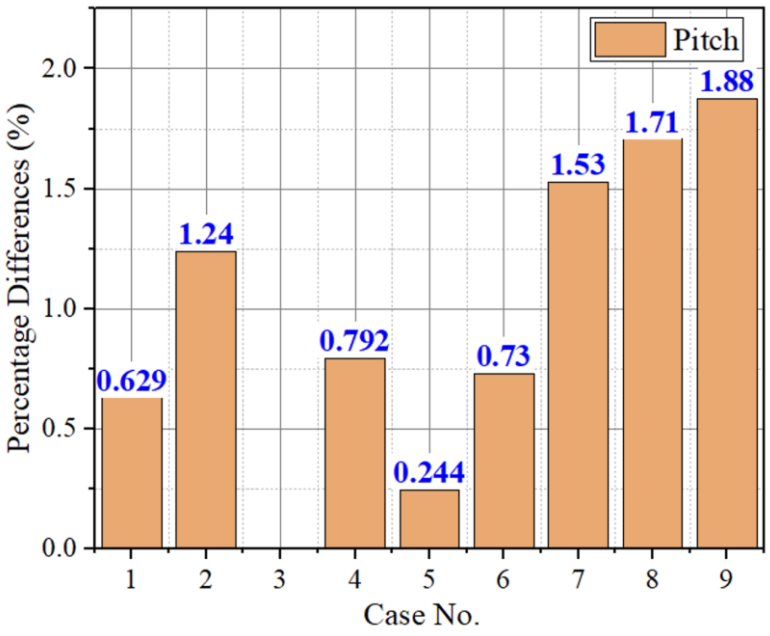

Figure 7.16 Percentage difference of Pitch in discrete model.

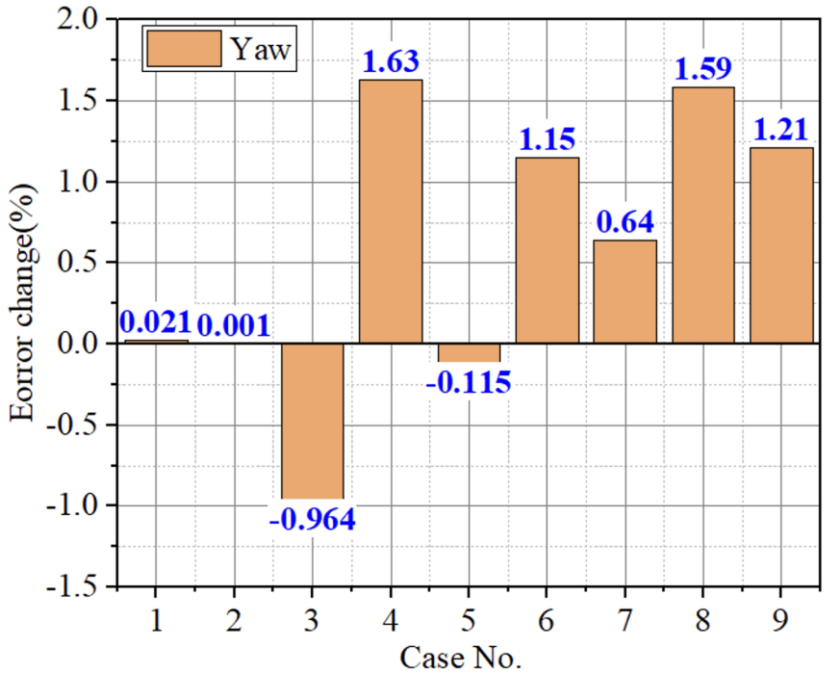

Figure 7.17 Percentage difference of Yaw in discrete model.

7.4.2. Continuous model

A multi-combination training mechanism is set according to the selected cases in the continuous model. In **Table 7.12**, the first three cases are training cases, and case 4 is the forecasting case.

Table 7.12 Test matrix of continuous model in DDPG.

Case No.	V_w	Wave			V_c
	m/s	H_s(m)	T_p(s)	γ	m/s
LC1	11.4	2	8	3.3	0.6
LC2	12.8	7.1	12.1	2.2	0.8
LC3	10.9	7.1	12.1	2.2	1.2
LC4	11.1	7.1	12.1	2.2	0.85

From **Table 7.13**, it can be pointed out that the optimisation effect of the CT method is more significant than that of the ST method. Case 2 has a general performance in the variation of difference of each motion. This may be caused by the wind load and the high rotor speed. Wind load can effectively restrain the platform motion, but too high rotor speed will increase the influence of gyro moment.

Table 7.13 Percentage difference of two methods (%) in continuous model.

Case No.	Surge		Heave		Pitch		Yaw	
	ST	CT	ST	CT	ST	CT	ST	CT
1	0.52	4.75	0.23	-19.60	-0.12	9.94	0.16	14.07
2	0.68	2.68	-0.06	-2.55	-0.15	0.86	-0.16	1.14
3	1.13	3.97	-0.46	-15.38	-0.03	11.32	0.15	12.74

The three cases defined in **Table 7.12** belong to the combination of wind, wave and current, and the percentage difference platform motions are carried out according to each action. In **Figure 7.18**-**Figure 7.21** the CT method has the advantages of rapid convergence compared with the ST method.

For example, in case 1, the KDPs of the CT reach the boundary after the sixth action and no more extended change. The ST model still tends to change after the 11-th action. This also means that the CT method can judge the next step more effectively according to the state obtained after each action.

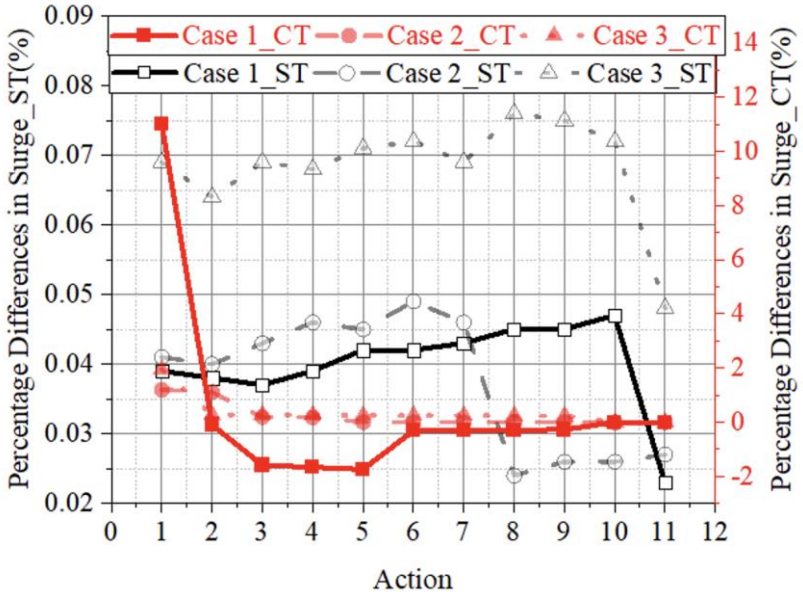

Figure 7.18 Actions of Surge in continuous model.

However, the ST method obtains the best KDPs after 25 operations which did not show in **Figure 7.18-Figure 7.21**, The difference in the first action of the CT method drops by 11%. The difference gradually increased in the following five actions, but the percentage increase was minimal (within 2%). This is also a reflection of the intelligence of the CT method. The model itself measures how to act to obtain better benefits. According to the reward engineering, if the difference of surge reaches within 10%, which represents the acceptable range.

For Heave, the ST model performs well initially, and the difference gradually decreases, but after the fifth action, it remains unchanged. The difference increases rapidly after the first action for the CT method, but it remains stable afterwards. However, the heave amplitude is only 0.411m in case 1. Even if the difference of the first action increases by 12%, the impact on the entire FOWTs system is tiny. This is also the intelligence of the CT model, which can effectively filter the weight of the maximum benefit by choosing between surge and Heave.

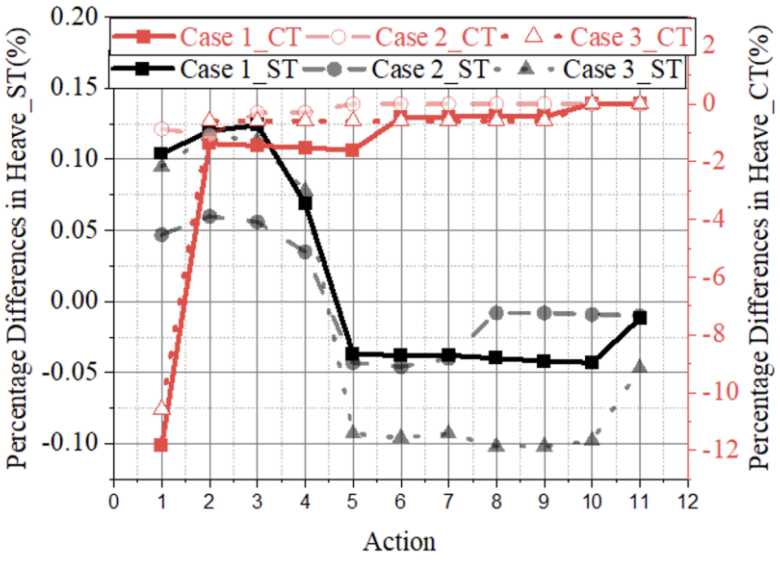

Figure 7.19 Actions of Heave in continuous model.

For pitch and yaw, the optimisation effect of the CT method is much better than that of the ST model, in case 1. The difference reduction of each step in the ST method is only

kept in a small interval. The CT method is consistent with the two motions discussed above. SADA made choice in the first action, reducing the difference by about 8%. In subsequent actions, on the one hand, the KDPs may reach the boundary, and it weighs other factors and benefits. Therefore, the difference no longer changes significantly and maintains fluctuations in a small range.

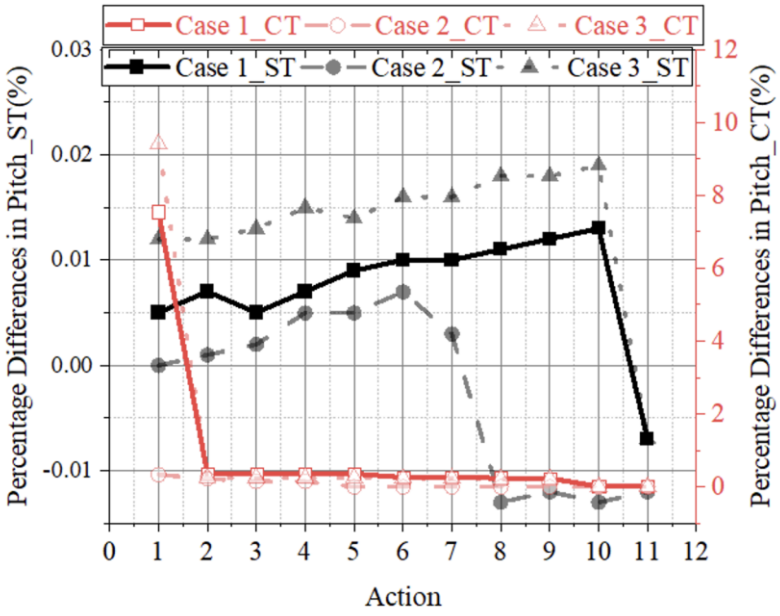

Figure 7.20 Actions of Pitch in continuous model.

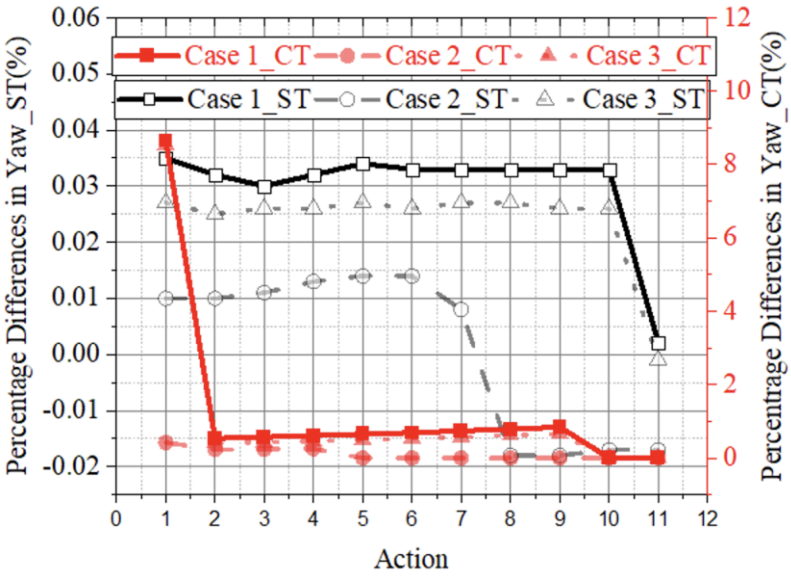

Figure 7.21 Actions of Yaw in continuous model.

7.4.3. Segmented model

This subsection will focus on three aspects: single impact, two sea loads impact, and fully wind/wave/current. A total of 12 experimental cases were selected, shown in **Table 7.14**.

Table 7.14 Training cases matrix of segmented model.

Case No.		V_w	Wave			V_c
		m/s	H_s (m)	T_p (s)	γ	m/s
1a	current only	-	-	-	-	0.3
1b		-	-	-	-	0.85
2a	wind only	9.4	-	-	-	-
2b		10.9	-	-	-	-
3a	wave only	-	2	8	3.3	-
3b		-	7.1	12.3	2.2	-
4a	wind and current	11.1	-	-	-	0.85
4b		10.9	-	-	-	1.2
5a	wind and wave	12.8	7.1	12.1	2.2	-
5b		10.9	7.1	12.1	2.2	-
6a	WWC	8	2	8	3.3	0.6
6b		11.4	7.1	12.1	2.2	0.8
6c		18	7.1	12.1	2.2	0.85

These cases include the wind only, wave only, current only, wind and wave, wind, wave and current (WWC). The impact here refers to the factors affecting the FOWTs system. The wind, waves, and currents will be considered in a single impact (case 1-3). Wind and wave, wind and current will be considered in coupling impact (case 4-5).

7.4.3.1. Single impact

A single impact includes current only (case 1 a & b), wind only (case 2 a & b) and wave only (case 3 a & b) cases in **Table 7.14**. **Figure 7.22** summarises the results of the 6 DOF motions of these 6 cases. The stacked histogram represents the percentage difference change, while the dotted line chart corresponding to the right axis represents the change in amplitude under the corresponding percentage.

In current cases (1 a & b), the current speed has a dominant influence on the FOWTs system. Except for surge motion, the amplitudes of other motions are small. The difference reductions of the surge are 46.35% and 32.68%, and the amplitude of the changes are between 0.16m and 0.4m. **Figure 7.23** shows the time history of the surge in 1b.

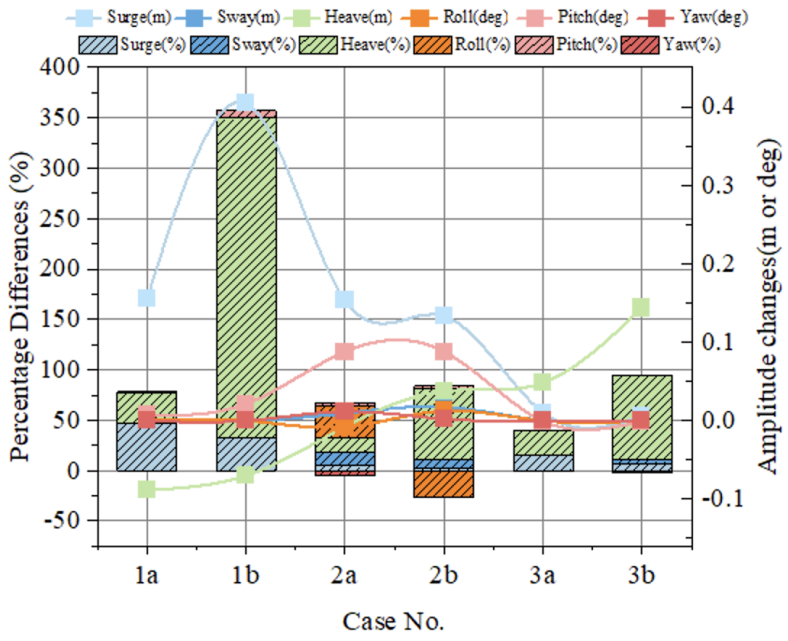

Figure 7.22 6DOF motions percentage difference in single impact cases.

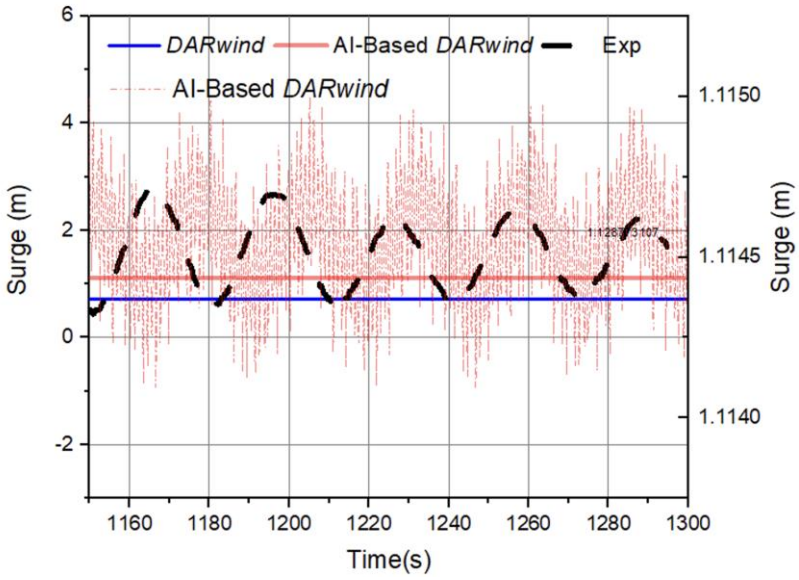

Figure 7.23 Time history of surge under case 1b in segmented model.

In wind only cases (case 2 a & b), the percentage difference of roll has increased, but its experimental amplitude does not exceed 0.03 deg. Taking case 2b as an example, the amplitude changed 0.01 deg. Although this may not be the optimal global solution, it is acceptable for the entire highly coupled FOWTs system. **Figure 7.24** shows the time history of the surge and sway in 2b. The amplitude of the surge in 2b changed 0.13m (from 5.52m to 5.65m). The tension difference of the fairleads at the connection of the three mooring lines is also reduced by 1.2%, 1.69% and 1.73% (29.66kN, 49.73kN and 50.83kN).

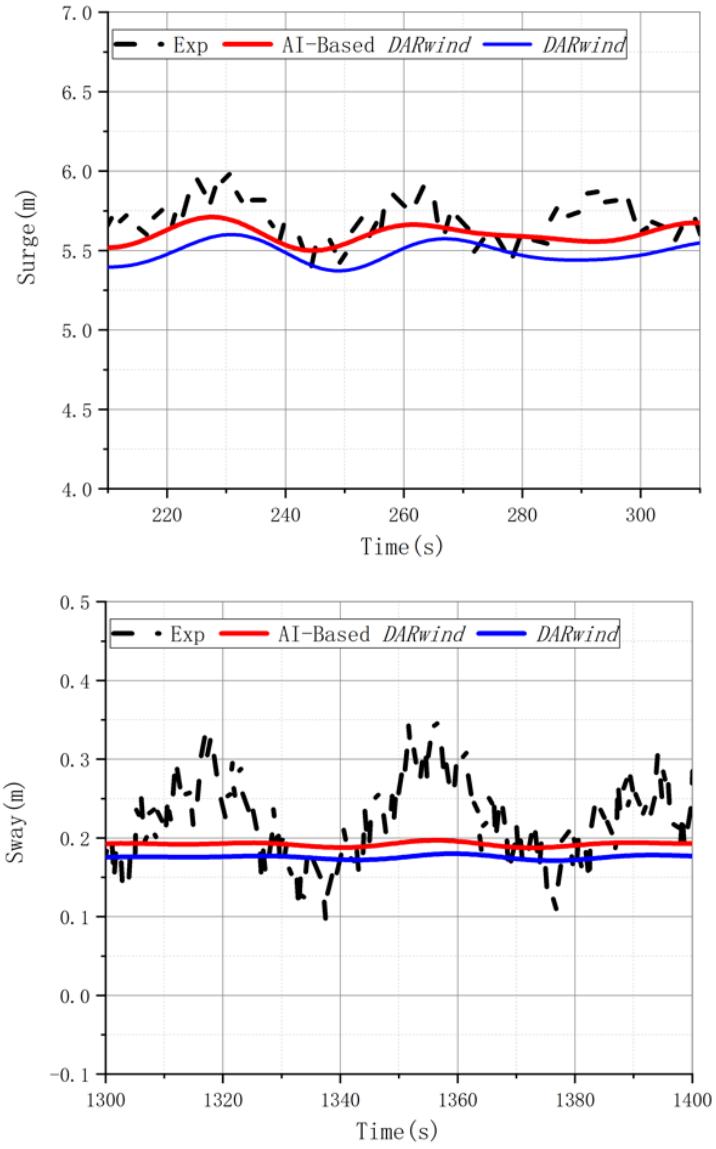

Figure 7.24 Time history of surge and sway in case 2b in segmented model.

In the case of the wave only (case 3 a & b), the platform is maintained in a stable state, and the wind turbine is in a parked state. Under this environment, heave and pitch motions are the dominating motions. Taking 3b as an example, the mean difference of Heave has been reduced by 83.71%, which is a satisfactory optimisation result in amplitude. **Figure 7.25** shows the frequency analysis in 3b. From the frequency domain, it can also better show that SADA has improved the motion induced by the natural frequency of the platform.

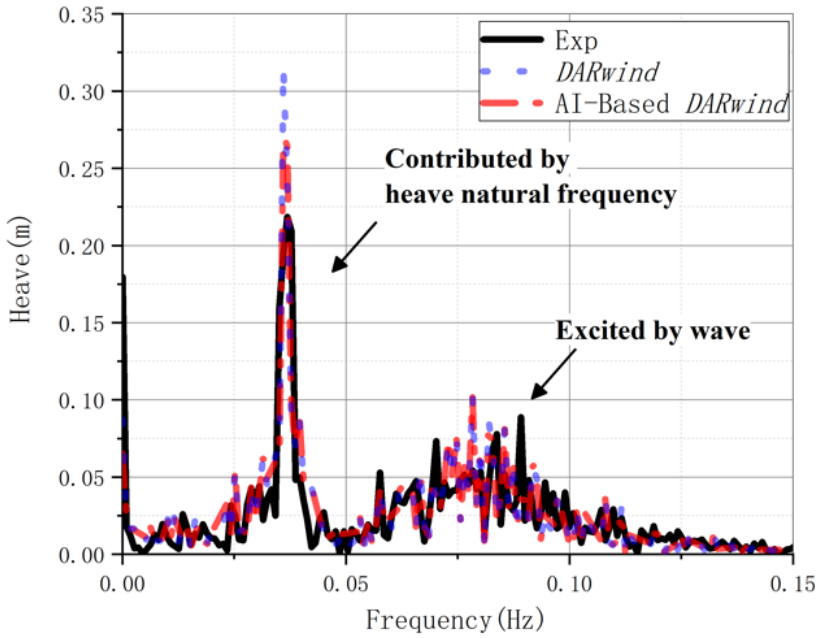

Figure 7.25 Frequency of heave in case 3b.

Figure 7.26 shows the change of heave motion in a random 60 explorations. The mooring system plays a vital role in maintaining the platform's stability in the waves. Since the boundary conditions of KDPs are determined initially based on empirical values, their characteristics can be further analysed according to the correlation during the training process. More accurate boundary conditions change with different environments and accelerate the convergence of the model.

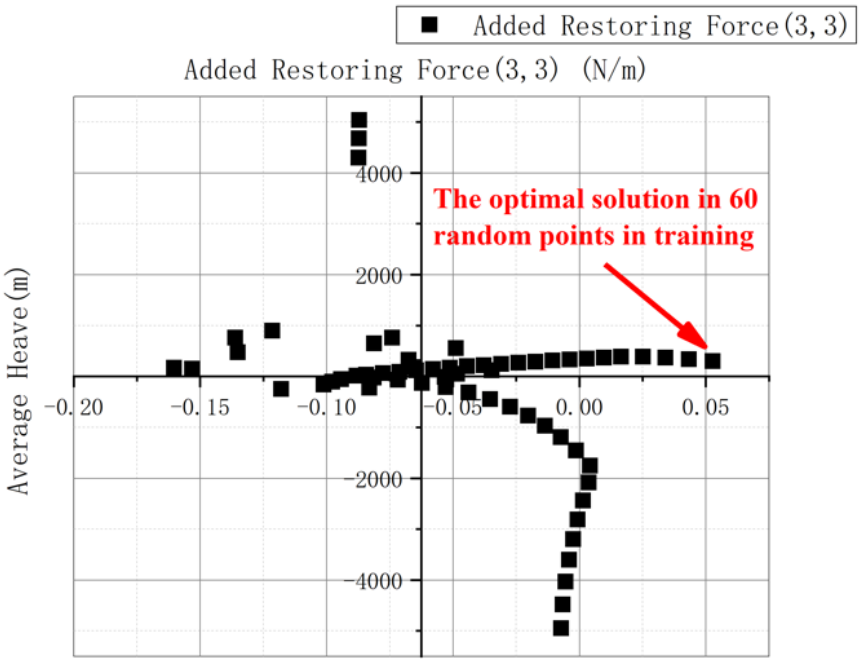

Figure 7.26 Heave and added restoring force (3,3) in case 3b.

7.4.3.2. Combined loads impact

In this section, The SADA method will be used to verify the optimization of the FOWTs system by the two sea loads, including wind and current cases (cases 4a, 4b) and wind and wave cases (cases 5a, 5b). The optimization effect of the six DOFs and the amplitude of the corresponding change are shown in **Figure 7.27**. Take case 4b as an example, through the optimization of the SADA method, the mean difference of surge is reduced from 3.7% to 0.8%. **Figure 7.28** shows the corresponding time history curve of surge. Although the mean difference of Heave has increased by 10%, it is still a relatively ideal change from the perspective of the change in the time history curve (**Figure 7.29**).

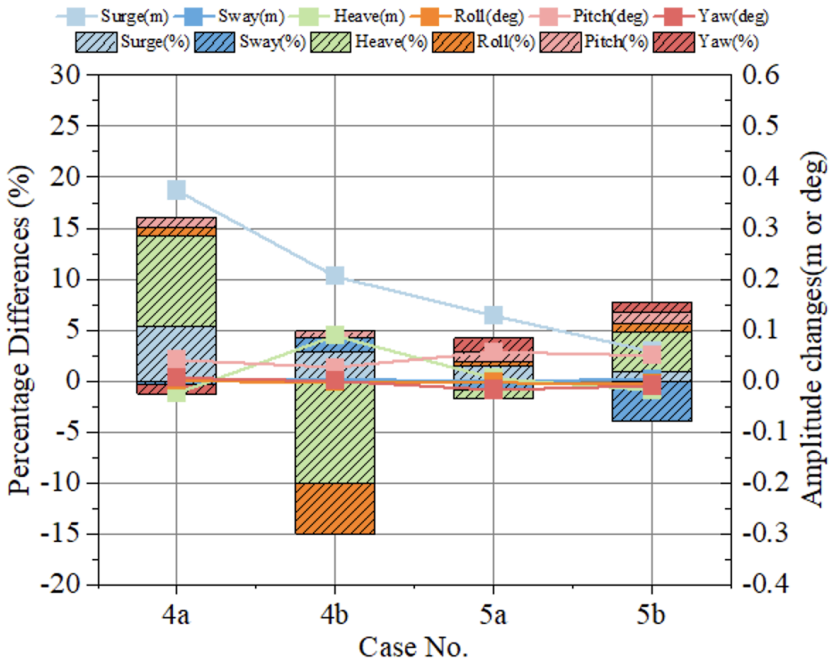

Figure 7.27 Percentage difference in two sea loads impact cases.

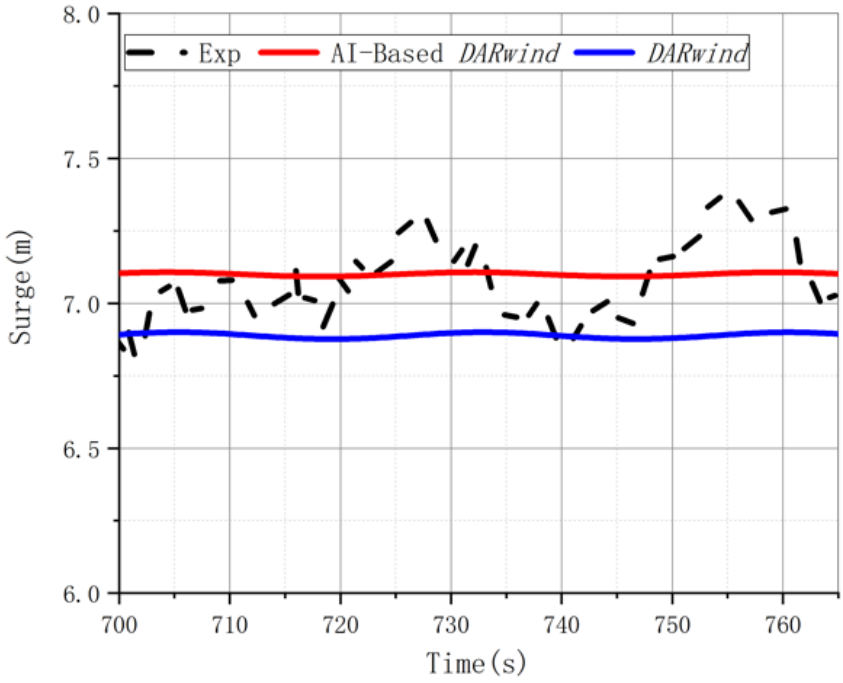

Figure 7.28 Time history of Surge in case 4b.

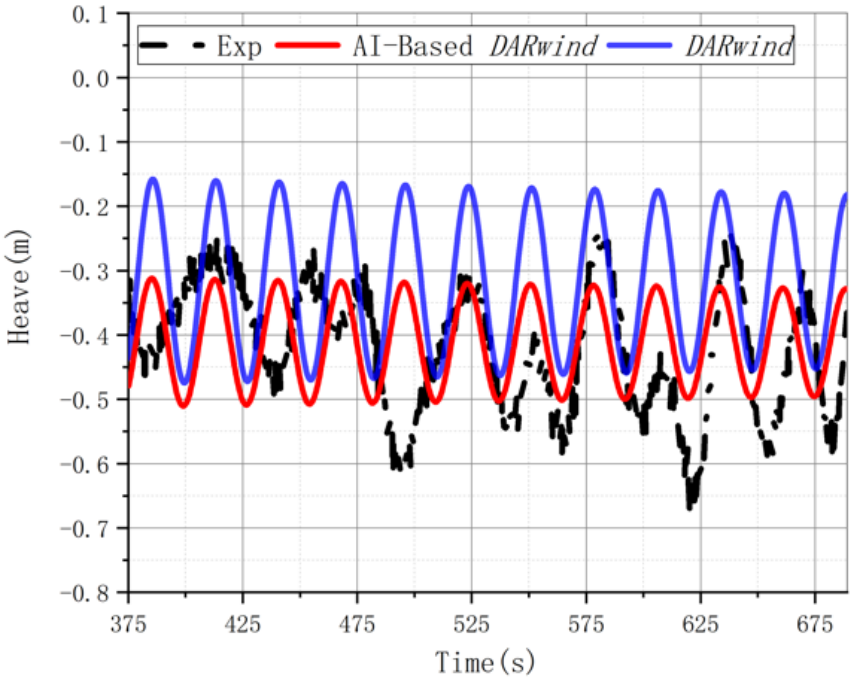

Figure 7.29 Time history of Heave in case 4b.

The coupling effect of wind and wave will inhibit some platform motion. Therefore, in the case of wind and waves, the motions of the platform have no apparent amplitude except for surge and pitch. For basin experiments and numerical simulations, the optimisation of a single impact is the most challenging. Because based on numerical assumptions, other parts will not affect the entire system apart from a single factor. In contrast, coupled conditions can better reflect the dynamic response of FOWTs in the actual sea state. In general, the SADA performed well in both single impact and two sea loads impact optimisation.

7.4.3.3. Wind/wave/current impact

This subsection will use SADA to optimise the dynamic response of FOWTs in a wind/wave/current sea environment (case 6 a, b and c). Case 6b will be adopted to train the Continuous model in SADA. The duration of the experimental data for Case 6b is 1 hour, and it will be divided into four segments, each containing 900-second target data for training. The axial thrust of the rotor is the most critical response that affects the motions of the FOWTs, especially on the pitch motion. For basin experiments, a more

matched thrust is the best choice to simulate the dynamic responses of the FOWTs better. However, if the rotor speed and wind speed in the experiment are fully used in the numerical simulation, the thrust force calculated by the numerical value will be different from the measured value due to the unmatching of low Re. Therefore, the rotor speed is also added to the adjustable KDPs better to simulate the axial thrust of FOWTs in this section.

Figure 7.30 shows the final difference and amplitude change of the four segments. The difference between surge and pitch increases slightly. Taking pitch as an example, the difference range of the four segments are all within 5 percent. This is a tolerable category in training. The actual amplitude changes are also within the range of 0.2deg.

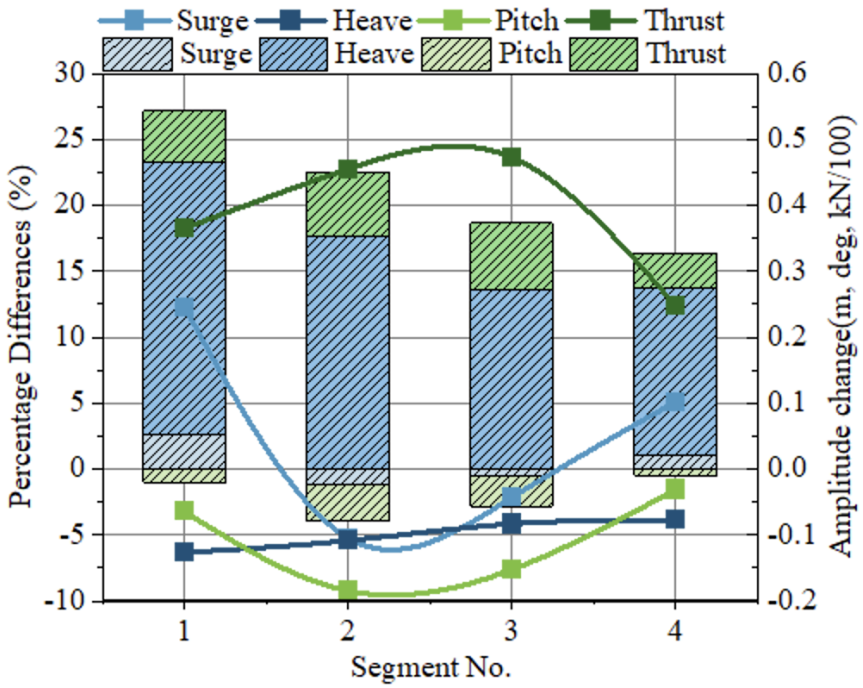

Figure 7.30 Percentage difference and amplitude change in case 6a.

The difference of Heave and Thrust has dropped significantly. Taking the third segment as an example, the average value of thrust has increased by 47.5kN. **Figure 7.31**-**Figure 7.33** show the time history of Surge, Heave and Thrust in first segments in case6b. The thrust increased by 36.5kN. They are all much closer to experimental value. In addition,

the mean value of each segment changed significantly from the initial KDPs through SADA. Taking the first segment as an example, the mean difference of surge is reduced by 2.6%. The time history curve of pitch and thrust optimised by SADA is closer to the experimental data.

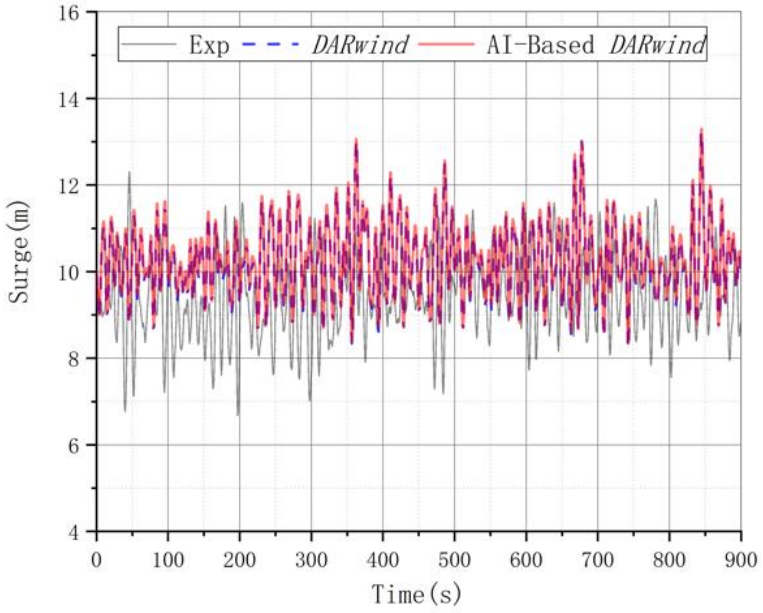

Figure 7.31 Time history of Surge in first segments in case 6b.

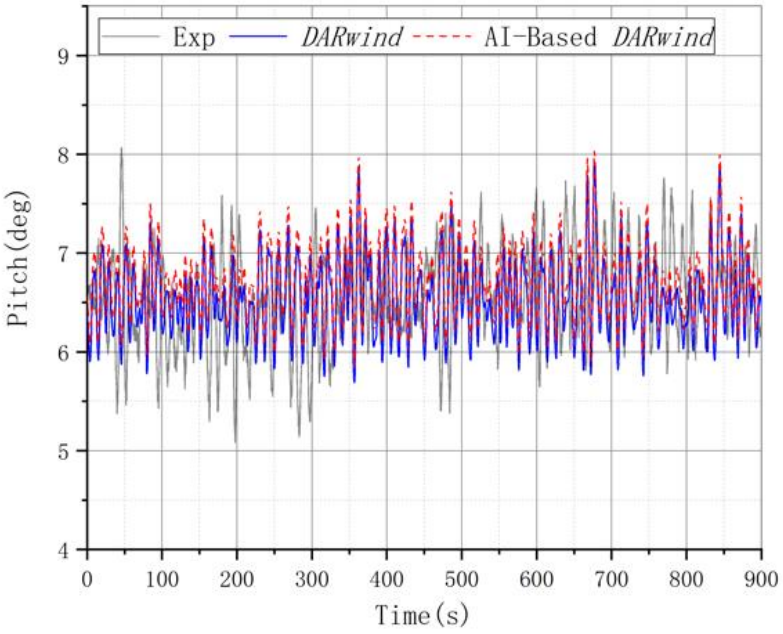

Figure 7.32 Time history of Pitch in first segments in case 6b.

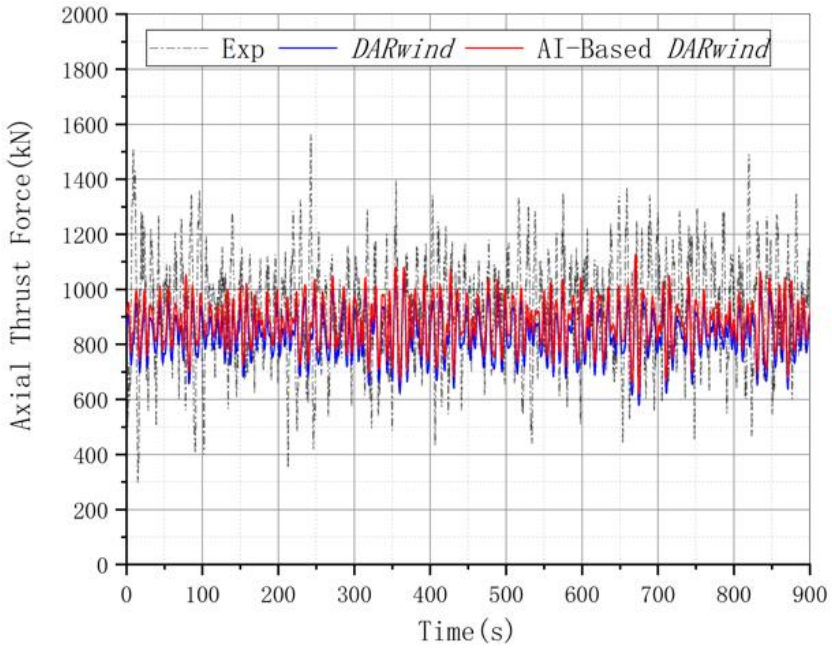

Figure 7.33 Time history of Thrust in first segments in case 6b.

It is difficult to see each segment's changes and training conditions only from the time history curve, so it is necessary to analyse the difference changes during the training, which first requires the classification of the random segment data. **Figure 7.34** shows the difference between surge and pitch in 500 iterations (Black lines represent trends). The four colour curves represent the difference changes of each segment in 500 iterations. It can be seen in the first 20 training sessions, the second group is randomly selected, and then the experimental means is automatically selected as the fourth group, and so on.

In the first and fourth segmented training (red and purple lines) of the surge, the difference gradually decreases, which is also the same as the final optimisation result in **Figure 7.34**. The pitch difference is stable within a range, although each segment slightly increases. Therefore, to better explore pitch performance in 500 iterations, its statistics are listed in **Table 7.15**.

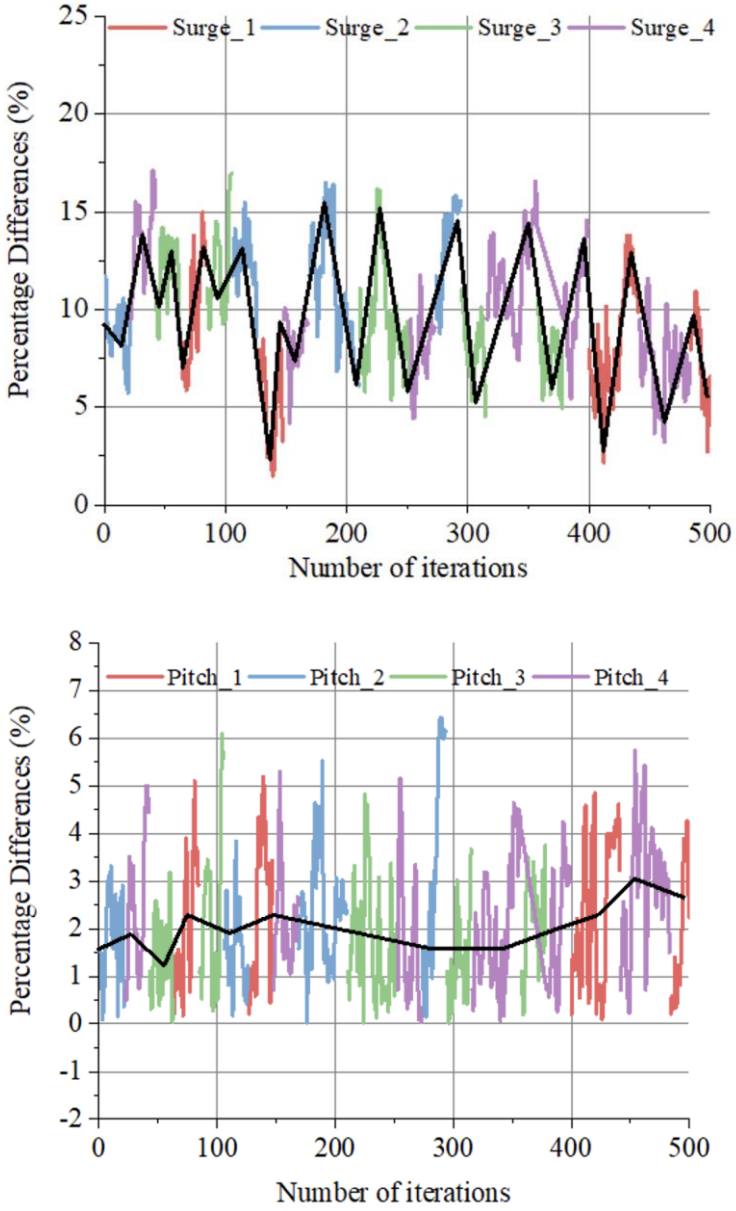

Figure 7.34 The difference of surge & pitch in 500 iterations.

Table 7.15 Statistical description for Pitch and KDPs

	Avg	Std	Min	Max
Pitch (deg)	6.49	0.174	6.19	6.90
Wind speed (m/s)	11.35	0.233	11	11.8
Rotor speed (m/s)	14.42	0.016	14.48	14.35
Current speed (m/s)	0.80	0.080	0.7	0.9

The average pitch values of the four segments are 6.54deg, 6.42deg, 6.45deg and 6.57deg, respectively. The mean value of 500 iterations of numerical simulation is close to the experimental value. The average value of other KDPs is also consistent with the initial setting of this working condition. The standard deviations of rotor speed and current speed, and the wet density of the mooring system are very close to zero. This is due to the boundary conditions of these three physical quantities, which are not allowed to change too much. From the maximum and minimum points of view, the wind speed, the rotation speed of the rotor, the axial stiffness of the mooring system and the current speed have been cut off after touching the boundary conditions. The wet weight of the mooring system is always within the boundary conditions.

The wind speed has a more significant impact on the aerodynamic load of FOWTs and affects the thrust. Because the blade pitch control is not considered in the experiment, the entire rotor is more sensitive to changes in wind speed. Therefore, it is a ubiquitous simulation technology to adjust the measured wind speed value in numerical simulation so that the axial thrust of the rotor matches the measured value as much as possible. Finally, SADA increased the wind speed to satisfy the thrust similarity as much as possible, although at the expense of some pitch accuracy. This also reflects the weighting effect on the main physical quantities in training. Therefore, it is essential for the users to understand the fundamental theories and practical technology of FOWTs.

7.4.3.4. Prediction by DDPG optimization

In this subsection, the deep neural network model trained in 6b will be applied to predict cases 6a and 6c. It is assumed that cases 6 a & b have not been carried out in the basin experiment, so there is no target value in the difference assessment, and the model is only used for weighting the feedback of each loop. There are ten iterations of forecast optimisation. **Figure 7.35** illustrates the mean difference and amplitude change of the four Experimental Physical Quantities (EPQs): surge, heave, pitch and thrust, in 6b and

6c. In 6b, the mean difference of Heave decreased by 35.4%. The most significant is the change in thrust, an increase of 51.8kN. The mean difference in 6c is all decreased.

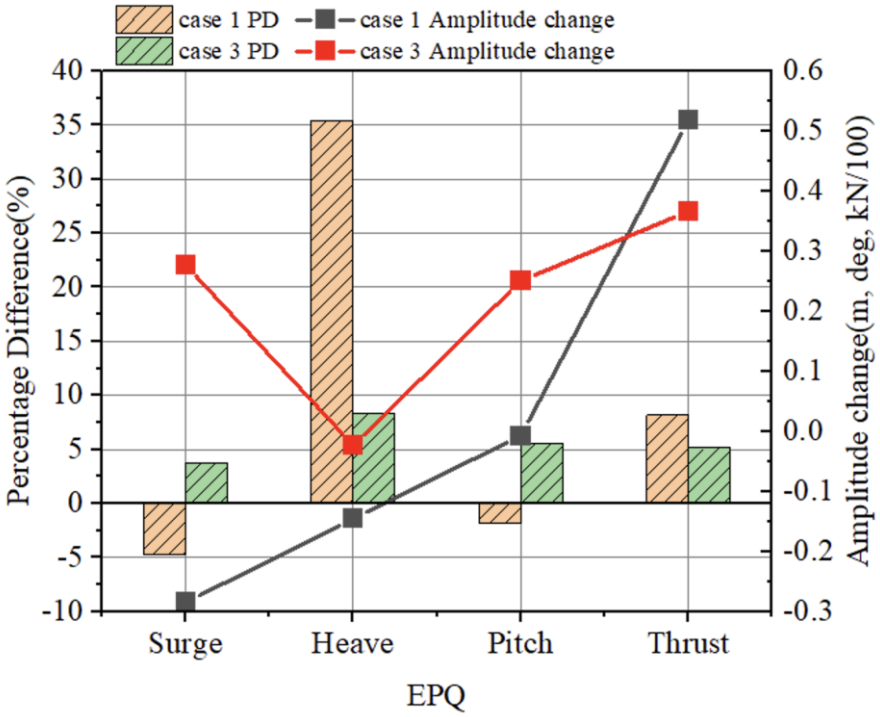

Figure 7.35 Percentage difference and amplitude change in 6a and 6c.

Through the forecast of SADA, the thrust in 6a can match better. As shown in **Figure 7.36-Figure 7.38**, the thrust change is quite significant, and although the difference of surge and pitch has decreased, it is still acceptable. The pitch curve shows that the mean difference has increased, but the trend of increase is closer to the experimental result. This also shows that the SADA method is not independent of the scope of traditional FOWTs numerical calculations. It must work together with a reliable dynamic response agent, such as *DARwind*, that allows SADA to make judgments and learn faster, more effectively, and more accurately. This is the character that the SADA method differs from traditional reinforcement learning methods.

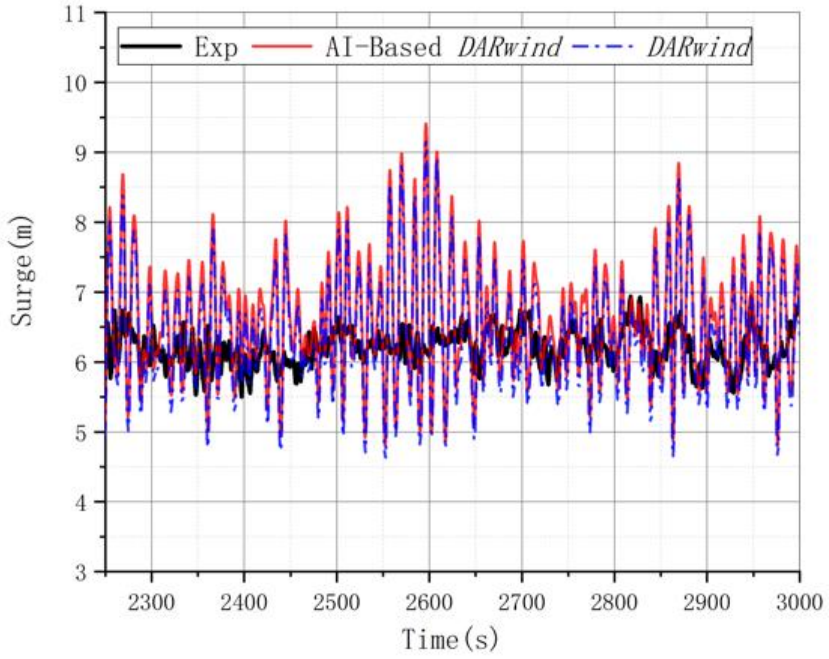

Figure 7.36 Time history of Surge in case 6a.

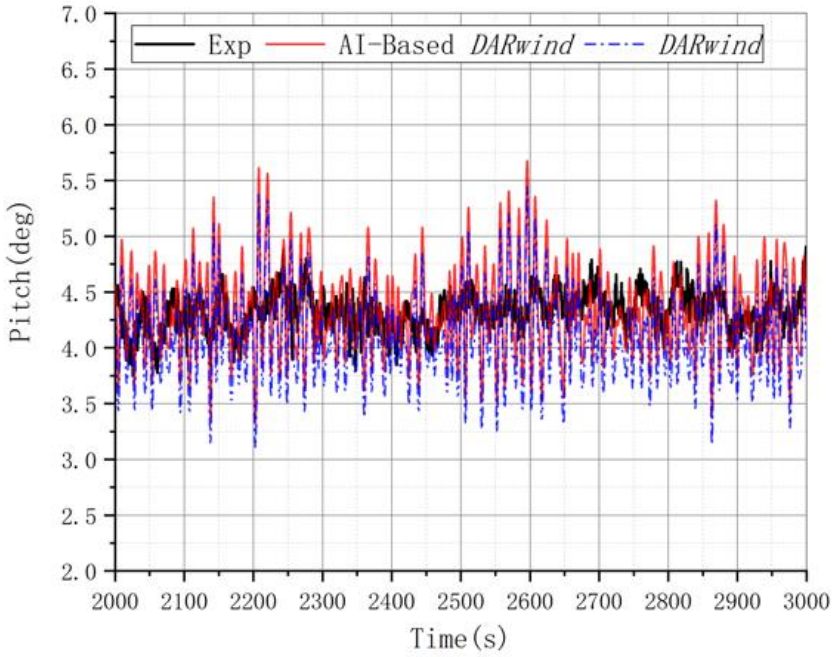

Figure 7.37 Time history of Pitch in case 6a.

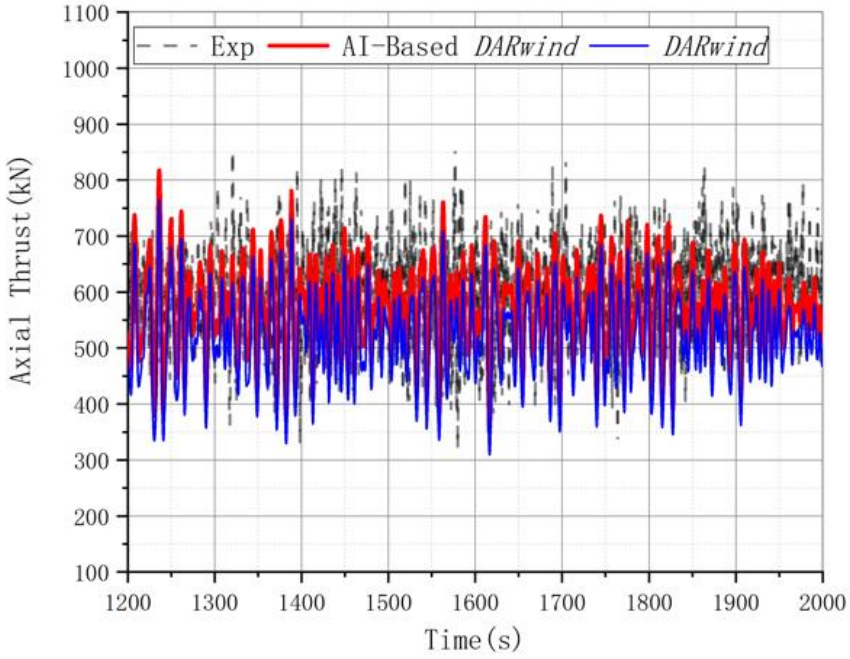

Figure 7.38 Time history of Thrust in case 6a.

For the result of 6c, the difference of the mean value of pitch and thrust is reduced through the optimised forecast of SADA from **Figure 7.39**-**Figure 7.41**.

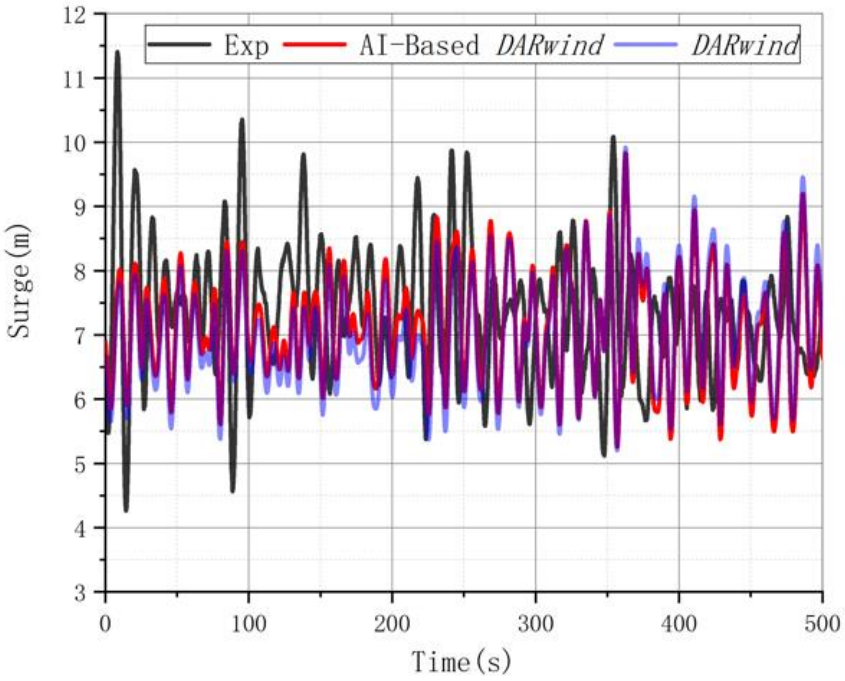

Figure 7.39 Time history of Surge t in case 6c.

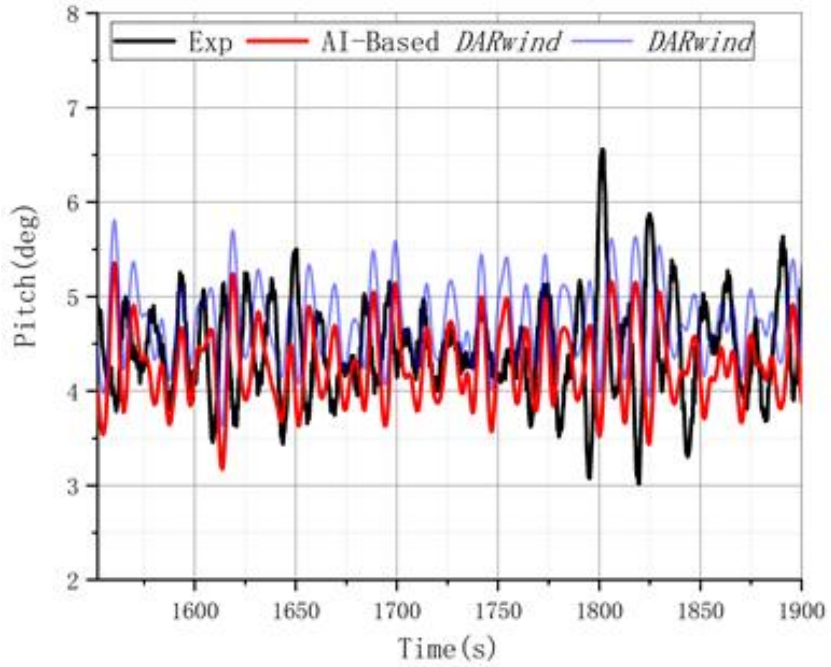

Figure 7.40 Time history of Pitch in case 6c.

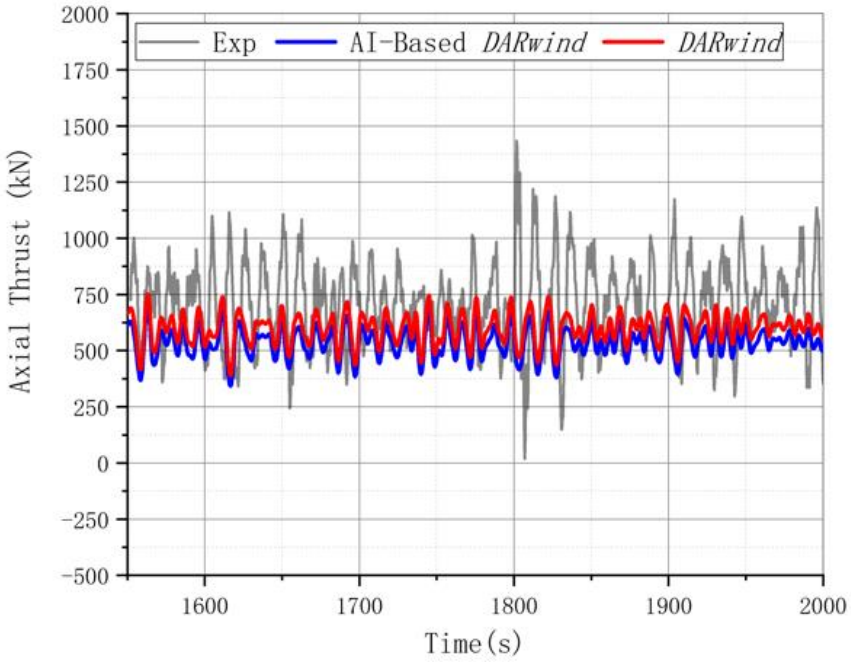

Figure 7.41 Time history of Thrust in case 6c.

In the numerical simulation, the KDPs corresponding to this result, especially the wind speed and the rotation speed of the rotor, did not reach the boundary conditions. According to the set difference weighting, SADA chooses equalisation optimisation instead of sacrificing the accuracy of some other physical quantities in 6a and 6b.

7.4.3.5. Blade and tower deformation prediction

Table 7.16 shows the *DARwind* and the AI-Based *DARwind* results of blade deformations and aerodynamic loads in segments 1. Aerodynamic loads represent the thrust and torque acting on the rotor. “BtDefx”, “BtDefy”, and “BtDefz” represent the three coordinate components of the blade tip deformation along with the blade follower coordinate system.

Table 7.16 Comparison of deformations and aerodynamic loads.

items		Avg	Std	Min	Max
BtDefx	AI-*Dar*	5.55	0.42	3.97	6.82
/m	*Dar*	5.97	0.47	4.19	7.41
BtDefy	AI-*Dar*	0.23	0.32	-0.31	0.78
/m	*Dar*	0.20	0.32	-0.33	0.76
BtDefz	AI-*Dar*	-0.42	0.06	-0.62	-0.21
/m	*Dar*	-0.50	0.08	-0.76	-0.25
Thrust	AI-*Dar*	881.07	83.88	621.75	1126.87
/kN	*Dar*	844.54	83.06	578.62	1081.70
Torque	AI-*Dar*	4374.14	860.16	2036.86	7200.79
/kN.m	*Dar*	3920.73	812.11	1721.87	6630.10

Time history comparison of blade tip deformation and the vibration is shown in **Figure 7.42**. The deformation of the blade tip in the flap-wise changes significantly, and it remains consistent edge-wise.

In the numerical simulation, the KDPs corresponding to this result, especially the wind speed and the rotation speed of the rotor, did not reach the boundary conditions. If the difference of the lowest thrust is pursued further, the difference of surge and pitch may change dramatically. According to the set difference weighting, SADA chooses equalisation optimisation instead of sacrificing the accuracy of some other physical quantities like case 1 and case 2.

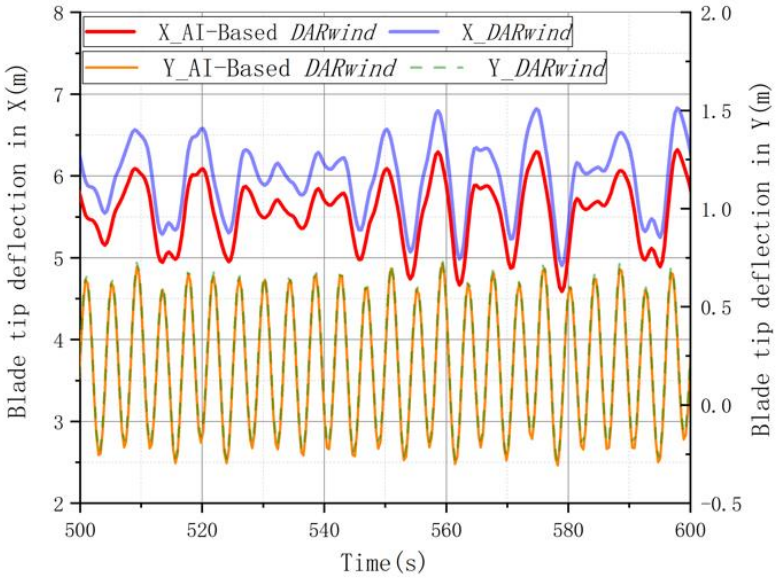

Figure 7.42 Time history of blade tip deformation in first segments.

Table 7.17 Comparison of deformations and aerodynamic loads in case 1.

items		Avg	Std	Min	Max
BtDefx	AI-*Dar*	3.93	0.41	2.38	5.34
/m	*Dar*	4.19	0.46	2.44	5.76
BtDefy	AI-*Dar*	0.09	0.32	-0.42	0.64
/m	*Dar*	0.07	0.32	-0.43	0.62
BtDefz	AI-*Dar*	-0.21	0.04	-0.38	-0.08
/m	*Dar*	-0.25	0.05	-0.46	-0.09
Thrust	AI-*Dar*	568.45	78.50	313.58	819.76
/kN	*Dar*	522.47	76.55	253.20	766.57
Torque	AI-*Dar*	1672.13	542.70	241.22	3722.78
/kN.m	*Dar*	1364.64	490.43	46.60	3228.32

Table 7.17 and **Table 7.18** show the statistical data of blade tip deformation and aerodynamic load for the two prediction cases. The deformation of the blade tip of case 1 and case 3 is reduced in flap-wise mean value, compared with the initial KDPs. The difference is that in case 1, the mean value of thrust increased, while in case 3, it decreased. **Figure 7.43** and **Figure 7.44** show the deformation of the blade tip in two directions.

Table 7.18 Comparison of deformations and aerodynamic loads in case 3

items		Avg	Std	Min	Max
BtDefx	AI-*Dar*	3.88	0.41	2.38	5.41
/m	*Dar*	4.34	0.47	2.92	5.90
BtDefy	AI-*Dar*	0.12	0.32	-0.37	0.62
/m	*Dar*	0.15	0.32	-0.35	0.68
BtDefz	AI-*Dar*	-0.21	0.04	-0.40	-0.08
/m	*Dar*	-0.26	0.06	-0.49	-0.12
Thrust	AI-*Dar*	542.37	68.21	318.65	770.24
/kN	*Dar*	589.05	74.61	348.99	820.60
Torque	AI-*Dar*	3556.10	706.78	1483.69	6068.72
/kN.m	*Dar*	3461.38	705.69	1429.56	5860.04

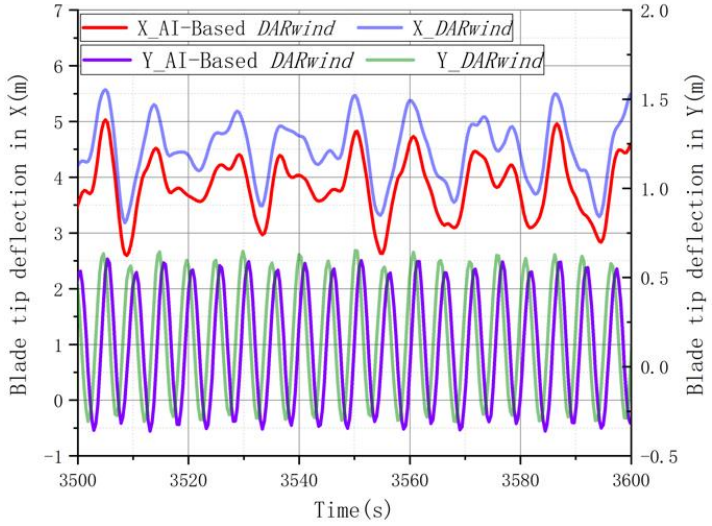

Figure 7.43 Time history of tower top deformation under case 1.

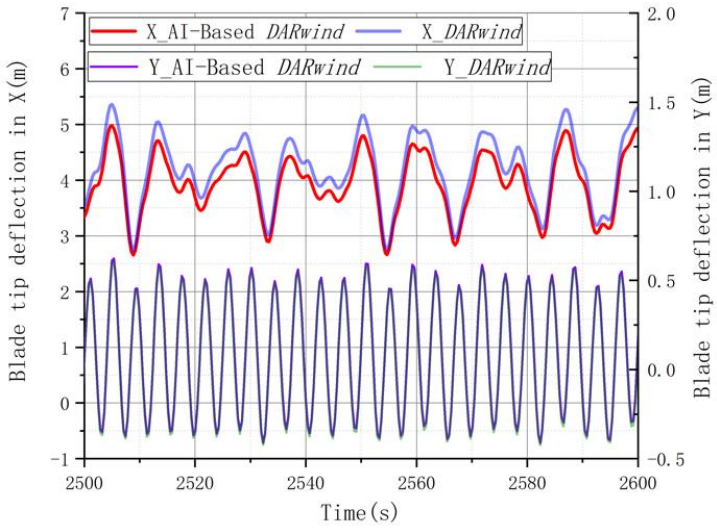

Figure 7.44 Time history of blade tip deformation under case 3.

7.5. Summary

This chapter uses the data from the basic experiment to study case studies of two AI technology applications in SADA, which are BP network and reinforcement learning optimisation. The BP network is weighted again on the *DARwind* result to be closer to the experimental result. However, supervised learning relies too much on the target data. Therefore, if specific physical quantities cannot be obtained from experiments, the BP neural network will not optimise the results of *DARwind*, such as the response on the blade. The framework based on KDPs, and reinforcement learning takes the SADA method one step further. The BF method verifies the application feasibility of the reinforcement learning framework. Randomly changing these KDPs through Gaussian distribution makes the SADA result closer to the target data. The physical quantities obtained in the basin experiment and other physical quantities cannot be measured.

Nevertheless, the BF method will no longer apply to those working conditions that have not been carried out in the basin experiment. The DDPG method based on the DRL framework has the advantages of combining the former methods. Not only can it fit the existing target data at the same time, but the trained deep neural network can also be used to predict the dynamic performance of FOWT under unknown working conditions.

Chapter 8. Application of SADA method with full-scale *Hywind* data

The purpose of this chapter is to demonstrate the engineering application of SADA on the full-scale measurement data of the *Hywind* FOWT, provided by Equinor and ORE Catapult. The intelligent SADA model is used to do comparisons and predictions, and the results show that the AI-trained numerical model can predict the motions of *Hywind* supporting floater with higher accuracy than original *DARwind* results. In addition, other physical quantities that cannot be obtained directly in full-scale measurement but are of great concern by industry can also be obtained from a more accurate perspective. Firstly, the dimension of the *Hywind* FOWT and the information about the wind farm where it is located, and the challenges in the actual measurement technology will be introduced. Secondly, more details of SADA applications are introduced, including data collection and KDPs selection. 11 cases are selected based on finding stationary environmental conditions relevant to doing simulations of the same events. Typical operational cases with a range in wind speed and wave height are provided. Finally, the application results of SADA will be displayed and divided into the training part and the forecast part.

8.1. *Hywind* Scotland

The basic information of the *Hywind* Scotland wind farm and the size of the *Hywind* is introduced in this section. There are five floating turbines and a wave buoy at the site. The full-scale measurement data is from FOWT HS4, and the FOWT is circled in red in **Figure 8.1**.

The turbine type for Hywind Scotland is SWT-66.0-154, supplied by Siemens Gamesa (Gamesa, 2021). Furthermore, the operational draft for the floater is 77.6 m. The main scantlings and a simple sketch of the supporting Spar-type floater can be found in **Table 8.1**. Delta-line arrangement is used for the mooring lines near the fairleads connecting to the Spar hull. The main characteristics of the mooring system are shown in **Table 8.2**. Nevertheless, for simplicity, delta-lines are not simulated in the analysis.

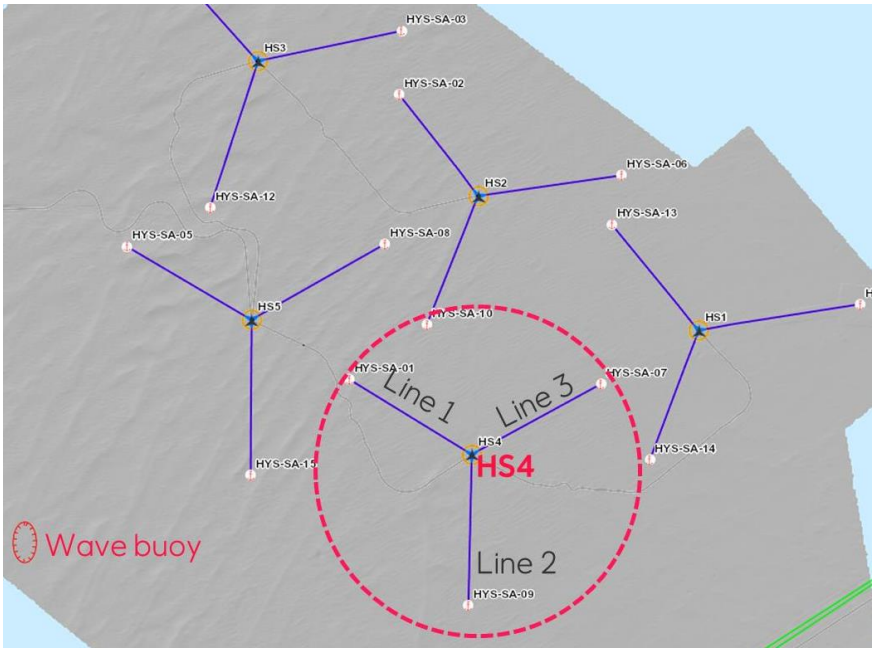

Figure 8.1 Location of HS4 in the Hywind Scotland.

Table 8.1 Main scantlings of the floater.

Z, bottom [m]	Z, top [m]	Length [m]	Diameter bottom [m]	Diameter top [m]
-77.6	-19.6	58	14.4	
-19.6	-4.6	15	14.4	9.45
-4.6	7.4	12	9.45	

Table 8.2 Characteristics of the mooring system.

Mooring system			
Property	Unit	Value	
Water depth	m	100	
Radius of the anchors	m	640	
Draft of mooring point	m	20.6	
Number of lines	-	3	
Connection point outside wall	m	0.8	
Segment name (from top to bottom)	-	Bridle	Main line
Segment Length	m	50	609.7
Nominal diameter	mm	132	147
Young's modulus	MPa	53941	43624
Segment Dry Mass per meter	kg/m	348.5	432.2
Weight in water per meter	kN/m	3.403	3.8707

8.2. Key technologies in full-scale measurement operation

The sea environment that *Hywind* FOWTs must bear is very complex. The motions of the floater and the mooring lines loads are critical and coupled with the dynamic responses of the entire FOWT system. A detailed description of the full-scale measurement key technologies and the collected data properties are introduced in this section.

8.2.1. Measurements of sea environmental loads

The definitions of sea environmental loads directions in full-scale measurement projects are different from those used in the basin experiments. The directions of wind, wave and ocean current are defined in this study according to the regulations used in the measurement facilities. In the numerical analysis of the SADA method, the directions of sea environmental loads are defined accordingly.

Wind direction is defined as the direction from which the wind is coming. Thus, “northerly wind” is coming from the North, and the wind direction is defined as 0 degrees, and “easterly wind” is coming from the East, and the wind direction is defined as 90 degrees. Wave direction is defined as the direction from which the waves are coming. Thus, “northerly waves” are coming from the North, and the wave direction is defined as 0 degrees, and “easterly waves” are coming from the East, and the wave direction is defined as 90 degrees.

Current direction is defined as the direction in which the current is going. Thus, “northerly current” is coming from the South, and the current direction is defined as 0 degrees, and “easterly current” is coming from the West towards the East, and the current direction is defined as 90 degrees. All coordinates’ definitions are shown in **Figure 8.2**.

The wind speed is the undisturbed wind speed measured by the turbine’s anemometer located at 99m above sea level. In this Chapter, the only steady wind is considered. The wave buoy measures the wave and current conditions.

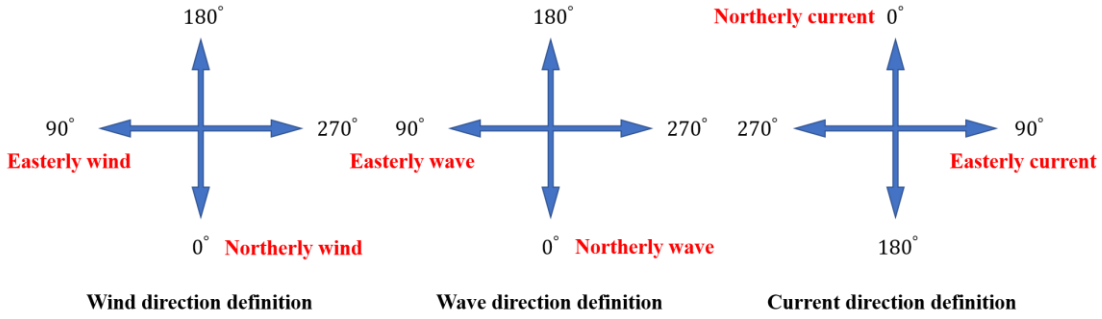

Figure 8.2 Definitions of environmental loads coordinates.

8.2.2. Measurements of dynamic response data

Floater motion is an essential part of monitoring work for the dynamic response of the entire FOWT system in different sea conditions. In this project, the measurement of the 5DOF motions of the floater will be introduced (while heave motion was not included in the full-scale data). The motion reference unit (MRU) in the nacelle is rotating along with the nacelle. These are Euler Angles in the ZYX convention. The roll-axis is pointing towards the rotor plane (and blades). With 0 as Yaw-Direction (rotor oriented towards North), the coordinate system of the nacelle and tower MRUs are coinciding in **Figure 8.3**.

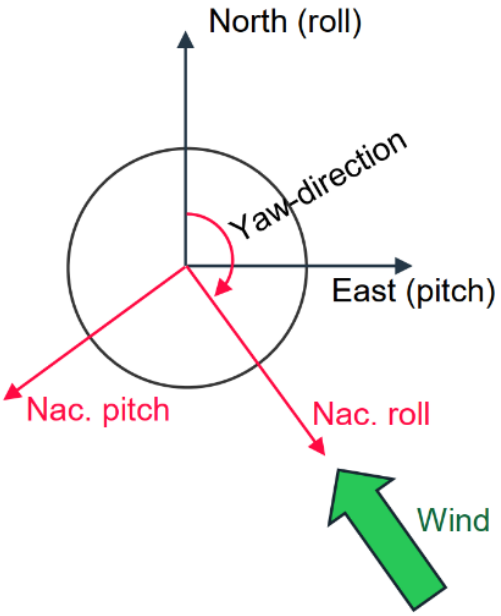

Figure 8.3 Coordinate system convention of the motion measurements.

Floater surge and sway GPS measurements are listed in **Table 8.3**. It is worth mentioning that since the GPS is located at the floater level, some of the translational motions may be due to rotations (roll/pitch motions).

Table 8.3 Tower roll & pitch and floater surge & sway measurements.

Tagname	Measurement	Unit	Location
HYS-HS4-MRUTower-RollAngle	Roll orientation	radian	Tower MRU is located at +16.9m rel. sea level
HYS-HS4-MRUTower-PitchAngle	Pitch orientation	radian	
HYS-HS4-MRUTower-YawAngle	Yaw orientation[1]	radian	
HYS-HS4-DGPS-LatitudeDriftOff	North-south motion	metre	GPS antenna is located at elevation +15.3m rel. sea level
HYS-HS4-DGPS-LongitudeDriftOff	East-west motion	metre	

8.2.3. Challenges of numerical validation with Full-scale data

The technology challenges of the FOWTs in the experiment can be improved to a large extent in the actual measurement verification. For example, the scaling problem between R_e and F_r, mass distribution, yaw and pitch control, etc (Chen *et al.*, 2020b). Nevertheless, it is not a simple matter to directly obtain the dynamic response of a full-scale FOWT through numerical simulations, especially in a real-time simulation. This subsection will introduce these challenges encountered in the numerical simulations in detail.

For full-scale measurement, its complexity is reflected in the uncertainty of the measurement data and a challenge to existing theories. The dynamic responses prediction of FOWTs involves multiple disciplines, including aerodynamics, hydrodynamics, structural mechanics, multi-body dynamics and kinematics, mooring dynamics, etc. Many of the functions and formulas involved in these theories are determined based on assumptions and empirical parameter values. However, these empirical parameter values

may not be proper for FOWTs due to their high nonlinear coupling effect. For example, the empirical aerodynamic parameter values, such as the wind resistance coefficient of blades, can bring potential problems to the later numerical simulation of the entire FOWTs system. Many other critical environmental parameters, such as wave parameters in hydrodynamics and mooring line damping values etc. are challenging to be issued unique values during the analysis.

The measured data used in this chapter is mainly based on the 5DOF motions of the floater. However, there are no published specific structural parameters of the SWT-6.0-154 wind turbine. Nevertheless, the goal of this chapter is to verify the feasibility of the AI-based SADA method in the actual measurement and forecasting, so there are several assumptions made for using full-scale measurement data in this chapter:

- The wind, wave and current are assumed to be in the same direction in the simulation.
- Only steady wind and ocean current acting on the floating body is considered.
- The parameters of the 5MW Hywind wind turbine and tower in OC3 (Jonkman and Musial, 2010) are used to replace the wind turbine of HS4.
- The delta-connection of mooring lines is simplified, directly connected to the hull, and an additional yaw stiffness is added.

8.3. Data collection and SADA analysis

This section mainly introduces the data collection in SADA. The measured data will train the action value network in DDPG in reinforcement learning by defining rewards in difference analysis.

8.3.1. Case setting

The setting of the working conditions has unique characteristics, which is to obtain enough sample data to train the deep neural network in SADA. There are 11 intervals with varying environmental conditions shared. **Table 8.4** and **Table 8.5** show that 8 of them are used for training, and the remaining three are used as forecasts, respectively. All-time references are given in Universal Time Coordinated (UTC) format. 0.5h of data is provided for 30 minutes. The 'Date' column represents the midpoint in the intervals.

Table 8.4 Training Cases in full-scale studies.

No.	Date	H_s	T_p	V_w	V_c
		(m)	(s)	(m/s)	(m/s)
1	2018-01-06T07.45.00+00.00_2018-01-06T08.15.00+00.00	2.2	10.6	8.5	0.24
2	2018-01-09T09.25.00+00.00_2018-01-09T09.55.00+00.00	4.2	8.7	20.4	0.32
3	2018-01-14T15.25.00+00.00_2018-01-14T15.55.00+00.00	2.1	10.5	5.2	0.32
4	2018-01-24T11.25.00+00.00_2018-01-24T11.55.00+00.00	2.5	7.3	14.1	0.17
5	2018-02-24T04.35.00+00.00_2018-02-24T05.05.00+00.00	4.4	10.9	13.7	0.21
6	2018-04-14T00.25.00+00.00_2018-04-14T00.55.00+00.00	2.3	6.5	15.6	0.12
7	2018-05-02T03.45.00+00.00_2018-05-02T04.15.00+00.00	3.9	8.3	30	0.27
8	2018-07-29T03.45.00+00.00_2018-07-29T04.15.00+00.00	3.9	8.3	30.3	0.3

Table 8.5 Prediction Cases in full-scale studies.

No.	Date	H_s	T_p	V_w	V_c
		(m)	(s)	(m/s)	(m/s)
9	2018-01-24T11.15.00+00.00_2018-01-24T11.45.00+00.00	2.1	6.5	15.5	0.27
10	2018-02-13T01.05.00+00.00_2018-02-13T01.35.00+00.00	3.2	9.3	13.9	0.09
11	2018-03-26T23.15.00+00.00_2018-03-26T23.45.00+00.00	3	7.9	16.6	0.33

8.3.2. KDP selection

In this Chapter, the selected KDPs are divided into two groups. The first group contains 51 selected KDPs, and the second group contains 108 selected KDPs. In addition to the most apparent quantitative difference between the second and first groups (adding some unknown dynamic structural parameters), some KDPs are also divided. For example, In the numerical simulation, the tower is divided into 11 stations and solved by the modal

superposition method. Each station has its own drag coefficient. However, the drag coefficient of the tower in aerodynamic in group 1 only be the same initial value (0.5) for each tower station. However, in the second group, they are divided into 11 KDPs, which all belong to the same tower, but they are arranged in different stations. Due to the symmetry, only the diagonal parameters are considered in hydrodynamics for the added viscous damping coefficient matrix and the restoring force coefficient matrix. As for the vibration mode, polynomial coefficients of the tower and blades are considered independent in the two sets of selected KDPs. Since many structural parameters are from similar models, the specific parameters are specially set for the corresponding wind turbine and tower structure to demonstrate SADA's optimisation effect better. **Table 8.6** and **Table 8.7** show the selected KDPs in group 1 and group 2, respectively.

Table 8.6 Selected basic KDPs in group 1.

No.	**KDPs**	
1	Aero	Wind speed
2		*Glauert* correction
3		Tower drag
4	Hydro	Current speed
5-10		Added linear viscous damping matrix
11-16		Added quadratic viscous damping matrix
17-22		Added linear restoring matrix
23-28		Added linear mass matrix
29		Added static force (3, 3)
30-32	Mooring	Wet density
33-35		Axial stiffness
36-40	Kinematics And Structural	Polynomial Flap 1st vibration modes
41-45		Polynomial Flap 2nd vibration modes
46-50		Polynomial Edge 1st vibration modes
51	Servo	Generator torque constant

Table 8.7 Selected additional KDPs in group 2.

No.	KDPs	
1	Aero	Wind speed
2		*Glauert* correction
3~13		Tower drag
14		Cone Angle of blade
15	Hydro	Current speed
16		Added static force
17-22		Added linear viscous damping matrix
23-28		Added quadratic viscous damping matrix
29-34		Added linear restoring matrix
35-40		Added linear mass matrix
41		Significant wave height
42		Peak period
43		Shape factor
44		water depth
45-47	Mooring	Wet density
48-50		Axial stiffness
51-53		Length
54-56		Diameter
57	Kinematics And Structural	Hub mass
58		Shaft angle of rotor
59		Nacelle mass
60		Floater mass
61		Floater volume
62-64		Hub refence point.
65-67		Hub dynamic refence point
68-70		Hub inertia about rotor axis.
71-73		Generator inertia about HSS
74-76		Nacelle refence point
77-79		Nacelle dynamic refence point
80-82		Nacelle inertia
83-85		Floater refence point
86-88		Center of Floater mass
89-91		Floater inertia
92-96		Polynomial Flap 1^{st} vibration modes
97-101		Polynomial Flap 2^{nd} vibration modes
102-106		Polynomial Edge 1^{st} vibration modes
107	Servo	Generator torque constant
108		Gearbox ratio

8.4. Application of SADA for Hywind FOWT

This section will discuss the SADA analysis results and the feasibility of the SADA method from 5DOF (except heave) of the floater and other physical quantities, including thrust, tower top and blade tip deformation, etc.

8.4.1. Natural period

Before starting numerical calculations, the numerical model is built in *DARwind* based on the dynamic properties of the complete HS4 system provided in **Table 8.8**. In addition, the natural frequency will be calibrated between *DARwind* and provided results in **Table 8.9**.

Table 8.8 Dynamic properties of the complete HS4 structure.

Property	**Unit**	**Value**		
Draft	m	77.6		
Displacement	tons	11754		
Dry mass	tons	11483		
Mooring tension	tonf	270.9		
		X	Y	Z
COG	m	-0.14	0	-50.03
COB	m	0	0	-42.04

Table 8.9 Comparison of numerical model with measured data.

	SADA			Measured Data
DOF	**Damping ratio**	**Natural angular frequency**	**Natural period**	**Eigen period**
	（-）	**(rad/s)**	**(s)**	**(s)**
Surge	0.0445	0.0654	96.1	96
Sway	0.0441	0.0654	96.1	96
Heave	0.0125	0.2436	25.8	25.8
Roll	0.0223	0.1864	33.7	33.7
Pitch	0.0233	0.1864	33.7	33.7
Yaw	0.0425	0.4828	13.0	13.0

8.4.2. Motion optimization

The surge motion of the floater has an apparent motion amplitude. The research on surge motion is helpful to understand the motion characteristics of the floater. Therefore, in this section, the surge motion of the floater and the 5DOF motions (except heave) will be optimised by the SADA method.

8.4.2.1. Surge motion optimization

This part will first show the surge motion of the floating Floater optimised by the SADA method. The optimisation of a single case can effectively reduce the difference of surge, mainly when the SADA contains 108 KDPs. **Table 8.10** and **Figure 8.4** show the optimisation results of 7 cases, which compare the differences between *DARwind* (the initial numerical simulation without any AI-based technology) and SADA.

Table 8.10 Comparison of numerical simulations and measured data.

Training	Amplitude of Surge	*DARwind*	AI-based SADA	
	Measured（m）	Initial (%)	51 KDPs (%)	108 KDPs (%)
Case 1	6.997	19.389	14.586	3.948
Case 2	9.751	55.141	51.545	11.399
Case 3	7.948	69.342	65.275	48.097
Case 4	3.327	68.973	50.198	42.342
Case 5	9.422	39.352	35.037	15.057
Case 6	3.850	21.873	13.127	11.879
Case 7	8.972	54.548	50.183	0.313

The orange colour in **Figure 8.4** represents the relative difference between the *DARwind* numerical results and the actual measurement results that do not include AI technology. Corresponding green and purple curves are the relative differences between the numerical results of *DARwind,* including AI technology and the measured data. It is not difficult to see from **Figure 8.4** that SADA with 108 KDPs has a significant optimisation effect for each working condition than that of 51 KDPs, and its difference has been reduced. Especially in case1 and case7. In contrast, SADA with 51 KDPs can only achieve a

relatively small difference reduction on the original basis. So, it is indicated that more reasonable selected KDPs in the SADA method can lead to a better AI-trained analysis tool. In addition, the direction of the waves and wind are 17 and 11 degrees under case 1, respectively, but the mean difference of the initial surge under this case is only 19%, which maintains a satisfactory degree of consistency in the same direction as the default wind and waves. In particular. the mean difference of surge also dropped significantly in case 2, case 5 and case 7. To optimise a single motion, SADA can effectively reduce the difference between numerical simulation and measured data, especially the model containing 108 KDPs.

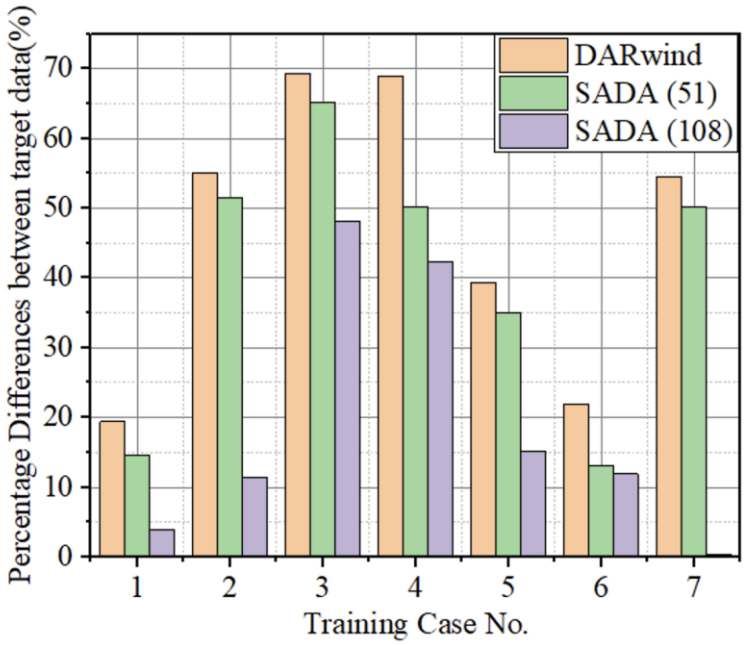

Figure 8.4 Comparison with different KDPs.

Figure 8.5 and **Figure 8.6** show the time history of the surge in case 1 and case 6. The green line tends to approach the measured data (gray line). For every single case, using SADA for training can obtain a more accurate mean performance of surge than that of *DARwind*.

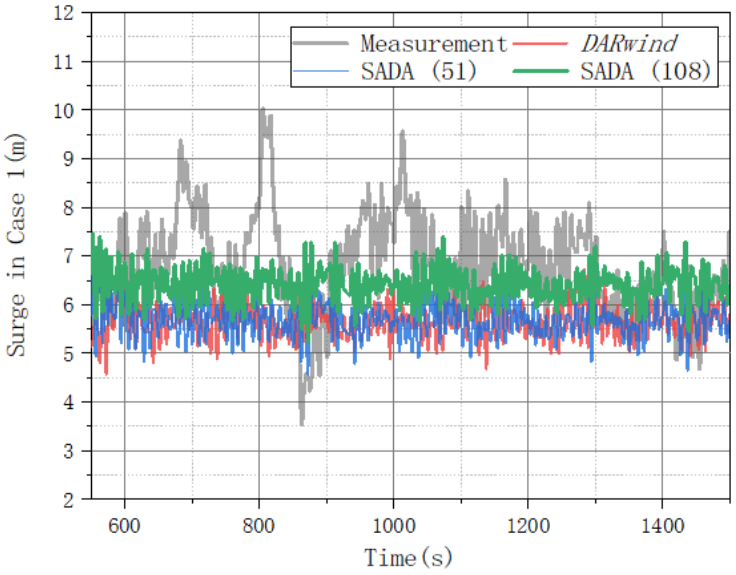

Figure 8.5 Time history of the Surge in case 1.

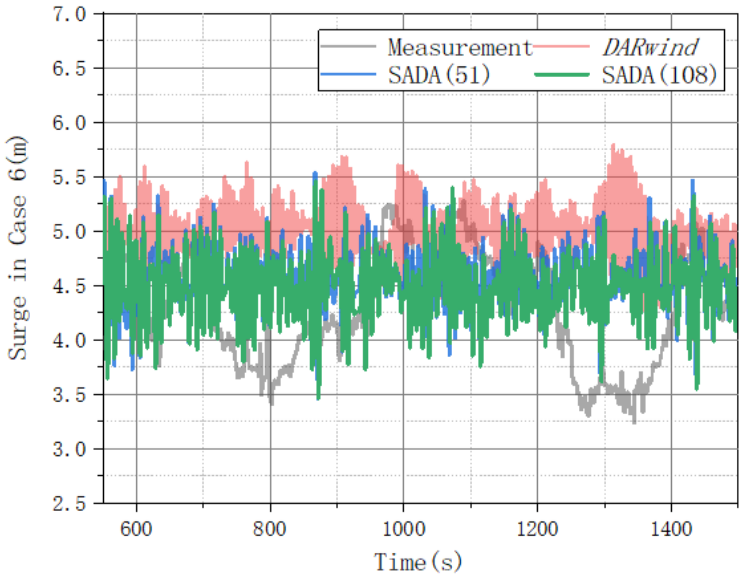

Figure 8.6 Time history of the Surge in case 6.

Then, the data of 7 cases will be used to train the deep neural network to obtain a model that can predict unknown operating conditions. **Table 8.11** and **Figure 8.7** show the comparison of the *DARwind* and SADA in prediction. The prediction data uses the trained deep neural network model to assess the states without any training and target data. By optimising SADA, the difference between the three cases has been reduced.

Table 8.11 Comparison differences of simulation with measured data.

Prediction	Amplitude of Surge	*DARwind*	AI-based SADA	
	Measured（m）	Initial (%)	51 KDPs (%)	108 KDPs (%)
Case 9	3.166	64.338	39.441	13.897
Case 10	8.854	36.497	30.881	11.119
Case 11	11.087	54.784	52.581	20.680

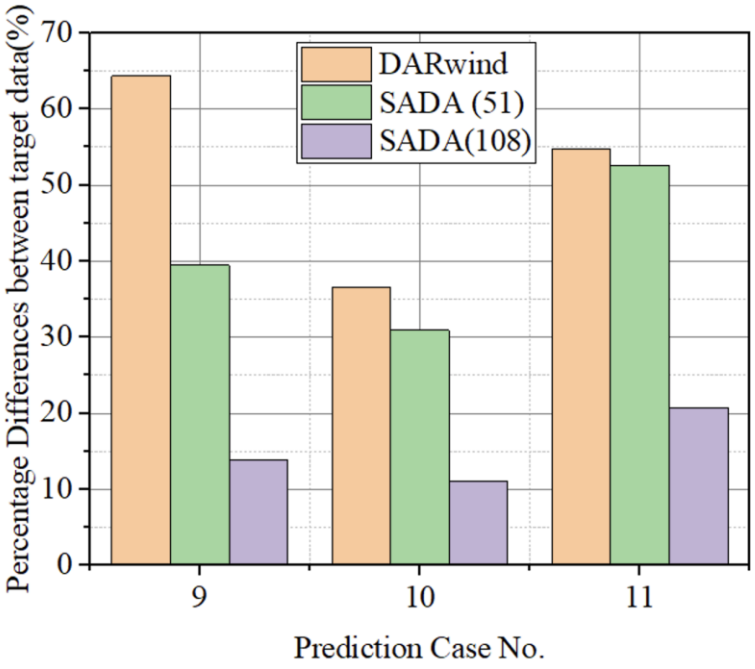

Figure 8.7 Mean difference between *DARwind* and SADA.

The results show that 108 SADAs can effectively reduce the average surge difference in the forecast's three cases, especially in case 9 and case 10. **Figure 8.8** and **Figure 8.9** compare the time history curves of the surge under these two cases. It is also worth mentioning that the average difference of SADA with 51 KDPs is lower than that of *DARwind*, but it is only reflected in the average. The changing trend of the entire time history curve is still consistent with those of *DARwind*.

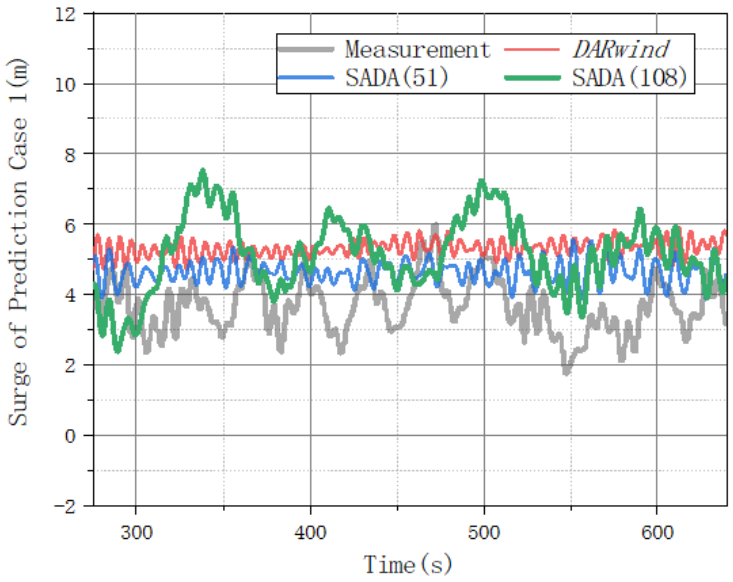

Figure 8.8 Time history of the Surge in case 9.

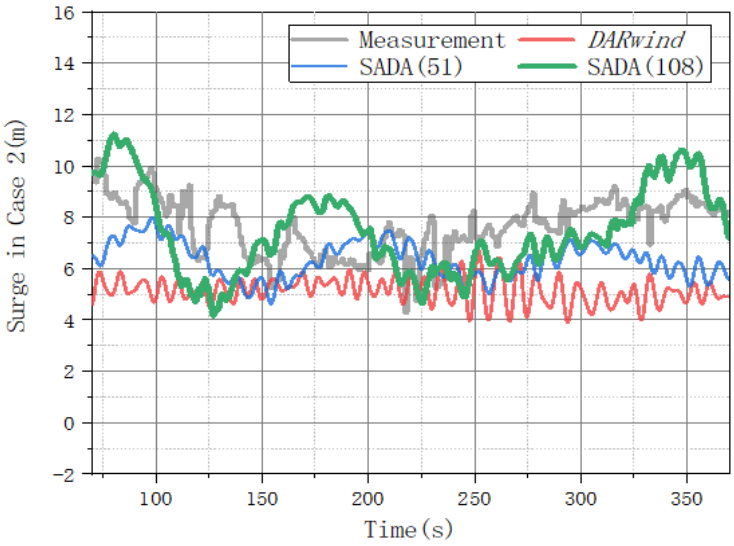

Figure 8.9 Time history of the Surge in case 10.

8.4.2.2. 5DOF motions optimization

In this part, SADA will use the average value of the five motions provided by the measured data of the floater motions for AI training. In this optimisation analysis, only the SADA with 108 KDPs is considered.

Figure 8.10 shows the training results of 8 cases. The ordinate on the left shows the difference changes of the five motions corresponding to the stacked graph, and the dot-line graph on the right ordinate is the corresponding amplitude change of each motion under 8 cases.

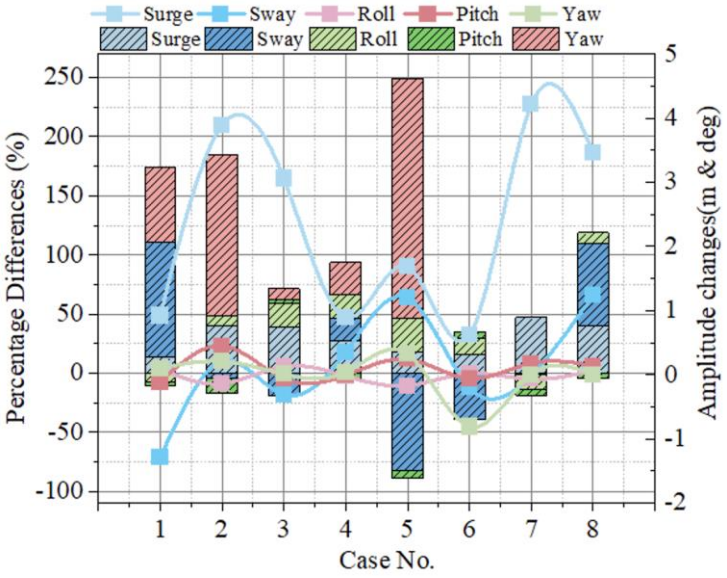

Figure 8.10 Comparison of the percentage differences in 5DOF.

Among the five motions, the difference reductions of surge and sway are of most significance, and the changes in amplitude are also relatively noticeable. Taking case 1 as an example, the differences of surge and sway have been reduced by nearly 14% and 98%, respectively, while the amplitudes of the corresponding mean values have changed by 1m and 1.29m, respectively. The yaw motion difference reduced significantly, but the amplitude changes are maintained between 0.1-0.81deg.

Figure 8.11-**Figure 8.13** show the comparison chart of the time history curves of the surge, sway and yaw in case 1. It can be pointed out that the optimisation results of SADA and the measured data are in good agreement with the mean value.

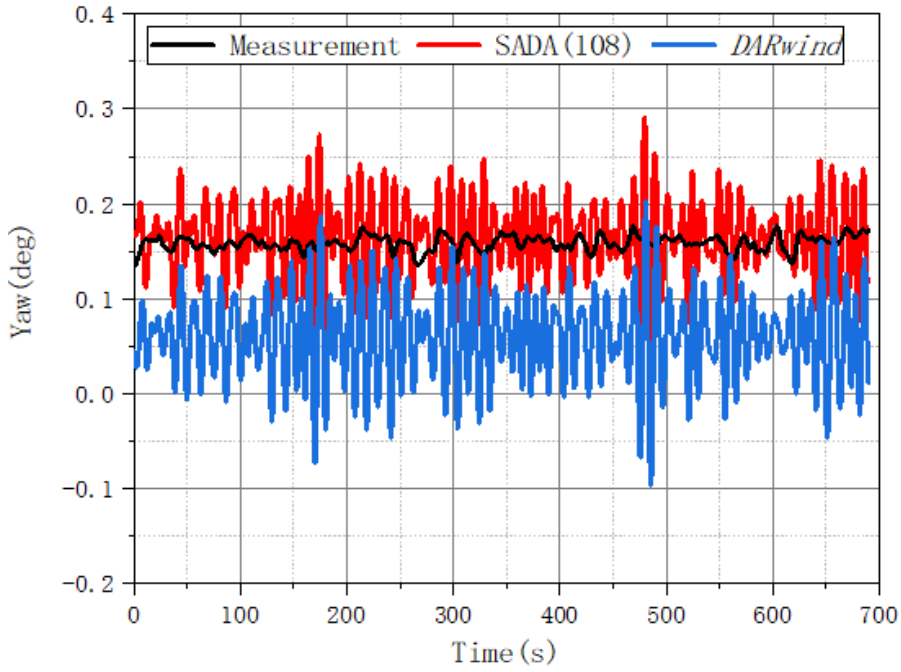

Figure 8.11 Time history of the Yaw under case 1.

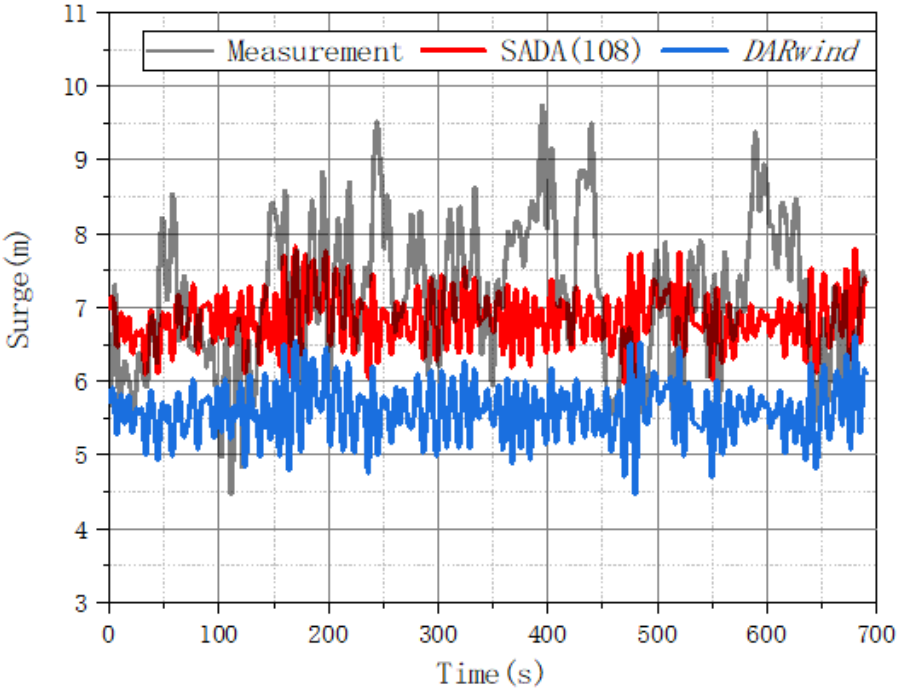

Figure 8.12 Time history of the Surge under case 1.

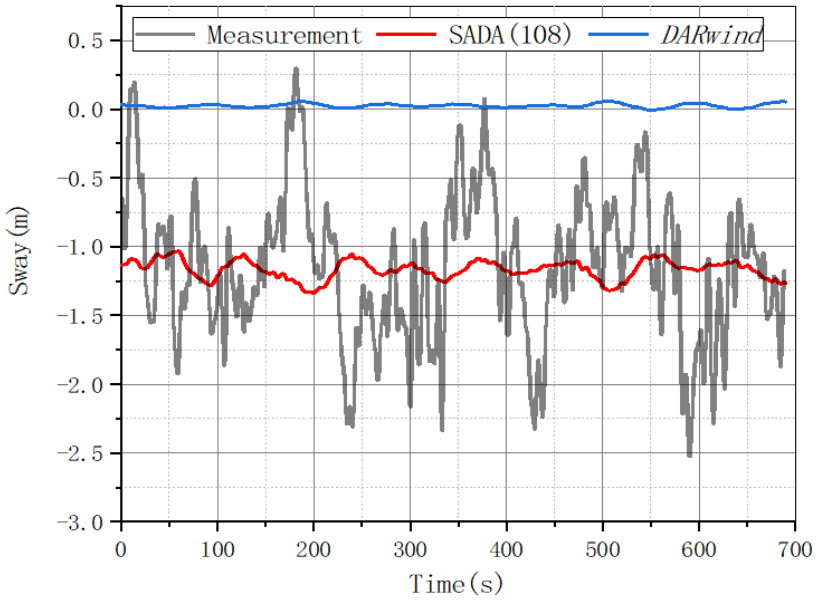

Figure 8.13 Time history of the Sway under case 1.

Figure 8.14 shows the results of the forecasting cases. In the 5DOF forecasting, the optimisation of the surge is still of the most significance. Taking case 1 as an example, the difference of surge and pitch is reduced by 30% and 172%, and the corresponding amplitude concept is 1m and 0.37deg, respectively.

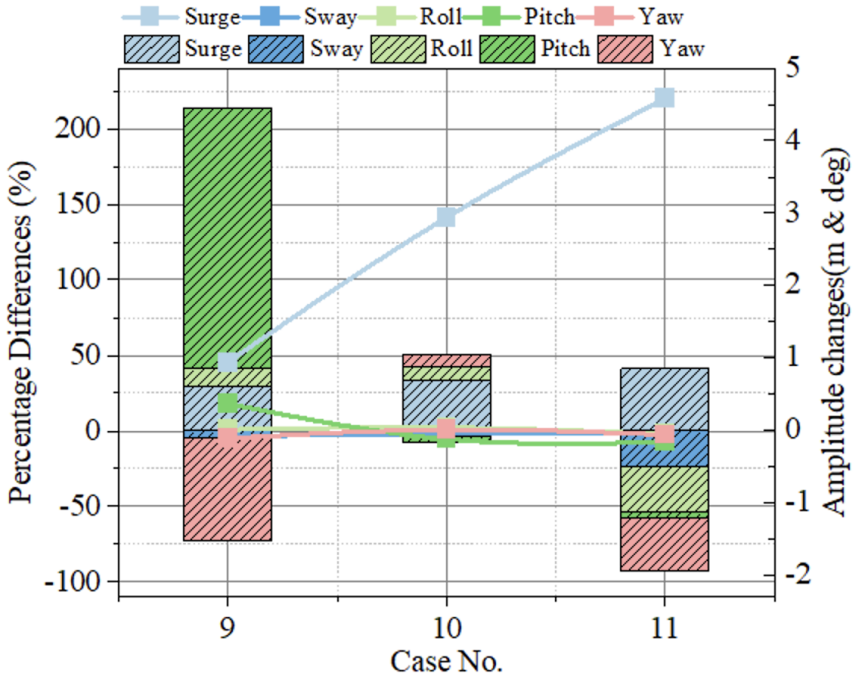

Figure 8.14 Mean difference between *DARwind* and SADA.

Figure 8.15 and **Figure 8.16** show the time history curve of roll and surge.

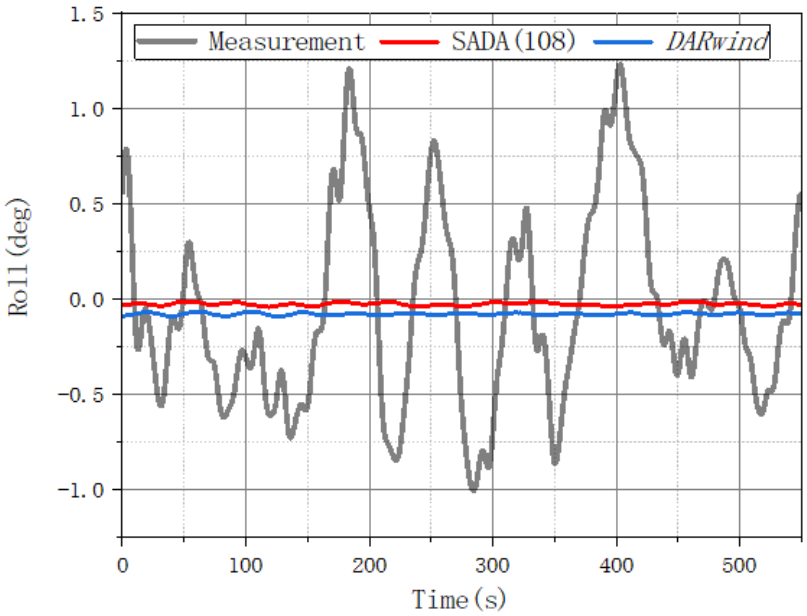

Figure 8.15 Time history of Roll between *DARwind* and SADA.

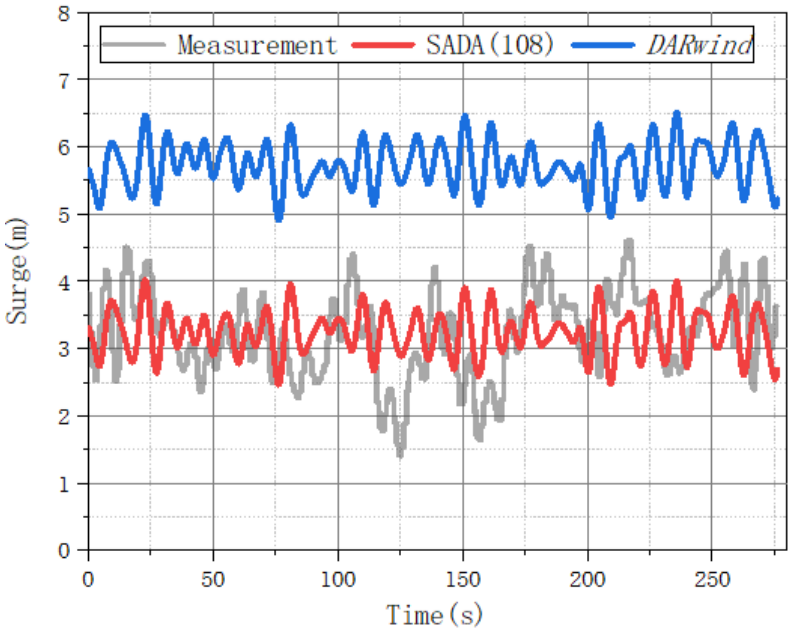

Figure 8.16 Time history of Surge between *DARwind* and SADA.

Unlike the 51 KDPs model, 108 KDPs model contains some structural parameters of wind turbine and tower, which will include more details and influences of the whole system, such as the mass distribution and inertia of the system. To optimise a single motion, SADA can effectively reduce the difference between numerical simulation and measured

data, especially the model containing 108 KDPs. From the results, the SADA method also can use AI technology to compensate for the impact of unknown structural parameters to the greatest extent and fit the surge that is more consistent with the actual situation. Therefore, in optimising 5DOF motions, the SADA containing 108 KDPs was comprehensively tested. The result proves that it can effectively reduce the difference in the average value.

8.4.3. Dynamic response prediction

In this subsection, based on the 5DOF optimisation of SADA, the prediction of other physical quantities will be demonstrated, including the thrust force, blade tip and tower top deformation. However, the benchmark in this subsection is not based on the measurement results but the more stable platform motions.

8.4.3.1. Axial thrust force and torque

Axial thrust is an essential physical quantity in the FOWT system, and it has a vital influence on the dynamic response of the entire system. **Table 8.12** compares the aerodynamic axial thrust of the FOWT system in case 9. SADA gives different statistical predictions of the thrust force from those of *DARwind*. This can be found as one of the effects of that AI-based SADA method giving a better dynamic response prediction model for the objective FOWT because all the dynamic responses of the FOWT system are tightly coupled. **Figure 8.17** shows the time history of Thrust under case 9.

A better prediction of FOWT motions by the SADA method can prove its capability to predict other critical physical quantities better.

Table 8.12 Comparison of aerodynamic loads under case 9.

items		Avg	Std	Min	Max
Thrust	SADA	426.973	28.102	326.854	522.893
/kN	*DARwind*	442.152	29.449	338.061	541.359
Torque	SADA	2208.890	293.327	1238.620	3261.036
/kN.m	*DARwind*	2303.343	308.704	1289.868	3394.313

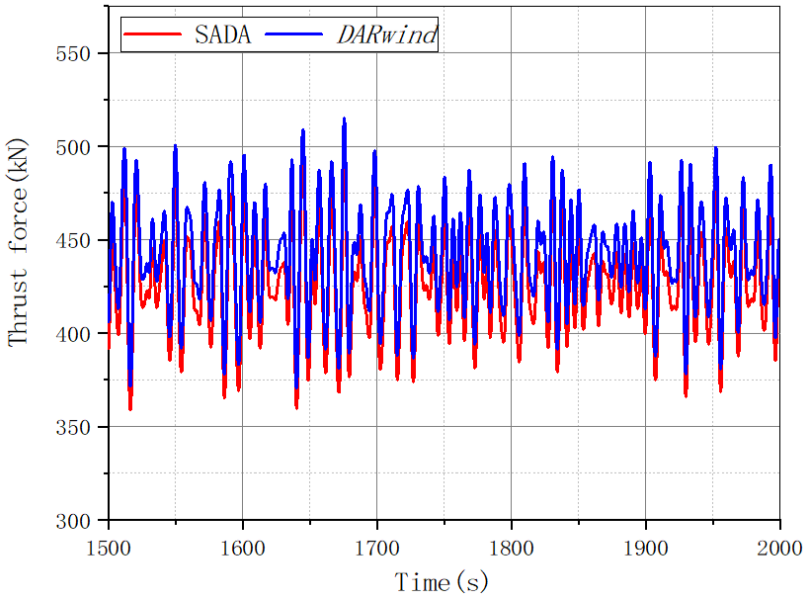

Figure 8.17 Time history of thrust force under case 9.

8.4.3.2. Tower top deformation

The deformation of the tower is divided into 11 stations in numerical simulation. Because the deformation of the tower top is the most significant, **Table 8.13** shows the tower top deformation of the FOWT system under case 9. The deformation of the top of the tower is also reduced due to the reduction of Floater motion. The deformation of the SADA in the X direction has not changed much, compared with the results from *DARwind*.

Table 8.13 Comparison of tower top deformation under case 9.

items		Avg	Std	Min	Max
Tower_x	SADA	0.164	0.044	0.003	0.298
/m	*DARwind*	0.170	0.046	0.002	0.311
Tower_y	SADA	-0.016	0.001	-0.019	-0.012
/m	*DARwind*	-0.015	0.000	-0.016	-0.014

Although the amplitude of the deformation in the Y direction is small, there is a big difference in the time history in **Figure 8.18**.

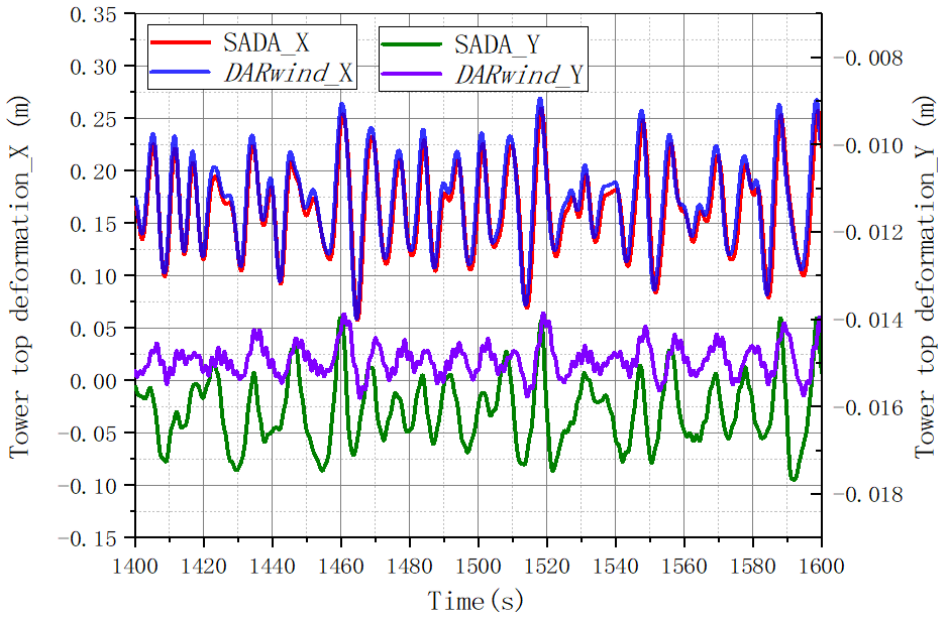

Figure 8.18 Time history of tower top deformation.

8.4.3.3. Blades tip deformation

Due to the large scale of FOWT, the flexible blades are long as 60-100 meters, so the deformation of the blade tip will be very significant. **Table 8.14** shows the blade tip deformation of the FOWT system under case 9. The deformation of the blade in the X direction changes significantly, which is due to the change of the normal force caused by the Floater motion. **Figure 8.19** shows the time history curves in both directions.

Table 8.14 Comparison of blade tip deformation under case 9.

items		Avg	Std	Min	Max
Blade_x	SADA	3.322	0.188	2.656	4.113
/m	*DARwind*	3.448	0.197	2.827	4.112
Blade_y	SADA	0.113	0.313	-0.334	0.581
/m	*DARwind*	0.120	0.318	-0.336	0.590
Blade_z	SADA	-0.152	0.017	-0.232	-0.097
/m	*DARwind*	-0.164	0.019	-0.232	-0.110

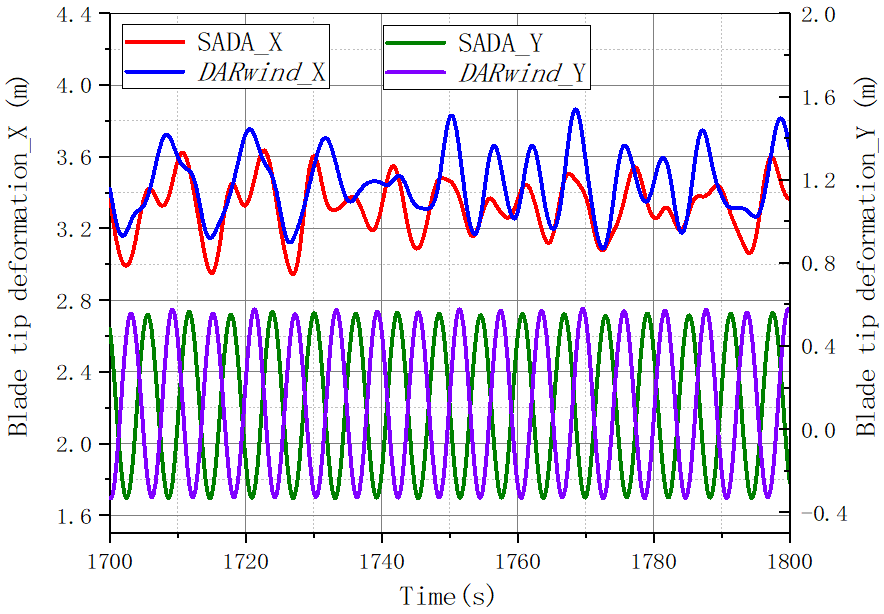

Figure 8.19 Time history of blade tip deformation.

The prediction results can be used as a reference for blade tip deformation because a 5MW wind turbine has replaced the 6MW wind turbine. The blades and towers data are usually not available in the full-scale measurement operation because installing deformation sensors on blades is a quite challenging and high-cost task. Therefore, it is impossible to find a method that can indirectly provide reliable data on blade tip deformation. The research in this chapter proved that the SADA method could be a promising solution for this challenge.

8.5. Summary

This chapter aims to demonstrate the feasibility of the SADA method on predicting the dynamic response of FOWT on full-scale measurement. The actual full-scale FOWT in operation has a more substantial nonlinear coupling effect, challenging to analyse and predict. The AI-based SADA method brings a potential solution to overcome this challenge. SADA uses deep reinforcement learning algorithms to allow numerical software to carry out self-learning to help traditional numerical tools to make decisions

intelligently. It can also effectively help them break through its theoretical and parameter limitations to a large extent.

SADA can reduce the difference between numerical calculation and the measured data and can fit missing unknown original design parameters. In contrast, the numerical results without SADA optimisation can only rely on the designer to adjust the relevant parameters during the design stage.

The advantages of the SADA method in full-scale measurement application are summarised as follows:

- In the case of the known sea conditions and measured data, SADA can optimise the numerical simulation results to achieve higher accuracy and obtain prediction results with a moderate increase of KDPs number.
- SADA can simulate the dynamic responses of the FOWT system, even if some design parameters are not available and be replaced by some approximated models. For example, the design parameters of the 6MW wind turbine are not available in this study by replacing it with a 5MW wind turbine instead.
- SADA gives different statistical predictions of the thrust force from those of *DARwind*. A better prediction of FOWT motions by the SADA method can prove its capability to predict other critical physical quantities better.

Chapter 9. Correlation analysis and KDP selection guidance

This chapter aims to use the SADA method to conduct deeper investigations on KDPs and show more details of KDPs in SADA. For example, how to choose KDPs in SADA, determine their boundary conditions, and which types of KDPs are more critical. Furthermore, how these important KDPs can affect the dynamic performance of FOWTs in a nonlinear robust coupling environment. Firstly, the number, boundary conditions, and types of KDPs are explored. Secondly, the correlation analysis is carried out between the changes of KDPs and the forecast results. Finally, guidance is provided, which can help other scholars have a deeper understanding of the SADA method in future.

9.1. Introduction

This section introduces a case setting and KDPs in this chapter. In addition, an essential process of selecting KDPs for analysis in terms of number and category. The specific boundary conditions are grouped and sorted for these KDPs. The case study is proposed from the results of the basin experiment. **Table 9.1** shows the experimental case used for the case of study analysis.

Table 9.1 Case matrix of KDPs analysis.

	V_c(m/s)	H_s(m)	T_p(s)	γ	V_c(m/s)
Case	11.4	7.1	12.1	2.2	0.8

9.1.1. KDPs selection

First, the KDPs involved in this chapter are introduced. According to the three KDPs discussed above, 39 of KDPs are selected as the basis for the analysis. **Table 9.2** shows the selected KDPs. Category A, B and C are the categories of Environmental KDPs, Disciplinary KDPs and Specific KDPs, respectively. For some KDPs, they will be subdivided into multiple values. For example, due to the symmetry of the floating body, only the diagonal parameters of the added viscous damping coefficient matrix and the

added restoring force coefficient matrix are considered hydrodynamic disciplinary KDPs. Therefore, there will be 6 KDPs in added linear viscous damping matrix.

Table 9.2 List of all selected KDPs.

No.	Category	Discipline	KDPs	Symbol
1	A	Aero	Wind speed	V_w
2		Hydro	Current speed	V_c
3			Significant wave height	H_s
4			Peak period	T_p
5			Shape factor	γ
6	B	Aero	*Glauert* correction	a_c
7			Tower drag	$C_{d_{Tower}}^{A}$
8~13		Hydro	Added linear viscous damping matrix	C_{ld}^{H}
14~19			Added linear restoring matrix	C_{r}^{H}
20			Added static force (3, 3)	$F_{static(3,3)}$
21	C		Platform drag	$C_{d_{Platform}}^{H}$
22		Mooring	Wet density	M_{WD}
23			Axial stiffness	M_{AS}
24			Mooring drag	M_{Cd}
25~29		Structural dynamics	Polynomial Flap 1st vibration modes	φ_x^1
30~34			Polynomial Flap 2nd vibration modes	φ_x^2
35~39			Polynomial Edge 1st vibration modes	φ_y^1

9.1.2. Grouping for quantitative analysis

To better study the impact of different numbers and types of KDPs on the dynamic response of the FOWTs system, 39 KDPs are divided into three groups:

- Group 1: A (5 KDPs).
- Group 2: A+B (20 KDPs).
- Group 3: A+B+C (39KDPs).

Environmental KDPs for wind, wave and current are included in the first group. In the second group, the environmental KDPs and disciplinary KDPs are included. In the third

group, all 39 KDPs are considered. To establish three groups, the optimisation effect of SADA, including different types and numbers of KDPs, can be compared.

9.1.3. Grouping for boundary condition analysis

The study of boundary conditions (BCs) for KDPs is also essential, and it is grouped based on the range definitions in **section 4.4**.

a) Fix (no range).

b) Small range.

c) Large range.

d) No limit ranges.

A total of 39 KDPs are divided into three categories (A, B, and C), and four BCs are used to permutate and combine to obtain eight sets of BCs in **Table 9.3**. This can maximise the impact of different types of KDPs and the effects of their boundary conditions for analysis. Taking the BC1 as an example, only A (Environmental KDPs) allows small changes, and B (Disciplinary KDPs) and C (Specific KDPs) remain unchanged in SADA calculation. Through this grouping method, not only can the influence of different types of KDPs on the dynamic response of the FOWTs system be analysed, but the optimisation effect comparison under different BCs can also be obtained.

Table 9.3 Boundary conditions of 39 KDPs in 8 cases.

No.	Fix	Small range	Large range	No range limit
BC1	B, C	A	-	-
BC2	C	A, B	-	-
BC3	-	A, B, C	-	-
BC4	-	B, C	A	-
BC5	-	C	A, B	-
BC6	-	-	A, B, C	-
BC7	-	-	B, C	A
BC8	-	-	C	A, B

9.2. SADA analysis results and discussions

This section conducts an in-depth analysis of KDPs with the SADA method using the above groupings in **section 9.1**. The experimental data will be used as the AI training data, and SADA calculation will be conducted to make the numerical calculation programme *DARwind* intelligent through the weighting and optimisation of KDPs. The optimisation effects of different numbers of KDPs and different BCs in SADA are compared and discussed.

9.2.1. The impact of KDP numbers

This section will discuss the optimisation effects of KDP numbers according to the analysis results and comparisons. The deep neural network is trained to optimise the correctness of its decision-making by storing the memory of each iteration. The trained SADA model uses the corresponding KDPs to calculate FOWTs dynamic response prediction, and the result are shown in **Figure 9.1**.

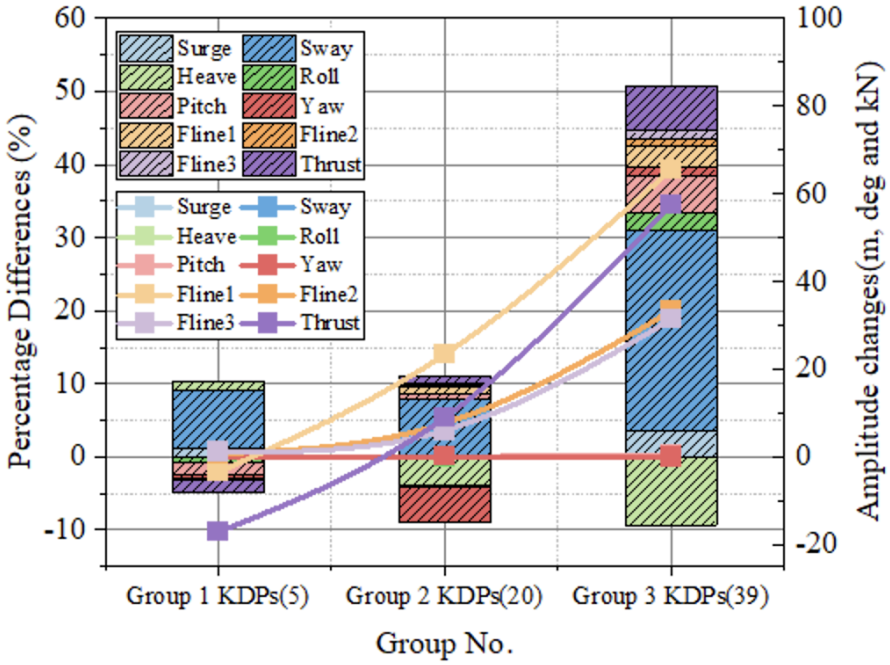

Figure 9.1 The difference and amplitude change of three groups.

The left-hand vertical axis represents the percentage difference change of the corresponding physical quantity. The right-hand vertical axis shows the corresponding amplitude change. If the percentage difference is positive, the difference between the experiment and numerical simulation has decreased by SADA. It can be seen from **Figure 9.1** that the stacked graphs of the optimisation results of the three groups of KDPs reached 10%, 11%, and 50 %, respectively.

This also means that the actual difference of the third group with the largest number 39 of KDPs is 50% lower than the traditional numerical calculation result that does not consider the change of KDPs. From the amplitude changes in these physical quantities, the fairlead tension and thrust are the most significant. From **Figure 9.1**, the overall optimisation effect of group 3, which has the largest KDPs number 39, is the best.

The influence of KDPs can be discussed by the differences of different physical quantities during the process of SADA training. **Figure 9.2** shows the percentage difference of four physical quantities in three groups in 100 training iterations. These four physical quantities are the surge motion of the platform, the pitch motion of the platform, the tension of the first fairlead (Fline1), and the axial thrust of the wind turbine. From **Figure 9.2**, one key point can be obtained that the case with the largest KDPs number can reduce the oscillation of four physical quantities differences in the SADA training process. The percentage difference of four physical quantities in group 1 changes significantly in the environmental KDPs only. Especially in the first group, the relationship between thrust and pitch is negatively correlated. The oscillations of the four physical quantities in the second group are smaller than that in the first group, because this group considers more KDP. The trend of pitch and thrust is similar, which can be observed in the third KDP group. Only environmental KDPs are considered, for example, simply increasing or decreasing wind speed, which cannot effectively improve the prediction of multiple physical quantities (due to coupling effect). Therefore, when more KDPs are considered, the prediction of these physical quantities can be effectively improved.

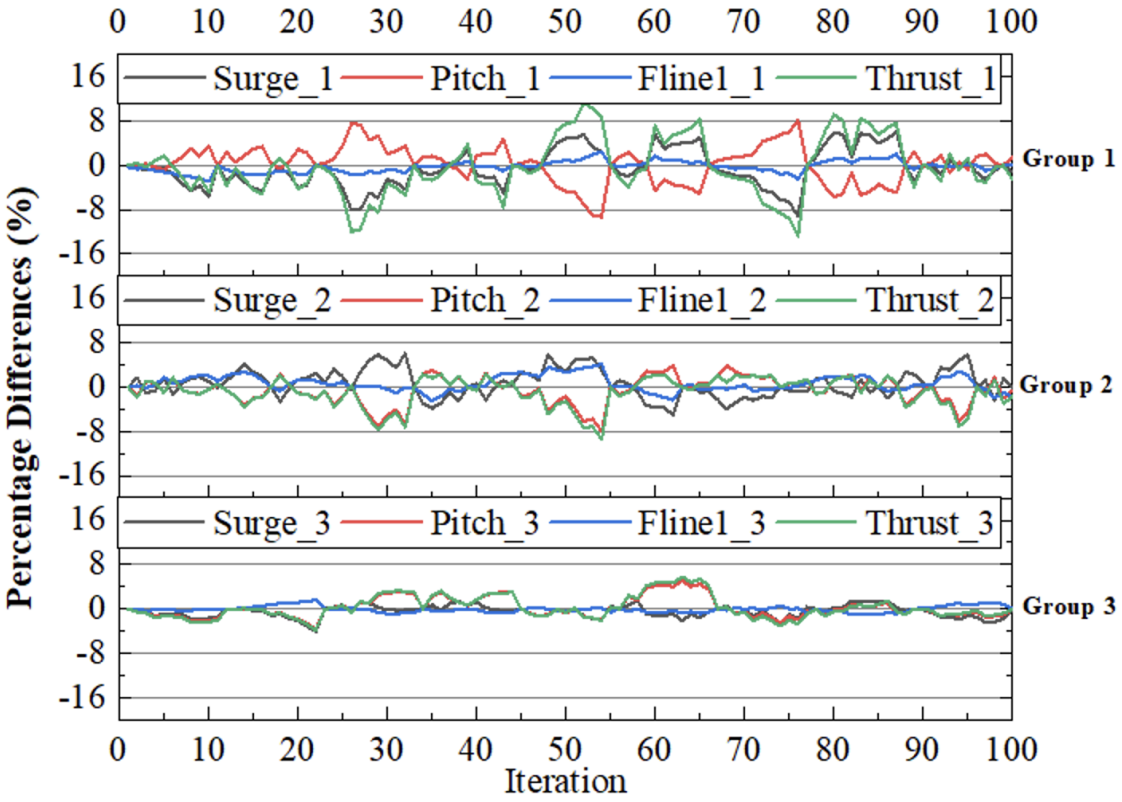

Figure 9.2 The difference variation of three group in iteration.

9.2.2. The impact of boundary conditions of KDPs.

This section discusses the boundary conditions (BCs) of KDPs in the SADA method from two aspects:

- Difference reduction
- Iterative difference variation

Through the analysis from these aspects, the influence of KDPs of different BCs on the prediction difference of the dynamic response of FOWTs can be found. By analysing the difference variation of each physical quantity in the SADA iteration process, the convergence effect of KDPs of different BCs can be evaluated. In addition, the statistical analysis of the difference variation of each physical quantity in the KDPs of different BCs can further determine the oscillating of physical quantities and the variation of the

difference values. However, the initial BCs also need to be revised for some exceptional cases.

9.2.3. Difference reduction analysis

This section uses the selected KDPs to analyse their impact on the FOWTs system under different BCs in the SADA method. The Gaussian distribution used for the weighting of KDPs is randomly weighted each time. **Figure 9.3** shows the percentage differences of 8 BCs.

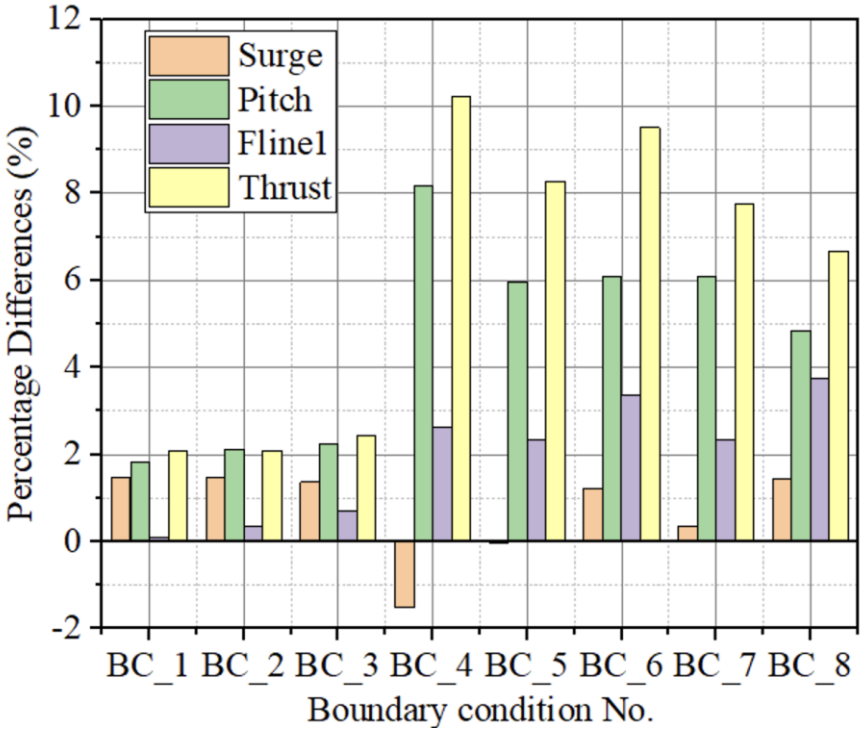

Figure 9.3 The difference variation of different BCs.

The more considerable the positive difference variation, the better the SADA optimisation effect, and the differences between original numerical and experimental have been significantly reduced. The optimisation effect of the last five cases is much better than that of the first three (BC1, BC2 and BC3). In general, SADA balances the optimisation of other physical quantities simultaneously by giving up the accuracy of part of the surge, which is also the intelligence of the SADA method. From the perspective of BC3 and

BC5, only the environmental KDPs have been considered with a more extensive boundary condition. The difference variation is noticeable. Comparing BC6 and BC7, the change of KDPs did not bring much difference to the four physical quantities. The environmental KDPs have a relative interval limit for the difference adjustment of the FOWTs system. In contrast, the effect of the last two BCs has declined. For example, in BC8, the thrust difference is reduced by about 6.5%, and the corresponding amplitude change is about 60kN.

The first three BCs are fixed or only allow for small changes. From the results, the environmental KDPs in the first three groups have a decisive effect on the surge, pitch and thrust. The difference of fairlead tension force gradually decreases with the change of BCs. Only the fairlead tension reflects little effect from the change of BCs on environmental KDPs. When BC2 and BC3 are included for the disciplinary KDPs, the difference began to decrease more obvious. BC3 allow three group KDPs to have changes, which shows a more reliable fairlead tension prediction. Comparing BC3 with BC4, the difference of the surge is increasing, and the differences of the other three physical quantities of BC4 have decreased significantly. For example, the difference of thrust is reduced by about 10%. That is, the corresponding amplitude change is 93kN. Although the difference changes were significant in BC4, BC 5 and BC6, the amplitude of surge and pitch did not change significantly relative to thrust and fairlead tension, shown in **Figure 9.4**.

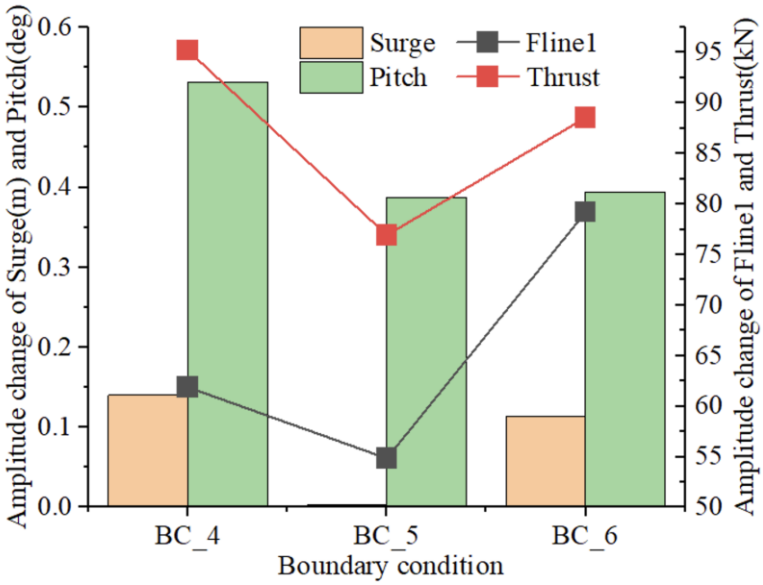

Figure 9.4 The amplitude changes of three BCs.

In general, as the combination of BCs of each group of KDPs changes, some summary can be roughly obtained:

1) **The environmental KDPs determine the relative maximum magnitude of the prediction accuracy.**

   The environmental KDPs have a vital influence on the forecast of the dynamic responses of the FOWTs system. Due to the measurement difference in the experiment or the simplification of the numerical model, larger BCs of the environmental KDPs is recommended. However, for the forecast of some physical quantities, such as Fairlead tension force, it is not enough to only consider the environmental KDPs.

2) **KDPs with large BCs improve the prediction accuracy significantly.**

KDPs with larger BCs can significantly improve the prediction accuracy of dynamic response prediction of FOWTs. In addition, SADA can intelligently balance the accuracy of each physical quantity by adjusting KDPs, to avoid overfitting a particular physical quantity.

9.2.4. Statistical analysis

This part will discuss the statistical results of difference variation. By analysing the difference changes of different physical quantities, the oscillation relationship between them and the BCs of KDPs can be found. The statistical results of different physical quantities under 8 BCs are shown in **Table 9.4** to **Table 9.7**, including average (Avg), standard deviation (Std), sum, minimum (Min), interquartile range (IQR), and maximum (Max). Among them, the interquartile range represents the width of a set of numbers from small to large, and the middle 50% of the numbers. It can also simply measure the degree of dispersion of a set of data. The smaller the interquartile range, the less scattered the data. According to the definition of the difference variation above, the Min (minimum value of the difference variation) in the table represents the maximum difference between numerical simulation and experimental results, vice versa (The Max).

From the average and standard deviation, the surge is basically in a state of increasing difference, especially under large BCs and no BCs. The combined standard deviation means that as the range of BCs increases, the data oscillation becomes more significant. Although the oscillation of pitch gradually increases with the expansion of BCs, its average value is relatively stable, except for BC8.

Table 9.4 Statistics of percentage difference of surge in KDPs analysis.

BC No.	Avg	Std	Sum	Min	IQR	Max
BC1	-1.15	1.87	-606.66	-5.45	-0.97	1.48
BC2	-1.06	1.81	-557.36	-5.70	-0.74	1.50
BC3	-1.23	1.92	-648.63	-6.34	-0.89	1.50
BC4	-7.76	5.32	-4088.86	-19.05	-7.80	1.50
BC5	-6.66	5.50	-3508.10	-21.94	-5.76	1.50
BC6	-6.15	5.56	-3241.39	-21.97	-4.96	1.49
BC7	-10.40	10.94	-5481.91	-56.95	-7.32	1.47
BC8	-17.38	16.47	-9160.83	-76.35	-12.34	1.49

Table 9.5 Statistics of percentage difference of pitch in KDPs analysis.

BC No.	Avg	Std	Sum	Min	IQR	Max
BC1	-0.12	1.79	-65.80	-2.46	-0.90	2.44
BC2	0.25	1.75	131.05	-2.74	0.66	2.82
BC3	-0.19	1.80	-101.72	-3.24	-0.36	3.10
BC4	-0.97	9.43	-510.39	-14.41	-1.71	15.64
BC5	-0.19	8.65	-98.20	-14.99	-0.81	15.64
BC6	5.43	7.24	2863.66	-16.25	5.95	15.65
BC7	-0.55	10.83	-290.98	-38.31	0.45	15.54
BC8	-8.90	14.82	-4689.82	-72.03	-8.14	15.65

Table 9.6 Statistics of percentage difference of Fline1 in KDPs analysis.

BC No.	Avg	Std	Sum	Min	IQR	Max
BC1	-0.64	2.22	-335.69	-4.19	-0.71	3.50
BC2	-0.40	2.20	-212.84	-4.43	-0.45	3.62
BC3	0.18	1.96	93.01	-4.80	0.31	4.40
BC4	0.59	3.31	309.60	-7.38	0.71	7.15
BC5	-0.64	3.57	-335.40	-10.31	-0.62	7.97
BC6	-1.25	3.34	-656.38	-10.51	-0.99	8.98
BC7	-1.20	4.35	-634.55	-12.94	-0.90	12.29
BC8	-0.84	7.14	-440.88	-20.89	-0.34	19.83

Table 9.7 Statistics of percentage difference of Thrust in KDPs analysis.

BC No.	Avg	Std	Sum	Min	IQR	Max
BC1	-0.22	1.89	-116.32	-2.08	-1.00	2.09
BC2	0.19	1.87	97.52	-2.09	0.66	2.10
BC3	-0.09	1.93	-45.08	-2.96	-0.20	2.64
BC4	-2.32	8.44	-1220.32	-14.97	-1.83	10.46
BC5	-1.86	7.60	-981.08	-14.97	-0.96	10.41
BC6	3.21	5.68	1691.42	-15.29	4.79	10.45
BC7	-3.37	10.53	-1776.66	-42.47	-1.07	10.44
BC8	-11.85	15.19	-6245.00	-79.02	-9.55	10.19

For the fairlead tension, the average value of the difference variation of the eight groups of BCs is not significant. The oscillation in the training process is also very small. The average performance of axial thrust shows different results according to different BCs.

However, the oscillation law of thrust is roughly the same as the other three physical quantities.

Comparing BC3 and BC4 from the above tables, it is not difficult to see that the oscillation of the four physical quantities has increased significantly. In this case, the BCs of the environmental KDPs become larger, and the remaining two groups of KDPs maintain small. In combination with BC4, 5, and 6, even if the BCs of disciplinary and specific KDPs expand the range, their impact on oscillation is small, even reducing its oscillation in pitch. It is not difficult to conclude that the environmental KDPs are the main reason for the more significant oscillation of optimisation. The same conclusion can be obtained by comparing BC6 and BC7 in the above tables.

Figure 9.5 and **Figure 9.6** show the statistical bar chart of difference variation statistics in 8 BCs in Min and Max. It can be seen from **Figure 9.5** that as the BCs increase, the maximum difference between numerical simulation and experimental results during training will increase significantly. The first three BCs of small boundaries and even fixed BCs is relatively stable. From **Figure 9.6**, with the expansion of the BCs, the maximum value of the mean difference decrease gradually increases. For example, in the last five BCs, the pitch difference is reduced by 15.6% compared to the initial difference without SADA. Combining the two figures, it can be found that although the best performance of BC4, 5, and 6 is similar to that under borderless KDPs (BC7 and 8), its worst performance is better than that of borderless KDPs. In general, larger BCs have a more robust oscillation of prediction accuracy. Based on the above analysis, it can be summarised that the oscillation of prediction accuracy is mainly caused by environmental KDPs, which play a decisive factor in this phenomenon. The other two types of KDPs may effectively reduce the oscillation of prediction accuracy based on specific conditions and physical quantities during the expansion of BCs.

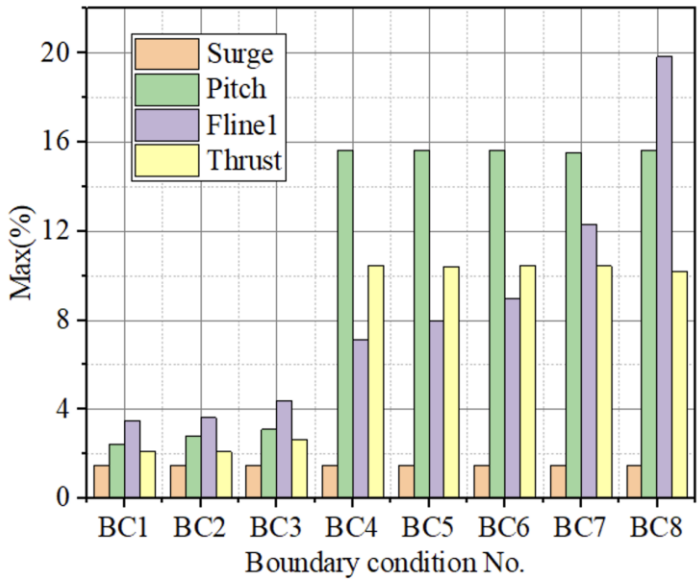

Figure 9.5 Maximum Difference variation statistics in 8 BCs.

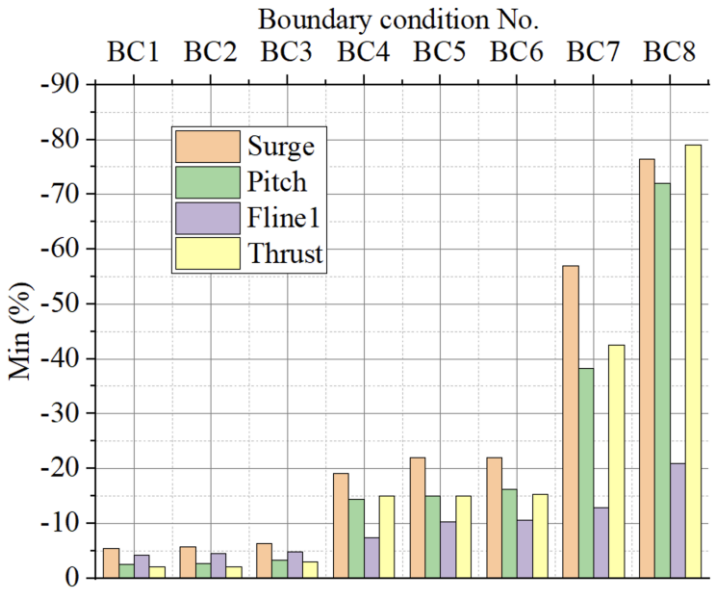

Figure 9.6 Minimum Difference variation statistics in 8 BCs.

9.2.5. BCs adjustment for specific situation

This subsection mainly adjusts BCs on the original basis for some specific situations. Through these adjustments, not only can the forecast accuracy be better, but also good results can be obtained more efficiently.

The result without AI-based surge motion is already close to the experimental value (the original difference between numerical simulation and experiment is 2%). If the KDPs are slightly changed, the difference of surge will have a relatively large oscillation. In addition, even though the differences of the first six groups of BCs have risen, they oscillated within a small range. For KDPs without limiting BCs, the oscillation of the mean difference of surge is very significant. For a specific situation, when one or more dynamic responses quantities of the FOWTs system already have a very high accuracy without AI-based, the BCs of the first six BCs may be more applicable for training, and they are fully capable of reducing the existing differences. For other physical quantities, the optimisation of small BCs is minimal for pitch motion. The optimisation effects of the 8 BCs on the fairlead tension are similar. Therefore, a larger boundary condition based on KDPs seems more reasonable for fairlead tension. The environmental KDPs only have limited optimisation of the thrust force. The latter two groups of BCs can reduce the differences of thrust force by up to about 8%.

In general, for the physical quantities of different initial differences between numerical simulation and target data, the effects of each BCs are different, which puts forward higher requirements for the adjustment of BCs. Based on the above analysis, it can be summarised as the following points:

1) The initial difference of target physical quantity is small

Due to the slight initial difference, selecting BCs with larger boundary conditions requires careful consideration. The significant difference oscillation may happen, affecting the prediction accuracy of other physical quantities due to the solid nonlinear coupling of the entire system. Therefore, it may be more appropriate to choose smaller BCs when the initial difference of target physical quantity is small.

2) Significant initial difference of target physical quantity

It is inevitable to encounter relatively significant initial differences of specific physical quantities (for example, greater than 20%). It may be necessary to choose between small BCs (disciplinary and specific KDPs) and large BCs (environmental KDPs).

9.3. Correlation analysis

This section will carry out correlation analysis on the relationship between the weighted KDPs and the dynamic response of FOWTs system during the loop of SADA optimisation.

9.3.1. Grouping of boundary conditions for KDPs.

Table 9.8 shows the categories of three sets of boundary conditions, where A, B and C refer to Experimental environment, Disciplinary KDPs, and Specific KDPs, respectively. Taking the first group (BC1) as an example, only the environmental KDPs (wind, current, and wave) allow small-scale changes, while the other two types of KDPs do not have any changes during the SADA loop.

Table 9.8 Different boundary conditions of 39 KDPs.

No.	Fix		Small	
BC1	B	C	A	
BC2	C		A	B

9.3.2. Correlation analysis

The correlation between the parameters can be obtained by changing the percentage difference of each KDP and related physical quantities during the training process.

9.3.2.1. BC1

The correlation coefficient is spearman, and the confidence interval is 95. Taking BC1 as an example, the correlation analysis results are shown in **Table 9.9** (*: the correlation is significant at 0.05). A unitless measure (correlation coefficient r) is used to describe the correlation in the table. The value of r is [-1, 1]. The closer r is to 0, the weaker the linear relationship. Greater than 0 is a positive correlation; less than zero is a negative correlation. When the p-value is small, the null hypothesis will be rejected, and its threshold is usually set to p=0.05. If p<0.05, the correlation coefficient is not 0.

It uses a two-tailed significance test, and the * in the table indicates that the correlation is significant at the 0.05 level. It is not difficult to see that the V_w and V_c have a strong correlation with the four physical quantities. Among the three parameters related to waves, only surge and fairlead tension are related to T_p and γ respectively. This shows that the percentage differences of the four physical quantities have no relation with the wave parameters during SADA optimisation. This also shows that the wave in the numerical model is more accurate. Therefore, following the experimental settings when simulating waves, even a small range of fluctuations will not significantly impact the overall dynamic response of the FOWTs system.

Table 9.9. Spearman correlation of KDPs in BC1.

		V_w	V_c	H_s	T_p	γ
Surge	r	-0.17*	-0.37*	-0.01	-0.06	0.13*
	p	0.00	0.00	0.89	0.20	0.00
Pitch	r	-0.91*	-0.41*	0.03	-0.06	0.05
	p	0.00	0.00	0.49	0.19	0.26
Fline1	r	0.22*	0.98*	-0.04	0.20*	-0.00
	p	0.00	0.00	0.32	0.00	0.96
Thrust	r	-0.95*	0.21*	0.00	0.07	0.03
	p	0.00	0.00	0.95	0.08	0.46

Figure *9.7* and **Figure *9.8*** show the scatter distribution diagrams of pitch percentage difference and wind speed, fairlead tension percentage difference, and current. The black

dots in the figure are data points. The red line is the curve of its linear fit. The percentage difference of pitch has a robust negative correlation with wind speed, and its r-value is -0.91. Correspondingly, the r-value of fairlead tension and the current speed is 0.98. Furthermore, F1 has a strong positive correlation with current speed.

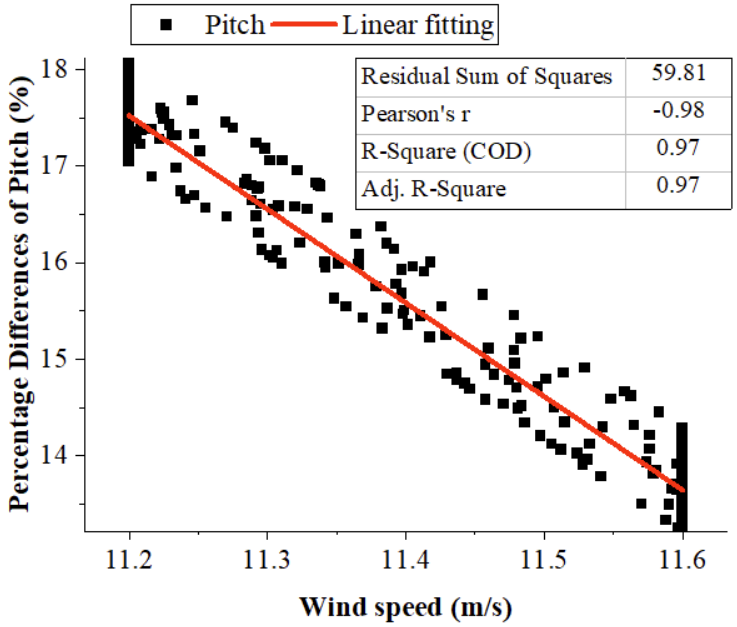

Figure 9.7 Linear fit between V_w and percentage difference of Pitch.

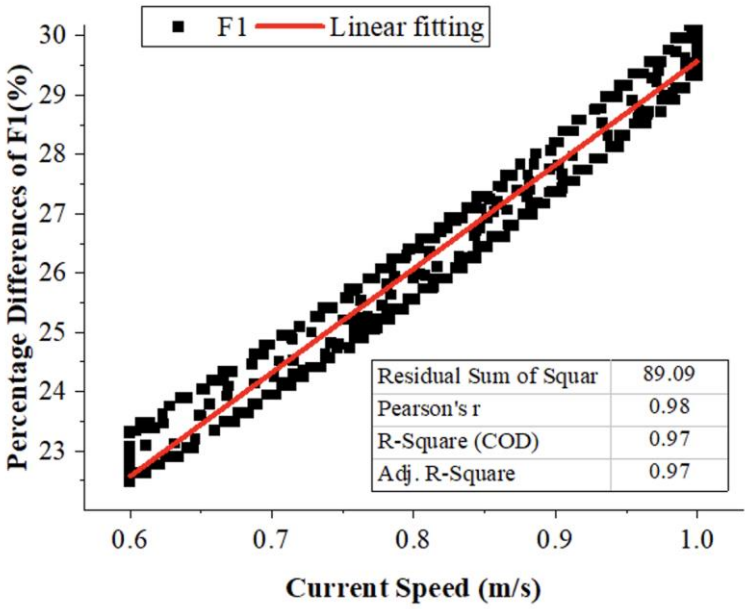

Figure 9.8 Linear fit between V_c and percentage difference of F1.

The percentage difference of pitch has a strong negative correlation with wind speed (r=-0.91) and current velocity (r=-0.41). A bubble chart is a multivariate chart that is a variation of a scatter chart. That is, three values are used to determine each data series. Data in two dimensions are mapped in a Cartesian coordinate system, replaced by X and Y, respectively. However, unlike scatter plots, bubble charts have categorical information for each bubble. Its area represents the value of the third data. For example, in **Figure *9.9***, X and Y represent wind speed and current speed, respectively. The bubbles are the difference changes of the normalised pitch motion. The size of its area and the corresponding colour represent the difference between the pitch and the target data. The larger the area, the larger the difference. The colour of the bubbles in the picture represents the difference in pitch. It is not difficult to see from **Figure *9.9*** that the decreasing trend of bubbles along the x-axis is more significant. This also echoes the -0.91 correlation between V_w and percentage difference of pitch in **Table 9.9**

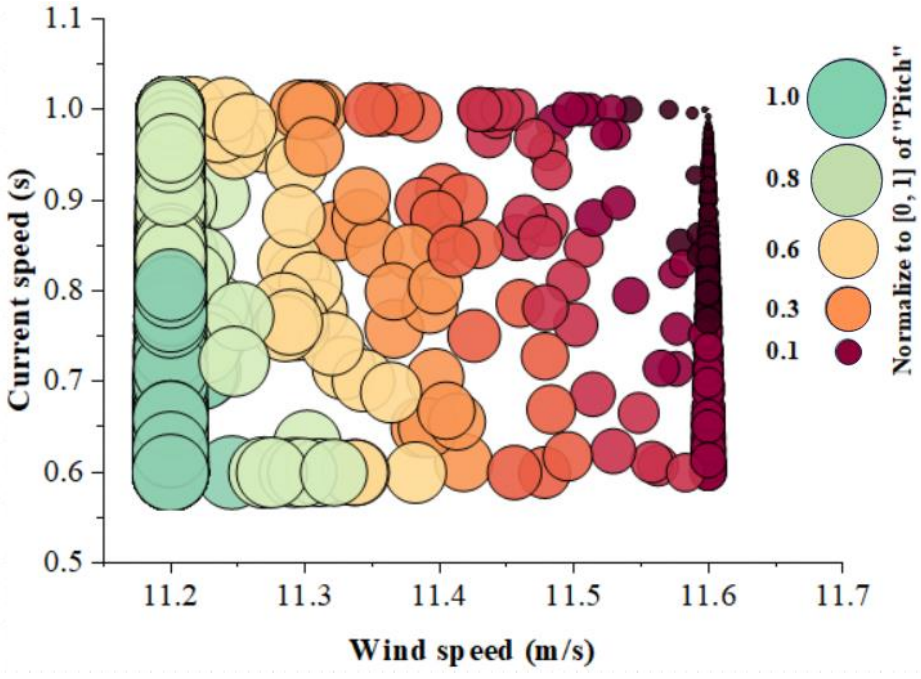

Figure 9.9 Bubble map of Pitch.

9.3.2.2. BC2

In BC2, not only the environmental KDPs are considered, but there are also some Disciplinary KDPs and Specific KDPs that designers often care about, such as the added restoring force matrix coefficient and the added first-order linear damping matrix coefficient. **Table *9.10*** shows the results of the correlation analysis in BC2.

Table 9.10 Spearman correlation of KDPs in BC2.

		Surge	Heave	Pitch	Fline1	Thrust
V_w	r	-0.17*	0.47*	-0.91*	0.18*	-0.95*
	p	0.00	0.00	0.00	0.00	0.00
V_c	r	-0.25*	0.88*	-0.30*	0.98*	0.09
	p	0.00	0.00	0.00	0.00	0.04
H_s	r	-0.07	0.21*	-0.07	0.24*	0.06
	p	0.12	0.00	0.14	0.00	0.19
T_p	r	-0.13*	0.22*	-0.11*	0.25*	0.00
	p	0.00	0.00	0.01	0.00	0.92
γ	r	0.03	0.13*	-0.11*	0.15*	-0.08
	p	0.51	0.00	0.01	0.00	0.07
$C^H_{r(1,1)}$	r	-0.05	0.00	0.15*	-0.05	-0.28*
	p	0.24	0.93	0.00	0.28	0.00
$C^H_{r(3,3)}$	r	-0.02	-0.04	-0.03	0.04	-0.04
	p	0.60	0.38	0.47	0.34	0.37
$C^H_{r(5,5)}$	r	-0.01	0.13*	-0.06	0.15*	-0.02
	p	0.82	0.00	0.21	0.00	0.74
$C^H_{ld(1,1)}$	r	0.19*	-0.37*	0.16*	-0.39*	0.04
	p	0.00	0.00	0.00	0.00	0.35
$C^H_{ld(3,3)}$	r	0.01	0.00	0.00	-0.03	-0.05
	p	0.74	0.98	0.99	0.55	0.29
$C^H_{ld(5,5)}$	r	0.04	-0.08	0.08	-0.09	0.04
	p	0.38	0.08	0.06	0.04	0.32
$F_{static(3,3)}$	r	-0.02	-0.07	-0.01	-0.03	-0.04
	p	0.71	0.12	0.77	0.52	0.36

The first-order linear added damping significantly affects platform motion and fairlead tension. Especially the correlation between percentage difference of heave, fairlead tension and $C^H_{ld(1,1)}$ reached -0.37 and -0.39, respectively. However, compared to the environmental KDPs, other KDPs have a limited impact due to their minor boundary

conditions. Unlike BC1, the three-wave parameters have a more significant impact on the percentage differences of the five physical quantities.

In the case of KDPs coupling except for the environment, the relationship between thrust and wind speed is consistent with BC1. **Figure *9.10*** shows the linear fitting results of wind speed and thrust.

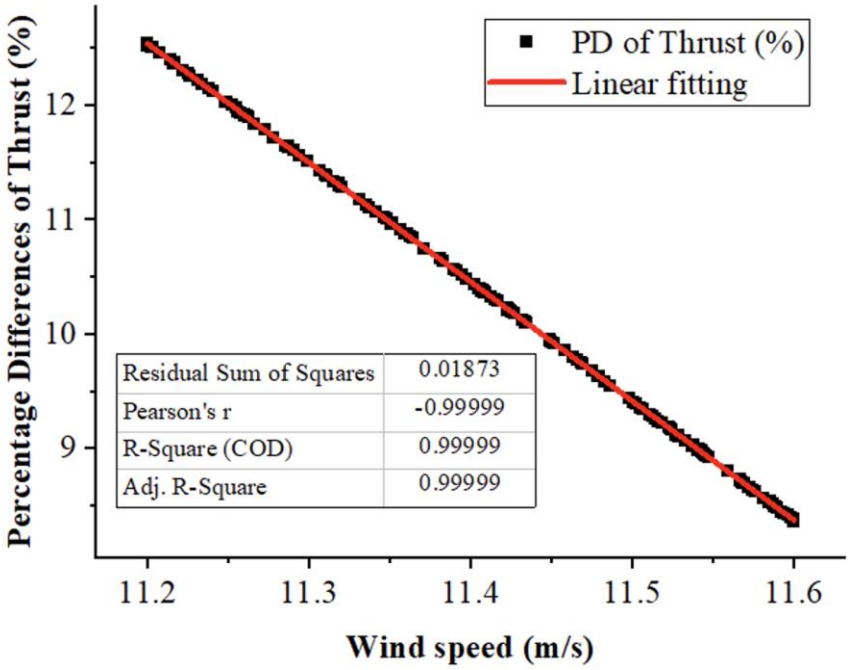

Figure 9.10 Linear fit between V_w and percentage difference of Thrust.

The percentage difference of heave is more sensitive, and the current speed also occupies the leading role and reaches 0.88. **Figure *9.11*** shows the bubble map between $C_{ld(1,1)}^{H}$, V_c and percentage difference of heave. Obviously, the heave percentage difference is minor with a lower current speed and a significant platform viscous damping. It can be seen in **Figure *9.12*** that when the current is determined, greater damping will reduce the percentage difference of the fairlead tension.

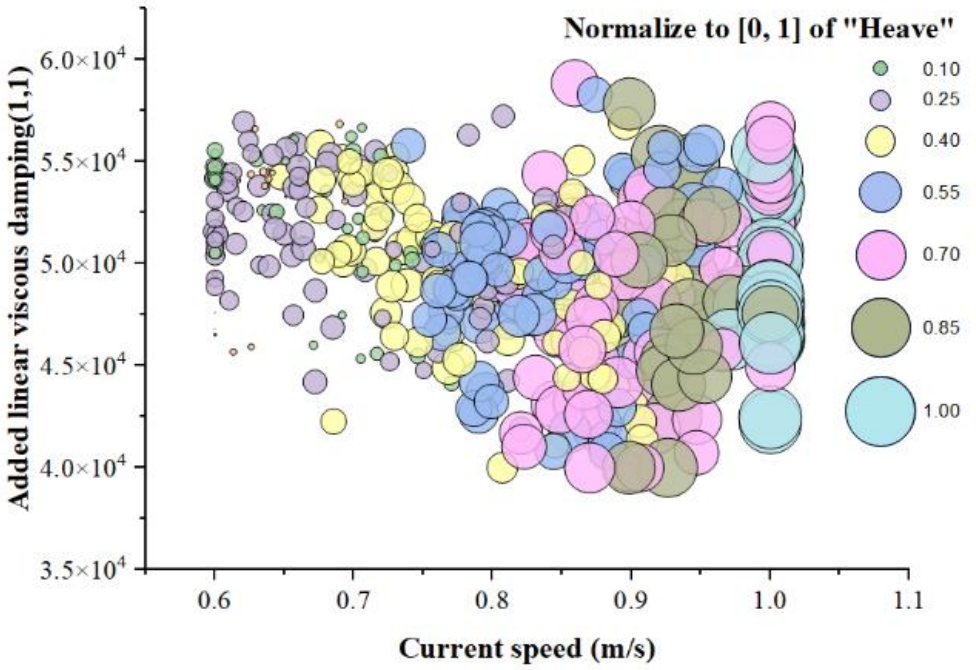

Figure 9.11 Bubble map of Heave.

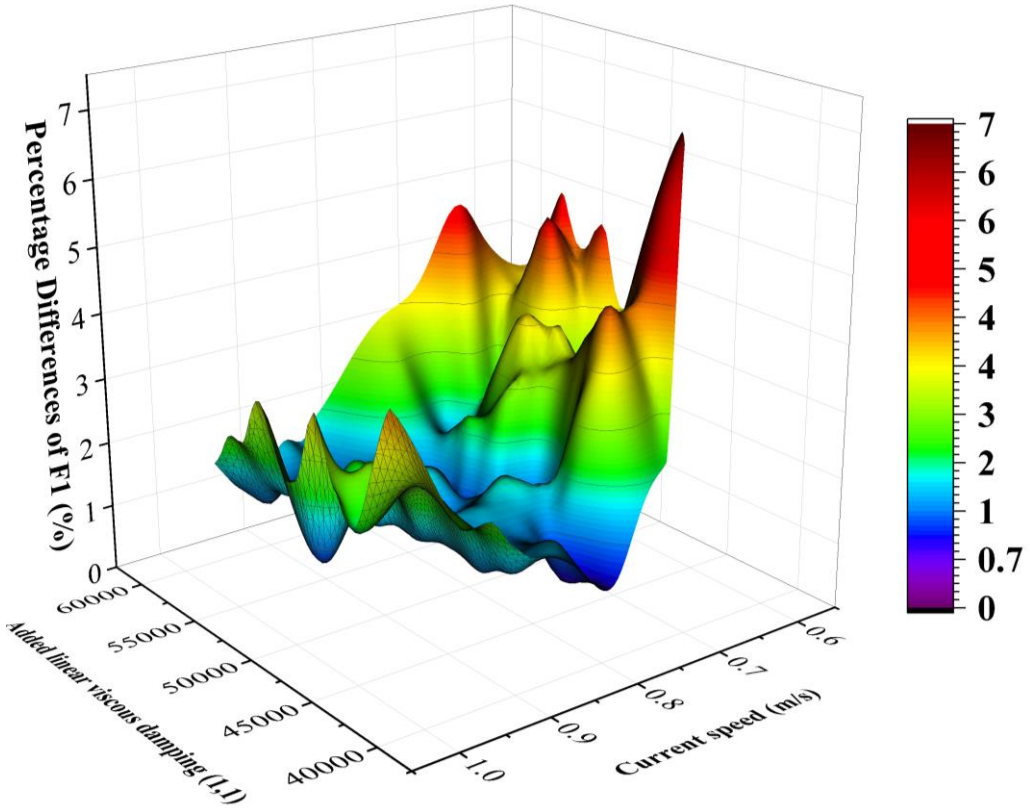

Figure 9.12 3D map of F1.

9.3.2.3. Discussion

In general, the study of KDPs is very challenging due to the nonlinear coupling characteristics of the FOWTs system. For the analysis of BC1, designers can initially understand the relationship between environmental KDP and the percentage difference of dynamic response. Ignoring the simplification of the numerical model and the limitations of the theoretical analysis method, the environmental KDPs can be modified to a certain extent to meet the more realistic essential experimental environment. This is primarily through correlation analysis to determine the percentage difference relationship between the experimental values or measured values. Taking the current speed as an example, it may not directly derive the specific, accurate distribution under the basin environment. However, it can be seen from the SADA iteration process that the percentage difference of dynamic response in the numerical calculation is more affected by the current than that by wave parameters. The metric to measure the size of this difference can be seen as a judgment on the importance of its correlation with the variation of the percentage difference of each physical quantity. It is supposed that the slight change of current has a significant correlation with the percentage difference change of other physical quantities. In that case, there is a particular gap between the experimental value of the basin, the numerical calculation model, and the actual design condition value.

The analysis of BC2 is more complicated because it also considers other types of KDPs. In the past, the designer could only modify these parameters based on the dynamic performance of FOWTs in the basin experimental environment to carry out static water attenuation as a reference. The SADA method provided in this article can optimise this type of KDP to a certain extent. On the one hand, the modification is based on previous basin experiment techniques. On the other hand, the optimisation results consider the specific basin environment, and the coupling results between different KDPs, especially the sea environment, is not limited to static water. Therefore, based on the correlation of such KDPs, designers can further understand the factors that have a more significant

impact on the FOWTs system in a specific environment. Some more exciting phenomena were also discovered, such as the correlation between added linear viscous damping with the heave. However, the current work does not provide the correlation between KDPs quantitively.

9.4. Summary and guidance

Based on the determination of physical phenomena, using AI technology to adjust these KDPs through self-learning intelligently is one of the critical technologies of the SADA method. In addition to a higher accurate numerical model, laws of KDPs are needed. This Chapter analyses and discusses the selection and boundary conditions of KDPs involved in the field of FOWTs. Finally, corresponding guidance methods and suggestions are given for KDPs.

Comprehensive guidance on the application of KDPs in the SADA method is shown in **Figure 9.13** to summarise the analysis on the proposed KDPs concept, including how to select and set BCs. The specific decision process is as follows:

- Step 1: Choose the corresponding KDPs in the three categories.
- Step 2: Use the concept of significant figures to set the boundary conditions according to the specific values of each KDP.
- Step 3: Determine the difference size between the numerical calculation result and the target data.
- Step 4: Adjust the boundary conditions appropriately.

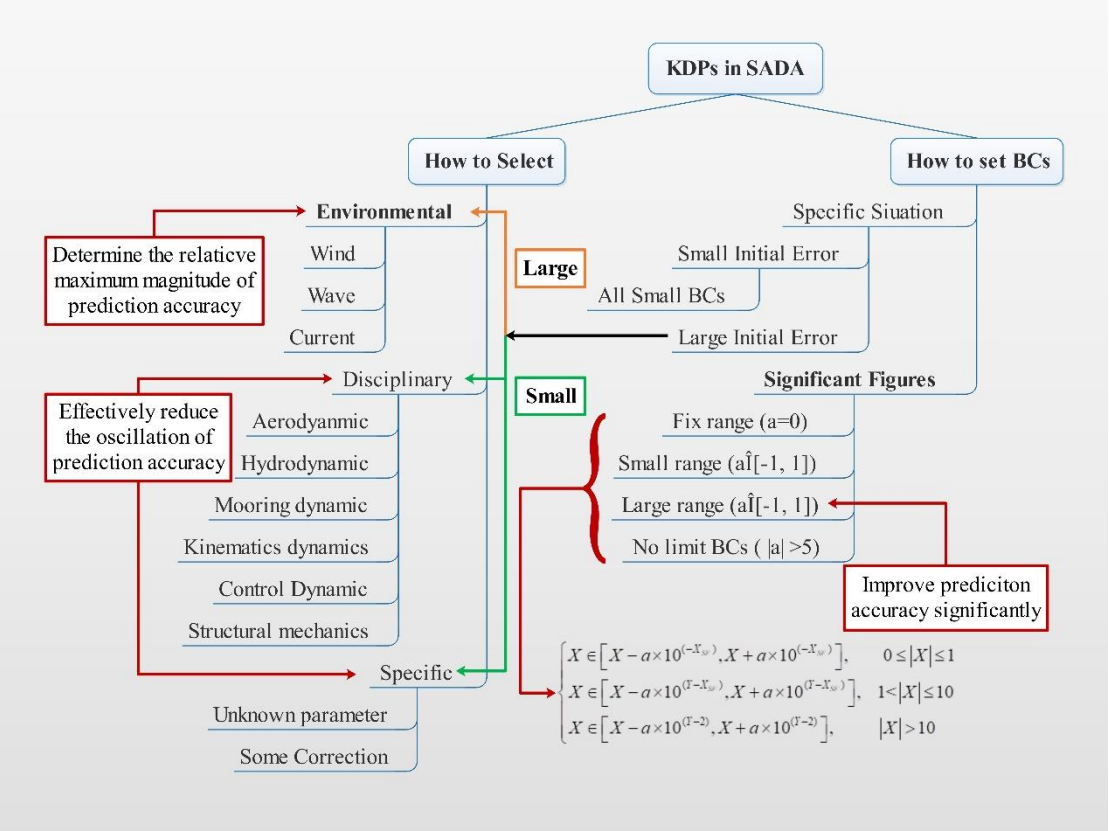

Figure 9.13 The flowchart of KDPs selection in SADA.

It can be pointed out that a better optimisation effect through the SADA method can be achieved with the greater number of KDPs, the Environmental KDPs are one of the most significant factors affecting the dynamic response of the entire FOWTs system, and all KDPs need to cooperate with a relatively suitable boundary condition. It is challenging to optimise and verify traditional empirical formulae or parameters involved in FOWTs. The SADA method can provide a reference for the verification, optimisation and coupling analysis of this type of KDPs. By analysing the environmental KDPs, the environment of FOWTs in numerical simulation can be corrected and provide a set of more reliable analyses and experimental environment basis.

The current theories based on the numerical calculation of FOWTs are all based on the improved products of onshore wind turbines. Although they have also withstood the test of experiments, there are still many gaps in basin experiments of FOWTs and new phenomena waiting to be discovered. Therefore, a deeper KDPs analysis was conducted

by the SADA method in **section 9.3**. The correlation analysis of different KDPs during the SADA loop is performed. The results can be summarised as the following:

1. By analysing the environmental KDPs, the sea environment of FOWTs in numerical simulation can be corrected and provide a set of more reliable analyses and experimental environment basis.
2. By analysing different categories of KDPs, the accuracy can be further improved based on the original values and provide a reference for the coupling analysis of FOWTs.

Chapter 10. Conclusions and Future work

As a clean and renewable energy source, wind energy harvesting technology is receiving more and more attention worldwide, with the improvement of wind power equipment-related technologies in recent years. FOWTs are currently one of the most popular ways to harvest wind energy at sea. Nevertheless, the dynamic responses prediction of FOWTs involves multiple disciplines, which is a strongly nonlinear coupled problem. It will show responses to the coupling effects, thus indicating that caution must be taken when simplifying the theories for the analysis of FOWTs (Amaral *et al.*, 2021).

10.1. Proposed SADA method

SADA is a novel and unprecedented method that can analyse and predict the dynamic responses of FOWTs, through the incorporation of an advanced AI training process. It can comprehensively optimise the numerical simulation results of adjusting KDPs to achieve higher accuracy in the prediction of the dynamic response of FOWTs under complex sea states. It can overcome the limitations of engineering-level software and optimise its own from the fundamental theoretical part through training experimental results or full-scale data. In addition, a better predict of FOWTs motions by the SADA method can prove its capability to better predicting other critical physical quantities. SADA can not only deal with existing target data but also work well to predict real-time cases. The correlation analysis of the KDPs changes in the process of SADA is helpful to promote and break through the existing theoretical research process of strongly coupled nonlinear phenomena in FOWTs.

At present, the academic community is focusing on the experimental verification methods of large-scale wind turbines (ultra-long blades) and innovative floating support platforms. Therefore, it is inevitable to face the steps of how to further develop the integrated design. As far as the industry is concerned, integrated design is one of the most important R&D directions in the future. At present, the design of FOWTs is mainly carried out by

combining numerical calculation with experimental measurement. However, there are strong uncertainties in numerical simulation and experiments of FOWTs. For example, the uncertainty of FOWTs was specifically proposed in the OC6 project (hosted by NREL), including the coupling of multiple factors such as hydrodynamics, aerodynamics, and innovative platforms.

The SADA method uses the advantages of reinforcement learning framework and software-in-the-loop to accumulate design experience and builds a numerical simulation optimization framework from dynamic response prediction and system characteristics. The action-value network in the reinforcement learning algorithm is used for iterative loop training, and a key parameter database integrating [response-design parameters-reward and punishment] is established. In this way, data mining can be carried out in-depth and can better meet the requirements of designers. Finally, combined with experiments, a unique design evaluation method can be developed for the design of proprietary FOWTs, and statistical models such as correlation analysis and principal component analysis can be used to further analyse some uncertain phenomena to provide reliable theory support.

In addition, the application prospect of SADA is not limited to FOWTs. Any industrial design and numerical simulation that needs to optimize uncertain factors can also be realized with the help of SADA. For example, fixed offshore wind turbines. In the design of fixed offshore wind turbines, the numerical simulation results can be optimized by SADA by using the data collected by sensors to obtain the optimal key design parameters based on data. There are also some phenomena observed in the actual measurement, which can also be discussed through the correlation analysis of the database. Therefore, the concept of SADA can be combined with the integrated design of FOWT to provide more contributions to industry and academia in the future.

10.2. Novelty of the work

From the case studies of the SADA method and long-term perspective, the novelty of the research work can be summarised as:

1) Optimize existing programs *DARwind* and combine the AI technology to create a novel methodology SADA using big data and numerical simulation.
2) Comprehensive use of aero-hydro-servo-elastic theories of FOWTs to build an integrated coupled dynamic model. And put forward the concept of interdisciplinary KDPs involved in the prediction of a full-scale *Hywind* FOWT.

10.3. Future work

The SADA method still faces many challenges. At present, only limited cases are used to prove its feasibility. More data and even various types of FOWTs data will be needed in the future.

From the perspective of the application of AI technology, the hyperparameters involved have not been sufficiently analysed. The reinforcement learning framework is developing rapidly, and more algorithms can be used as SADA options. The most important of these is the reliability of *DARwind* as an agent. Therefore, the reliability of *DARwind* needs to be further improved. The closer its numerical results are to the target data, the more accurate and efficient the optimisation effect.

It is not only dependent on the agent, in addition to the hyperparameters of the deep neural network, whether it is the weight of the difference, the setting of the boundary conditions of each KDP, or the limitation of each action, etc., there are more verifications and needs optimisation. Further exploration takes time and experience. For example, according to the designer's needs, whether the BP optimisation in the ANN can be applied to the measured data. In this way, specific physical quantities in the dynamic performance of FOWT can be predicted more quickly. In terms of reinforcement learning, more control

mechanisms can be added to FOWT to improve its dynamic performance. Others include more specific case studies on the mooring, blades, etc.

List of reference

Ahn, H.-J. and Shin, H. (2017) 'Model test & numerical simulation of OC3 spar type floating offshore wind turbine', *International Journal of Naval Architecture and Ocean Engineering*, 11(1), pp. 1-10 https://doi.org/10.1016/j.ijnaoe.2017.09.010.

Alpaydin, E. (2020) *Introduction to machine learning*. 3 edn. IEEE Xplore: MIT press https://ieeexplore-ieee-org.libproxy.ncl.ac.uk/servlet/opac?bknumber=6895440 (Accessed: Jan 20 2022).

Amaral, G.A., Mello, P.C., do Carmo, L.H., Alberto, I.F., Malta, E.B., Simos, A.N., Franzini, G.R., Suzuki, H., Gonçalves, R.T.J.J.o.M.S. and Engineering (2021) 'Seakeeping Tests of a FOWT in Wind and Waves: An Analysis of Dynamic Coupling Effects and Their Impact on the Predictions of Pitch Motion Response', 9(2), p. 179 https://doi.org/10.3390/jmse9020179.

Andreaus, U., Baragatti, P. and Placidi, L. (2016) 'Experimental and numerical investigations of the responses of a cantilever beam possibly contacting a deformable and dissipative obstacle under harmonic excitation', *International Journal of Non-Linear Mechanics*, 80, pp. 96-106 https://doi.org/10.1016/j.ijnonlinmec.2015.10.007.

Antonutti, R., Poirier, J.-C. and Gueydon, S. (2020) 'Coupled testing of floating wind turbines in waves and wind using winches and software-in-the-loop', *Offshore Technology Conference*. Houston, Texas, USA, May 4–7, 2020. OnePetro. Available at: https://onepetro.org/OTCONF/proceedings-abstract/20OTC/2-20OTC/D021S019R001/110536.

Bachynski, E.E., Chabaud, V. and Sauder, T. (2015) 'Real-time hybrid model testing of floating wind turbines: sensitivity to limited actuation', *Energy Procedia*, 80, pp. 2-12 https://doi.org/10.1016/j.egypro.2015.11.400.

Bachynski, E.E., Etemaddar, M., Kvittem, M.I., Luan, C. and Moan, T. (2013) 'Dynamic analysis of floating wind turbines during pitch actuator fault, grid loss, and shutdown', *Energy Procedia*, 35, pp. 210-222 https://doi.org/10.1016/j.egypro.2013.07.174.

Bachynski, E.E., Thys, M., Sauder, T., Chabaud, V. and Sæther, L.O. (2016) 'Real-Time Hybrid Model Testing of a Braceless Semi-Submersible Wind Turbine: Part II—Experimental Results', *ASME 2016 35th International Conference on Ocean, Offshore and Arctic Engineering*. Busan, South Korea, June 19–24. ASME: American Society of Mechanical Engineers, pp. V006T09A040-V006T09A040. Available at: https://doi.org/10.1115/OMAE2016-54437 (Accessed: Jan 20 2022).

Bahramiasl, S., Abbaspour, M. and Karimirad, M. (2018) 'Experimental study on gyroscopic effect of rotating rotor and wind heading angle on floating wind turbine responses', *International Journal of Environmental Science and Technology*, 15, pp. 2531-2544 https://doi.org/10.1007/s13762-017-1519-4.

Bayati, I., Belloli, M., Bernini, L., Fiore, E., Giberti, H. and Zasso, A. (2016) 'On the functional design of the DTU10 MW wind turbine scale model of LIFES50+ project',

Journal of Physics: Conference Series, 753(5), p. 052018 https://doi.org/10.1088/1742-6596/753/5/052018.

Bayati, I., Belloli, M., Bernini, L. and Zasso, A. (2017) 'Aerodynamic design methodology for wind tunnel tests of wind turbine rotors', *Journal of Wind Engineering and Industrial Aerodynamics*, 167, pp. 217-227 https://doi.org/10.1016/j.jweia.2017.05.004.

Bayati, I., Belloli, M. and Facchinetti, A. (2013) *Wind Tunnel Tests on Floating Offshore Wind Turbines: A Proposal for Hardware-in-the-Loop Approach to Validate Numerical Codes*. https://doi.org/10.1260/0309-524X.37.6.557 (Accessed: 24 Jan 2022).

Bayati, I., Belloli, M., Ferrari, D., Fossati, F. and Giberti, H. (2014) 'Design of a 6-DoF Robotic Platform for Wind Tunnel Tests of Floating Wind Turbines', *Energy Procedia*, 53 https://doi.org/10.1016/j.egypro.2014.07.240.

Berthelsen, P.A., Bachynski, E.E., Karimirad, M. and Thys, M. (2016) 'Real-Time Hybrid Model Tests of a Braceless Semi-Submersible Wind Turbine: Part III—Calibration of a Numerical Model', *ASME 2016 35th International Conference on Ocean, Offshore and Arctic Engineering*. American Society of Mechanical Engineers. Available at: https://doi.org/10.1115/OMAE2016-54640 (Accessed: 24 Jan 2022).

Beyer, F., Choisnet, T., Kretschmer, M. and Cheng, P.W. (2015) 'Coupled MBS-CFD simulation of the IDEOL floating offshore wind turbine foundation compared to wave tank model test data', *The Twenty-fifth International Ocean and Polar Engineering Conference*. Kona, Hawaii, USA, June 21-26. OnePetro. Available at: https://elib.uni-stuttgart.de/bitstream/11682/3990/1/15TPC_0475Beyer.pdf (Accessed: Jan 19 2022).

Blusseau, P. and Patel, M.H. (2012) 'Gyroscopic effects on a large vertical axis wind turbine mounted on a floating structure', *Renewable Energy*, 46, pp. 31-42 https://doi.org/10.1016/j.renene.2012.02.023.

Bottasso, C.L., Campagnolo, F. and Petrović, V. (2014) 'Wind tunnel testing of scaled wind turbine models: Beyond aerodynamics', *Journal of Wind Engineering and Industrial Aerodynamics*, 127, pp. 11-28 https://doi.org/10.1016/j.jweia.2014.01.009.

Bredmose, H., Lemmer, F., Borg, M., Pegalajar-Jurado, A., Mikkelsen, R.F., Larsen, T.S., Fjelstrup, T., Yu, W., Lomholt, A.K. and Boehm, L. (2017) 'The Triple Spar campaign: Model tests of a 10MW floating wind turbine with waves, wind and pitch control', *Energy Procedia*, 137, pp. 58-76 https://doi.org/10.1016/j.egypro.2017.10.334.

Browning, J.R., Jonkman, J., Robertson, A. and Goupee, A.J. (2014) 'Calibration and validation of a spar-type floating offshore wind turbine model using the FAST dynamic simulation tool', *Journal of physics: conference series*. Oldenburg, Germany. IOP Publishing, p. 012015. Available at: https://doi.org/10.1088/1742-6596/555/1/012015 (Accessed: 22 Jan 2022).

Butterfield, S., Musial, W., Jonkman, J. and Sclavounos, P. (2007) 'Engineering Challenges for Floating Offshore Wind Turbines', *The 2005 Copenhagen Offshore Wind Conference*. Copenhagen, Denmark, 2007-09-01. Research Org.: National Renewable

Energy Lab. (NREL), Golden, CO (United States). Available at: http://www.osti.gov/scitech/servlets/purl/917212.

Cao, Q., Xiao, L., Cheng, Z. and Liu, M. (2021) 'Dynamic responses of a 10 MW semi-submersible wind turbine at an intermediate water depth: A comprehensive numerical and experimental comparison', *Ocean Engineering*, 232, p. 109138 https://doi.org/10.1016/j.renene.2018.08.042.

Cao, Y. and Tahchiev, G. (2013) 'A study on an active hybrid decomposed mooring system for model testing in ocean basin for offshore platforms', *ASME 2013 32nd International Conference on Ocean, Offshore and Arctic Engineering*. Nantes, France, June 9–14, 2013. American Society of Mechanical Engineers. Available at: https://doi.org/10.1115/OMAE2013-11471 (Accessed: 23 Jan 2022).

Carrion, J.E. and Spencer Jr, B.F. (2007) *Model-based strategies for real-time hybrid testing* (1940-9826). Newmark Structural Engineering Laboratory. University of Illinois at Urbana-Champaign. Urbana-Champaign., N.S.E.L.U.o.I.a. [Online]. Available at: http://hdl.handle.net/2142/3629 (Accessed: 23 Jan 2022).

Cermelli, C., Aubault, A., Roddier, D. and McCoy, T. (2010) 'Qualification of a Semi-Submersible Floating Foundation for Multi-Megawatt Wind Turbines', *Offshore Technology Conference*. Houston, Texas, USA, 2010/1/1/. OTC: Offshore Technology Conference. Available at: https://doi.org/10.4043/20674-MS (Accessed: 21 Jan 2022).

Cermelli, C., Roddier, D. and Aubault, A. (2009) 'WindFloat: A Floating Foundation for Offshore Wind Turbines—Part II: Hydrodynamics Analysis', *ASME 2009 28th International Conference on Ocean, Offshore and Arctic Engineering*. Honolulu, Hawaii, USA. Volume 4: Ocean Engineering; Ocean Renewable Energy; Ocean Space Utilization, Parts A and B. Available at: https://doi.org/10.1115/OMAE2009-79231 (Accessed: 21 Jan 2022).

Chabaud, V., Steen, S. and Skjetne, R. (2013) 'Real-time hybrid testing for marine structures: challenges and strategies', *ASME 2013 32nd International Conference on Ocean, Offshore and Arctic Engineering*. Nantes, France, June 9–14, 2013. American Society of Mechanical Engineers. Available at: https://doi.org/10.1115/OMAE2013-10277.

Chakrabarti, S. (1998) 'Physical model testing of floating offshore structures', *Dynamic positioning conference*. Houston. Citeseer, pp. 1-33. Available at: https://citeseerx.ist.psu.edu/viewdoc/download?doi=10.1.1.594.9516&rep=rep1&type=pdf (Accessed: 22 Jan 2022).

Chen, J., Hu, Z., Liu, G. and Tang, Y. (2017) 'Comparison of different dynamic models for floating wind turbines', *Journal of Renewable Sustainable Energy*, 9(6), p. 063304 https://doi.org/10.1063/1.5002750.

Chen, J., Hu, Z., Liu, G. and Wan, D. (2019a) 'Coupled aero-hydro-servo-elastic methods for floating wind turbines', *Renewable Energy*, 130, pp. 139-153 https://doi.org/10.1016/j.renene.2018.06.060.

Chen, J., Hu, Z., Wan, D. and Xiao, Q. (2018) 'Comparisons of the dynamical characteristics of a semi-submersible floating offshore wind turbine based on two different blade concepts', *Ocean Engineering*, 153, pp. 305-318 https://doi.org/10.1016/j.oceaneng.2018.01.104.

Chen, J., Pei, A., Zhaorong, M. and Chengyan, P. (2020a) 'A Review of the Key Technologies for Floating Offshore Wind Turbines', *SOUTHERN ENERGY CONSTRUCTION*, 7(1), pp. 8-20 https://doi.org/10.16516/j.gedi.issn2095-8676.2020.01.002.

Chen, J.-h., Pei, A.-g., Chen, P. and Hu, Z.-q. (2021a) 'Study on Gyroscopic Effect of Floating Offshore Wind Turbines', *China Ocean Engineering*, 35(2), pp. 201-214 https://doi.org/10.1007/s13344-021-0018-z.

Chen, P., Chen, J. and Hu, Z. (2020b) 'Review of Experimental-Numerical Methodologies and Challenges for Floating Offshore Wind Turbines', *Journal of Marine Science and Application*, 19(3), pp. 339-361 https://doi.org/10.1007/s11804-020-00165-z.

Chen, P., Chen, J. and Hu, Z. (2021b) 'Software-in-the-Loop Combined Reinforcement Learning Method for Dynamic Response Analysis of FOWTs', *Frontiers in Marine Sciense*, 7(1242) https://doi.org/10.3389/fmars.2020.628225.

Chen, P., Hu, Z. and Hu, C. (2019b) 'Software-In-the-Loop Method to Predict the Global Dynamic Responses of Full-scale Floating Wind Turbines by Artificial Neural Network', *11th International Workshop on Ship and Marine Hydrodynamics*. Hamburg, Germany, Sep. Available at: http://hdl.handle.net/11420/9015 (Accessed: Jan 20 2022).

Chen, P., Jia, C., Ng, C. and Hu, Z. (2021c) 'Application of SADA method on full-scale measurement data for dynamic responses prediction of Hywind floating wind turbines', *Ocean Engineering*, 239, p. 109814 https://doi.org/10.1016/j.oceaneng.2021.109814.

Cordle, A. and Jonkman, J. (2011) 'State of the art in floating wind turbine design tools', *The Twenty-first International Offshore and Polar Engineering Conference*. Maui, Hawaii, June 19 – 24, 2011. NREL: International Society of Offshore and Polar Engineers. Available at: https://www.nrel.gov/docs/fy12osti/50543.pdf (Accessed: 23 Jan 2022).

Coulling, A.J., Goupee, A.J., Robertson, A.N., Jonkman, J.M. and Dagher, H.J. (2013) 'Validation of a FAST semi-submersible floating wind turbine numerical model with DeepCwind test data', *Journal of Renewable and Sustainable Energy*, 5(2), p. 023116 https://doi.org/10.1063/1.4796197.

Courbois, A., Ferrant, P., Flamand, O. and Rousset, J.-M. (2011) 'Wind Generation on Wave Tank for Floating Offshore Wind Turbine Applications', *Proceedings of the 13th international conference on wind engineering (ICWE13)*. Amsterdam, 10–15 July 2011. Multi-Science Publishing Co. Ltd. Available at: https://research.tue.nl/en/publications/proceedings-of-the-13th-international-conference-on-wind-engineer (Accessed: 22 Jan 2022).

Cruz, J. and Atcheson, M. (2016) *Floating Offshore Wind Energy: The next generation of wind energy*. Springer https://doi.org/10.1007/978-3-319-29398-1 (Accessed: Jan 20 2022).

De Klerk, D. (2009) *Dynamic response characterization of complex systems through operational identification and dynamic substructuring*. Doctoral thesis thesis. Delft University of Technology, The Netherlands [Online]. Available at: http://resolver.tudelft.nl/uuid:2e4dd63e-68d5-41a4-8201-1e784f2f752c (Accessed: 23 Jan 2022).

de Ridder, E., Otto, W., Zondervan, G., Savenije, F. and Huijs, F.A. (2013) 'State of the art model testing techniques for floating wind turbines', *EWEA Offshore*. Frankfurt Germany, Nov. Available at: https://www.marin.nl/en/publications/state-of-the-art-model-testing-techniques-for-floating-wind-turbines (Accessed: 21 Jan 2022).

de Ridder, E.-J., Otto, W., Zondervan, G.-J., Huijs, F. and Vaz, G. (2014) 'Development of a scaled-down floating wind turbine for offshore basin testing', *ASME 2014 33rd International Conference on Ocean, Offshore and Arctic Engineering*. San Francisco, California, USA, Oct. American Society of Mechanical Engineers. Available at: https://doi.org/10.1115/OMAE2014-23441 (Accessed: 21 Jan 2022).

De Wilde, J.J., Van Dijk, A.W., van den Berg, J. and Dekker, J. (2009) 'Direct time domain downtime assessment for LNG operations using computer cluster', *The Nineteenth International Offshore and Polar Engineering Conference*. Osaka, Japan, July 21–26, 2009. International Society of Offshore and Polar Engineers. Available at: https://onepetro.org/ISOPEIOPEC/proceedings-abstract/ISOPE09/All-ISOPE09/ISOPE-I-09-170/7546 (Accessed: 23 Jan 2022).

Delbene, L., Bayati, I., Facchinetti, A., Fontanella, A. and Belloli, M. (2015) 'A 6DoF hydrodynamic model for real time implementation in hybrid testing', https://www.sintef.no/globalassets/project/eera-deepwind-2018/posters/g_bayati_web.pdf.

Dong, H., Dong, H., Ding, Z., Zhang, S. and Chang (2020) *Deep Reinforcement Learning*. 1 edn. Springer, Singapore https://doi.org/10.1007/978-981-15-4095-0.

Driscoll, F., Jonkman, J., Robertson, A., Sirnivas, S., Skaare, B. and Nielsen, F.G. (2016) 'Validation of a FAST Model of the Statoil-hywind Demo Floating Wind Turbine', *Energy Procedia*, 94, pp. 3-19 https://doi.org/10.1016/j.egypro.2016.09.181.

Du, W., Zhao, Y., He, Y. and Liu, Y. (2016) 'Design, analysis and test of a model turbine blade for a wave basin test of floating wind turbines', *Renewable Energy*, 97, pp. 414-421 https://doi.org/10.1016/j.renene.2016.06.008.

Duan, F., Hu, Z., Liu, G. and Wang, J. (2016a) 'Experimental comparisons of dynamic properties of floating wind turbine systems based on two different rotor concepts', *Applied Ocean Research*, 58, pp. 266-280 https://doi.org/10.1016/j.apor.2016.04.012.

Duan, F., Hu, Z. and Niedzwecki, J. (2016b) 'Model test investigation of a spar floating wind turbine', *Marine Structures*, 49, pp. 76-96 https://doi.org/10.1016/j.marstruc.2016.05.011.

Duan, F., Hu, Z. and Wang, J. (2015) 'Model tests of a spar-type floating wind turbine under wind/wave loads', *International Conference on Offshore Mechanics and Arctic Engineering*. St. John's, NL, Canada, May 31–June 5, 2015. American Society of Mechanical Engineers. Available at: https://doi.org/10.1115/OMAE2015-41391.

EPRSC (2018) *Transforming our world with AI: UKRI's role in embracing the opportunity*. Available at: https://epsrc.ukri.org/research/ourportfolio/themes/artificial-intelligence-and-robotics/ (Accessed: Jan 20).

Equinor (2019) *Equinor and ORE Catapult collaborating to share Hywind Scotland operational data*. Available at: https://www.equinor.com/en/news/2019-11-28-hywind-scotland-data.html (Accessed: Jan 19).

Faltinsen, O. (1993) *Sea loads on ships and offshore structures*. Cambridge university press https://www.cambridge.org/gb/academic/subjects/engineering/engineering-design-kinematics-and-robotics/sea-loads-ships-and-offshore-structures?format=PB&isbn=9780521458702.

Farrugia, R., Sant, T. and Micallef, D. (2014) 'Investigating the aerodynamic performance of a model offshore floating wind turbine', *Renewable Energy*, 70, pp. 24-30 https://doi.org/10.1016/j.renene.2013.12.043.

Farrugia, R., Sant, T. and Micallef, D. (2016) 'A study on the aerodynamics of a floating wind turbine rotor', *Renewable energy*, 86, pp. 770-784 https://doi.org/10.1016/j.renene.2015.08.063.

Filippo, C., Carlo, L.B. and Paolo, B. (2014) 'Design, manufacturing and characterization of aero-elastically scaled wind turbine blades for testing active and passive load alleviation techniques within a ABL wind tunnel', *Journal of Physics: Conference Series*, 524(1), p. 012061 https://doi.org/10.1088/1742-6596/524/1/012061.

Fowler, M.J., Kimball, R.W., Thomas, D.A. and Goupee, A.J. (2013) 'Design and testing of scale model wind turbines for use in wind/wave basin model tests of floating offshore wind turbines', *ASME 2013 32nd International Conference on Ocean, Offshore and Arctic Engineering*. Nantes, France. American Society of Mechanical Engineers. Available at: https://doi.org/10.1115/OMAE2013-10122 (Accessed: 21 Jan 2022).

Froese, M. (2019) *Excipio Energy unveils new hybrid floating offshore wind platform*. Available at: https://www.windpowerengineering.com/excipio-energy-unveils-new-hybrid-floating-offshore-wind-platform/ (Accessed: Jan 19).

Fujiwara, H., Tsubogo, T. and Nihei, Y. (2011) 'Gyro Effect of Rotating Blades On the FloatingWind Turbine Platform InWaves', *The Twenty-first International Offshore and Polar Engineering Conference*. Maui, Hawaii, USA, Jun. International Society of Offshore and Polar Engineers. Available at:

http://legacy.isope.org/publications/proceedings/ISOPE/ISOPE%202011/data/papers/11TPC-530Fujiwa.pdf (Accessed: 21 Jan 2022).

Fylling, I. and Soedahl, N. (1995) *RIFLEX-Flexible Riser System Analysis Program. General Description* (STF-70A95217) (STF-70A95217). [Online]. Available at: https://www.osti.gov/etdeweb/biblio/282709.

Galván, J., Sánchez-Lara, M., Mendikoa, I., Pérez-Morán, G., Nava, V. and Rodríguez-Arias, R. (2018) 'NAUTILUS-DTU10 MW Floating Offshore Wind Turbine at Gulf of Maine: Public numerical models of an actively ballasted semisubmersible', *Journal of Physics: Conference Series: Global Wind Summit 2018*. Hamburg, 25-28 Sep. IOP Publishing. Available at: https://iopscience.iop.org/article/10.1088/1742-6596/1102/1/012015/pdf (Accessed: Jan 19 2022).

Gao, Z., Bingham, H.B., Ingram, H.B., Kolios, A., Karmakar, D., Utsunomiya, T., Catipovic, I., Colicchio, G., Rodrigues, J.M. and Adam, F. (2018) 'Committee V. 4: Offshore Renewable Energy', *Proceedings of the 20th International Ship and Offshore Structures Congress (ISSC 2018) Volume 2*. IOS Press. Available at: https://ebooks.iospress.nl/publication/49526 (Accessed: Jan 20 2022).

Gao, Z., Moan, T., Wan, L. and Michailides, C. (2016) 'Comparative numerical and experimental study of two combined wind and wave energy concepts', *Journal of Ocean Engineering and Science*, 1(1), pp. 36-51 https://doi.org/10.1016/j.joes.2015.12.006.

Garcia-Pineda, O., MacDonald, I.R., Li, X., Jackson, C.R., Pichel, W.G.J.I.J.o.S.T.i.A.E.O. and Sensing, R. (2013) 'Oil spill mapping and measurement in the Gulf of Mexico with textural classifier neural network algorithm (TCNNA)', *IEEE Journal of Selected Topics in Applied Earth Observations and Remote Sensing*, 6(6), pp. 2517-2525 http://dx.doi.org/10.1109/JSTARS.2013.2244061.

Goupee, A.J., Fowler, M.J., Kimball, R.W., Helder, J. and de Ridder, E.-J. (2014) 'Additional Wind/Wave Basin Testing of the DeepCwind Semi-Submersible With a Performance-Matched Wind Turbine', *ASME 2014 33rd International Conference on Ocean, Offshore and Arctic Engineering*. San Francisco, California, USA, OCt. Volume 9B: Ocean Renewable Energy: ASME. Available at: https://doi.org/10.1115/OMAE2014-24172.

Goupee, A.J., Kimball, R.W. and Dagher, H.J. (2017) 'Experimental observations of active blade pitch and generator control influence on floating wind turbine response', *Renewable Energy*, 104, pp. 9-19 https://doi.org/10.1016/j.renene.2016.11.062.

Gueydon, S. (2016) 'Aerodynamic Damping on a Semisubmersible Floating Foundation for Wind Turbines', *Energy Procedia*, 94, pp. 367-378 https://doi.org/10.1016/j.egypro.2016.09.196.

Guo, X. and Hernández-Lerma, O. (2009) 'Continuous-time Markov decision processes', in *Continuous-Time Markov Decision Processes. Stochastic Modelling and Applied Probability*. Springer, Berlin, Heidelberg, pp. 9-18 https://doi.org/10.1007/978-3-642-02547-1_2.

Halkyard, J. (2005) 'Floating Offshore Platform Design', in CHAKRABARTI, S.K. (ed.) *Handbook of Offshore Engineering*. Elsevier, pp. 419-661 https://doi.org/10.1016/B978-008044381-2.50010-2.

Hall, M., Goupee, A. and Jonkman, J. (2018) 'Development of performance specifications for hybrid modeling of floating wind turbines in wave basin tests', *Journal of Ocean Engineering and Marine Energy*, 4(1), pp. 1-23 https://doi.org/10.1007/s40722-017-0089-3.

Hall, M. and Goupee, A.J. (2018) 'Validation of a hybrid modeling approach to floating wind turbine basin testing', *Wind Energy*, 21, pp. 391-408 https://doi.org/10.1002/we.2168.

Hall, M., Moreno, J. and Thiagarajan, K. (2014) 'Performance specifications for real-time hybrid testing of 1: 50-scale floating wind turbine models', *ASME 2014 33rd International Conference on Ocean, Offshore and Arctic Engineering*. San Francisco, California, USA, Oct. American Society of Mechanical Engineers. Available at: https://doi.org/10.1115/OMAE2014-24497 (Accessed: 21 Jan 2022).

Hansen, A.M., Laugesen, R., Bredmose, H., Mikkelsen, R. and Psichogios, N. (2014) 'Small scale experimental study of the dynamic response of a tension leg platform wind turbine', *Journal of Renewable and Sustainable Energy*, 6(5), p. 053108 https://doi.org/10.1063/1.4896602.

Hansen, M.O.L. (2015) *Aerodynamics of wind turbines*. 3rd edn. London: Routledge https://doi.org/10.4324/9781315769981 (Accessed: 23 Jan 2022).

Hansen, M.O.L., Sørensen, J.N., Voutsinas, S., Sørensen, N. and Madsen, H.A. (2006) 'State of the art in wind turbine aerodynamics and aeroelasticity', *Progress in aerospace sciences*, 42(4), pp. 285-330 https://doi.org/10.1016/j.paerosci.2006.10.002.

Hanson, T.D., Skaare, B., Yttervik, R., Nielsen, F.G. and Havmøller, O. (2011) 'Comparison of measured and simulated responses at the first full scale floating wind turbine Hywind', *Proceedings of the European Wind Energy Association Annual Event*. Brussels, Belglum. Available at: https://www.ewea.org/annual2011/conference/ (Accessed: Jan 20 2022).

Hasager, C.B., Stein, D., Courtney, M., Peña, A., Mikkelsen, T., Stickland, M. and Oldroyd, A.J.R.S. (2013) 'Hub height ocean winds over the North Sea observed by the NORSEWInD lidar array: measuring techniques, quality control and data management', *Remote Sensing*, 5(9), pp. 4280-4303 https://doi.org/10.3390/rs5094280.

Holcomb, S.D., Porter, W.K., Ault, S.V., Mao, G. and Wang, J. (2018) 'Overview on deepmind and its alphago zero ai', *Proceedings of the 2018 international conference on big data and education*. Honolulu, HI, USA. Available at: https://doi.org/10.1145/3206157.3206174.

Hou, P., Zhu, J., Ma, K., Yang, G., Hu, W. and Chen, Z. (2019) 'A review of offshore wind farm layout optimization and electrical system design methods', *Journal of Modern*

Power Systems and Clean Energy, 7(5), pp. 975-986 https://doi.org/10.1007/s40565-019-0550-5.

Hovanky, V.N. (2017) 'The Mutation of Altruistic Intents in Scientific Research', *Intersect: The Stanford Journal of Science, Technology, and Society*, 10(2) https://ojs.stanford.edu/ojs/index.php/intersect/article/view/995/973.

Howard, R.A. (2002) 'Comments on the origin and application of Markov decision processes', *Operations Research*, 50(1), pp. 100-102 https://doi.org/10.1287/opre.50.1.100.17788.

IEA (2022) *IEA Wind TCP Task 30 Offshore Code Comparison Collaboration, Continuation, with Correlation and unCertainty*. Available at: https://iea-wind.org/task30/ (Accessed: 13 May).

Jain, A., Robertson, A.N., Jonkman, J.M., Goupee, A.J., Kimball, R.W. and Swift, A.H.P. (2012) 'FAST Code Verification of Scaling Laws for DeepCwind Floating Wind System Tests: Preprint', *The 22nd International Offshore and Polar Engineering Conference*. Rhodes, Greece, Jun. National Renewable Energy Laboratory (NREL), Golden, CO. Available at: https://www.nrel.gov/docs/fy12osti/54221.pdf (Accessed: 22 Jan 2022).

James, R. and Ros, M.C. (2015) *Floating offshore wind: market and technology review*. The Carbon Trust. 11-15 [Online]. Available at: https://prod-drupal-files.storage.googleapis.com/documents/resource/public/Floating%20Offshore%20Wind%20Market%20Technology%20Review%20-%20REPORT.pdf (Accessed: Jan 19 2022).

Jamieson, P. (2018) *Innovation in Wind Turbine Design, Second Edition*. John Wiley & Sons https://doi.org/10.1002/9781119137924 (Accessed: 21 Jan 2022).

Jeon, M., Lee, S. and Lee, S. (2014) 'Unsteady aerodynamics of offshore floating wind turbines in platform pitching motion using vortex lattice method', *Renewable Energy*, 65, pp. 207-212 https://doi.org/10.1016/j.renene.2013.09.009.

Jonkman, J. (2008) 'Influence of control on the pitch damping of a floating wind turbine', *The 2008 ASME Wind Energy Symposium*. Reno, Nevada, Jan. p. 1306. Available at: https://www.nrel.gov/docs/fy08osti/42589.pdf (Accessed: 22 Jan 2022).

Jonkman, J. (2010) *Definition of the floating system for Phase IV of OC3* (NREL/TP-500-47535). Golden, CO: National Renewable Energy Laboratory. [Online]. Available at: http://purl.access.gpo.gov/GPO/LPS123215 (Accessed: 22 Jan 2022).

Jonkman, J., Larsen, T., Hansen, A., Nygaard, T., Maus, K., Karimirad, M., Gao, Z., Moan, T. and Fylling, I. (2010) 'Offshore Code Comparison Collaboration within IEA Wind Task 23: Phase IV Results Regarding Floating Wind Turbine Modeling; Preprint', *2010 European Wind Energy Conference and Exhibition*. Warsaw Poland. National Renewable Energy Lab.(NREL), Golden, CO (United States). Available at: https://doi.org/10.13140/2.1.3576.5768 (Accessed: 23 Jan 2022).

Jonkman, J. and Musial, W. (2010) *Offshore code comparison collaboration (OC3) for IEA Wind Task 23 offshore wind technology and deployment* (NREL/TP-5000-48191 TRN: US201105%%1051). OSTI.GOV: National Renewable Energy Lab.(NREL), Golden, CO (United States). [Online]. Available at: https://www.osti.gov/biblio/1004009 (Accessed: Jan 19 2022).

Jonkman, J. and Sclavounos, P. (2006) 'Development of fully coupled aeroelastic and hydrodynamic models for offshore wind turbines', *44th AIAA Aerospace Sciences Meeting and Exhibit*. Reno, Nevada. p. 995. Available at: https://arc.aiaa.org/doi/abs/10.2514/6.2006-995 (Accessed: Jan 19 2022).

Jonkman, J.M. (2009) 'Dynamics of offshore floating wind turbines—model development and verification', *Wind Energy: An International Journal for Progress and Applications in Wind Power Conversion Technology*, 12(5), pp. 459-492 https://doi.org/10.1002/we.347.

Jonkman, J.M. and Buhl Jr, M.L. (2005) *Fast user's guide-updated august 2005* (NREL/TP-500-38230). National Renewable Energy Lab. (NREL), Golden, CO (United States): National Renewable Energy Laboratory (NREL), Golden, CO. [Online]. Available at: https://www.osti.gov/biblio/15020796 (Accessed: 23 Jan 2022).

Jonkman, J.M., Robertson, A. and Hayman, G.J. (2014) 'HydroDyn user's guide and theory manual', *National Renewable Energy Laboratory*, https://www.nrel.gov/wind/nwtc/assets/downloads/HydroDyn/HydroDyn_Manual.pdf.

José, A., Faisal, B., Marta, G., Joseba, G., Xabier, M., Felix, K. and Tor, A.N. (2014) 'Aerodynamic Thrust Modelling in Wave Tank Tests of Offshore Floating Wind Turbines Using a Ducted Fan', *Journal of Physics: Conference Series*, 524(1), p. 012089 http://dx.doi.org/10.1088/1742-6596/524/1/012089.

Karimirad, M. (2011) *Stochastic dynamic response analysis of spar-type wind turbines with catenary or taut mooring systems*. Norwegian University of Science and Technology [Online]. Available at: http://hdl.handle.net/11250/237877 (Accessed: 21 Jan 2022).

Karimirad, M., Bachynski, E.E., Berthelsen, P.A. and Ormberg, H. (2017) 'Comparison of Real-Time Hybrid Model Testing of a Braceless Semi-Submersible Wind Turbine and Numerical Simulations', *ASME 2017 36th International Conference on Ocean, Offshore and Arctic Engineering*. Trondheim, Norway, June 25–30, 2017. American Society of Mechanical Engineers. Available at: https://doi.org/10.1115/OMAE2017-61121 (Accessed: 24 Jan 2022).

Karimirad, M. and Moan, T. (2011) 'Extreme dynamic structural response analysis of catenary moored spar wind turbine in harsh environmental conditions', *Journal of offshore mechanics and Arctic engineering*, 133(4), p. 041103 https://doi.org/10.1115/1.4003393.

Kausche, M., Adam, F., Dahlhaus, F. and Großmann, J. (2018) 'Floating offshore wind - Economic and ecological challenges of a TLP solution', *Renewable Energy*, 126, pp. 270-280 https://doi.org/10.1016/j.renene.2018.03.058.

Klerk, D.d., Rixen, D.J. and Voormeeren, S.N. (2008) 'General framework for dynamic substructuring: history, review and classification of techniques', *AIAA journal*, 46(5), pp. 1169-1181 https://doi.org/10.2514/1.33274.

Koo, B.J., Goupee, A.J., Kimball, R.W. and Lambrakos, K.F. (2014) 'Model tests for a floating wind turbine on three different floaters', *Journal of Offshore Mechanics and Arctic Engineering*, 136(2), p. 020907 https://doi.org/10.1115/1.4024711.

Kopperstad, K.M., Kumar, R. and Shoele, K. (2020) 'Aerodynamic characterization of barge and spar type floating offshore wind turbines at different sea states', *Wind Energy*, 23(11), pp. 2087-2112 https://doi.org/10.1002/we.2547.

Kusiak, A., Zheng, H. and Song, Z. (2009) 'Wind farm power prediction: a data‐mining approach', *Wind Energy: An International Journal for Progress Applications in Wind Power Conversion Technology*, 12(3), pp. 275-293 https://doi.org/10.1002/we.295.

Kyrychko, Y.N., Blyuss, K.B., Gonzalez-Buelga, A., Hogan, S.J. and Wagg, D.J. (2006) 'Real-time dynamic substructuring in a coupled oscillator–pendulum system', *Proceedings of the Royal Society of London A: Mathematical, Physical and Engineering Sciences*. The Royal Society. Available at: https://doi.org/10.1098/rspa.2005.1624 (Accessed: 23 Jan 2022).

Larsen, T.J. and Hansen, A.M. (2007) *How 2 HAWC2, the user's manual*. Risø National Laboratory: Technical University of Denmark. [Online]. Available at: http://tools.windenergy.dtu.dk/HAWC2/manual/How2HAWC2_12_9.pdf.

Larsen, T.J. and Hanson, T.D. (2007) 'A method to avoid negative damped low frequent tower vibrations for a floating, pitch controlled wind turbine', *Journal of Physics: Conference Series*, 75(1), p. 012073 http://dx.doi.org/10.1088/1742-6596/75/1/012073.

Lee, K.H. (2005) *Responses of floating wind turbines to wind and wave excitation*. Massachusetts Institute of Technology [Online]. Available at: http://hdl.handle.net/1721.1/33564 (Accessed: 23 Jan 2022).

Li, G. (2014) 'A generic dynamically substructured system framework and its dual counterparts', *IFAC Proceedings Volumes*, 47(3), pp. 10101-10106 https://doi.org/10.3182/20140824-6-ZA-1003.01369.

Li, G. and Shi, J. (2010) 'On comparing three artificial neural networks for wind speed forecasting', *Applied Energy*, 87(7), pp. 2313-2320 https://doi.org/10.1016/j.apenergy.2009.12.013.

Li, H., Steurer, M., Shi, K.L., Woodruff, S. and Zhang, D. (2006) 'Development of a unified design, test, and research platform for wind energy systems based on hardware-in-the-loop real-time simulation', *IEEE Transactions on Industrial Electronics*, 53(4), pp. 1144-1151 https://doi.org/10.1109/TIE.2006.878319.

Li, L., Gao, Y., Hu, Z., Yuan, Z., Day, S. and Li, H. (2018) 'Model test research of a semisubmersible floating wind turbine with an improved deficient thrust force correction

approach', *Renewable Energy*, 119, pp. 95-105 https://doi.org/10.1016/j.renene.2017.12.019.

Li, L., Gao, Y., Ning, D. and Yuan, Z. (2020) 'Development of a constraint non-causal wave energy control algorithm based on artificial intelligence', *Renewable Sustainable Energy Reviews*, 138, p. 110519 https://doi.org/10.1016/j.rser.2020.110519.

Li, L., Gao, Z. and Yuan, Z.-M. (2019) 'On the sensitivity and uncertainty of wave energy conversion with an artificial neural-network-based controller', *Ocean Engineering*, 183, pp. 282-293 https://doi.org/10.1016/j.oceaneng.2019.05.003.

Li, S. (2003) 'Wind power prediction using recurrent multilayer perceptron neural networks', *2003 IEEE Power Engineering Society General Meeting (IEEE Cat. No. 03CH37491)*. Toronto, ON, Canada, 13-17 July IEEE. Available at: https://doi.org/10.1109/PES.2003.1270992 (Accessed: Jan 20 2022).

LIFES50+ (2022) *Innovative Floating offshore wind energy*. Available at: https://lifes50plus.eu (Accessed: 13 May).

Lillicrap, T.P., Hunt, J.J., Pritzel, A., Heess, N., Erez, T., Tassa, Y., Silver, D. and Wierstra, D. (2015) 'Continuous control with deep reinforcement learning', *Computing Research Repository*, abs/1509.02971 https://arxiv.org/abs/1509.02971.

Liu, X., Lu, C., Liang, S., Godbole, A. and Chen, Y. (2019) 'Improved dynamic stall prediction of wind turbine airfoils', *Energy Procedia*, 158, pp. 1021-1026 https://doi.org/10.1016/j.egypro.2019.01.247.

Liu, Y., Li, S., Yi, Q. and Chen, D. (2016) 'Developments in semi-submersible floating foundations supporting wind turbines: A comprehensive review', *Renewable and Sustainable Energy Reviews*, 60, pp. 433-449 https://doi.org/10.1016/j.rser.2016.01.109.

Liu, Y., Peng, Y. and Wan, D. (2015) 'Numerical investigation on interaction between a semi-submersible platform and its mooring system', *ASME 2015 34th International Conference on Ocean, Offshore and Arctic Engineering*. St. John's, Newfoundland, Canada. American Society of Mechanical Engineers. Available at: https://doi.org/10.1115/OMAE2015-41294 (Accessed: 23 Jan 2022).

Lu, Z. and Zhou, S. (2018) *Integration of large scale wind energy with electrical power systems in China*. John Wiley & Sons https://10.1002/9781118910054.

Luan, C., Michailides, C., Gao, Z. and Moan, T. (2014) 'Modeling and analysis of a 5 MW semi-submersible wind turbine combined with three flap-type Wave Energy Converters', *ASME 2014 33rd International Conference on Ocean, Offshore and Arctic Engineering*. San Francisco, California, USA. American Society of Mechanical Engineers. Available at: https://doi.org/10.1115/OMAE2014-24215.

Lugsdin, A. (2012) 'Real-time monitoring of FPSO mooring lines, risers', *Sea Technology*, 53(7), pp. 21-24 https://www.tritech.co.uk/uploaded_files/RAMS_SeaTech%20editorial.pdf.

Ma, Y., Hu, Z., Qu, Y. and Lu, G.J.O.e. (2013) 'Research on the characteristics and fundamental mechanism of a newly discovered phenomenon of a single moored FPSO in the South China Sea', *Ocean Engineering*, 59, pp. 274-284 https://doi.org/10.1016/j.oceaneng.2012.12.020.

Ma, Y., Hu, Z.-q. and Xiao, L.-f. (2014) 'Wind-wave induced dynamic response analysis for motions and mooring loads of a spar-type offshore floating wind turbine', *Journal of Hydrodynamics*, 26(6), pp. 865-874 https://doi.org/10.1016/S1001-6058(14)60095-0.

Mahmuddin, F., Klara, S., Sitepu, H. and Hariyanto, S. (2017) 'Airfoil Lift and Drag Extrapolation with Viterna and Montgomerie Methods', *Energy Procedia*, 105, pp. 811-816 https://doi.org/10.1016/j.egypro.2017.03.394.

Mahmuddina, F. (2016) 'The Effect of Flat Plate Theory Assumption in Post-Stall Lift and Drag Coefficients Extrapolation with Viterna Method', *Journal of Subsea and Offshore*, 6, pp. 9-13 https://isomase.org/JSOse/Vol.6%20Jun%202016/6-2.pdf.

Make, M. (2014) *Predicting scale effects on floating offshore wind turbines*. master thesis thesis. Delft University of Technology [Online]. Available at: http://resolver.tudelft.nl/uuid:78d0c912-47fb-4efb-8953-ad33d8fc7e96 (Accessed: 21 Jan 2022).

Martin, H.R. (2011) *Development of a scale model wind turbine for testing of offshore floating wind turbine systems*. The University of Maine [Online]. Available at: http://digitalcommons.library.umaine.edu/etd/1578 (Accessed: 21 Jan 2022).

Martin, H.R., Kimball, R.W., Viselli, A.M. and Goupee, A.J. (2014) 'Methodology for Wind/Wave Basin Testing of Floating Offshore Wind Turbines', *Journal of Offshore Mechanics and Arctic Engineering*, 136(2), pp. 020905-020905-3 https://doi.org/10.1115/1.4025030.

Masciola, M., Jonkman, J. and Robertson, A. (2013) 'Implementation of a multisegmented, quasi-static cable model', *The Twenty-third International Offshore and Polar Engineering Conference*. Anchorage, Alaska, June 30–July 5, 2013. OnePetro. Available at: https://onepetro.org/ISOPEIOPEC/proceedings-abstract/ISOPE13/All-ISOPE13/ISOPE-I-13-127/14583 (Accessed: 27 Jan 2022).

Matha, D., Schlipf, M., Cordle, A., Pereira, R. and Jonkman, J. (2011) 'Challenges in simulation of aerodynamics, hydrodynamics, and mooring-line dynamics of floating offshore wind turbines', *The Twenty-first International Offshore and Polar Engineering Conference*. Maui, Hawaii, USA. National Renewable Energy Laboratory (NREL), Golden, CO. Available at: https://onepetro.org/ISOPEIOPEC/proceedings-abstract/ISOPE11/All-ISOPE11/ISOPE-I-11-608/12370 (Accessed: 23 Jan 2022).

Matos, V.c.L., Ribeiro, E.O., Simos, A.N. and Sphaier, S.H. (2010) '2nd order pitch and roll slow motions of a semi-submersible platform: full scale measurements and theoretical predictions comparative study', *International Conference on Offshore Mechanics and Arctic Engineering*. Shanghai, China, June 6-11. ASME. Available at: https://doi.org/10.1115/OMAE2010-20898 (Accessed: Jan 19 2022).

McClelland, J.L., Rumelhart, D.E. and Group, P.R. (1987) *Parallel Distributed Processing, Volume 2: Explorations in the Microstructure of Cognition: Psychological and Biological Models*. MIT press https://web.stanford.edu/~jlmcc/papers/PDP/Volume%201/Chap1_Part1_PDP86.pdf.

Michailides, C., Gao, Z. and Moan, T. (2016) 'Experimental and numerical study of the response of the offshore combined wind/wave energy concept SFC in extreme environmental conditions', *Marine Structures*, 50, pp. 35-54 https://doi.org/10.1016/j.marstruc.2016.06.005.

Michailides, C., Luan, C., Gao, Z. and Moan, T. (2014) 'Effect of flap type wave energy converters on the response of a semi-submersible wind turbine in operational conditions', *ASME 2014 33rd International Conference on Ocean, Offshore and Arctic Engineering*. San Francisco, California, USA, Oct. American Society of Mechanical Engineers. Available at: https://doi.org/10.1115/OMAE2014-24065 (Accessed: 21 Jan 2022).

Muliawan, M.J., Karimirad, M. and Moan, T. (2013) 'Dynamic response and power performance of a combined Spar-type floating wind turbine and coaxial floating wave energy converter', *Renewable Energy*, 50, pp. 47-57 https://doi.org/10.1016/j.renene.2012.05.025.

Müller, K., Sandner, F., Bredmose, H., Azcona, J., Manjock, A. and Pereira, R. (2014) 'Improved tank test procedures for scaled floating offshore wind turbines', *Proceedings of the IWEC 2014*. Hannover, Sep 2-3. Available at: http://dx.doi.org/10.18419/opus-8261 (Accessed: 20 Jan 2022).

Munteanu, I., Bratcu, A.I., Bacha, S., Roye, D. and Guiraud, J. (2010) 'Hardware-in-the-loop-based simulator for a class of variable-speed wind energy conversion systems: Design and performance assessment', *IEEE Transactions on Energy Conversion*, 25(2), pp. 564-576 https://doi.org/10.1109/TEC.2010.2042218.

Murai, M. and Nishimura, R. (2010) 'A study on an experiment of behavior of a SPAR type offshore wind turbine considering rotation of wind turbine blades', *OCEANS 2010 IEEE-Sydney*. Sydney, NSW, Australia. IEEE. Available at: https://doi.org/10.1109/OCEANSSYD.2010.5603861 (Accessed: 21 Jan 2022).

Musial, W., Butterfield, S. and Boone, A. (2004) 'Feasibility of Floating Platform Systems for Wind Turbines', *42nd AIAA Aerospace Sciences Meeting and Exhibit*. Reno, Nevada, 5-8 January. Research Org.: National Renewable Energy Lab., Golden, CO. (US), p. 1007. Available at: http://www.osti.gov/scitech/servlets/purl/15005820 (Accessed: Jan 19 2022).

Myhr, A., Maus, K.J. and Nygaard, T.A. (2011) 'Experimental and computational comparisons of the OC3-Hywind and tension-leg-buoy (TLB) floating wind turbine conceptual designs', *The Twenty-first International Offshore and Polar Engineering Conference*. Maui, Hawaii, USA, June. International Society of Offshore and Polar Engineers. Available at: https://onepetro.org/ISOPEIOPEC/proceedings-abstract/ISOPE11/All-ISOPE11/ISOPE-I-11-560/12386 (Accessed: 21 Jan 2022).

Naciri, M., Waals, O. and de Wilde, J. (2007) 'Time Domain Simulations of Side-by-Side Moored Vessels: Lessons Learnt From a Benchmark Test', *ASME 2007 26th International Conference on Offshore Mechanics and Arctic Engineering*. San Diego, California, USA, June 10–15, 2007. American Society of Mechanical Engineers. Available at: https://doi.org/10.1115/OMAE2007-29756 (Accessed: 23 Jan 2022).

Namik, H. and Stol, K. (2013) 'A review of floating wind turbine controllers', in *Handbook of Wind Power Systems*. Springer, Berlin, Heidelberg, pp. 415-441 https://doi.org/10.1007/978-3-642-41080-2_13.

Nematbakhsh, A., Bachynski, E.E., Gao, Z. and Moan, T. (2015) 'Comparison of wave load effects on a TLP wind turbine by using computational fluid dynamics and potential flow theory approaches', *Applied Ocean Research*, 53, pp. 142-154 https://doi.org/10.1016/j.apor.2015.08.004.

Newton, J.M., Cameron, M.P., Urbina, R., Kimball, R.W., Goupee, A.J. and Thiagarajan, K.P. (2015) 'Characterization of a Wind Tunnel for Use in Offshore Wind Turbine Development', *ASME 2015 34th International Conference on Ocean, Offshore and Arctic Engineering*. St. John's, Newfoundland, Canada, Oct. American Society of Mechanical Engineers. Available at: https://doi.org/10.1115/OMAE2015-41979 (Accessed: 22 Jan 2022).

Nichols, J., Ronold, K.O. and Hopstad, A.L. (2016) 'Key Design Considerations', in Cruz, J. and Atcheson, M. (eds.) *Floating Offshore Wind Energy: The Next Generation of Wind Energy*. Cham: Springer International Publishing, pp. 241-269 https://doi.org/10.1007/978-3-319-29398-1_5.

Nishi, A., Miyagi, H. and Higuchi, K. (1993) 'A Computer-Controlled Wind Tunnel', in Murakami, S. (ed.) *Computational Wind Engineering 1*. Oxford: Elsevier, pp. 837-846 https://doi.org/10.1016/B978-0-444-81688-7.50095-4.

Ocean, S. (2017) *SIMO 4.10.3 User Guide*. [Online]. Available at: https://home.hvl.no/ansatte/tct/FTP/H2021%20Marinteknisk%20Analyse/SESAM/SESAM%20UM%20Brukermanualer/SIMO%20User%20Manual.pdf.

ORCA (2021) *Publications - Robot & Asset Self-Certification*. Available at: https://orcahub.org/latest/publications/publications-robot-asset-self-certification (Accessed: Jan 20).

Ormberg, H. and Bachynski, E.E. (2012) 'Global analysis of floating wind turbines: Code development, model sensitivity and benchmark study', *The Twenty-second International Offshore and Polar Engineering Conference*. Rhodes, Greece, June 17–22, 2012. International Society of Offshore and Polar Engineers. Available at: https://onepetro.org/ISOPEIOPEC/proceedings-abstract/ISOPE12/All-ISOPE12/ISOPE-I-12-166/12462 (Accessed: 23 Jan 2022).

Pao, L.Y. and Johnson, K.E. (2011) 'Control of wind turbines', *IEEE Control Systems*, 31(2), pp. 44-62 https://doi.org/10.1109/MCS.2010.939962.

Pardalos, P.M., Rebennack, S., Pereira, M.V.F., Iliadis, N.A. and Pappu, V. (2013) *Handbook of wind power systems*. Springer, Berlin, Heidelberg https://doi.org/10.1007/978-3-642-41080-2 (Accessed: 22 Jan 2022).

Pegalajar-Jurado, A., Bredmose, H., Borg, M., Straume, J.G., Landbø, T., Andersen, H.S., Yu, W., Müller, K. and Lemmer, F. (2018) 'State-of-the-art model for the LIFES50+ OO-Star Wind Floater Semi 10MW floating wind turbine', *Journal of Physics: Conference Series*. IOP Publishing. Available at: https://iopscience.iop.org/article/10.1088/1742-6596/1618/3/032033/meta (Accessed: Jan 19 2022).

Pelletier, F., Masson, C. and Tahan, A. (2016) 'Wind turbine power curve modelling using artificial neural network', *Renewable Energy*, 89, pp. 207-214 https://doi.org/10.1016/j.renene.2015.11.065.

Philippe, M., Courbois, A., Babarit, A., Bonnefoy, F., Rousset, J.-M. and Ferrant, P. (2013) 'Comparison of simulation and tank test results of a semi-submersible floating wind turbine under wind and wave loads', *ASME 2013 32nd International Conference on Ocean, Offshore and Arctic Engineering*. Nantes, France, Nov. American Society of Mechanical Engineers. Available at: https://doi.org/10.1115/OMAE2013-11271 (Accessed: 22 Jan 2022).

Pinto, A.V., Pegon, P., Magonette, G. and Tsionis, G. (2004) 'Pseudo - dynamic testing of bridges using non - linear substructuring', *Earthquake Engineering & Structural Dynamics*, 33(11), pp. 1125-1146 https://doi.org/10.1002/eqe.393.

Plummer, A.R. (2006) 'Model-in-the-loop testing', *Proceedings of the Institution of Mechanical Engineers, Part I: Journal of Systems and Control Engineering*, 220(3), pp. 183-199 https://doi.org/10.1243/09596518JSCE207.

Robertson, A., Jonkman, J., Masciola, M., Song, H., Goupee, A., Coulling, A. and Luan, C. (2014) *Definition of the semisubmersible floating system for phase II of OC4* (NREL/TP-5000-60601). OSTI.GOV: National Renewable Energy Lab.(NREL), Golden, CO (United States). [Online]. Available at: https://www.osti.gov/biblio/1155123 (Accessed: Jan 19 2022).

Robertson, A.N., Gueydon, S., Bachynski, E., Wang, L., Jonkman, J., Alarcón, D., Amet, E., Beardsell, A., Bonnet, P. and Boudet, B. (2020) 'OC6 Phase I: Investigating the underprediction of low-frequency hydrodynamic loads and responses of a floating wind turbine', *Journal of Physics: Conference Series*. IOP Publishing. Available at: https://doi.org/10.1088/1742-6596/1618/3/032033 (Accessed: 24 Jan 2022).

Robertson, A.N., Wendt, F., Jonkman, J.M., Popko, W., Dagher, H., Gueydon, S., Qvist, J., Vittori, F., Azcona, J. and Uzunoglu, E. (2017) 'OC5 project phase II: validation of global loads of the DeepCwind floating semisubmersible wind turbine', *Energy Procedia*, 137(Part of special issue: 14th Deep Sea Offshore Wind R&D Conference, EERA DeepWind'2017), pp. 38-57 https://doi.org/10.1016/j.egypro.2017.10.333.

Rockel, S., Camp, E., Schmidt, J., Peinke, J., Cal, R.B. and Hölling, M. (2014) 'Experimental study on influence of pitch motion on the wake of a floating wind turbine model', *Energies*, 7(4), pp. 1954-1985 https://doi.org/10.3390/en7041954.

Ronold, K.O., Hansen, V.L., Godvik, M., Landet, E., Jørgensen, E.R. and Hopstad, A.L.H. (2010) 'Guideline for Offshore Floating Wind Turbine Structures', *ASME 2010 29th International Conference on Ocean, Offshore and Arctic Engineering*. Shanghai, China. ASME. Available at: https://doi.org/10.1115/OMAE2010-20344 (Accessed: 1/20/2022).

Salehyar, S. and Zhu, Q. (2015) 'Aerodynamic dissipation effects on the rotating blades of floating wind turbines', *Renewable Energy*, 78, pp. 119-127 https://doi.org/10.1016/j.renene.2015.01.013.

Sauder, T., Chabaud, V., Thys, M., Bachynski, E.E. and Sæther, L.O. (2016) 'Real-Time Hybrid Model Testing of a Braceless Semi-Submersible Wind Turbine: Part I — The Hybrid Approach', *ASME 2016 35th International Conference on Ocean, Offshore and Arctic Engineering*. Busan, South Korea, June 19–24. Volume 6: Ocean Space Utilization; Ocean Renewable Energy, p. V006T09A039. Available at: https://doi.org/10.1115/OMAE2016-54435 (Accessed: Jan 20 2022).

Savenije, F. and Peeringa, J. (2014) 'Control development for floating wind', *Journal of Physics: Conference Series*. IOP Publishing. Available at: https://doi.org/10.1088/1742-6596/524/1/012090 (Accessed: 22 Jan 2022).

Schepers, J. and Snel, H. (1995) *Dynamic inflow. Yawed conditions and partial span pitch control* (ECN-C-95-056). Netherlands Energy Research Foundation (ECN), Petten (Netherlands). [Online]. Available at: https://www.osti.gov/etdeweb/biblio/195573 (Accessed: 26 Jan 2022).

Sebastian, T. and Lackner, M. (2012) 'Analysis of the induction and wake evolution of an offshore floating wind turbine', *Energies*, 5(4), pp. 968-1000 https://doi.org/10.3390/en5040968.

Sebastian, T. and Lackner, M.A. (2013) 'Characterization of the unsteady aerodynamics of offshore floating wind turbines', *Wind Energy*, 16(3), pp. 339-352 https://doi.org/10.1002/we.545.

Serraris, J.-J. (2009) 'Time domain analysis for DP simulations', *ASME 2009 28th International Conference on Ocean, Offshore and Arctic Engineering*. Honolulu, Hawaii, USA, May 31–June 5, 2009. American Society of Mechanical Engineers. Available at: https://doi.org/10.1115/OMAE2009-79587 (Accessed: 23 Jan 2022).

Sethuraman, L. and Venugopal, V. (2013) 'Hydrodynamic response of a stepped-spar floating wind turbine: Numerical modelling and tank testing', *Renewable Energy*, 52, pp. 160-174 https://doi.org/10.1016/j.renene.2012.09.063.

Shao, X. and Griffith, C. (2013) 'An overview of hybrid simulation implementations in NEES projects', *Engineering Structures*, 56, pp. 1439-1451 https://doi.org/10.1016/j.engstruct.2013.07.008.

Shin, H. (2011) 'Model Test of the OC3-Hywind Floating Offshore Wind Turbine', *The Twenty-first International Offshore and Polar Engineering Conference*. Maui, Hawaii, USA, Jun. ISOPE: International Society of Offshore and Polar Engineers. Available at:

https://onepetro.org/ISOPEIOPEC/proceedings-abstract/ISOPE11/All-ISOPE11/ISOPE-I-11-572/12280 (Accessed: 21 Jan 2022).

Signorelli, C., Villegas, C. and Ringwood, J. (2011) 'Hardware-in-the-loop simulation of a heaving wave energy converter', *Proceedings of the 9th European Wave and Tidal Energy Conference (EWTEC)*. School of Civil Engineering and the Environment, University of Southampton. Available at: https://doi.org/10.1007/s11012-021-01320-8 (Accessed: 23 Jan 2022).

Skaare, B., Nielsen, F.G., Hanson, T.D., Yttervik, R., Havmøller, O. and Rekdal, A. (2015) 'Analysis of measurements and simulations from the Hywind Demo floating wind turbine', *Wind Energy*, 18(6), pp. 1105-1122 https://doi.org/10.1002/we.1750.

Snel, H. and Schepers, J. (1995) *Joint investigation of dynamic inflow effects and implementation of an engineering method*. ECN-C- 94-107.

Spera, D.A. (2009) *Wind Turbine Technology: Fundamental Concepts in Wind Turbine Engineering*. ASME Press https://doi-org.libproxy.ncl.ac.uk/10.1115/1.802601 (Accessed: 26 Jan 2022).

Stetco, A., Dinmohammadi, F., Zhao, X., Robu, V., Flynn, D., Barnes, M., Keane, J. and Nenadic, G. (2019) 'Machine learning methods for wind turbine condition monitoring: A review', *Renewable Energy*, 133, pp. 620-635 https://doi.org/10.1016/j.renene.2018.10.047.

Stewart, G., Lackner, M., Robertson, A., Jonkman, J. and Goupee, A. (2012) 'Calibration and Validation of a FAST Floating Wind Turbine Model of the DeepCwind Scaled Tension-Leg Platform: Preprint', *The 22nd International Offshore and Polar Engineering Conference*. Rhodes, Greece, 17-22 June. National Renewable Energy Lab. (NREL), Golden, CO (United States): National Renewable Energy Laboratory (NREL), Golden, CO. Available at: https://www.osti.gov/servlets/purl/1040929. (Accessed: 22 Jan 2022).

Stewart, G. and Muskulus, M. (2016a) 'Aerodynamic Simulation of the MARINTEK Braceless Semisubmersible Wave Tank Tests', *Journal of Physics: Conference Series*, 749, p. 012012 https://doi.org/doi:10.1088/1742-6596/749/1/012012.

Stewart, G. and Muskulus, M. (2016b) 'A Review and Comparison of Floating Offshore Wind Turbine Model Experiments', *Energy Procedia*, 94, pp. 227-231 https://doi.org/10.1016/j.egypro.2016.09.228.

Sun, H., Gao, X. and Yang, H. (2020a) 'A review of full-scale wind-field measurements of the wind-turbine wake effect and a measurement of the wake-interaction effect', *Renewable Sustainable Energy Reviews*, 132, p. 110042 https://doi.org/10.1016/j.rser.2020.110042.

Sun, H., Qiu, C., Lu, L., Gao, X., Chen, J. and Yang, H.J.A.E. (2020b) 'Wind turbine power modelling and optimization using artificial neural network with wind field experimental data', 280, p. 115880 https://doi.org/10.1016/j.apenergy.2020.115880.

Sutton, R.S. and Barto, A.G. (2018) *Reinforcement learning: An introduction*. MIT press https://web.stanford.edu/class/psych209/Readings/SuttonBartoIPRLBook2ndEd.pdf.

Tanaka, K., Sato, I., Utsunomiya, T. and Kakuya, H. (2020) 'Validation of dynamic response of a 2-MW hybrid-spar floating wind turbine during typhoon using full-scale field data', *Ocean Engineering*, 218, p. 108262 https://doi.org/10.1016/j.oceaneng.2020.108262.

Thiagarajan, K.P. and Dagher, H.J. (2014) 'A review of floating platform concepts for offshore wind energy generation', *Journal of Offshore Mechanics and Arctic Engineering*, 136(2), p. 020903 https://doi.org/10.1115/1.4026607.

Tran, T., Kim, D. and Song, J. (2014) 'Computational fluid dynamic analysis of a floating offshore wind turbine experiencing platform pitching motion', *Energies*, 7(8), pp. 5011-5026 https://doi.org/10.3390/en7085011.

Utsunomiya, T., Sato, I., Yoshida, S., Ookubo, H. and Ishida, S. (2013) 'Dynamic Response Analysis of a Floating Offshore Wind Turbine During Severe Typhoon Event', *ASME 2013 32nd International Conference on Ocean, Offshore and Arctic Engineering*. Nantes, France, Nov 26. V008T09A032. Available at: https://doi.org/10.1115/OMAE2013-10618 (Accessed: Jan 20 2022).

Utsunomiya, T., Sato, T., Matsukuma, H. and Yago, K. (2009) 'Experimental Validation for Motion of a SPAR-Type Floating Offshore Wind Turbine Using 1/22.5 Scale Model', *ASME 2009 28th International Conference on Ocean, Offshore and Arctic Engineering*. Honolulu, Hawaii, USA, 16 Feb. ASEM. Available at: https://doi.org/10.1115/OMAE2009-79695 (Accessed: 21 Jan 2022).

Utsunomiya, T., Yoshida, S., Ookubo, H., Sato, I. and Ishida, S. (2014) 'Dynamic Analysis of a Floating Offshore Wind Turbine Under Extreme Environmental Conditions', *Journal of Offshore Mechanics and Arctic Engineering*, 136(2), p. 11 https://doi.org/10.1115/1.4025872.

Van den Boom, H., Koning, J. and Aalberts, P. (2005) 'Offshore monitoring; Real world data for design, engineering, and operation', *Offshore Technology Conference*. Houston, Texas. Offshore Technology Conference. Available at: https://onepetro.org/OTCONF/proceedings-abstract/05OTC/All-05OTC/OTC-17172-MS/29497 (Accessed: Jan 19 2022).

Vittori, F., Bouchotrouch;, F., Lemmer;, F. and Azcona., J. (2018) 'Hybrid scale testing of a 5 MW floating wind turbine using the SIL method compared with numerical models', *Ocean, Offshore and Arctic Engineering OMAE*. Madrid, Spain, June 17–22, 2018. Available at: https://doi.org/10.1115/OMAE2018-77853 (Accessed: 24 Jan 2022).

Walczak, S. (2019) 'Artificial neural networks', in *Advanced Methodologies and Technologies in Artificial Intelligence, Computer Simulation, and Human-Computer Interaction*. IGI Global, pp. 40-53 https://doi.org/10.4018/978-1-5225-7368-5.

Wan, L., Gao, Z. and Moan, T. (2015) 'Experimental and numerical study of hydrodynamic responses of a combined wind and wave energy converter concept in

survival modes', *Coastal Engineering*, 104, pp. 151-169 https://doi.org/10.1016/j.coastaleng.2015.07.001.

Wan, L., Gao, Z., Moan, T. and Lugni, C. (2016) 'Comparative experimental study of the survivability of a combined wind and wave energy converter in two testing facilities', *Ocean Engineering*, 111, pp. 82-94 https://doi.org/10.1016/j.oceaneng.2015.10.045.

Wan, L., Greco, M., Lugni, C., Gao, Z. and Moan, T. (2017) 'A combined wind and wave energy-converter concept in survival mode: Numerical and experimental study in regular waves with a focus on water entry and exit', *Applied Ocean Research*, 63, pp. 200-216 https://doi.org/10.1016/j.apor.2017.01.013.

Wang, K., Ji, C., Xue, H. and Tang, W. (2017) 'Frequency domain approach for the coupled analysis of floating wind turbine system', *Ships and Offshore Structures*, 12(6), pp. 767-774 https://doi.org/10.1080/17445302.2016.1241365.

Wayman, E.N. (2006) *Coupled dynamics and economic analysis of floating wind turbine systems*. Massachusetts Institute of Technology [Online]. Available at: https://dspace.mit.edu/handle/1721.1/35650 (Accessed: Jan 19 2022).

Wayman, E.N., Sclavounos, P.D., Butterfield, S., Jonkman, J. and Musial, W. (2006) 'Coupled Dynamic Modeling of Floating Wind Turbine Systems: Preprint', *The Offshore Technology Conference*. Houston, Texas, USA,, May. National Renewable Energy Lab.(NREL), Golden, CO (United States). Available at: https://doi.org/10.4043/18287-MS (Accessed: 23 Jan 2022).

Wehmeyer, C., Ferri, F., Frigaard, P.B. and Skourup, J. (2013) 'Experimental study of an offshore wind turbine TLP in ULS Conditions', *The Twenty-third International Offshore and Polar Engineering Conference*. Anchorage, Alaska, Jun. International Society of Offshore and Polar Engineers. Available at: https://onepetro.org/ISOPEIOPEC/proceedings-abstract/ISOPE13/All-ISOPE13/ISOPE-I-13-011/13638 (Accessed: 21 Jan 2022).

Wei, K., Arwade, S.R. and Myers, A.T. (2014) 'Incremental wind-wave analysis of the structural capacity of offshore wind turbine support structures under extreme loading', *Engineering Structures*, 79, pp. 58-69 https://doi.org/10.1016/j.engstruct.2014.08.010.

Wei, Q., Song, R., Li, B. and Lin, X. (2018) *Self-Learning Optimal Control of Nonlinear Systems*. Springer Singapore https://doi.org/10.1007/978-981-10-4080-1.

Wen, C. and Ru, F. (2019) *Artificial Neural Network Theory and Application*. Xidian University Press.

Wilson, R.E., Walker, S.N. and Heh, P. (1999) 'Technical and User's Manual for the FAST_AD Advanced Dynamics Code', *OSU/NREL Report*, (99-01) https://citeseerx.ist.psu.edu/viewdoc/download?doi=10.1.1.519.1005&rep=rep1&type=pdf.

Withee, J.E. (2004) *Fully coupled dynamic analysis of a floating wind turbine system*. Massachusetts Institute of Technology [Online]. Available at: https://dspace.mit.edu/handle/1721.1/43619 (Accessed: 23 Jan 2022).

Wu, J., Ding, J.-h., He, Y.-p. and Zhao, Y.-s. (2015) 'Study on unsteady aerodynamic performance of floating offshore wind turbine by CFD method', *The Twenty-fifth International Ocean and Polar Engineering Conference*. Kona, Hawaii, USA. International Society of Offshore and Polar Engineers. Available at: https://onepetro.org/ISOPEIOPEC/proceedings-abstract/ISOPE15/All-ISOPE15/ISOPE-I-15-016/14395 (Accessed: 21 Jan 2022).

Wu, X., Hu, Y., Li, Y., Yang, J., Duan, L., Wang, T., Adcock, T., Jiang, Z., Gao, Z. and Lin, Z. (2019) 'Foundations of offshore wind turbines: A review', *Renewable and Sustainable Energy Reviews*, 104, pp. 379-393 https://doi.org/10.1016/j.rser.2019.01.012.

Yu, W., Lemmer, F., Bredmose, H., Borg, M., Pegalajar-Jurado, A., Mikkelsen, R.F., Larsen, T.S., Fjelstrup, T., Lomholt, A.K., Boehm, L., Schlipf, D., Armendariz, J.A. and Cheng, P.W. (2017) 'The Triple Spar Campaign: Implementation and Test of a Blade Pitch Controller on a Scaled Floating Wind Turbine Model', *Energy Procedia*, 137, pp. 323-338 https://doi.org/10.1016/j.egypro.2017.10.357.

Zhao, W. and Wan, D. (2014) 'Wind turbine impacts on its semi-submersible floating supporting system for phase II of OC4', *The Twenty-fourth International Ocean and Polar Engineering Conference*. Busan, Korea, June 15–20, 2014. International Society of Offshore and Polar Engineers. Available at: https://onepetro.org/ISOPEIOPEC/proceedings-abstract/ISOPE14/All-ISOPE14/ISOPE-I-14-004/13623.

Zhou, H.F., Dou, H.Y., Qin, L.Z., Chen, Y., Ni, Y.Q. and Ko, J.M. (2014) 'A review of full-scale structural testing of wind turbine blades', *Renewable and Sustainable Energy Reviews*, 33, pp. 177-187 https://doi.org/10.1016/j.rser.2014.01.087.

Appendices

A. Tables

Table A.1 Different experimental methodologies of FOWTs.

Methodologies		Advantages	Disadvantages
Replace thrust	Use static lines or cables to replace a static thrust from a given turbine' thrust curve.	Easy to simulate static wind loads. Easy layout and preparation.	Lack of control or wind variability. No coupling effect (wind loads and the platform response). Inertial problems. No gyroscopic effects.
	Use the drag discs to reproduce the static wind loading.	Easy to calibrate wind loads. Any wind turbine can be simulated. Easy to simulate steady wind loads for the first part of the thrust curve (below rated speed). The gyroscopic effect available by means of a spinning disk.	Need a low turbulence wind generation system. The drag disk generates vortex shedding behind the disk induced vibrations. No control system. No negative damping (wind speed above the rated speed).
Scaled turbine	Use scaled turbines	Better represents the real scheme. Avoid anomalous phenomena due to vortex shedding. Easy to simulate gyroscopic forces.	Complex mechanical system (complex to calibrate wind loads). Low flexibility due to various blade geometry. Need a low turbulence wind generation system. Wind variability (intensity and directional variations) cannot be simulated with standard wind generation systems. Limited control strategies.
Real-time Hybrid	Use synchronized numerical models and actuator (fans and winches) to replace wind turbine loads without using wind generators.	The scalability and fidelity of basin experiment can be improved. The dissimilar scaling issue can be avoided. Any scale can be modelled.	The accurate estimation of the influence of sensor cables. The quality of virtual subsystems will affect results. Almost all the theories are adopted in numerical simulation which relies on assumptions. More problems (design, manufacture and optimization) may come, due to the need to find alternatives actuation system.
	Use a hydraulic transmission system to simulate 6DOF platform motions in a wind tunnel with a scaled wind turbine model.		

Table A.2 The algorithm of DDPG.

Algorithm 1 DDPG algorithm

Randomly initialize critic network $Q(s, a|\theta^Q)$ and actor $\mu(s|\theta^\mu)$ with weights θ^Q and θ^μ.
Initialize target network Q' and μ' with weights $\theta^{Q'} \leftarrow \theta^Q$, $\theta^{\mu'} \leftarrow \theta^\mu$
Initialize replay buffer R
for episode = 1, M **do**
  Initialize a random process $\mathcal{N}$ for action exploration
  Receive initial observation state s_1
  for t = 1, T **do**
    Select action $a_t = \mu(s_t|\theta^\mu) + \mathcal{N}_t$ according to the current policy and exploration noise
    Execute action a_t and observe reward r_t and observe new state s_{t+1}
    Store transition (s_t, a_t, r_t, s_{t+1}) in R
    Sample a random minibatch of N transitions (s_i, a_i, r_i, s_{i+1}) from R
    Set $y_i = r_i + \gamma Q'(s_{i+1}, \mu'(s_{i+1}|\theta^{\mu'})|\theta^{Q'})$
    Update critic by minimizing the loss: $L = \frac{1}{N}\sum_i (y_i - Q(s_i, a_i|\theta^Q))^2$
    Update the actor policy using the sampled policy gradient:

$$\nabla_{\theta^\mu} J \approx \frac{1}{N} \sum_i \nabla_a Q(s, a|\theta^Q)|_{s=s_i, a=\mu(s_i)} \nabla_{\theta^\mu} \mu(s|\theta^\mu)|_{s_i}$$

    Update the target networks:

$$\theta^{Q'} \leftarrow \tau\theta^Q + (1-\tau)\theta^{Q'}$$
$$\theta^{\mu'} \leftarrow \tau\theta^\mu + (1-\tau)\theta^{\mu'}$$

  end for
end for